The quantification of fibrosis in cleared human and mouse liver tissues by light-sheet fluorescence microscope using a slide-free approach

by

Buket ALPDOĞAN

A Dissertation Submitted to the
Graduate School of Health Sciences in
Partial Fulfilment of the Requirements for
the Degree of

Doctor of Philosophy

in

Cellular and Molecular Medicine

KOÇ ÜNİVERSİTESİ

August 26, 2022

The quantification of fibrosis in cleared human and mouse liver tissues by light-sheet fluorescence microscope using a slide-free approach

Koç University

Graduate School of Health Sciences

This is to certify that I have examined this copy of a doctoral dissertation by

Buket ALPDOĞAN

and have found that it is complete and satisfactory in all respects,
and that any and all revisions required by the final
examining committee have been made.

Committee Members:

Assoc. Prof. Dr. Müjdat Zeybel (Advisor)

Assist. Prof. Dr. Serçin Karahüseyinoğlu

Prof. Dr. Yasemin Gürsoy Özdemir

Prof. Dr. Alper Kiraz

Prof. Dr. Murat Dayangaç

Assoc. Prof. Dr. Onur Ferhanoğlu

Date: 26 August 2022

Dedicated to my family and lovely husband

For their endless love, support and encouragement

ABSTRACT

Background & Aim: Liver fibrosis is a common end point of any type of liver injury. Liver biopsy is the only reliable modality for determining the extent of fibrosis and subsequently providing patients with appropriate treatment. However, liver biopsy is not without limitations. Sampling error, observer variability, and semi-quantitative assessment are the significant limitations of the procedure, which may limit the accurate assessment of hepatic fibrosis. Besides, the utility of such small samples increases the staging inaccuracy. Problems in assessment of hepatic fibrosis limit the development of effective biomarkers and therapeutics particularly in NASH clinical trials. A slide-free examination of optically cleared liver biopsy samples may assist in accurate quantification of hepatic fibrosis. To this end, we developed a platform for quantifying hepatic fibrosis in human and mouse liver tissues utilizing a modified-CLARITY and custom-made light sheet fluorescence microscope.

Material and Method: A hundred and sixty-eight liver specimens from human subjects were included in this study. The cohort included fifty-seven NAFLD, thirty-eight viral hepatitis patients, and thirteen healthy subjects who underwent hepatic resection due to benign liver diseases. Sirius-red stained mouse and human liver sections were scored by an expert pathologist and Collagen proportionate area (CPA) analysed for 2D quantification of liver fibrosis. Liver specimens were cleared using the modified-CLARITY method and visualized with a custom-made light sheet microscope. To test the applicability of the method in intermediate stages of fibrosis, five animal models of liver disease were employed in C57Bl/6 mice. Collagen type I and Elastin were quantified in cleared human liver tissues using a slide-free approach via custom-made light sheet microscope. Multiple optical sections of whole liver samples were used to calculate collagen proportionate volume (CPV) and elastin proportionate volume (EPV).

Results: In this project, we successfully obtained transparent liver tissues for volumetric quantification of hepatic fibrosis. The modified-CLARITY method efficiently cleared human and mouse liver tissues. The major ECM proteins, Collagen type I and Elastin, were quantified in the human NAFLD and viral hepatitis cohort. Cut-off values were determined for CPV and EPV values for each fibrotic stages of human

NASH. Further analysis demonstrated substantial sectional variability between optical slices of volumetric imaging data. Coefficient of variation analysis determined the extent of variation and found 84.6% intermediate and high level variation for CPV and EPV sections of F3-4 groups of NAFLD. 3D fibrosis staging of optical sections with established cut-off values for CPV and EPV demonstrated that only 44% and 47% of optical sections would be staged the same for F3 and F4, respectively.

Conclusion: We developed a slide-free method for assessing the 3D pathology of hepatic fibrosis using a custom-made light sheet microscope. Volumetric image analysis of whole liver biopsies revealed substantial heterogeneity within the biopsy. Comprehensive profiling of extracellular matrix proteins in hepatic fibrosis and quantification with a slide-free non-destructive platform may improve the staging accuracy. Thus, utilizing this method may advance the treatments for NASH clinical studies.

ÖZETÇE

Fibrozun şeffaflaştırılmış insan ve fare karaciğer dokularında slaytsız bir yöntem kullanarak ışık tabakalı floresan mikroskobu ile kantifikasyonu

Plan ve amaç: Karaciğer fibrozu, her türlü karaciğer hasarında gelinen ortak bir son noktadır. Karaciğer biyopsisi, fibroz derecesini belirlemek ve ardından hastalara uygun tedaviyi sağlamak için kullanılan tek güvenilir yöntemdir. Ancak, karaciğer biyopsisinin bazı sınırlamaları vardır. Numune alma hatası, gözlemci değişkenliği ve yarı kantitatif değerlendirme, hepatik fibrozun doğru şekilde değerlendirilmesini sınırlandırabilecek yöntemin önemli bir kısıtlamalarıdır. Buna ek olarak, küçük parça numunelerin kullanımı da derecelendirme yanlışlığını artırabilir. Hepatik fibroz değerlendirmesindeki sorunlar, özellikle NASH klinik çalışmalarında etkili biyobelirteçlerin ve terapötiklerin gelişimini sınırlandırmaktadır. Şeffaflaştırılan karaciğer biyopsinin kesit alınmadan değerlendirilmesi, karaciğer fibrozunun doğru şekilde tayinine yardımcı olabilir. Bu amaçla, insan ve fare karaciğer dokularında hepatik fibrozun miktarını belirlemek için modifiye edilmiş CLARITY ve özel olarak üretilmiş bir ışık tabakalı floresan mikroskop kullanarak bir platform geliştirdik.

Materyal ve yöntem: Bu çalışmaya insan gönüllülerinden yüz altmış sekiz karaciğer örneği dahil edilmiştir. Kohort elli yedi NAFLD, otuz sekiz viral hepatit hastası ve on üç iyi huylu karaciğer hastalıkları nedeniyle hepatik rezeksiyon geçirmiş olguyu içeriyor. Sirius-Red boyalı fare ve insan karaciğer kesitleri, karaciğer fibrozunun 2B değerlendirilmesi için uzman patolog tarafından incelenmiş ve kolajen orantısal alan (CPA) ölçümleri hesaplanmıştır. Karaciğer numuneleri, modifiye ediliş CLARITY yöntemi kullanılarak temizlenmiş ve özel olarak hazırlanmış bir ışık levhası mikroskopuyla görüntülenmiştir. Yöntemin fibrozun ara aşamalarında uygulanabilirliğini test etmek için C57Bl/6 farede beş farklı karaciğer hastalığı modeli geliştirilmiştir. Kollajen tip I ve Elastin proteinleri, özel olarak hazırlanmış ışık tabakalı mikroskop aracılığıyla kesitsiz bir yaklaşım kullanılarak, temizlenmiş insan karaciğer dokularında miktarları belirlenmiştir. Kolajen orantılı hacmi (CPV) ve elastin orantılı hacmi (EPV) hesaplamak için tüm karaciğer numunelerinin birden fazla optik kesit kullanılmıştır.

Bulgular: Bu projede hepatik fibrozun volümetrik değerlendirilmesi için şeffaf karaciğer dokuları elde ettik. Modifiye edilmiş CLARITY yöntemi, insan ve fare karaciğer dokularını etkili bir şekilde şeffaflaştırmıştır. Karaciğer fibrozunda en çok üretilen ECM proteinleri, kolajen tip I ve Elastin, insan NAFLD ve viral hepatit kohortlarında miktarları belirlenmiştir. CPV ve EPV kesme değerleri, insan NASH kohortunda her bir fibrotik aşama için belirlenmiştir. Analizler, volümetrik görüntüleme verilerinin optik kesitleri arasında önemli kesitsel değişkenlik olduğunu göstermiştir. Varyasyon katsayısı analizi varyasyon derecesini belirlemiş ve F3-4 NAFLD gruplarının CPV ve EPV kesitleri için %84.6 ara ve yüksek seviyeli varyasyon bulmuştur. CPV ve EPV için belirlenmiş kesme değerlerine sahip optik kesitlerinin 3B derecelendirmesi, optik kesitlerinin yalnızca %44 ve %47'sinin F3 ve F4 için aynı şekilde derecelenebileceğini göstermiştir.

Sonuç: Özel olarak üretilmiş bir ışık tabakalı mikroskop kullanarak hepatik fibrozun 3B patolojisini değerlendirmek için slaytsız bir yöntem geliştirdik. Tüm karaciğer biyopsileri hacimsel görüntü analizi, biyopsi içinde önemli heterojenite olduğunu ortaya çıkardı. Hepatik fibrozda hücre dışı matriks proteinlerinin kapsamlı profillemesi ve kesitsiz ve tahrip etmeyen bir yöntemle miktarının belirlenmesi derecelendirme doğruluğunu artırabilir. Bu nedenle, bu yöntemin kullanılması NASH klinik çalışmalarına katkı sağlayabilir.

ACKNOWLEDGEMENTS

I would like to express my deepest gratitude to my advisor to Dr. Müjdat Zeybel, for being supportive and courageous. He assisted me in improving my research skills by providing me with the opportunity to work on this project.

I would also like to thank my committee members: Firstly, to Dr. Serçin Karahüseyinoğlu, for her guidance during this project. She was always there when I needed her guidance. Secondly, to Dr. Onur Ferhanoğlu for always listening to me with a huge interest and giving great opinions. Also, I would like to thank all other committee members for supporting this project with their brilliant ideas and great patience.

I could not have undertaken this journey without Dr. Yağmur Çetin Taş. I would like to extend my sincere thanks to her for supporting me in this project, even if you are very far away from Turkey. And thank you for being a good friend.

My special thanks is to Dr. Bürge Ulukan for her endless support and for being the best lab mate ever. She inspired me with her infinite questioning and hardworking character. I would also like to express my deepest thanks and love to my beautiful friend Dr. Noushin Zibandeh, for being one of the best lab mates ever and being supportive. This journey would not be easy without their love and support.

Thanks should also go to my family for their endless support and patience along this journey. I could not make this work possible without their love and support.

And lastly, the words cannot express my love and gratitude to my lovely husband. He was always there to figure out things with me and helped me even if the topic was not his interest. This work cannot be tolerable without his love and support.

TUBITAK 1001 (117S440) of Dr. Müjdat Zeybel funded this research.

TABLE OF CONTENTS

LIST OF TABLES

LIST OF FIGURES

ABBREVIATIONS

%	percent
α-SMA	alpha-smooth muscle actin
μL	microliter
Mm	micrometer
ACT-PRESTO	Active clearing pressure-related efficient and stable transfer of macromolecules into organs
AI	Artificial intelligence
ALT	Alanine aminotransferase
APRI	AST to Platelet Ratio Index
ARFI	Acoustic radiation force impulse imaging
AST	Aspartate aminotransferase
AUROC	Area under receiver operative curve
BABB	Benzyl alcohol benzyl benzoate
BMI	Bady mass index
BSA	Bovine serum albumin
CCD	Charge coupled device
CI	Confidence interval
CLARITY	Clear Lipid-exchanged Acrylamide-hybridized Rigid Imaging, Immunostaining, in situ-hybridization-compatible Tissue hYdrogel
CLD	Chronic liver disease
CMCD	Control methionine choline deficient diet
CMOS	Complementary metal–oxide–semiconductor
CNS	Central nervous system
COL1A1	Collagen type I alpha I
COL3A1	Collagen type III alpha I
CPA	Collagen proportionate area
CPV	Collagen proportionate volume
CT	Computed tomography
CTGF	Connective tissue growth factor
CV	Coefficient of variation
DISCO	Imaging of solvent-cleared organs
DLS	Digital light sheet
DMAB	para-Dimethyl amino benzaldehyde
DMSO	Dimethyl sulfoxide
ECM	Extra cellular matrix
ELF	Enhanced liver fibrosis
EPV	Elastin proportionate volume
ETC	Electrophoretic tissue clearing

FFPE	formalin fixed paraffin embedded
FIB4	Fibrosis-4 index
FISH	Fluorescence in situ hybridization
FLIP	Fatty liver inhibition of progression
FP	Fibrosis parameters
GAPDH	Glyceraldehyde-3-phosphate dehydrogenase
GFP	Green fluorescent protein
GGT	gamma-glutamyl transferase
HBV	Hepatitis B virus
HCC	Hepatocellular carcinoma
HCL	Hydrochloric acid
HCV	Hepatitis C virus
HFHS	High fat high sucrose
HIV	human immunodeficiency virus
HM	Hydrogel monomer
HSC	Hepatic stellate cell
IASL	International Association for the Study of the Liver
IHC	Immunohistochemistry
IJM	ImageJ Macro language
IQR	Interquartile range
IRB	Institutional Review Board
kPA	kilo pascal
LD	Low dose
LF	Low fat
LOX	Lysyl oxidase
LSFM	Light sheet fluorescence microscopy
MCD	Methionine choline deficient
MFAP-4	Microfibril-associated glycoprotein 4
MMP-2	Matrix metallo proteinase 2
MMP-9	Matrix metallo proteinase 9
MRE	Magnetic resonance elastography
MRI	Magnetic resonance imaging
NA	Numerical aperture
NAFLD	Nonalcoholic fatty liver disease
NASH	Nonalcoholic steatohepatitis
ND	Normal dose
NFS	NAFLD fibrosis score
PACT	passive CLARITY technique
PARS	perfusion-assisted agent release

PAS-D	Periodic acid–Schiff–diastase
PBS	Phosphate buffered saline
PCR	Polymerase chain reaction
PFA	Paraformaldehyde
PIIINP	Type III Procollagen Peptide
PSF	Point spread function
RGB	Red, green blue
RIMs	Refractive index matching solution
SAF	Steatosis activity fibrosis
SBB	Sudan black blocking
SDS	Sodium dodecyl sulfate
SHG	Second harmonic generation
SWE	Shear wave elastography
TE	Transient elastography
TGF-β	Transforming growth factor beta
TIMP-1	Tissue inhibitors of metalloproteinases 1
UPL	Universal prolibrary
US	Ultrasound
UV	Ultraviolet
VLDL	Very low density lipoprotein

Chapter 1: Introduction

1.1 General Information

1.1.1 Liver fibrosis and cirrhosis

Liver fibrosis is a dynamic process that occurs in response to persistent liver injuries. Metabolic diseases, chronic hepatitis, alcoholic and non-alcoholic fatty liver diseases are such types of injuries that may cause the progression of liver fibrosis to cirrhosis if the injury is not eliminated. Cirrhosis is the outcome of any type of chronic liver disease (CLD) irrespective of the aetiology. CLD is associated with a high rate of morbidity and mortality. Even though 1% of the population is estimated to be affected by liver fibrosis, autopsy studies recorded over 5-10% as affected. Chronic liver disease constitutes 2.4% of global deaths (Younossi et al., 2018). Despite medical advances and developments in treatment strategies, the prevalence and mortality of liver disease are increasing (Pimpin et al., 2018).

A wide range of chronic liver injuries, including viral hepatitis, cholestatic liver diseases, excessive alcohol consumption, and non-alcoholic fatty liver disease (NAFLD), may induce chronic hepatic inflammation and finally lead to liver fibrosis. Fibrotic matrix is mainly generated by hepatic stellate cells (HSCs) that reside in the space of Disse, i.e., a location between hepatocytes and a sinusoid, and secret excessive extracellular matrix (ECM) proteins (Bataller & Brenner, 2005). In healthy liver, HSCs are quiescent and vitamin A storing cells responsible for retinoic acid homeostasis. However, when persistent injuries stimulate them, they transdifferentiate into myofibroblasts (ECM-producing cells) and release vitamin A content. Upon activation of HSCs by the stimulants, the hepatocellular environment is replaced with fibrotic bundles. Collagen type I and type III are the major ECM proteins secreted from the HSCs. Glycoproteins and proteoglycans are also accumulated in fibrotic liver, such as elastin, fibronectin, and laminin. Furthermore, portal fibroblasts serve as a significant source of extracellular matrix proteins in cholestatic and viral liver injury. Bone marrow-derived Collagen type I producing cells, fibrocytes, can

also contribute to tissue fibrosis by secreting fibronectin and growth factors that promote deposition of ECM (Xu & Kisseleva, 2015).

When the therapeutic approaches are not sufficient to prevent disease progression, cirrhosis is predictable. Cirrhosis leads to further complications that cause life-threatening consequences, such as portal hypertension, capillarization of sinusoids, and regenerative nodules. Postal hypertension is the most common method to measure portal hypertension that causes further hepatocellular damage and systemic inflammation (Suk, 2014).

When the injury is removed , liver fibrosis is reversible in most of the cases; even cirrhosis may be resolved to some extent. Therefore, appropriate treatments are vital. To apply suitable therapies to the patients, determination of the accurate fibrotic stages have significant impact on the patients' stratification and prognosis.

1.1.2 Extracellular matrix remodelling in chronic liver diseases

The extracellular matrix (ECM) is a network for crosslinking macromolecular proteins providing structural support and a key element for the maintenance of tissue homeostasis. Cells are connected to the ECM by receiving information and degrading proteins and replacing them with new ones in order to maintain tissue homeostasis. To do so, cell surface receptors such as integrins provide interaction and transmit signals that regulate migration, cell adhesion, proliferation, apoptosis, survival, and differentiation (Wells, 2008).

The basement membrane is a type of ECM that consists of laminins, nidogen/entactin and non-fibrillar collagens, such as collagen type IV and keeps epithelium and mesenchyme separate. In contrast, the interstitial matrix is a type of ECM that is produced by all hepatocellular cells in normal conditions. Hepatocytes, cholangiocytes and sinusoidal endothelial cells synthesize fibrillar ECM to contribute the hepatic ECM in liver. Kupffer cells contributes to hepatic ECM by secreting ECM associated factors to regulate ECM (Arteel & Naba, 2020). It is unclear that quiescent HSCs contributes to fibrillar ECM in normal conditions (Friedman, 2010). However, upon activation, they secrete an excessive amount of ECM proteins, leading to scarred liver tissue. Collagen types I, III and V are primarily found in fibrillar collagens in the interstitial matrix. In chronic diseases,

such as viral hepatitis, non-alcoholic steatohepatitis (NASH), and alcohol abuse, persistent inflammation activates ECM-producing cells (HSCs) and thus liver fibrosis.

In healthy conditions, ECM synthesis is balanced by the matrix metalloproteinases (MMPs) and their inhibitors (tissue inhibitors of matrix metalloproteinases-TIMPs) to regulate ECM components within the liver. MMPs can degrade proteins within the ECM in normal liver; however, once HSCs are activated and secret collagens, increased stiffness of the liver leads to impaired tissue homeostasis. HSCs contribute to the synthesis of degradation proteins but lead to ECM imbalance in the fibrotic liver. Therefore, HSCs play a crucial role in controlling fibrosis production and degradation.

As the liver fibrosis progresses, increased amount of collagen crosslinking is observed (Iredale et al., 2013). The basement membrane collagen IV and laminin are also increased during the progression of fibrosis. Since the inflammation and ongoing deposition of collagens provoke the activation of HSCs and ECM production, liver matrix stiffness increases and correlates with the disease severity. In chronic liver diseases, there are significant imbalance of ECM regulators (MMPs and TIMPs) and signalling molecules, which results in the alterations of matrix degradation and production. Altered matrix degradation results in increased matrix stiffness because of the accumulated collagen deposits and their cross-linking. Cross-linking enzymes play a pivotal role in fibrosis and cancer progression by affecting the mechanical properties of the matrix.

In cirrhosis, cross-linking of collagen fibrils stabilize the matrix stiffness and prevent fibrosis reversibility. The cross-linking enzymes are lysyl oxidase (LOX) family enzymes and give resistance to proteolytic degradation and further promote excess deposition of ECM. Collagens and other ECM proteins, such as elastin, are cross-linked through specific LOX or LOX-like enzymes in order to enhance matrix stabilization. ECM is a reservoir for the signalling molecules, cytokines such as TGF-β and growth factors; thus, irregular ECM protein degradation leads to the release of these signalling molecules and, in turn, stimulates collagen production and promotes matrix maturation. TGF-β is released in latent form and stored in ECM and remains in inactive form until activated by MMP-dependent proteolysis. Activated TGF-β enhances ECM production and upregulates ECM-related gene expressions, revealing aggressive disease progression (Friedman, 2008).

1.1.3 Non-alcoholic fatty liver disease

Non-alcoholic fatty liver disease (NAFLD) is a chronic liver disease with a spectrum of liver pathologies, i.e., simple steatosis, non-alcoholic steatohepatitis (NASH), cirrhosis, and ultimately hepatocellular carcinoma (HCC). NAFLD prevalence is increasing globally in parallel to the prevalence of obesity and type 2 diabetes (Buzzetti 2016). Patients usually have no symptoms, or clinical features are vague. The presence of fibrotic disease is frequently detected by hepatic imaging, particularly by transient ultrasonography (FibroScan), and together with elevated liver enzymes (ALT and GGT) (Tovo et al., 2019). However, NASH diagnosis and staging is frequently determined by liver biopsy, which evaluates histological features; regarding steatosis, hepatocellular ballooning, and inflammation, as well as the presence of presinusoidal fibrosis.

NAFLD is a complex and multifactorial condition with many inflammatory factors and pathways known to be involved from hepatic or extrahepatic origins. Excess free fatty acid production and uptake can cause sustained inflammation in hepatocytes, triggering lipotoxic reactions within the liver and activating pro-inflammatory, pro-fibrotic, and pro-apoptotic signalling pathways. Extrahepatic organs such as adipose tissue may induce inflammation by releasing hormones such as leptin, low levels of adiponectin, and pro-inflammatory cytokines and chemokines.

Diagnosis of NASH may require a core liver biopsy procedure and assessment of histological specimens by an expert pathologist. Liver biopsy procedure is invasive with a low risk of morbidity and mortality. However, it is able to assess a full spectrum of histological lesions from steatosis to cirrhosis (Bedossa, 2016). Fibrosis has a unique pattern in perisinusoidal spaces in zone 3 that can be identified by connective tissue stains (Sirius Red or Masson Trichrome) in NAFLD. Limitations of liver biopsy, such as sampling error and observer variability, significantly affect the diagnosis and staging of NAFLD. Moreover, NASH clinical trials suffer from an inadequate precision to evaluate histological efficacy due to the biopsy-related limitations (Ratziu & Friedman, 2020). To date, there is no precise non-invasive marker that can be used to monitor fibrosis progression in NAFLD, nevertheless, there are biomarkers of fibrosis (e.g., proC3, FIB-4, ELF) which can be used for excluding significant fibrosis (Daniels et al., 2019; Masuzaki et al., 2020)

1.1.4 Assessment of liver fibrosis

Liver fibrosis evaluation is a critical element for determining the extent of hepatic scarring. The liver biopsy procedure is currently the most reliable method of measuring hepatic disease ; however, non-invasive procedures such as serum biomarkers and imaging techniques are also available. Both procedures will be discussed in the following sections:

Liver biopsy and scoring systems

Liver biopsy is used for histological assessment for diagnostic purposes, staging the severity of liver disease, and investigating liver lesions. Paul Ehrlich reported the first liver needle biopsy procedure in 1883. The procedure is central for patient management and clinical trials for histological efficacy of the treatment regimens in chronic liver diseases (Khalifa & Rockey, 2020). Although there is risk of complications such as bleeding and pain, liver biopsy remains the "gold standard". The procedure involves obtaining small pieces of liver tissue with a needle and examination under the light microscope for the liver lesions by highlighting disease-specific structures. Usually, a 16 gauge needle is recommended for sampling, and the length of the sample should be at least 20 mm (Neuberger et al., 2020). Nevertheless, this assessment is imperfect. Liver biopsy represents only 1/50,000 of total liver mass and it may lead to some widely accepted limitations. Sampling variability is a significant limitation of biopsy procedures, which was previously demonstrated by dual core biopsy assessments (Ratziu et al., 2005). This limitation can affect the diagnosis, staging, and grading accuracy of liver disease since the liver disease does not always affect the liver in a homogenous pattern. Hence, it is widely accepted as an "imperfect gold standard" to evaluate and manage liver disease.

Liver biopsy specimens are subjected to serial processes for histological examination and diagnosis. After formalin fixation and paraffin embedding, 5 micrometre-thick liver biopsy sections are stained with Masson trichrome (or Sirius Red), PAS-D, iron, reticulin, and copper stains, and Haematoxylin & Eosin (H&E) to diagnose liver disease. Masson trichrome and H&E dyes are used for semi-quantitative staging of fibrosis and grading disease activity, respectively. Other abovementioned stains are used for diagnosing or excluding other aetiologies.

There are histological scoring systems for chronic liver disease to characterize and predict disease progression and to conclude the prognosis (**Table 1.1**). In chronic liver disease, the main purpose of the examination of liver biopsies is the determination of fibrosis stage and parenchymal alterations (architectural disruption). Knodell system was introduced which evaluates the feature of chronic hepatitis and proposed a histopathological activity index (Knodell et al., 1981). It gives the information based on four features: periportal and/or bridging necrosis, hepatocyte degeneration and/or focal necrosis, portal inflammation, and fibrosis. The major limitation of this score is that combining the score for activity and fibrosis; therefore, it is relatively insensitive to alterations in fibrosis. Later in 1995, Ishak et al. proposed a modification of this system, which is on a wider scale and is frequently used for viral hepatitis (Ishak et al., 1995) . In the meantime, the Scheuer system, followed by the International Association for the Study of the Liver (IASL) system, the Batts and Ludwig system, and the Meta-analysis of Histological Data in Viral Hepatitis (METAVIR) system has been proposed. More importantly, Ishak score is a 7-tier scoring system while others have only a 5-tier, which makes this system more sensitive to changes in fibrosis progression in chronic hepatitis. Since fibrosis is assessed semi-quantitatively in 5 or 7-tier systems, the variation within the systems is less in the early stages of fibrosis, but it is high regarding cirrhosis. Finally, Laennec et al. proposed a system for sub-classification of cirrhosis regarding the thickness of fibrous septa and nodule size (Kim et al., 2011). Furthermore, features of sub-classification are correlated with the clinical stage and portal hypertension. Then, this correlation was stressed by the need for comprehensive classification systems when developing new systems in several studies (Garcia-Tsao et al., 2010; Nagula et al., 2006).

Table 1.1. Classification systems used for staging fibrosis in chronic hepatitis

	Knodell (Knodell et al., 1981)
Fibrosis	**Description**
0	No fibrosis
1	Fibrous septal expansion
3	Bridging fibrosis (portal-portal or portal-central linkage)
4	Cirrhosis

	Scheuer (Scheuer, 1991)
Fibrosis	**Description**
0	No fibrosis
1	Enlarged portal tracts
2	Periportal fibrosis ± Periportal septa
3	Fibrosis with architectural distortion but no obvious cirrhosis
4	Cirrhosis (probable or definite)

	Batts and Ludwig (Batts & Ludwig, 1995)
Fibrosis	**Description**
0	No fibrosis
1	Portal/periportal fibrosis
2	Septal fibrosis
3	Bridging fibrosis with architectural distortion
4	Cirrhosis

	METAVIR (Group, 1994)
Fibrosis	**Description**
0	No fibrosis
1	Portal fibrosis without septa
2	Portal fibrosis few septa
3	Numerous septa without cirrhosis
4	Cirrhosis

	Laennec (Kutami et al., 2000)
Fibrosis	**Description**
0	No fibrosis
1	Minimal fibrosis
2	Mild fibrosis
3	Moderate fibrosis
4	Cirrhosis
4A	Cirrhosis, mild or probable
4B	Cirrhosis, moderate, at least two broad septa
4C	Cirrhosis, severe, at least one very broad septum or many minor nodules

	ISHAK (modified Knodell) (Ishak et al., 1995)
Fibrosis	**Description**
0	No fibrosis
1	Fibrous expansion of some portal areas with or without short fibrous septa
2	Fibrous expansion of most portal areas with or without short fibrous septa
3	Fibrous expansion of most portal areas with occasional portal to portal bridging
4	Fibrous expansion of portal areas with marked bridging (portal to portal as well as portal to central)
5	Marked bridging with occasional nodules (incomplete cirrhosis)
6	Cirrhosis

*The table contains the classification systems for staging fibrosis in chronic hepatitis patients.

NAFLD term includes a range of histopathological patterns (Bondini et al., 2007). Several scoring systems have been developed to evaluate steatosis, activity, and fibrosis. In 1999 Brunt et al. proposed a system for chronic hepatitis but then adjusted for the features of fatty liver disease (Brunt et al., 1999). This system evaluates steatosis, lobular inflammation, portal inflammation and hepatocyte ballooning degeneration to determine a grade. Fibrosis is staged on a 4-tier scale from 1 to 4 depending on zone 3 perisinusoidal and periportal fibrosis, bridging fibrosis and cirrhosis. The NASH Clinical Research Network (NASH-CRN) proposed a system which includes the evaluation of the whole spectrum of NAFLD in 2005 (Kleiner et al., 2005). The final score was based on the unweighted scores of each and ranged from 0 to 8. However, this system gives steatosis more weight and decreases sensitivity to changes in hepatocellular damage. Fibrosis is separately evaluated from the overall score, similar to the Brunt staging system. Notably, fibrosis stage 1 is subdivided into three as stage 1a (zone 3 perisinusoidal fibrosis, delicate), stage 1b (zone 3 perisinusoidal fibrosis, dense) and stage 1c (periportal fibrosis only). Finally, Bedossa et al. reported the SAF score (steatosis, activity, fibrosis), which measures activity as lobular inflammation and ballooning. Steatosis is graded from 0 to 3, and fibrosis is evaluated as the Brunt system from 1 to 4 (Bedossa & Consortium, 2014).

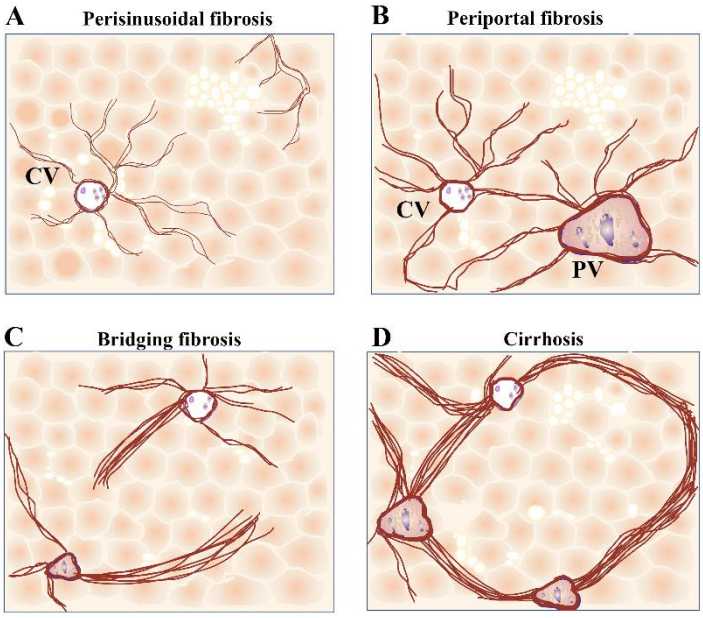

Figure 1.1 Histology images of fibrosis stages in NASH. The characteristic pattern of NASH fibrosis is displayed. Fibrosis is initiated in perisinusoidal area (A), then progresses to central/pericentral or portal/periportal regions (B), following that, ECM fibers span from portal to centrilobular regions (C), finally cirrhosis occurs (D).

Table 1.2 Classification systems for staging fibrosis in NAFLD

	Brunt (Brunt et al., 1999)
Fibrosis	**Description**
0	No fibrosis
1	Zone 3 perisinusoidal, focal or extensive fibrosis
2	Zone 3 perisinusoidal/pericellular fibrosis with associated focal or extensive periportal fibrosis
3	Zone 3 perisinusoidal/pericellular fibrosis and portal fibrosis with associated focal or extensive bridging fibrosis
4	Cirrhosis

	Kleiner (Kleiner et al., 2005)
Fibrosis	**Description**
0	No fibrosis
1a	Mild, zone 3 perisinusoidal fibrosis
1b	Moderate, zone 3 perisinusoidal fibrosis
1c	Portal/periportal fibrosis
2	Perisinusoidal and portal/periportal fibrosis
3	Bridging fibrosis
4	Cirrhosis

	NASH Score (Kleiner et al., 2005)
Steatosis	0-3
Lobular Inflammation	0-3
Hepatocyte ballooning	0-2
Total	unweighted scores of each to diagnose NASH
0-2	not NASH
3-4	borderline
5-8	NASH
Fibrosis	same as Kleiner system

	SAF score (Bedossa & Consortium, 2014)
Lobular Inflammation	0-2
Hepatocyte ballooning	0-2
Total	Activity score
Fibrosis	same as Kleiner system
Steatosis	0-3

*The table contains classification systems for staging fibrosis in NAFLD.

*NASH CRN and SAF scores use Kleiner classification system for staging fibrosis.

*Numeric values of NASH CRN and SAF scores can give the idea about the diagnosis of patients.

Liver biopsy procedure is regarded as an “imperfect gold standard” due to the several drawbacks. Firstly, it is an invasive procedure with a high cost and risk of complications such as bleeding and pain. Secondly, sampling error is a significant concern due to the investigating small piece of tissue which is taken from a relatively large tissue (1/50,000). Indeed, examination of one slice from a liver biopsy sample may aggravate the sampling variability. Inter- and intra-observer variability is also considered a significant problem for diagnosing NAFLD (Pournik et al., 2014). Importantly, semi-quantitative evaluation is another significant limitation of this procedure. Since the classification systems estimate fibrosis content from a small piece of tissue may lead to over or under-estimation of the fibrosis stage. All these limitations result in the inaccuracy of patient management, stratification, and unsuccessful validation of therapeutic modalities in clinical trials. To overcome the biopsy-based limitations, Standish et al. proposed a method to

quantify fibrosis content in liver biopsy samples by collagen proportionate area (CPA) measurement (Standish et al., 2006). They showed the nonlinear relationship between the Ishak score and fibrosis content as the stage increases. Later in 2014, Tsochatzis et al. validated the CPA measurements with the clinical outcomes to sub-classify cirrhosis (Tsochatzis et al., 2014). To validate the ability of CPA to quantify fibrosis in NAFLD patients, Buzzetti et al. revealed a study, which assessed 437 NAFLD patients from three European centres. The group tested the different magnifications for digital analysis to quantify pericellular fibrosis and validated CPA against clinical outcomes in NAFLD. They concluded that CPA is a useful additional assessment method to standard histological evaluations in NAFLD (Buzzetti et al., 2019).

Excess deposition of ECM within liver tissue is a significant landmark to determine the grade of scarring. Second harmonic generation microscopy (SHG) was used by Gailhouste et al. in 2010 to determine accumulated fibrillar collagen in liver biopsy sections at 60 μm depth (Gailhouste et al., 2010). This method detects triple helical structures in biomolecules using nonlinear endogenous signals. They developed a method to quantify fibrosis accurately using unstained liver biopsy sections and generated a Fibrosis-SHG-index. This application is based on the multiphoton microscopy technique and used to accurately quantify hepatic fibrosis in CLD. Furthermore, a dual-photon-based method was conducted by Wang et al. and suggested automated quantification of fibrosis-related parameters (qFPs) in NASH. They visualized unstained liver sections using SHG, followed by computer analysis of qFPs are determined for fibrosis assessment (Wang et al., 2020). Moreover, the machine learning approach has been gaining interest in recent years. Forlano et al. introduced a study that used this approach to quantify histological features in NAFLD in 2020 (Forlano et al., 2020). This method determined disease-specific histological features in NAFLD with a high level of inter- and intra-observer agreement ranging from 0.95 to 0.99. A recent study demonstrated 3D spatially resolved geometrical and functional models of optically cleared human liver in various stages of NAFLD using multiphoton microscopy (Segovia-Miranda et al., 2019). They found that the 3D spatial model might enable quantitative multi-parametric cellular and tissue signature identification to predict disease progression and new findings in NAFLD pathogenesis.

The assessment of liver fibrosis is critical in identifying the extent of damage in the liver. Improvements in anti-fibrotic and anti-viral therapies for attenuating chronic liver diseases have revealed that fibrosis is reversible if the underlying cause is eliminated (Ellis & Mann, 2012). Therefore, accurate assessment of the fibrosis stage is critical for the patient's prognosis, and there is an unmet need for better quantification modalities to accurately detect liver fibrosis stages in patients with chronic liver disease.

Non-invasive assessment methods of liver fibrosis

There are research studies that focus on finding non-invasive tests to predict liver injury. Non-invasive methods for assessing liver injury include serum biomarkers and imaging approaches. Liver fibrosis is a dynamic process which involves fibrogenesis and fibrolysis. Serum biomarkers can be calculated by serological tests that directly reflect extracellular matrix deposition/degradation or indirect biochemical tests to predict changes in liver function. Direct serum biomarkers such as hyaluronan, PIIINP (Procollagen Type I Carboxy terminal peptide and Procollagen type III amino-terminal peptide), MMPs, TIMPs, Laminin, TGF-B, CTGF, YKL-40, MFAP-4 (Microfibril-associated glycoprotein-4), and Cytokeratin 18 fragments. Hyaluronan is accepted as one of the best direct serum biomarkers, validated in NAFLD patients by having sensitivity and specificity values of 86%-100% and 88%, respectively (Suzuki et al., 2005). However, PIIINP is not only specific to liver fibrosis. Elevated levels of PIIINP are also reported in lung fibrosis, chronic pancreatitis, and rheumatologic diseases (Gressner et al., 2007). Indirect serum biomarkers are simple and inexpensive; thus, they can be calculated using routine biochemical tests. The first diagnostic test was ALT/AST ratio which is suggested for patients with NAFLD and having >1 should be associated with the presence of liver cirrhosis. AST to platelet ratio Index (APRI), Fibrosis-4 (FIB-4) and NAFLD fibrosis score (NFS) are commonly used in patients with NAFLD as well as HIV/HCV infected patients to detect liver fibrosis (Lee et al., 2021). Many of the non-invasive serum tests were developed in chronic hepatitis C patients, and cut-off values have been modified and adapted for advanced fibrosis in NAFLD patients. However, some non-invasive serum biomarkers are patented, such as FibroTest® , Fibrometer®, ELF score and Hepascore (Adams et al., 2005; Boursier et al., 2016; Leroy et al., 2014; Lichtinghagen et al., 2013).

Moreover, the abovementioned non-invasive serological tests have several drawbacks. They do not discriminate each fibrosis stages, and their ability is poor in detecting intermediate stages, thus requiring a secondary evaluation. Non-patented tests are simple and inexpensive; however, patented tests are not readily available and costly Even though their specificity is low in detecting in the "grey zone", they have a good performance in excluding or confirming cirrhosis (Patel & Sebastiani, 2020).

Imaging techniques are non-invasive tools to detect hepatic morphological changes and liver stiffness. The techniques comprise conventional ultrasound (US), computed tomography (CT) and magnetic resonance imaging (MRI), as well as ultrasound and magnetic resonance elastography techniques. Morphological assessment of the presence of liver fibrosis can be evaluated through US, CT, or MRI by characterizing disease-specific changes in advanced fibrosis. However, these techniques are unreliable and have poor sensitivity in detecting those changes in the early stages of liver fibrosis. Elastography is the most widely used imaging technique, which measures liver stiffness to detect liver fibrosis. Transient elastography (TE) is the type of elastography technique that uses shear wave elastography (SWE) to measure liver stiffness (de Lédinghen & Vergniol, 2008). Acoustic or mechanical pulses are used for the quantitative measurement of stiffness and expressed as kPA (kilopascal). TE is a tool that is largely studied on chronic hepatitis B/C, NASH, and autoimmune cholestatic liver diseases (Abenavoli & Beaugrand, 2012; Sporea et al., 2010; Tovo et al., 2019; Xu et al., 2017). TE does not provide morphological assessment since the ultrasound detector is one-dimensional. Acoustic radiation force impulse imaging (ARFI) and two-dimensional (2D) shear wave elastography (2D-SWE) are the type of other SWE methods. However, their performance in staging liver fibrosis needs validation by further studies (Agbim & Asrani, 2019). Magnetic resonance elastography (MRE) is a non-invasive imaging tool to measure the viscoelastic properties of the liver. Liver stiffness is a consequence of liver fibrosis, and it can be assessed using the propagation of mechanical waves. MRE has the capability to scan entire organ and can be applicable to patients with ascites and obesity as well. Several studies have demonstrated that MRE has better diagnostic performance than ARFI or TE in detecting mild fibrosis (Cui et al., 2016; Guo et al., 2015). Moreover, MRE has a high accuracy of

detecting significant, advanced fibrosis or cirrhosis, independent of BMI (body mass index) and aetiology of chronic liver disease (Singh et al., 2015).

1.1.5 Animal model of liver fibrosis

Animal models are one of the main approaches to improve our knowledge of human pathology to identify new targets and for testing new drugs. The main animal models used in this study are summarized in the following sections.

The methionine and choline deficient (MCD) diet

MCD model is a dietary model to mimic human NASH disease. It provides high sucrose and fat contents but lacks methionine and choline. Since methionine is an essential amino acid, it cannot be synthesized de novo, which is vital for producing many macromolecules. Likewise, choline is a major component of cells and the mitochondrial membrane and a precursor of acetylcholine. The deficiency of both components results in impaired phosphatidylcholine synthesis and decreased VLDL assembly and release. Thus, triglyceride removal is diminished, and lipids accumulate in hepatocytes. Furthermore, this model exhibits impairment in mitochondrial β-oxidation and activation of oxidative stress, hence promoting the generation of reactive oxygen species and steatohepatitis (Nevzorova et al., 2020). Thus, mice develop hepatic steatosis, inflammation leading to hepatic fibrosis. In general, three weeks of feeding is sufficient for developing steatohepatitis, while 5-8 weeks is sufficient for developing fibrosis. The most significant limitation of this model is the showing of an inverted metabolic profile of human NASH. Notably, there is a low concordance of gene expression profile in this model and human NASH (Parlati et al., 2021).

The high fat and high sucrose (HFHS) diet

High fat and high sucrose (HFHS) diets are used to create obesity and NAFLD profile in rodents. HFHS-induced animal model is the most widely used for the induction of NAFLD in mice. This model displays metabolic abnormalities such as obesity and insulin resistance, leading to hepatic steatosis and fibrosis. When mice were treated with an HFHS diet for 16 weeks, the hepatic fibrosis was not severe (Parlati et al., 2021). HFHS diet

develops insulin resistance and histological features of NASH in mice. A recent study has developed a simple-diet and chemical-induced NASH model of mice for rapid progression of fibrosis and hepatocellular carcinoma. A simple diet high in fat, fructose, and cholesterol was combined with a weekly low-dose intraperitoneal injection of carbon tetrachloride. The chemical induction was used to accelerate the fibrogenesis while the development of hepatic steatosis and inflammation was provided with diet (Tsuchida et al., 2018). A combination of high-fat diets with fructose or cholesterol has a significant effect on hepatic injury. Fructose intake induces de novo lipogenesis and prevents hepatic β-oxidation, which results in fat deposition in the liver. Similarly, using cholesterol in high-fat diets leads to more liver damage, inflammation, and fibrosis than in high-fat diets only.

The carbon tetrachloride injury model

Carbon tetrachloride (CCl4) is a widely used chemical to induce hepatocellular damage in rodents. Upon induction of CCl4, it is metabolized by cytochrome P450 enzymes in liver and converted to extremely reactive trichloromethyl (CCl3). Thus, reactive forms of CCl4 lead to hepatotoxic damage, inflammation, and fibrosis. Generally, 2-3 times injections per week is used for the induction of chronic liver disease. Depending on the dose and species employed in the study, the duration of the experiment can vary. It is common to maintain the experiment between 6 to 12 weeks. Longer than 15 weeks of exposure to CCl4 induces the development of hepatocellular carcinoma in mice (Fujii et al., 2010). In the development of cirrhosis and its complications, CCl4 is administered through inhalation in rodents. Typically, animals are exposed to air with CCl4 2-3 times per week. Animals develop ascites after 13-16 weeks, indicating the onset of decompensated cirrhosis (Nevzorova et al., 2020).

1.1.6 Three-dimensional (3D) Imaging tools for biological samples

Three-dimensional imaging has become more popular than ever, as it allows imaging of deep tissue structures in their inherent conformation. To perform 3D imaging, tissues have to be transparent. Tissue clearing is an important tool that allows the transparency of various types of tissues to interrogate deep structures within the sample. Investigating molecular events in their inherent conformation has been an intriguing

approach over the years. Biological samples are 3D and consist of various macromolecular structures such as proteins and lipids. Molecular structures within the cells have different light properties; thus, refractive indices are distinct. Therefore, the common aim of the clearing methods is to preserve those molecular structures such as proteins, nucleotides, DNAs, and RNAs while matching the internal refractive index of the sample by a different mode of action. Therefore, refractive indices are equilibrated using different tissue clearing techniques to obtain optically transparent samples for deep tissue imaging via multiphoton or light sheet microscopy systems.

1.1.7 Tissue Clearing Techniques

Tissue clearing is a technique that facilitates the assessment of tissue properties in physiological and pathological conditions by providing tissue integrity. The clearing term is used for the equilibration of the density of light scatterers. The major light scatterers are lipids within the tissue, and clearing techniques aim to minimize those light scatterers by a different mode of action.

In 1914, Werner Spalteholz had emerged the first clearing technique based on the incubation of the biological samples in benzyl alcohol and methyl salicylate solution (Spalteholz, 1914). Over the years, many other clearing techniques have been developed and adopted by researchers in order to image various biological samples, including bone, brain, lung, liver, kidney, and ovary. Clearing methods perform their action by a different mode of action and can be divided into four major groups; organic solvents, simple immersion, hyperhydration, and hydrogel embedding. Each group will be discussed in the following sections.

Organic Solvent-based methods

The pioneer Werner Spalteholz, a German scientist, established the first organic solvent-based method to clear large biological samples in 1914. Spalteholz method was unrivalled at the time and paved the way for the field of anatomy (Spalteholz, 1914). However, it was only suitable for large tissues, as it inflicted centimetre-deep damage to the tissue (Steinke & Wolff, 2001). The method was based on substituting water with a mixture of benzyl benzoate and methyl salicylate, reaching a refractive index of about 1.55.

Later, researchers have emerged various techniques and modified the Spalteholz method. In 2007, Dodt et al. implemented a dehydration step based on ethanol and reintroduced the protocol as an index-matching solution (benzyl alcohol and benzyl benzoate (BABB). BABB solution was exceptional for clearing mouse brains, embryos, and fruit flies (Dodt et al., 2007). However, several groups reported that using BABB solution as a clearing agent leads to the quenching of the fluorophores, shrinkage of the tissue, and labelling of artefacts (Hama et al., 2011; Ke et al., 2013; Yushchenko & Schultz, 2013). Over the years, researchers focused on achieving those obstacles by modifying former methods. Moreover, Ertürk et al. introduced 3DISCO, which was derived from the original BABB method, by changing the ethanol-based dehydration step with tetrahydrofuran (THF) dehydration and using dibenzyl ether (DBE) as a clearing agent (1.56) (Erturk et al., 2012). The method is compatible with most antibodies, which works well with immunofluorescence staining. Furthermore, it uses secondary antibodies conjugated with the Alexa fluorophore dye family that emit the signal in the far-red spectrum. They showed successful clearing with the 3DISCO method on various large tissues, including adult human brains. 3DISCO is very fast and compatible with the various labelling methods, including endogenous fluorophore expression. However, there are several drawbacks to this method. Cleared tissues cannot be stored in DBE since it degrades fluorophores over time. Significantly, labelling before the clearing step limits our choice of this method. Because one may choose which protein to target after obtaining cleared tissues. For that reason, we used other clearing protocols, which will be discussed and explained in the following sections.

In 2014, Reiner et al. focused on establishing a protocol for whole mount immunolabeling of deep tissue structures for volumetric imaging in mouse embryos and human brain slices. They combined the whole-mount immunolabeling method and 3DISCO for labelling of deep structures in dense adult tissues (Renier et al., 2014). The intention to develop a new method was due to the limitation on morphological alterations of 3DISCO. The new method is called iDISCO (immunolabeling-enabled three-dimensional imaging of solvent-cleared organs), which uses methanol treatment for deep antibody diffusion and reducing tissue autofluorescence (Renier et al., 2014). They visualised intact adult mouse brainstem, cerebellum, and entire mouse embryonic head to image dopaminergic neurons.

Importantly, transgenic reporters are compatible with the iDISCO protocol to highlight endogenous molecular structures. It enables the study of various biological events, such as cell proliferation, click chemistry and the detection of phosphorylated epitopes.

Meantime, another group was investigating the improvement of fluorescence preservation efficiency of the original BABB method in 2015 and generated the FluoclearBABB method. This method was based on managing the entire pH value throughout the experiment using either 1-propanol or tert-butanol during the dehydration process. They visualized neuronal connectivity in the whole mouse brain and concluded that adjusting dehydration agents not only resulted in better preservation of fluorescence but also improved the clearing efficiency (Schwarz et al., 2015).

Regarding iDISCO fundamental role in volumetric imaging, Reiner et al. created a new method for automated analysis of whole mouse brains and named iDISCO+ (Renier et al., 2016). They developed this protocol to reduce tissue shrinkage and better preserve brain samples. Light sheet fluorescence-based imaging of whole brains automatically transfers the data to the reference brain atlas via software (ClearMap) designed and realized by the group (Renier et al., 2016). ClearMap enables the analysis of counted cells in 3D, creates a distribution map and provides statistical analysis of whole brain samples in an hour.

One of the significant shortcomings of the 3DISCO method is the poor retention of endogenous fluorescence. Ertürk et al. created the uDISCO approach in 2016 to address this issue (Pan et al., 2016). The main aim was to prolong the preservation of endogenous fluorophores by changing the dehydration reagent with tert-butanol instead of THF. Additionally, the method includes diphenyl ether and vitamin E to improve the clearing efficiency. Although such techniques result in high transparent samples, there are few drawbacks which encourage researchers to develop new methods. The fluorescent signal can be loss dramatically and long period of time is required for clearing of the samples. Besides, the methods rely on carcinogenic substances which may have diverse effects on researchers. Therefore, Kleinberg et al. employed and described a different chemical from the BABB technique in 2017 (Wang et al., 2016). They used pH-sensitive ethanol dehydration and ethyl-3-phenyl- prop-2-enoate (ethyl cinnamate (Eci) as a refractive index matching solution. Due to the safety concerns on organic solvents, the group sought nontoxic compounds and found Eci, which is an FDA-approved food flavour used by

cosmetic companies. In chronic renal failure models, they imaged the vascular system of murine kidneys, including the heart, bones, and lungs (Klingberg et al., 2017). Due to the partial success in clearing rigid tissues, a new method introduced in order to improve the clearing efficiency of rigid structures in the whole body. Jing et al. described the method PEGASOS (polyethylene glycol (PEG)-associated solvent system), which has the ability to clear most of the tissues and better preservation of endogenous fluorescence. There are two ways to apply this method depending on which body parts will be cleared. The recirculation method includes a decalcification step for bones and teeth; however, passive immersion is used only for body parts. They successfully cleared a transgenic mouse head, including the skull, brain, muscles, and other tissues, and visualized it with a second harmonic generation (SHG) filter of two-photon microscopy. They showed the clearing efficiency of the PEGASOS method in murine tissues, including the liver, spleen, and brain (Jing et al., 2018). However, it has remained challenging to get consistent imaging and quantification of fluorescent protein signals deep into tissues. The recently released nanobody (VHH)-boosted 3D imaging of solvent-cleared organs (vDISCO) is a recently released method to investigate intact whole mouse bodies. Nanobodies are used to promote the signalling of fluorescence proteins in the mouse body, including bone. Delivery of nanobodies is provided with high-pressure cardiac perfusion to ensure the infiltration of nanobodies into the intact organs. They accomplished head-to-toe panoptic imaging of the whole mouse. By this method, they reached the subcellular resolution of neurons with light sheet fluorescence microscopy imaging and also built a map of a transgenic mouse in 3D (Cai et al., 2019).

To increase the signal-to-noise ratio for GFP (green fluorescent protein) tagged cellular event, Liu et al. improved the uDISCO method by determining the optimal pH value for the GFP signal. The new method is named alkaline pH-based uDISCO (a-uDISCO). The group reported that either short or long time preservation ability of a-uDISCO was remarkable and provided good cell morphology. They noted that the method is not only for whole brain tissue; it can also be used for other types of tissues, including muscle and the stomach (Li et al., 2018). Improvements in the a-uDISCO method on the preservation of GFP signals have encouraged other researchers to overcome the limitation of quenching fluorescence proteins in a short time in the original 3DISCO method. They

adjusted the temperature and pH conditions of the 3DISCO method and named the protocol FDISCO. They tested the efficacy of the method on various fluorescent probes in order to compare it with previous clearing methods. They realized that FDISCO preserves most of the fluorescent probes better than the original 3DISCO method (Qi et al., 2019).

In the meantime, an Eci-based new method was released, named second-generation Eci (2Eci). They introduced a 1-propanol-based dehydration reagent and used Eci for clearing. This method had better fluorescence preservation with various fluorescence dyes; however, it still has some limitations regarding the clearing ability of pigmented tissues. It needs further studies to be used in other organs. This method was shown to have clearing efficiency on cerebral organoids, Drosophila melanogaster, zebrafish, axolotl, and Xenopus laevis (Masselink et al., 2019). In the same year, to clear whole eyes, Henning et al. invented a protocol by combining iDISCO+ and Eci clearing methods named EyeCi. They visualized whole eye's vascular structures by light sheet microscope (Henning et al., 2019). After a while, researchers developed combination methods to obtain transparent organs while preserving fluorescent signals better. Merz et al. introduced a new method combining bleaching-augmented solvent-based non-toxic clearing (BALANCE) using ethyl cinnamate (ECi) to three-dimensional imaging of myocardial I/R (ischemia/reperfusion) injury models in mice. They performed hydrogen peroxide bleaching to improve the clearing of hearts while preserving fluorescence intensity. Additionally, they have tested the BALANCE method in human heart (left atrial appendage) biopsy and displayed the clearing efficiency by imaging autofluorescence of cardiomyocytes. Moreover, they showed the applicability of this protocol to other murine tissues, such as liver. However, this protocol is optimized for the endogenous expression of fluorescent protein in mice. Since the perfusion of human biopsy is not feasible, they only could visualize autofluorescence. This protocol would not fit our project regarding our aim (Merz et al., 2019). DBE or BABB solvents enable deep tissue imaging of various biological samples. However, due to the continuous peroxidase reaction in enhanced green fluorescent protein (EGFP)-expressing samples, a new method was developed. Stabilized DISCO (sDISCO) method has an additional chemical, antioxidant propyl gallate, to preserve EGFP signals efficiently. They purified peroxidase from clearing chemicals by using the column chromatography technique. sDISCO method enabled the imaging of the spine and whole brain imaging of a transgenic mouse with a

better EGFP signal than uDISCO and FluoclearBABB (Fluorescent-Protein Stabilization and High-Resolution) (Hahn et al., 2019).

Recently, Liu et al. released an iDISCO-based method to specifically investigate neural innervations and innate immunity in lung tissues and named iDISCO(ace). The protocol was invented based on the iDISCO+ protocol. They used acetone as a dehydration agent instead of methanol and reported that it produced better antibody compatibility with immune cell surface markers when compared with the original iDISCO+ method (Liu et al., 2020). Additionally, this method needs further validation on compatibility with other tissues. To improve the efficiency of the method to clear large specimens, other methods were developed. Recently, Dodt et al. published a study which focuses on analysing large malignant breast tissue samples with the pathoDISCO method via ultramicroscopy light-sheet. This method was based on the 3DISCO approach, but they added a selective autofluorescence enhancement agent to highlight tumorous structures in breast tissue. Moreover, they used 2,2-dimethoxypropane (DMP) as an active dehydration agent to accelerate the dehydration process. An important advantage of this method is the reversibility of the clearing process to a phase in which standard histopathology techniques are applicable. And this technique allows pathologists to analyse large tissue samples three-dimensionally and aids the histological diagnosis in clinical pathology (Sabdyusheva Litschauer et al., 2020).

Researchers developed several new methods to obtain transparent human brain samples. However, the time for efficient transparency was too long due to the human brain's high myelin content, lipids, and ageing molecules. The small-micelle-mediated human organ efficient clearing and labelling (SHANEL) approach for human brain and kidney samples was reported to address these issues. SHANEL method uses ethanol, dichloromethane (DCM) and BABB solution for dehydration, delipidation, and RI matching, respectively. In this method, they used zwitterionic detergent CHAPS (3-[(3-cholamidopropyl) dimethylammonio]-1-propanesulfonate), allowing rapid deep tissue permeabilization. Notably, CHAPS small micelles disrupt and loosen intensely organized extracellular matrix structures. As a result, this approach was not tested on fibrotic liver tissues; if tested, ECM loosening and disruption might be a significant constraint (Zhao et al., 2020).

Lately, a new method was released based on combining two clearing approaches. Zhu et al. combined the 3DISCO method and aqueous-based clearing CUBIC-L reagent, which will be discussed in the following section, termed Dec-DISCO (Decolorization DISCO), to efficient decolourization of heme-rich tissues. They reported successful clearing and decolourization of heme-rich tissues, including transgenic and wild-type rodent brain, heart, spleen, lung, and kidney, compared to the 3DISCO method. Further, they visualized and built 3D images of nerve branches in skeletal muscles in transgenic mice (Zhu et al., 2021).

Finally, a newly released method investigated the imaging of the mammalian body en bloc, which is challenging for using one type of clearing method. HYBRID (hydrogel-based reinforcement of three-dimensional imaging solvent-cleared organs (DISCO)) method was released in order to visualize large heterogenous body parts of mammals. They used a hydrogel-based clearing approach (CLARITY, which will be discussed in the following sections) and the 3DISCO approach for efficient clearing without perfusion of the clearing agents or antibodies. Interestingly, they visualized the chest of a SARS-COV-2 infected mouse and showed the convenience of the method to study systemic diseases like viral infections since it preserves the physical integrity (Nudell et al., 2022).

In summary, organic-solvent-based methods are substantially improved and widen the application scope.

Table 1.3 Organic solvent-based methods

Method	RI	Validated tissues	Clearing Time	Morphology Alterations	Toxicity	Refs
Spalteholz	1.55	human tissues	months	Shrinkage	Yes	(Spalteholz, 1914)
BABB	1.56	mouse brains, embryos, and fruit flies	days	Shrinkage	Yes	(Dodt et al., 2007)
3DISCO	1.56	whole mouse brain, lung, spleen, lymph nodes, mammary glands, rodent CNS	hours-days	Shrinkage	Yes	(Erturk et al., 2012)
iDISCO	1.56	adult mouse brainstem, cerebellum, and entire mouse embryonic head	hours-days	Shrinkage	No	(Renier et al., 2014)
iDISCO+	1.56	lung	days	Shrinkage	No	(Renier et al., 2014)
uDISCO	1.58	whole rodent body	weeks-months	Shrinkage	No	(Pan et al., 2016)
Eci	1.56	murine kidneys, heart, bones, and lungs	weeks	Shrinkage	No	(Klingberg et al., 2017)
PEGASOS	1.57	mouse head, skull, brain, muscles, and other tissues, rat body	days-months	Shrinkage	No	(Jing et al., 2018)
vDISCO	1.57	whole mouse body		Shrinkage	No	(Cai et al., 2019)
a-uDISCO	1.56	whole mouse brain, muscle, stomach	days	Shrinkage	Yes	(Li et al., 2018)
FDISCO	1.56	whole organs and bodies	days	Shrinkage	Yes	(Qi et al., 2019)
2Eci	1.56	human organoids, Drosophila melanogaster, zebrafish, axolotl, and Xenopus laevis	hours	Shrinkage	No	(Masselink et al., 2019)
BALANCE	1.56	human heart biopsy, mouse heart	hours	Shrinkage	No	(Merz et al., 2019)
sDISCO	1.56	transgenic whole mouse brain	days-weeks	Shrinkage	No	(Hahn et al., 2019)
iDISCO(ace)	1.56	transgenic whole mouse lung tissue	days	Shrinkage	No	(Liu et al., 2020)
pathoDISCO	1.56	human breast tumour biopsy	days	Shrinkage	No	(Sabdyusheva Litschauer et al., 2020)
SHANEL	1.56	human brain, pig brain and pancreas	days-months	Shrinkage	No	(Zhao et al., 2020)
Dec-DISCO	1.56	mouse spleen, kidney, lungs, spinal cord	days	Shrinkage	No	(Zhu et al., 2021)

*RI: Refractive index

Simple Immersion Methods

Simple immersion techniques are based on incubating a sample with a high RI solution without a delipidation agent. The mode of action of these techniques depends on removing water passively from the samples and diffusion of clearing solutions such as sucrose, fructose (SeeDB, (see deep brain), glycerol, and formamide (ClearT) (Aoyagi et al., 2015; Costantini et al., 2015; Hou et al., 2015; Ke et al., 2013; Kuwajima et al., 2013; Meglinski et al., 2003; Staudt et al., 2007; Tsai et al., 2009)

Refractive indexes of simple immersion methods are quite high but not as organic solvents, which range between 1.44-1.49. In simple immersion, a tissue sample is located in an immersion solution comprising a high refractive index molecule and awaits until complete transparency. However, the clearing efficiency of simple immersion methods is not so high and requires a long incubation time. In addition, the high viscosity of simple immersion solutions is major limitation due to the risk of precipitation at room temperature and the formation of air bubbles.

The commercially available proprietary FocusClear is used as a clearing agent; however, the high cost limits its use by the researchers. The alternative options are 2,2′-thiodiethanol (TDE) and the FRUIT method. Besides, they have lower costs; the abovementioned shortcomings are sealed. TDE was first released as an immersion media for super-resolution microscopy, but then researchers have described its usage as a clearing agent for a large sample (Costantini et al., 2015; Staudt et al., 2007). The one drawback of TDE is the reduction of fluorescence at high concentrations. On the other hand, FRUIT is a hybrid method that mixes urea with fructose to lower the overall viscosity of the SeeDB fructose solution and enhance tissue penetration and clearing efficiency (Hou et al., 2015).

Nevertheless, simple immersion-based methods do not have high transparency efficiency in clearing thick samples; therefore, other clearing methods should be considered if high-resolution images are required.

Table 1.4 Simple immersion methods

Method	RI	Validated tissues	Clearing Time	Morphology Alterations	Toxicity	Refs
Sucrose	1.44	mouse and rat brain	Days	Shrinkage	No	(Ohtsuki et al., 2012)
FocusClear	1.45	animal brain, kidney, heart, stomach, intestine, liver, lung, pancreas, skin	Hours-days	No	Yes	(Richardson & Lichtman, 2015)
SeeDB	1.48	mouse brain	Days	No	No	(Ke et al., 2013)
FRUIT	1.48	whole mouse brain	Days	Minimal expansion	No	(Hou et al., 2015)
TDE	1.42	mouse brain	Days-weeks	No	No	(Staudt et al., 2007)

*RI: Refractive index

Hyperhydration Methods

Hyperhydration methods aim to remove lipids without hydrophobic solvents in order to maintain an aqueous environment for fluorescence proteins while lowering the refractive indices by a hyperhydration mechanism. The common hyperhydration agents are urea, formamide, thiourea, 1,3-BAC, and MXDA. Urea is the most common agent used in hyperhydration techniques. ScaleA2 comprises from 4 M urea, 10% glycerol and 0.1 Triton-X-100. This combination has a good clearing capability on mouse brain samples. However, it leads to tissue swelling, possibly due to the relaxation of the protein scaffold by the urea, such as collagen fibers (Hama et al., 2011). Further, the *Scale*S protocol was released by combining urea, sorbitol and dimethyl sulfoxide (DMSO) to improve the penetration of the agents (Hama et al., 2015). The implementation of sorbitol and DMSO speeded up the clearing time of the process with an excellent retaining of fluorescent proteins.

Clear, Unobstructed Brain/Body Imaging Cocktails and Computational analysis (CUBIC) method was developed based on the *Scale* protocol. CUBIC uses two reagents (ScaleCUBIC-1, CUBIC-1 or reagent-1) to remove the lipids and provide relaxation to a tissue. Afterwards, a second reagent with high RI is used (ScaleCUBIC-2, CUBIC-2 or reagent-2) to match the overall refractive indices. This method efficiently provides whole brain and whole body clearing (Susaki et al., 2015). The applicability of the method was validated by the Nojima et al. in 2017. They tested the clearing performance of the CUBIC method on various formalin-fixed paraffin-embedded mm-thick tissue blocks of human organs, including brains, hearts, lungs, livers, kidneys, spleens, intestines, and lymph nodes. However, they observed that the CUBIC reagents did not clear the human brain, heart, liver, kidney, spleen, and intestine as efficiently as the lungs and lymph nodes (Nojima et al., 2017). Moreover, the same group developed the CUBIC-derived protocols such as CUBIC-cancer analysis based on the immersion of N-butyl diethanolamine and antipyrine/nicotinamide for whole-body profiling of cancer metastasis and CUBIC-X to expand and provide transparency to the samples. Furthermore, formamide is an agent used in the ClearT simple immersion method and partially may act by a hyperhydration mechanism (Kuwajima et al., 2013). ClearT and ClearT2 solutions were developed to image cell morphology and neuronal connections, which comprised concentrated formamide and polyethylene glycol (PEG) solutions. This protocol can clear mouse embryos and whole and thick brain slices. This method preserves

lyophilic dyes and fluorescent labels since it does not use detergents and solvents in the mechanism of action.

CUBIC-L and CUBIC-HL cocktails contain 1,3-bis(amino methyl)cyclohexane (1,3-BAC) hyperhydration agent, which has high lipid solubility and decolouring efficiency. These protocols are used for clearing mouse organs and bodies or even large human tissues (Tainaka et al., 2018).

Recently, the MXDA-based Aqueous Clearing System (MACS) was released to clear whole adult brains efficiently within 2.5 days and is also a suitable method for other intact organs. It is compatible with multiple fluorescent antibodies and lipophilic dyes. MACS is used for the 3D imaging of intact mouse brain, spinal cord, kidney, spleen, heart, and intestine (Zhu et al., 2020).

Tabel 1.5 Hyperhydration methods

Method	RI	Validated tissues	Clearing Time	Morphology Alterations	Toxicity	Refs
ScaleA2	1.38	mouse brain slices	weeks-months	Expansion	No	(Hama et al., 2011)
ScaleS	1.47	mouse and human brain	days-weeks	Expansion, then restored	No	(Hama et al., 2015)
CUBIC	1.47	whole mouse body, human FFPE brain, kidney liver, lungs, spleen, intestine, lymph nodes	days-weeks	Expansion	No	(Nojima et al., 2017; Susaki et al., 2014; Susaki et al., 2015)
ScaleCUBIC	1.47	whole mouse brain and body	days-weeks	Expansion, tissue becomes very fragile	No	(Susaki et al., 2014)
ClearT	1.44	whole mouse embryo, thick slices	hours-days	No	Yes	(Kuwajima et al., 2013)
ClearT2	1.44	whole mouse embryo, thick slices	hours-days	No	Yes	(Kuwajima et al., 2013)
CUBIC-L, CUBIC-HL	1.47	mouse kidney, liver, lungs spleen, human kidney, brain		Expansion	No	(Tainaka et al., 2018)
MACS	up to 1.52	whole adult mouse brain (lipophilic dye)	days	No	No	(Zhu et al., 2020)

*RI: Refractive index

Hydrogel embedding methods

Imaging comprehensive information of intact biological samples has been a fundamental challenge across many fields of biology. Hydrogel embedding methods ensure physically support of biomolecules to retain the biological information throughout the process. CLARITY, Clear Lipid-exchanged Acrylamide-hybridized Rigid Imaging / Immunostaining / in situ-hybridization-compatible Tissue hYdrogel, is the pioneer method of this type of clearing technique which is based on the diffusion of monomers to crosslink the biomolecules to a tissue-hydrogel hybrid. Chung et al. first developed the CLARITY method using mouse brain samples to observe cellular relationships, subcellular structures, proteins, nucleic acids, and neurotransmitters (Chung et al., 2013). They proposed an efficient clearing method based on the hydrogel embedding and clearing with electrophoresis with an 8% protein loss. Notably, the best advantage of the CLARITY method is enabling multiple rounds of immunostaining.

In this method, biomolecules are covalently bonded and crosslinked to the monomers through paraformaldehyde after polymerization. Chung et al. proposed an electrophoretic tissue clearing (ETC) approach that uses sodium dodecyl sulfate (SDS) micelles with low electric fields. Using high voltage for electrophoresis-assisted clearing may damage tissue; therefore, low-level electric fields are recommended. They reported that clearing of adult whole mouse brain can be achieved within eight days. The yellow tissue discoloration and potential tissue disruption are the shortcomings of active clearing with ETC. Further, Chung's group introduced the ETC-based clearing method, which uses stochastic electro transport via a rotational electric field. This method provides selective distribution of highly electro-mobile molecules to ensure efficient clearing without damaging the tissue (Kim et al., 2015). They shortened the clearing time using the stochastic electro transport method to 1-3 days. Further, the method was investigated to use with large organ and whole body imaging. Therefore, Lee et al. introduced an active clearing technique (ACT) based on the pressure-related efficient and stable transfer of macromolecules into organs (PRESTO). ACT-PRESTO method enables clearing of the whole organ within 4-20 hours and is scalable for large organs or even whole bodies of adult animals (mouse, zebrafish) (Lee et al., 2016). They modified the ETC method to regulate the inconsistent electric field, pH changes, heat generations and air bubble

formations. In 12 hours, the adult mouse brain was cleared without protein loss. Further, the perfusion approach was used for supporting detergent delivery to the organs or whole body through the circulatory system (or cerebrospinal fluid route) in the perfusion-assisted agent release method (PARS) for rapid delipidation, labelling and efficient clearing (Yang et al., 2014). All the steps of the method are performed in situ till the extraction of the organ from the body. The PARS method allows imaging of whole intact organisms while conserving fluorescent signals and tissue structures.

In contrast to the active clearing in the CLARITY method, passive clearing does not need special chambers. The group provided a method without a need for electrophoretic tissue chamber. The clearing is performed in 4-8% SDS solution while passively rotating at 37°C. Chung et al. used an 8% SDS clearing solution to remove lipids passively from the samples, and they called the method passive CLARITY technique (PACT) (Tomer et al., 2014). However, the most significant disadvantage of PACT is the time required for complete transparency. The removal of phospholipids is provided with the incubation and rotating passively at 37°C, and the clearing buffer is refreshed daily. In order to speed up the time for clearing with PACT, Chung et al. introduced the SWITCH (system-wide control of interaction time and kinetics of chemicals) method, which regulates the chemical reactions between exogenous and endogenous biomolecules using SWITCH-ON/OFF buffers. This method transforms tissue into heat- and chemical-resistant mode without damaging tissue structures and enabling multiplexed proteomic imaging. The clearing was performed at 80°C with SDS, and they successfully cleared the adult mouse brain within four days (Murray et al., 2015).

Further, in order to speed up the time needed for clearance of the specimens, Yu et al. suggested that 42-47°C is an alternative temperature range for PACT (Yu et al., 2017). They used 1-mm thick brain slices and concluded that thicker samples might require a longer time, and high temperature leads to a decrease in Green fluorescent signal (GFP). Therefore, they recommended using 42°C for thicker samples. Furthermore, there are methods which are developed based on PACT. Modified PACT (mPACT) is a method which uses 0.5% α-thioglycerol in 8% SDS clearing buffer for the removal of lipids, gentle shaking at 150 rm at 37°C. They showed improvements in clearing time compared to the original PACT. Additionally, there are methods which use the combination of the perfusion

and PACT methods (PARS-mPACT). This method uses transcardial fixation of organs or the whole body, and then the mPACT clearing protocol is applied. However, they concluded that there are no transparency differences in the mouse central nervous system (CNS) between PARS-mPACT and mPACT. Another method which does not include 0.5% α-thioglycerol in an 8% SDS clearing buffer is psPACT (process-separate PACT). psPACT is based on the divided incubation with 4%PFA, acrylamide and thermal initiator. Regarding whole mouse CNS, mPACT cleared efficiently within 14 days (Woo et al., 2016). As a simplified and less expensive CLARITY-based method, Zheng et al. developed a new method to investigate the pre- and postnatal development of central brainstem/hypothalamic/limbic forebrain circuits in the rat. They processed tissues with the passive CLARITY method but used 2,20-Thiodiethanol (TDE) to match refractive indices to 1.45. The embryonic whole rat brains were cleared within a week (Zheng & Rinaman, 2016).

In order to improve the preservation of fluorescence protein, antigenicity, transcripts and tissue architecture, SHIELD (Stabilization to Harsh conditions via Intramolecular Epoxide Linkages to prevent Degradation) method was introduced by Park et al. (Park et al., 2019). They used SHIELD to investigate system-level circuitry, synaptic architecture, and molecular features of virally tagged neurons and their targets in mice at single-cell resolution. SHIELD method uses the SWITCH technique to preserve fluorescent signals, proteins, and transcripts while SHIELD applies stochastic electro transport. SHIELD method can be combined with fluorescent in situ hybridization (FISH) techniques in order to investigate spatial genomics. Moreover, they suggested that SHIELD can be used for molecular phenotyping of rodents and human clinical samples.

Table 1.6 Hydrogel embedding methods

Method	RI	Validated tissues	Clearing Time	Morphology Alterations	Toxicity	Refs
CLARITY	1.45	whole mouse brain	days	expansion	Yes	(Chung et al., 2013)
Act-PRESTO	1.45	mouse thymus, intestine, testis lung, spleen, liver, kidney	hours	expansion	Yes	(Lee et al., 2016)
PARS	1.46	whole mouse body	days	No	Yes	(Yang et al., 2014)
PACT	1.46	whole mouse body, intact tissues	days-weeks	slight expansion	Yes	(Tomer et al., 2014; Yu et al., 2017)
SWITCH	1.47	whole adult mouse brain, lung, kidney, heart, spinal cord, rat brain and spinal cord, human brain	hours-weeks	minimal expansion	Yes	(Murray et al., 2015)
mPACT	1.46	mouse liver, lung, heart, salivary gland, pancreas, lung, stoma	days	expansion	Yes	(Woo et al., 2016)
psPACT	1.46	mouse liver, lung, heart, salivary gland, pancreas, lung, stoma	days-weeks	expansion	Yes	(Woo et al., 2016)
SHIELD	1.45	human brain biopsy, mouse kidney biopsy, mouse hemisphere	weeks	expansion	Yes	(Park et al., 2019)

*RI: Refractive index

1.1.8 Microscopy techniques in 3D pathology

The attention to 3D pathology evolved substantially over the years. Previous studies aided the future of high throughput slide-free imaging techniques to interrogate whole biopsy and surgical specimen imaging (Li et al., 2010; McCormick et al., 2004). Two-dimensional (2D) pathology is applied to small fraction of a specimens to examine with a slide-based workflow which is time-consuming and destructive. Additionally, limited amount of sample is examined through 2D pathology workflow. Even though they improved the 3D pathology approach, they are destructive and cause sectioning artefacts (Liu et al., 2021).

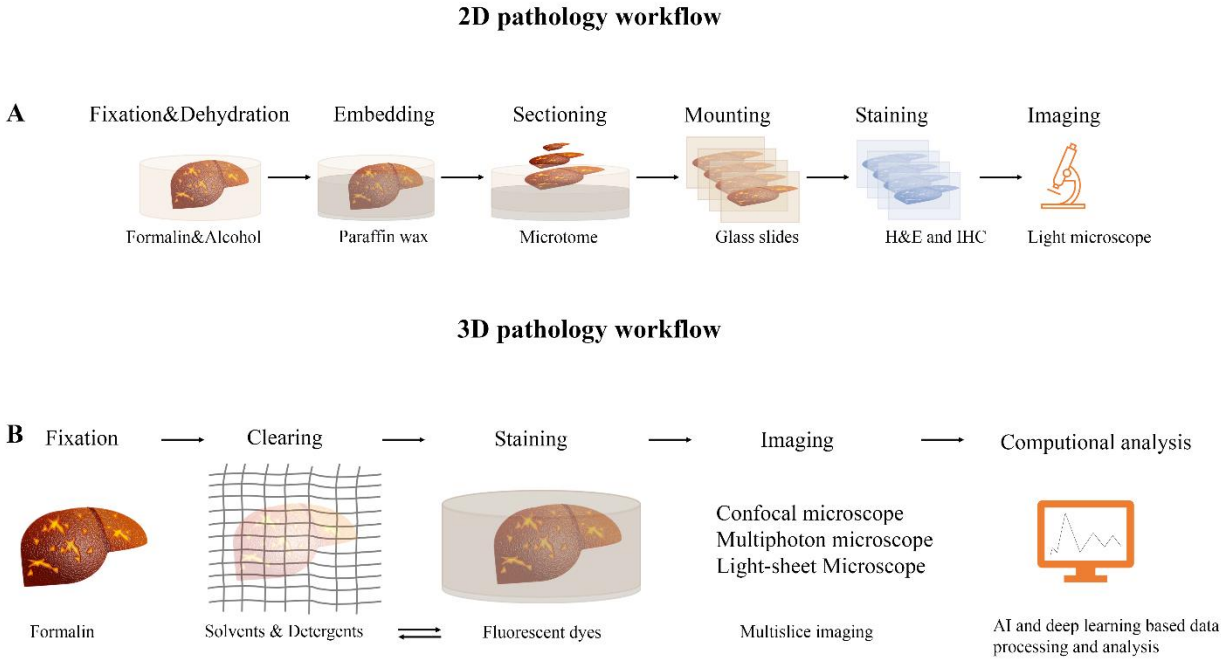

Figure 1.2 Destructive versus non-destructive pathology workflow. Conventional histology uses harsh chemical to fixate and dehydrate the specimen, followed by paraffin is used for embedding and sectioning. Specimens are stained such as H&E and IHC. The procedure is time-consuming and destructive yet enables to examine only small fragments of tissue (A). With the improvements in optical clearing techniques, volumetric imaging of a core biopsy have enabled with minimal requirements of tissue processing and mounting. 3D pathology provides comprehensive information from large intact tissues and enables digital pathology using AI and deep learning based models.

Non-destructive imaging technique has been improved with the developments in confocal microscopy. Later on, multiphoton imaging impacted the future of 3D pathology together with the light-sheet microscopy techniques. Confocal microscopy is the most widely used system in volumetric imaging of biological samples. Laser scanning technology provides

multiple 2D images and uses them for the 3D reconstruction of the specimens. Multiphoton microscopy has been widely adopted in many research fields due to the detection capacity of linear and nonlinear signals (autofluorescence, second harmonic generation). Recently, the multiphoton microscopy approach has been used in optically cleared kidney and liver biopsies to expand the current knowledge in the fields (Olson et al., 2016; Segovia-Miranda et al., 2019). Due to the point-by-point scanning principle, confocal and multiphoton systems have restrictions. One of the limitations is the long scanning time, which limits the 3D imaging of large samples. Furthermore, the loss of fluorescence signal caused by the excitation laser leads to photobleaching and photodamage of the samples (Fischer et al., 2011) (**Table 1.7**).

Light sheet microscopy (LSFM) is the selective illumination technique that allows rapid 3D imaging of relatively transparent samples such as embryos and transparent samples (Stelzer et al., 2021). LSFM systems coupled with highly sensitive and fast scientific complementary metal–oxide–semiconductor (sCMOS) detectors in order to capture 2D images from a specimen to generate 3D volumetric images. LSFM methods enable faster 3D imaging of large samples with less photobleaching and photodamage than confocal microscopes. Recently, LSFM has been investigated for usage in 3D pathology (Barner et al., 2020). Although commercially available light sheet microscopes have ability to image various types of samples and provide high quality images, they are not designed to examine clinical samples. Researchers improved the LSFM systems to efficiently image larger biological specimens such as whole mouse brain or heart using tissue-clearing techniques (Ding et al., 2018; Tomer et al., 2014). Imaging of large samples requires special embedding and sample preparation techniques. Therefore, researchers have developed LSFM derivatives which enable multi-immersion open-top light sheet microscopes for imaging cleared tissues (Glaser et al., 2019).

Table 1.7 Comparison of non-destructive imaging systems

	Confocal Microscope	Multiphoton Microscope	Light-Sheet Microscope
Resolution	<micron	<micron	micron
Size of the specimen	micron	mm	>cm
Imaging speed	slow	slow	fast
Detection	Point detection	Point detection	Wide field detection
Imaging depth	Up to 1 mm	Up to 2 mm	Up to 4.5 mm
Photobleaching	Yes	Less	Least
Main limitations	*Long acquisition time *High sample toxicity and photobleaching *Not good for thick samples	*Long acquisition time *High cost in equipment and maintenance *Difficulty to image more than two color due to the lack of dye and laser availability	*Unusual sample preparation techniques are required

*The table contains the information for standard imaging systems.
*mm; millimetres, cm; centimetres,

In recent years, studies have been exploring new technologies to enhance the current knowledge and utilize new modalities to provide comprehensive information to the field. Traditional histology techniques provide two-dimensional information to aid routine histopathology for disease stratification and prognosis. Improvements in tissue clearing and microscopy techniques, particularly non-destructive slide-free imaging of biological specimens, may make structural and molecular information from intact tissues more accessible.

Chapter 2: Materials and Methods

2.1 MATERIALS

2.1.1 Establishment of human cohorts

We recruited a hundred and sixty-eight human liver tissues from various chronic liver disease patients and non-fibrotic subjects who underwent hepatectomy due to benign liver diseases at Koç University Hospital and Medipol University Hospital. Fifty-seven NAFLD, thirty-eight of viral hepatitis transplanted patients, thirteen non-fibrotic, and thirty-five liver biopsy samples from NASH patients constitute our analysis cohort. Samples and clinical data were obtained under conditions of informed consent and following approval of a local Institutional Review Board numbers (2015.053.IRB1.014, 2016.024.IRB2.005, 2017.139.IRB2.048).

2.1.2 Animal models

We generated five different animal models to perform the modified-CLARITY method in this project. We used dietary and injection models to develop NASH and chronic liver fibrosis in mice. Koç University Animal Research Facility provided C57Bl/6 mice for animal models of liver fibrosis. Older than eight weeks and adult male mice were used in this study. Diets and water were refreshed two days intervals along the experiment. The animal models are explained in the following sections. (Ethics number 2019.HADYEK.001)

Methionine Choline Deficient Diet (MCD): We used fifty mice for MCD dietary model of NASH. The model consisted of 7 groups, and they were harvested a week interval. The control group were fed with a control MCD diet (*Research Diets, A02082003B*) for six weeks which is the longest time period with MCD diet (*Research Diets, A02082002B*) feeding.

High Fat High Sucrose Diet (HFHS): We conducted two different HFHS models for this project. The first one consisted of 11 weeks and 16 weeks groups of HFHS diet (Research Diets, D11092103) and 16 weeks of low fat (LF) diet (Research Diets, D11092101) group

as control. We used twenty-one mice for this model. The latter model was HFHS diet feeding and once a week injection of carbon tetrachloride (CCl4) at 0.2 µl/gr. The CCl4 (*Sigma Aldrich, 270652*) was given to the mice in olive oil (*Sigma Aldrich, O1514*) at 1:3 dilution. We used forty-eight mice and they were weighed before injecting CCl4, and doses were calculated for each mouse.

Carbon tetrachloride model (CCl4): We executed two different CCl4 models for this project. The first one consisted of five different groups which have two weeks of interval between CCl4 groups. The experiment prolonged for six weeks (2 weeks, 4 weeks, and 6 weeks groups) and control group were injected with olive oil for six weeks. In this model, two groups of mice injected with CCl4 for 6 weeks, but one of those eight mice did not take CCl4 injection for one week and harvested. The mice were injected with CCl4/Olive oil mixture (1:3) at 1 µL/gr concentration. We used thirty-four mice for this project, and they were weighed before injecting CCl4, and doses were calculated for each mouse. The latter model consisted of two main groups as normal and low doses of CCl4. The normal dose (ND) group was divided into three groups as 4-weeks, 6-weeks, and 8-weeks. The low dose (LD) group was divided into four groups as 6-weeks, 8-weeks, 10-weeks, and 12 weeks. The ND and LD groups were injected at 1 µL/gr and 0.5 µL/gr concentrations of CCl4 in 1:3 olive oil, respectively. The groups were harvested at the end of the week.

2.1.3 Material List

Table 2.1 Material list used in this study

Reagents	Supplier	Cat no.
40% Acrylamide Solution	Bio-Rad	1610140
2% Bis Solution	Bio-Rad	1610142
16% Paraformaldehyde Solution	Electron Microscopy Sciences	100503-020
Thermal initiator	Wako	VA-044
Saponin	Sigma Aldrich	47036
Boric acid	Sigma Aldrich	B6768
Sodium dodecyl sulfate	Sigma Aldrich	L3771
Nycodenz	Axis Shield	AXS-1002424
Ultrapure™ Low Melting Point Agarose	Thermo Scientific	16520050
10X PBS	Gibco	70011044
86-89% Glycerol	Sigma Aldrich	49781
Tween-20	Sigma Aldrich	P9416
Triton X-100	Sigma Aldrich	T9284
Hoechst 33342	Invitrogen	H1399
Phosphomolybdic acid	Sigma Aldrich	79560

Picric acid solution	TCS Biosciences	HS655
Sirius Red	Polysciences	09500
Sodium azide	Sigma Aldrich	71289
RPMI 1640	Lonza	12-702F-LONZA
Antibiotics-Antimycotics(100X)	Thermo Scientific	15240062
Fetal Bovine Serum	Gibco	10082147
Hydroxyproline Assay	Sigma Aldrich	MAK008-1KT
Sudan Black B	Sigma Aldrich	199664

2.2 METHODS

2.2.1 Modified-CLARITY method for 3D imaging of human and mouse liver tissues

Preparation of solutions

***Modified Hydrogel Monomer Solution*:** The original hydrogel monomer (HM) solution can be adjusted to balance rigidity and porosity in specific tissues. Therefore, we have adjusted the HM protocol for explants, biopsy liver samples and animal tissues. Modified HM solution consists of 1% of 40% Acrylamide, 4% of paraformaldehyde, 0.25% of VA-044 thermal initiator, 1X Phosphate buffered saline, 0.05% of Saponin and distilled water for transplanted liver tissues. In this protocol, we have decreased the acrylamide concentration and excluded bisacrylamide. Additionally, we have adjusted the original CLARITY protocol for biopsy and mouse liver tissues and used acrylamide and bisacrylamide at the concentration of 1% and 0.025%, respectively. Since the thermal initiator is inert at low temperatures, the solution should be prepared on ice to prevent polymerisation. After preparations, aliquots of 20 mL HM can be stored at -20°C. While handling paraformaldehyde and acrylamide, necessary precautions should be taken into consideration, and all the preparations should be performed with equipment of personal protection in a fume hood.

***Clearing Solution*:** The clearing solution of the CLARITY technique consists of 200 mM boric acid, 4% sodium dodecyl sulphate (SDS) and distilled water. Firstly, we prepared a boric acid solution in 400 mL of water and added NaOH to adjust the pH to 8.5. Then, we added the boric acid solution to a container with 80 gr of SDS and filled it to 2 L with water. Finally, pH was checked and stored at room temperature. It should be considered that working in a fume hood and person should avoid skin contact or inhalation when preparing a clearing solution.

***Refractive Index Matching Solution*:** The refractive index matching solution (RIMs) is used for matching the internal refractive index of clarified tissue. Therefore, 40 gr of Nycodenz was dissolved in 30 mL of 0.02 M phosphate buffer at 37°C on a stirrer. After completely dissolving Nycodenz, pH was adjusted to 7.50 and stored at +4°C. RIMs has ~1,45 refractive index, which is matched with cleared liver tissues. It is important to image cleared samples in an environment that has matched refractive index with the imaging subject since the scattering of light is a significant limitation for proper resolution.

***Mounting Media Solution*:** The imaging environment needs to be matched with clarified tissues. For this reason, we prepared an embedding solution by mixing Low melting agarose and RIMs. 10 mL of RIMs and 200 mg of agarose were mixed and heated in a water bath up to 75°C. After the proper dissolving of agarose, the refractive index was measured with a refractometer and stored at +4°C.

2.2.2 Modified clearing protocols of human liver tissues

All liver tissues from human and mouse were transferred to the KUTTAM laboratory in transfer media (RPMI-1640, 20% Fetal Bovine Serum and 1% Penicillin-Streptomycin). Then, liver tissues were immediately incubated in HM solution on a shaker at +4°C for 3-7 days to ensure homogenous monomer diffusion. Originally, the remaining oxygen is removed from the container with degassing chamber. As an alternative, we poured a layer of sunflower oil on top of the hydrogel solution and polymerized it at 37°C for 3 hours to preserve biomolecules while eliminating phospholipids from the sample. After the incubation, samples were put into a clearing buffer and changed daily (passive CLARITY) until tissues got utterly transparent. PBS was used for removing SDS artefacts from the tissue overnight. Cleared liver tissues were kept in glycerol (86-89%) or PBS-T (with 0.01% sodium azide) at +4°C for further experiments.

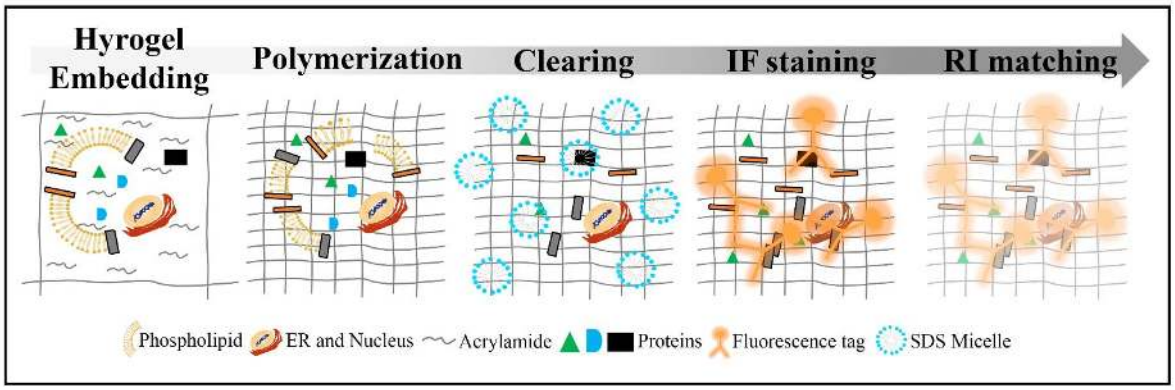

Figure 2.1 A schematic representation of the CLARITY method. The representative image summarizes the CLARITY method comprised of hydrogel embedding, polymerization, clearing, immunofluorescence staining and refractive index matching.

2.2.3 Modified clearing protocols of mouse liver tissues

The non-perfusion method of modified-CLARITY

Mice were anaesthetized with isoflurane. The layers of the skin and peritoneum were carefully cut near the abdomen with scissors. The horizontal incisions were performed in order to reach the liver easily. Liver tissue was carefully extracted from the abdomen and sliced from the median lobe of the liver. Sliced liver tissue directly placed into hydrogel embedding solution and incubated for five days on a shaker at 40 rpm at +4°C. Following the incubation, sunflower oil was poured onto HM solution and incubated at 37°C for 3 hours. After the polymerization, samples were placed into a clearing buffer and changed solution daily (passive CLARITY) until tissues became utterly transparent. PBS was used for removing SDS artefacts from the tissue overnight. Cleared liver tissues were kept in glycerol (86-89%) or PBST (with 0.01% sodium azide) at +4°C for further experiments. The non-perfusion method was applied to HFHS and CCl4 animal models.

The perfusion method of modified-CLARITY

Mice were anaesthetised with isoflurane. The layers of the skin and peritoneum were carefully cut near the abdomen with scissors. The horizontal incisions were performed to reach the liver and heart easily. Then, the transition of 10 U/L heparin in PBS was provided through the heart to prevent the blood clothing during the perfusion. Afterwards, 20 mL of HM solution was given to the mice through cardiac perfusion. The change in the colour of liver was observed as it flushed with solutions. After the perfusion, entire liver was extracted and placed into HM solution. The whole liver tissues were incubated in HM solution for five days to ensure monomer diffusion. Following the incubation, sunflower oil was poured onto HM solution and incubated at 37°C for polymerisation. After the incubation, samples were put into a clearing buffer and changed solution every day (passive CLARITY) until tissues got utterly transparent. PBS was used for removing SDS artefacts from the tissue overnight. Cleared liver tissues were kept in glycerol (86-89%) or PBS-T (with 0.01% sodium azide) at +4°C for further experiments. The perfusion was applied to MCD, HFHS+CCl4, and dose dependent CCl4 animal models.

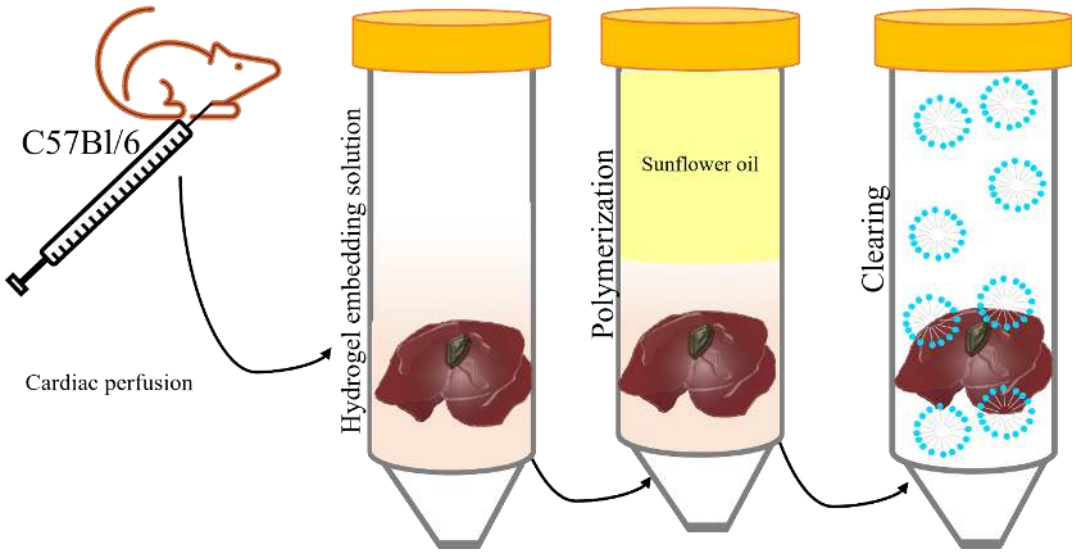

Figure 2.2 A schematic representation of perfusion-guided CLARITY of mouse models. After cardiac perfusion was performed for hydrogel monomer diffusion to the liver and other organs, liver was extracted carefully and directly placed into hydrogel embedding solution, polymerized, and finally placed into a clearing buffer for passive clearing.

2.2.4 Staining of extracellular matrix proteins for 3D liver fibrosis imaging

Preparation of Solutions

Wash Solution

PBSTw: 0.1% (vol/vol) Tween-20 was added to 1X Phosphate buffered saline (PBS).

Antibody Incubation Solutions

PBST: 0.01% (wt/vol) sodium azide and 0.1% (vol/vol) Tween-20 in 1X PBS.

Blocking Reagents

B1:10% (vol/vol) Goat serum, 0.2% Triton-X-100, 0.05% Sodium azide were added to 1X PBS.

Goat serum: 5% (vol/vol) Goat serum in PBSTw or 5% (vol/vol) Goat serum in PBST

Horse serum: 5% (vol/vol) Horse serum in PBSTw

Sudan Black Blocking: Sudan black B (SBB) was dissolved in 70% ethanol in the dark and filtered through a 0.2 µm strainer. 0.2% (wt/vol) was prepared and diluted as 0.02, 0.002, 0.0002, 0.00002% with 70%ethanol. The cleared mouse liver samples were incubated on a shaker at 40 rpm for 2 hours, followed by a rinse with 70% ethanol and PBS before incubating with primary antibodies.

***Human liver tissue staining against Collagen type I and Elastin*:** For Collagen type I and Elastin staining of human cohort, clarified liver tissues were incubated at +4°C in PBST (with 0.01% (wt/vol) sodium azide and 0.1% (vol/vol) Tween-20) with anti-Collagen type I and anti-Elastin antibodies at 1:2500 dilutions for 3 days incubation, followed by a wash at +4°C in PBSTw (with 0.1% (vol/vol) Tween-20) for two days. Non-specific binding of antibodies was blocked with normal goat serum at +4°C, followed by incubated with CY3-conjugated secondary antibody. Unconjugated antibodies were rinsed with PBSTw and incubated with 1:1000 Hoechst (Thermo Scientific, Vienna, Austria) in PBS for nuclei staining. Finally, after washing excess solution in PBS, samples were kept in RIMs at +4°C until imaging was performed.

***Mouse liver tissue staining protocol*:** The following steps were attended for staining experiments in mouse. Primary antibodies were incubated for 2 days or 4 days, followed by washing out with PBSTw, and then blocking reagents were applied for 1 day in PBSTw. Secondary antibodies were applied in blocking reagents for 2 days. Finally, samples were washed with PBSTw for 1 day, then Hoechst solution was applied for nuclei staining, and then 1 day wash was performed with PBS. Samples were stored in RIMs at +4°C until imaging was performed. **Table 2.2** and **Table 2.3** contain the information of tested primary and secondary antibodies, dilutions, blocking reagents and the duration of the antibody incubation for human and mouse staining experiments in this project.

Table 2.2 Tested primary antibody list and optimization conditions

Primary antibody	**Host**	**Clonality**	**Catalog no, Provider**	**Tested incubation time for Primary antibody**	**Blocking Reagent**	**Tested Dilutions**	**Tested Secondary ab**
Anti α-smooth muscle actin	mouse	mAb	F3777, Sigma	2 days	None	1:100	None (conjugated)
Anti-Collagen type I	rabbit	pAb	ab34710, Abcam	2 days	5% Goat serum, 5%Horse serum and B1 reagent	1:500, 1:1000	Alexa fluor 594 & 488, Cy3
Anti-Collagen type I	mouse	mAb	ab90395, Abcam	2 days, 3 days	5%Goat serum	1:500, 1:1000, 1:2500, 1:5000, 1:10000, 1:25000	Cy3 and Alexa fluor 488
Anti-Collagen type I	rabbit	pAb	2150-2210, Bio-Rad	2 days, 3 days	5% Goat serum, 5%Horse serum and B1 reagent	1:50, 1:100, 1:500, 1:1000, 1:2500	Alexa fluor 488
Anti-Collagen type I	rabbit	pAb	2150-1410, Bio-Rad	4 days	5%Goat serum	1:100, 1:500	Alexa fluor 488
IgG Isotype Control	mouse	pAb	ab37355, Abcam	2 days	5%Goat serum	1:500	Cy3
IgG Isotype Control	rabbit	pAb	ab27478, Abcam	2 days	5%Goat serum	1:500	Alexa fluor 488

Anti-Collagen type I/III	rabbit	pAb	2150-2210, Bio-Rad	2 days	5% Goat serum, 5%Horse serum and B1 reagent	1:50, 1:100, 1:500, 1:1000, 1:2500	Cy3 and Alexa fluor 488
Anti-Collagen type III	rabbit	pAb	ab277278, Abcam	2 days	Goat serum	1:50, 1:100, 1:500, 1:2500	None (conjugated)
Anti-Collagen type III	rabbit	pAb	PA534787, Invitrogen	2 days, 3 days	5% Goat serum	1:50, 1:100, 1:500, 1:1000, 1:2500	Cy3 and Alexa fluor 488
Anti-Elastin	mouse	mAb	MAB2503, Merck Millipore	2 days	Goat serum	1:500, 1:1000, 1:2500, 1:5000	Cy3 and Alexa fluor 488
Anti-Fibronectin	mouse	mAb	SAB4200760, Sigma	2 days	5% Goat serum, 5%Horse serum and B1 reagent	1:100, 1:500	Cy3 and Alexa fluor 488
Anti-Fibronectin	rabbit	pAb	ab2413, Abcam	2 days	Sodium azide	1:100, 1:500, 1:1000	Cy3 and Alexa fluor 488
Anti-Laminin	mouse	mAb	LN82-13, Invitrogen	2 days	5% Goat serum	2 mg/mL, 0.2 mg/mL	Cy3 and Alexa fluor 488
Anti-Laminin	rabbit	pAb	ab11575, Abcam	2 days	5% Goat serum	1:500	Cy3 and Alexa fluor 488
Anti MMP-2	mouse	mAb	436000, Invitrogen	2 days	5% Goat serum	1:100	Cy3 and Alexa fluor 488
Anti MMP-9	mouse	mAb	MA5-15886, Invitrogen	2 days	5% Goat serum	1:100	Cy3 and Alexa fluor 488
Anti TIMP-1	mouse	mAb	MS-608-PABX, Invitrogen	2 days	5% Goat serum	1:100	Cy3 and Alexa fluor 488

Table 3. Tested secondary antibody list and optimization conditions

Secondary antibody	Host	Clonality	Catalog no, Provider	Tested incubation time for Secondary antibody	Tested Dilutions
Goat anti-rabbit Alexa Fluor 488 IgG (H+L)	Rabbit	pAb	A-11008, Invitrogen	2 days, 3 days	1:500, 1:750, 1:1000, 1:2000
Goat anti-mouse Alexa Fluor 488 IgG (H+L)	Mouse	pAb	A-11001, Invitrogen	2 days, 3 days	1:500, 1:750, 1:1000, 1:2000
Cy3 Goat anti-Mouse IgG (H+L)	Mouse	pAb	115-165-003, Jackson ImmunoResearch	2 days	1:500, 1:750, 1:1000, 1:2000

2.2.5 2D immunohistochemical staining and histopathological assessment

Liver tissue samples were formalin-fixed, paraffin-embedded and cut 2 or 4 μm in thickness to stain with Sirius red and haematoxylin/eosin for fibrosis staging and semi-histopathological classification. For Sirius red staining, after following deparaffinization steps, sections were incubated in Phosphomolybdic acid for 5 minutes, then applied 0.5% of Sirius red for 2 hours, followed by sections were dipped into 0.1% HCl and mounted with Entellan. Afterwards, ten different areas were captured with x10 magnification of a light microscope for CPA analysis. The portal tracts, lumens and vascular collagen were excluded from the total area. The CPA values were expressed as the percentage of fibrosis areas to total areas. Additionally, mouse tissues were formalin-fixed, paraffin-embedded and cut 4 μm in thickness to stain with Sirius red and haematoxylin/eosin for fibrosis staging and semi-histopathological classification. Haematoxylin/ eosin staining was performed at the Department of Pathology at Koç University Hospital. The expert pathologist assessed liver tissues from NAFLD patients according to the SAF classification system. Chronic hepatitis patients were scored for inflammation and fibrosis stages for this project.

2.3 Real-time PCR and Hydroxyproline Assay

2.3.1 Real time PCR

Total RNA was isolated from liver tissues using the Qiagen RNeasy Micro Kit (74004) and converted to complementary DNA (cDNA). The TaqMan probe was used to detect Collagen type I (COL1A1) gene expression for human tissues. The following steps were utilized; 5 µl of Light Cycler 480 Probes Master Mix (Roche-04887301001), 0,5 µl of COL1A1 TaqMan probe (Thermo Scientific-COL1A1 Hs00164004_m1) and 0,5 µl of GAPDH TaqMan probe (Thermo Scientific-GAPDH Hs02786624_g1) as housekeeping gene, and 4 µl of cDNA was used. All samples run as duplicates and "Dual Colour Hydrolysis Probes/UPL Probe" protocol was used in the Light Cycler 480-II machine. We employed the SYBR green technique to express the Collagen type III gene (COL3A1). In this protocol, 10 µl of Light Cycler 480 SYBR Green I Master (2X) (Roche-04887352001), 2 µl of forward and reverse primer for COL3A1 and 2 µl of cDNA was used. All samples run as duplicates and "SYBR Green" protocol was used in the Light Cycler 480-II machine.

2.3.2 Hydroxyproline Assay

We used Sigma Hydroxyproline Assay Kit (Sigma, MAK008-1KT) for the detection of hydroxyproline content. The protocol was optimized for human and mouse liver tissues. For human samples, 10 mg of liver tissue were lysed in 100 µl distilled water and 100 µl of hydrochloric acid (12 M HCL) added to provide hydrolyzation for 16 hours at 105°C. However, for mouse samples, 5 mg of liver tissue was lysed in 100 µl distilled water and 100 µl of hydrochloric acid (12 M HCL) was added to provide hydrolyzation for 3 hours at 120°C. After the hydrolyzation process, it was centrifugated for 3 minutes at 10,000 xg and then removed 10 µl from the supernatant and placed on the 96-well plate in two iterations. These supernatants were evaporated in the 60°C pastor oven approximately for 90 mins. After the evaporation, manufacturer's instructions were followed. A mixture of 100 µl Chloramine T/Oxidation Solution was added to each well and incubated at room temperature for 5 minutes. Then a mixture of 100 µl DMAB concentrated/Perchloric Acid-Isopropanol mixture was added and incubated for 90 minutes in the 60°C pastor oven. After

the incubation, the spectrophotometer was utilized for absorbance measurement at 560 nm. The concentrations of hydroxyproline were calculated based on the standard curves.

2.4 Sample preparation for Confocal imaging of cleared liver tissues

We used upright Confocal microscope at KUTTAM imaging Center. Clarified liver tissues were placed on glass petri plates and encircled with tack-it to maintain the tissue in mounting medium for imaging experiments (**Figure 2.3**). Then, cover slides were utilized carefully to cover the sample and glycerol.

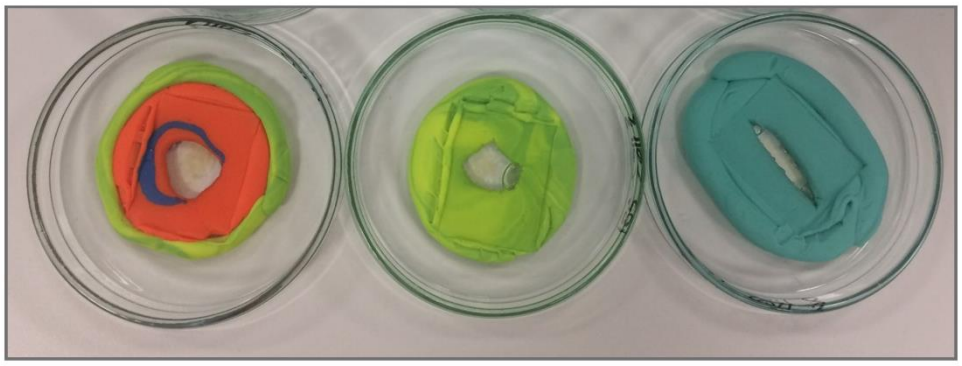

Figure 2.3 Sample preparation for Confocal imaging of clarified liver tissues. The preparation of three different liver samples for Confocal imaging.

2.5 3D imaging with in-house light sheet fluorescence microscopy

Stained liver tissues were embedded in a borosilicate tube which was filled with agarose/RIMs mixture. First, a 6 cm borosilicate tube was partially filled with a mounting solution. Then, liver tissue was placed, and the tube was fully filled with the mounting solution by paying attention to bubble formation and alignment of the sample. The mounting solution is solid after incubating at +4°C or room temperature for several minutes. The borosilicate tube ends were closed with parafilm and placed in the custom-designed sample holder (**Figure 2.4**)**.** For LSFM imaging, the embedded sample was submerged in a glycerol-filled sample cage which was horizontally located to the in-house developed LSFM set-up. The sample orientation was then identified, and image capturing was conducted with custom microscope controller software, enabling automatic image acquisition with the indicated directions. The software is responsible for the shutters' operation and the filter wheel's location via serial communication with the Arduino

microcontroller, translating the sample and triggering the image acquisition from the camera with API calls in sync. In the imaging settings, we began from the start of the sample to specify the number of tiles, and a 25% overlap was applied. The z-step value was between 2-10 μm for all liver tissues.

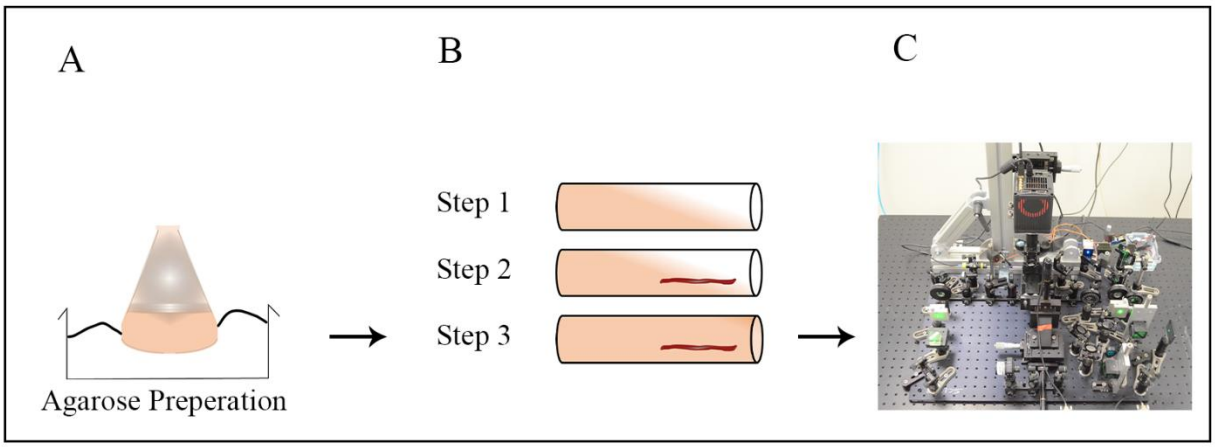

Figure 2.4 Sample preparation for light sheet imaging. Low melting agarose is dissolved in RIMs on a water bath (A). Then, the borosilicate tubes are filled with the mixture and sample is placed (B). After solidifying the mounting solution, the tube containing the sample can be placed in the sample cage to proceed with LSFM imaging (C).

2.6 Image processing, analysis, and 3D reconstruction

In house developed LSFM creates images at 16-bit depth gray scale images in .tiff format with ORCA-Flash4.0 v3 CMOS camera. Raw image data is stored in an external disc of 20 TB repository capacity (WD Elements, California, USA). The imaging computer is equipped with 64 GB DDR 3200 RAM (G-Skill, Walnut, USA), 1 TB of a hard disk drive and intel core i7 8700 (6c-12t) operators. To assess fibrosis, stitched images were analysed using collagen proportional area (CPA) analysis. Image J software was used to create the macro code for CPA analysis. The following steps were carried out; contrast enhancement of raw images, binarization of enhanced images, thresholding, and area measurement (**Figure 2.5**). The image stitching was done automatically with macrocode by Image J (Fiji, Suva, Fiji) software (**Figure 2.6**). The ideal threshold for positive pixels was set for area selection and computed using Image J's measurement function (**Figure 2.7**). The Huang

thresholding algorithm was used to calculate the total tissue area from corresponding nuclei stained optical sections. After estimating the area, the macro code divides the fibrosis area by the total area of the optical segment, yielding a CPA value for each. Estimations are provided for each section, and the outcome is calculated as an average. CPA estimations were used to calculate collagen proportionate volume (CPV) values for each biopsy sample. Elastin proportionate area (EPA) was also measured through the abovementioned analysis and used to calculate Elastin proportionate volume (EPV) values.

The coefficient of variation (CV) values was computed using CPV/EPV values , and the standard deviations between slices were to determine the extent of variations in fibrosis groups. The CV values of the fibrosis groups (F1-2 and F3-4) were calculated using the group mean and standard deviation of CV. To categorize CV values in fibrosis groups, three categories (low, middle, and high) were chosen based on published CV classification studies. The utilized classification method was $CV\% < CV_{mean} - CV_s$ rated "low"; $CV_{mean} - CV_s < CV\% < CV_{mean} + CV_s$ rated "intermediate"; $CV\% > CV_{mean} + CV_s$ rated "high", where CV_{mean} is the group means of the coefficient of variation and CV_s is the standard deviation of the coefficient of variation.

CPA, CPV, and EPV cut-off values for fibrosis stages were calculated using the area under the receiver operator curve (AUROC). According to the Youden index, the best suited cut-off values were determined (≥50%). The AUROC of CPA cut-offs used are F1:0.89 ($p<0.001$, 95% CI 0.78-1.00), F2:0.87 ($p<0.05$, 95% CI 0.67-1.07), F3:0.71 ($p=0.205$, 95% CI 0.36-1.05), F4: 0.93 ($p<0.001$, 95% CI 0.84-1.02). The AUROC of CPV cut-offs are F1:0.64 ($p=0.151$, 95% CI 0.46-0.83), F2:0.86 ($p<0.05$, 95% CI 0.71-1.01), F3:0.95 ($p<0.01$, 95% CI 0.85-1.06) and F4:0.73 ($p<0.05$, 95% CI 0.53-0.94). The AUROC of EPV cut-offs are F1:0.62 ($p=0.324$, 95% CI 0.37-0.87), F2:0.80 ($p= 0.128$, 95% CI -0.45-1.14), F3:1 ($p= 0.033$, 95% CI 1-1), F4:0.85 ($p<0.05$, 95% CI 0.63-1.08).

Initially, 3D reconstructions were built on Image J software using 3D function of the software. Then, 3D reconstructions were built on Lasx software (Leica, Wetzlar, Germany). The stitched images were uploaded, and channels were merged and cropped by the software. Then, the intensity, gamma and opacity for each channel were individually

established. High-resolution images and 3D videos were produced using the movie editor panel.

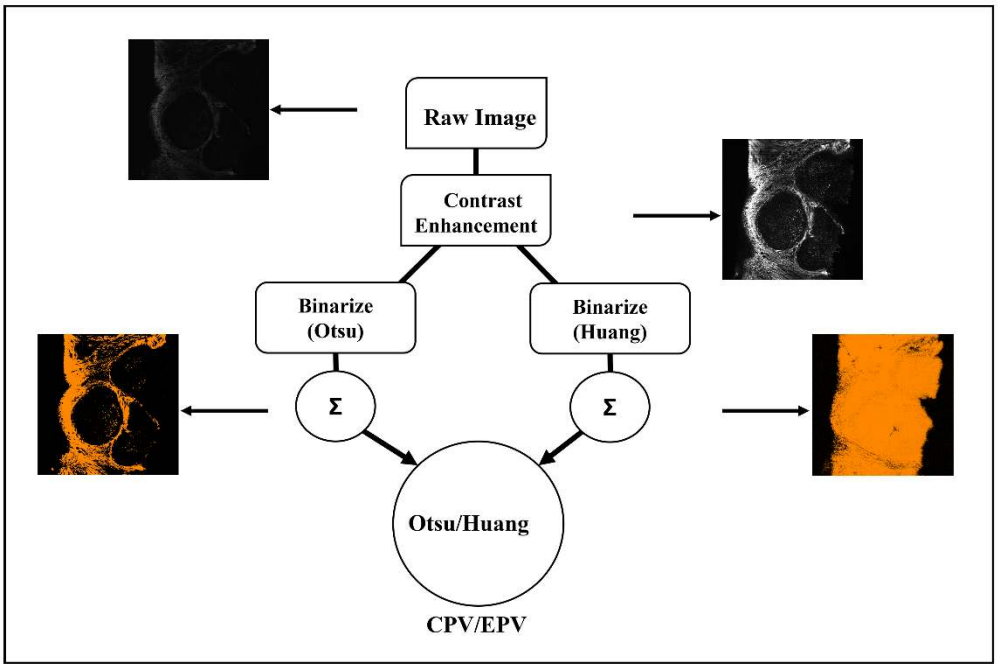

Figure 2.5 The followed analysis chart for LSFM images by Image J software. The determined contrast enhancement values are applied to the raw images then the binarization function of Image J executes the thresholding of positive pixels. Finally, CPV and EPV values are calculated after analysing multiple optical sections of whole liver tissue. CPV: Collagen proportionate volume, EPV: Elastin proportionate volume.

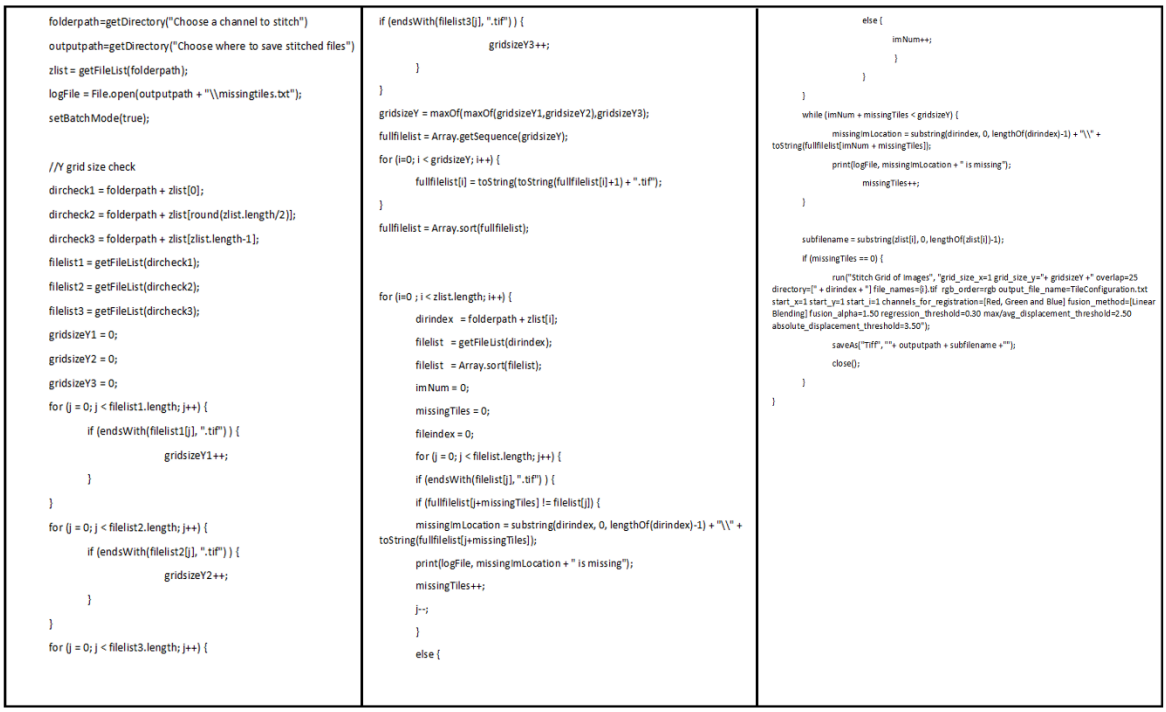

```
folderpath=getDirectory("Choose a channel to stitch")
outputpath=getDirectory("Choose where to save stitched files")
zlist = getFileList(folderpath);
logFile = File.open(outputpath + "\\missingtiles.txt");
setBatchMode(true);

//Y grid size check
dircheck1 = folderpath + zlist[0];
dircheck2 = folderpath + zlist[round(zlist.length/2)];
dircheck3 = folderpath + zlist[zlist.length-1];
filelist1 = getFileList(dircheck1);
filelist2 = getFileList(dircheck2);
filelist3 = getFileList(dircheck3);
gridsizeY1 = 0;
gridsizeY2 = 0;
gridsizeY3 = 0;
for (j = 0; j < filelist1.length; j++) {
        if (endsWith(filelist1[j], ".tif") ) {
                gridsizeY1++;
        }
}
for (j = 0; j < filelist2.length; j++) {
        if (endsWith(filelist2[j], ".tif") ) {
                gridsizeY2++;
        }
}
for (j = 0; j < filelist3.length; j++) {
        if (endsWith(filelist3[j], ".tif") ) {
                gridsizeY3++;
        }
}
gridsizeY = maxOf(maxOf(gridsizeY1,gridsizeY2),gridsizeY3);
fullfilelist = Array.getSequence(gridsizeY);
for (i=0; i < gridsizeY; i++) {
        fullfilelist[i] = toString(toString(fullfilelist[i]+1) + ".tif");
}
fullfilelist = Array.sort(fullfilelist);


for (i=0 ; i < zlist.length; i++) {
        dirindex  = folderpath + zlist[i];
        filelist  = getFileList(dirindex);
        filelist  = Array.sort(filelist);
        imNum = 0;
        missingTiles = 0;
        fileindex = 0;
        for (j = 0; j < filelist.length; j++) {
        if (endsWith(filelist[j], ".tif") ) {
        if (fullfilelist[j+missingTiles] != filelist[j]) {
        missingImLocation = substring(dirindex, 0, lengthOf(dirindex)-1) + "\\" +
toString(fullfilelist[j+missingTiles]);
        print(logFile, missingImLocation + " is missing");
        missingTiles++;
        j--;
        }
        else {
                imNum++;
                }
        }
        while (imNum + missingTiles < gridsizeY) {
                missingImLocation = substring(dirindex, 0, lengthOf(dirindex)-1) + "\\" +
toString(fullfilelist[imNum + missingTiles]);
                print(logFile, missingImLocation + " is missing");
                missingTiles++;
        }

        subfilename = substring(zlist[i], 0, lengthOf(zlist[i])-1);
        if (missingTiles == 0) {
                run("Stitch Grid of Images", "grid_size_x=1 grid_size_y="+ gridsizeY +" overlap=25
directory=[" + dirindex + "] file_names=i{i}.tif  rgb_order=rgb output_file_name=TileConfiguration.txt
start_x=1 start_y=1 start_i=1 channels_for_registration=[Red, Green and Blue] fusion_method=[Linear
Blending] fusion_alpha=1.50 regression_threshold=0.30 max/avg_displacement_threshold=2.50
absolute_displacement_threshold=3.50");
                saveAs("Tiff", ""+ outputpath + subfilename +"");
                close();
        }
}
```

Figure 2.6 The stitching code used in this study. The code was written IJM language and created in Image J software.

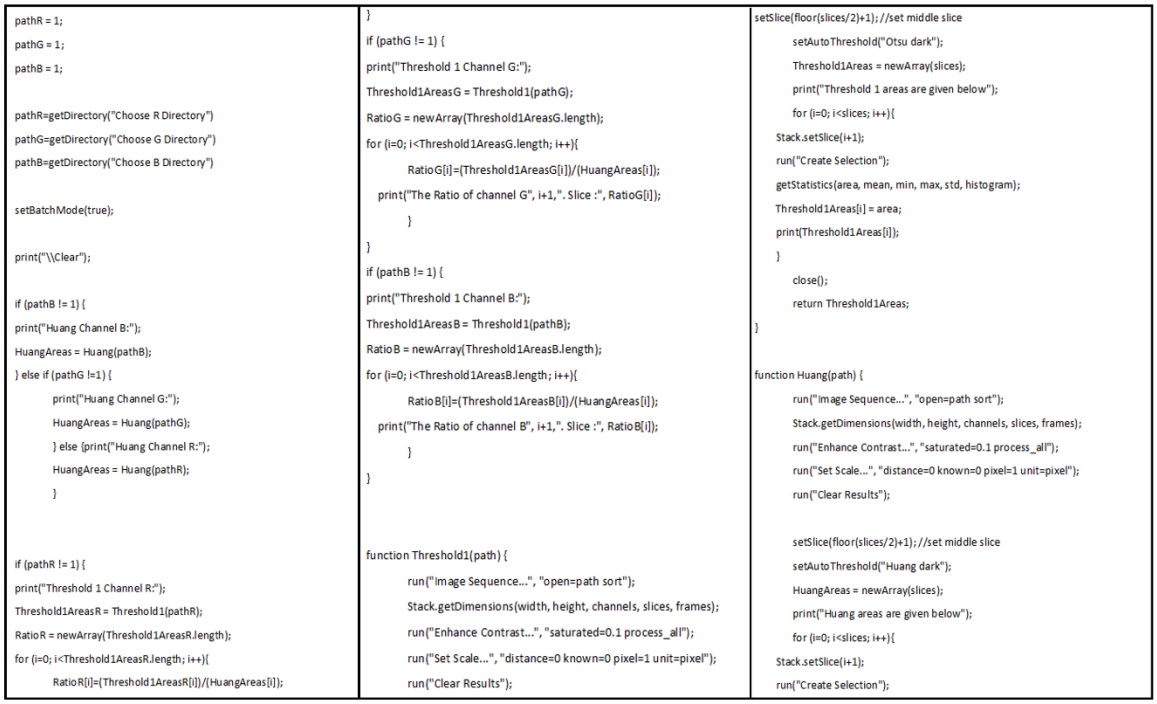

```
pathR = 1;
pathG = 1;
pathB = 1;

pathR=getDirectory("Choose R Directory")
pathG=getDirectory("Choose G Directory")
pathB=getDirectory("Choose B Directory")

setBatchMode(true);

print("\\Clear");

if (pathB != 1) {
print("Huang Channel B:");
HuangAreas = Huang(pathB);
} else if (pathG !=1) {
        print("Huang Channel G:");
        HuangAreas = Huang(pathG);
        } else {print("Huang Channel R:");
        HuangAreas = Huang(pathR);
        }


if (pathR != 1) {
print("Threshold 1 Channel R:");
Threshold1AreasR = Threshold1(pathR);
RatioR = newArray(Threshold1AreasR.length);
for (i=0; i<Threshold1AreasR.length; i++){
        RatioR[i]=(Threshold1AreasR[i])/(HuangAreas[i]);
}
if (pathG != 1) {
print("Threshold 1 Channel G:");
Threshold1AreasG = Threshold1(pathG);
RatioG = newArray(Threshold1AreasG.length);
for (i=0; i<Threshold1AreasG.length; i++){
        RatioG[i]=(Threshold1AreasG[i])/(HuangAreas[i]);
  print("The Ratio of channel G", i+1,". Slice :", RatioG[i]);
        }
}
if (pathB != 1) {
print("Threshold 1 Channel B:");
Threshold1AreasB = Threshold1(pathB);
RatioB = newArray(Threshold1AreasB.length);
for (i=0; i<Threshold1AreasB.length; i++){
        RatioB[i]=(Threshold1AreasB[i])/(HuangAreas[i]);
  print("The Ratio of channel B", i+1,". Slice :", RatioB[i]);
        }
}


function Threshold1(path) {
        run("Image Sequence...", "open=path sort");
        Stack.getDimensions(width, height, channels, slices, frames);
        run("Enhance Contrast...", "saturated=0.1 process_all");
        run("Set Scale...", "distance=0 known=0 pixel=1 unit=pixel");
        run("Clear Results");
        setSlice(floor(slices/2)+1); //set middle slice
        setAutoThreshold("Otsu dark");
        Threshold1Areas = newArray(slices);
        print("Threshold 1 areas are given below");
        for (i=0; i<slices; i++){
    Stack.setSlice(i+1);
    run("Create Selection");
    getStatistics(area, mean, min, max, std, histogram);
    Threshold1Areas[i] = area;
    print(Threshold1Areas[i]);
    }
        close();
        return Threshold1Areas;
}

function Huang(path) {
        run("Image Sequence...", "open=path sort");
        Stack.getDimensions(width, height, channels, slices, frames);
        run("Enhance Contrast...", "saturated=0.1 process_all");
        run("Set Scale...", "distance=0 known=0 pixel=1 unit=pixel");
        run("Clear Results");

        setSlice(floor(slices/2)+1); //set middle slice
        setAutoThreshold("Huang dark");
        HuangAreas = newArray(slices);
        print("Huang areas are given below");
        for (i=0; i<slices; i++){
    Stack.setSlice(i+1);
    run("Create Selection");
```

Figure 2.7 The analysis code used in this study. The code was written IJM language and created in Image J software.

2.7 Statistical analysis

The measurement of spread analysis performed using interquartile range (IQR) measurement for all fibrosis stages. The CPV/EPV results of fibrosis groups and COL1A1 and COL3A1 gene expression levels were compared using Man-Whitney U test. The cut-off values for CPA, CPV and EPV were determined by calculating the area under receiver operator (AUROC) curves and using the Youden index over. 3D histogram analysis executed using MATLAB R2021b. The significance level was set at 0.05 or below for all results. (*$p \leq 0.05$, **$p \leq 0.01$, ***$p \leq 0.001$)

Chapter 3: Results

3.1 Clarification of human and mouse liver tissues

3.1.1 Human liver tissues

This study employed the modified-CLARITY method to obtain transparent human liver tissues. **Figure 3.1** shows the transparency process of non-fibrotic liver tissues. The transparency of the samples was evaluated based on how much visible light they transmit. **Figure 3.2** shows the clearing process of cirrhotic liver tissues, which seem more opaque than non-fibrotic livers. The reason for that is the ECM content of cirrhotic livers. If one looked carefully at the cleared cirrhotic liver tissues, macro nodules of advanced stage liver diseases would be observed. **Figure 3.3** shows the clearing process of liver biopsy samples. Importantly, the time for clearing phospholipids from the tissue depends on the tissue size, the lipid and protein content of the sample. Since we passively remove phospholipids from the tissue, 6-8 weeks is needed. Initially, we tried an active clearing system for the biopsy sample, but unfortunately, tissue shrinkage and morphology disruption were our significant limitations.

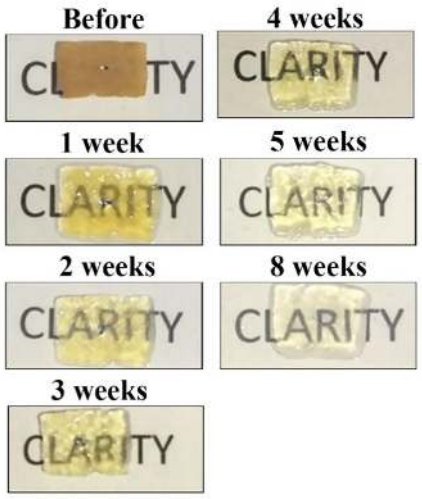

Figure 3.1 Clearing process of non-fibrotic liver tissues. The clearing efficiency of the modified-CLARITY method is depicted in non-fibrotic liver samples. Images were taken before relocating into clearing buffer and throughout the clearing process.

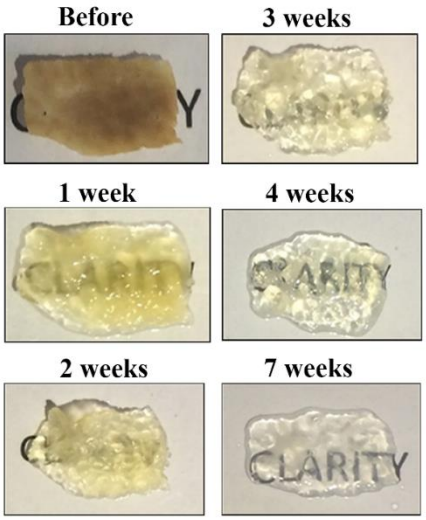

Figure 3.2 Clearing time of cirrhotic liver tissues. The clearing efficiency of the modified-CLARITY method is displayed in cirrhotic liver samples. Images were taken before relocating into clearing buffer and throughout the clearing process.

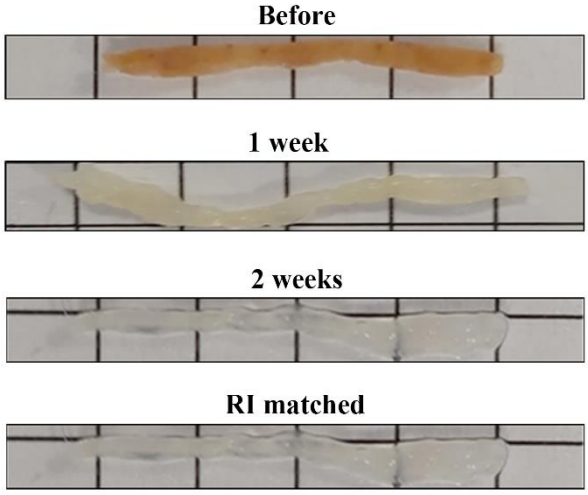

Figure 3.3 Clearing time of liver biopsy specimen. The clearing efficiency of the modified-CLARITY method is shown in liver biopsy specimen. Images were taken before relocating into clearing buffer and throughout the clearing process. (a single line represents 5 mm).

In this project, we cleared a hundred and sixty-eight human liver tissues. However, there were limitations; occasionally, some of the samples turned yellowish, possibly due to the Maillard reaction, i.e., a chemical reaction between the amino acids and reducing sugar. Generally, lowering the clearing temperature or adding 0.5% a-thioglycerol helps to

discolouration of samples. We also observed that those samples that turned yellowish had more autofluorescence. The other problem was the clearing time due to the passive extrusion of lipids. To speed up the time for the clearing can be managed by using more concentrated SDS (up to 8%) and increasing the temperature. However, this adjustment was unsuitable for biopsy samples due to being fragile after the clearing.

3.1.2 Mouse liver tissues

We performed perfusion and non-perfusion guided delivery of hydrogel monomers to the mouse liver tissues in animal models of liver fibrosis and NASH. **Figure 3.4** shows cleared mouse liver tissue pieces of the high fat high sucrose (HFHS) animal model, and transparency was observed. Additionally, **figure 3.5** displays liver tissue pieces of carbon tetrachloride (CCl4) animal models and shows the clearing efficiency of the non-perfused protocol. The major limitation would have been less diffusion of monomers, resulting in poor preservation of proteins and tissue morphology. However, we saw that tissue integrity was maintained throughout the clearing process.

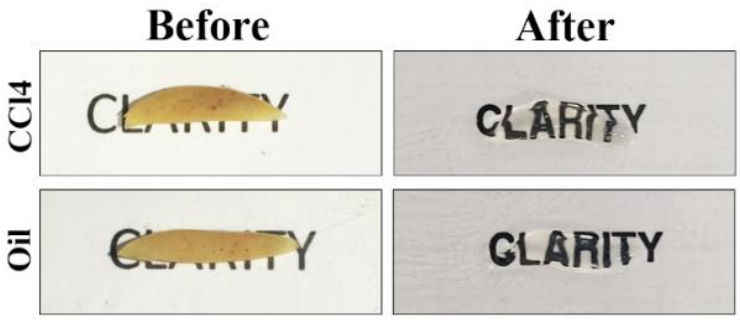

Figure 3.4 Clearing efficiency of mouse liver slices in CCl4 animal model. The non-perfusion approach of the modified-CLARITY method shows the clearing efficiency of liver pieces in the CCl4 animal model. The images are captured before and after the clearing procedure is completed.

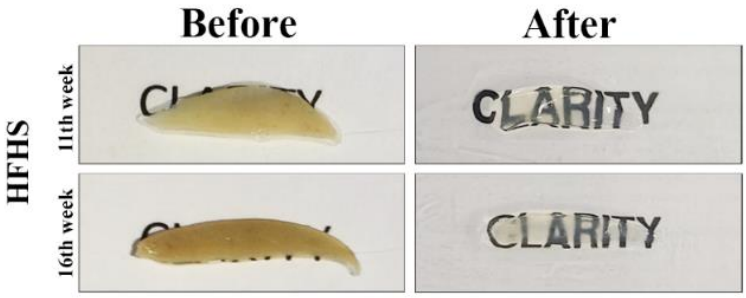

Figure 3.5 Clearing efficiency of mouse liver slices in HFHS animal model. The images show the efficiency of the non-perfused approach of the modified-CLARITY method on the HFHS model.

The latter approach for clearing mouse liver tissues was the perfusion-guided delivery of hydrogel monomers. In this method, after cardiac perfusion of the liver, we incubated whole livers for several days in a hydrogel monomer solution to ensure the monomer diffusion efficiency. **Figure 3.6** shows the clearing process of mouse whole livers with modified-CLARITY protocol in CCl4 induced liver fibrosis model. Additionally, for the purpose of individual imaging of mouse liver lobes, we divided liver lobes as a whole and showed the high clearing efficiency in **figure 3.7**. Also, whole mouse liver clearing was performed in the methionine and choline deficient (MCD) diet model of NASH and showed the cleared whole liver in different groups of the MCD model. (**Figure 3.8**)

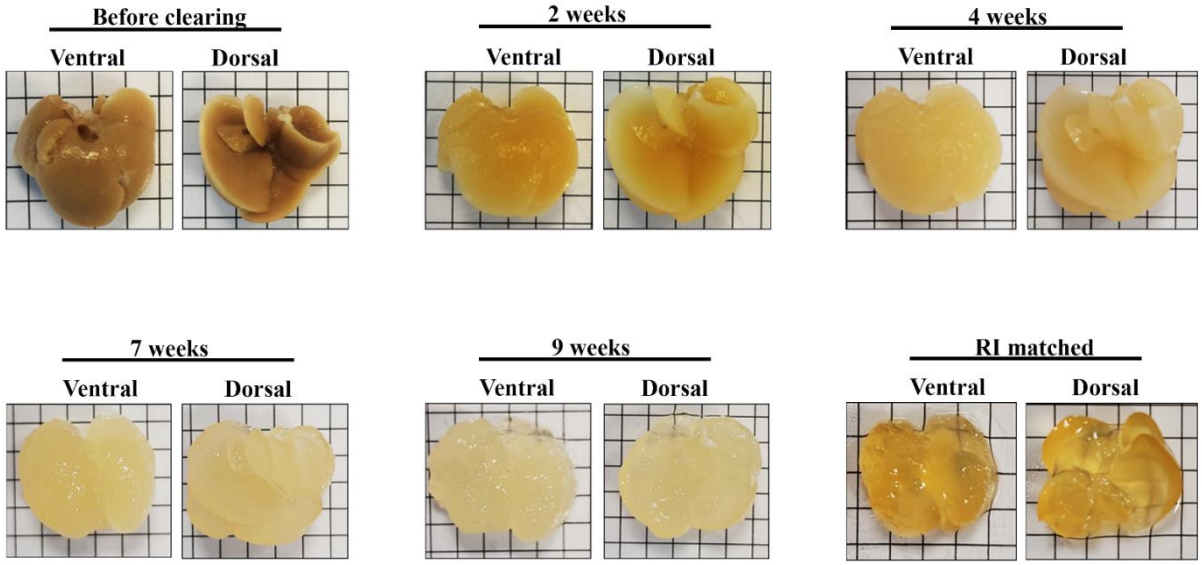

Figure 3.6 Clearing efficiency of whole mouse livers in CCl4 animal model. The perfusion guided approach of the modified-CLARITY method is able to clear whole mouse livers. The images were captured before the clearing process began and throughout the process until they became completely transparent. (a single line represents 5 mm).

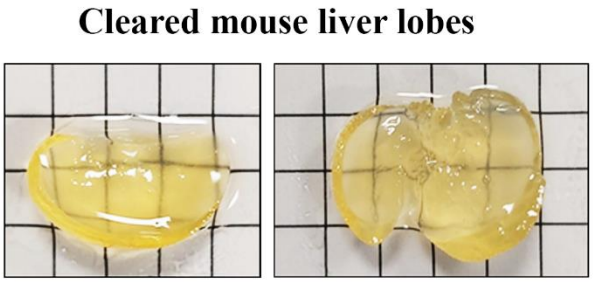

Figure 3.7 Clearing efficiency of mouse liver lobes. The separated liver lobes show the high clearing efficiency of the method. (a single line represent 5 mm).

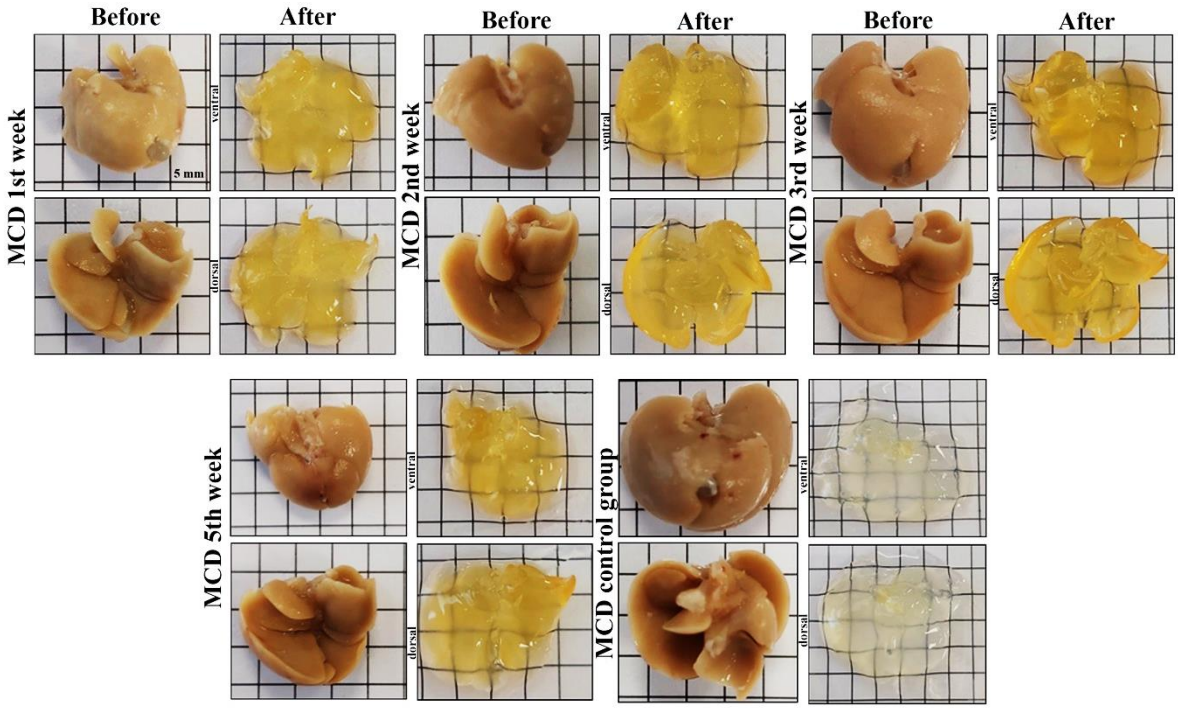

Figure 3.8 Clearing efficiency of whole mouse livers in MCD animal model. The clearing efficiency of the method is displayed and maintained between the groups in MCD animal model. (a single line represents 5 mm).

However, there were some limitations in clearing mouse liver tissues, such as the clearing time of liver tissues of the HFHS model was long, possibly due to the high lipid contents. Additionally, some of the tissues remained opaque, leading to less clearing efficiency.

3.2 Extracellular matrix protein staining of cleared liver tissues

3.2.1 Staining of cleared human liver tissues

Once we had cleared liver tissues, we tested our method to visualize ECM proteins and fibers. First, we used fluorescence microscope to image our samples, in order to see if the method is successful and able to stain ECM proteins. **Figure 3.9** shows the 3D fluorescence images from a cleared cirrhotic liver, which is stained with antibodies against α-smooth muscle actin (α-SMA) (Sigma Aldrich, F3777) and collagen type I (Abcam, ab34710) proteins. Here, we observed that the method is successfully cleared liver tissues and staining was promising. However, collagen type I staining was non-specific and further optimization was needed. Nevertheless, these results were promising and showed the applicability of method on human liver tissues.

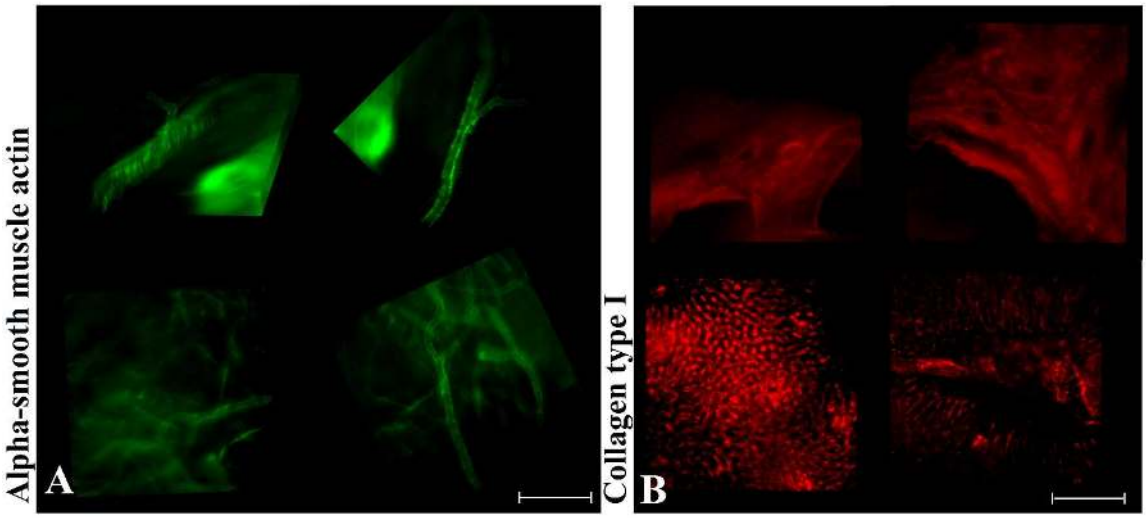

Figure 3.9 The first fluorescence images of CLARITY-processed human liver tissues. The fluorescence images represent the clearing and staining quality of the method. A) In α-SMA staining (left side), protein localization and structure of the vein is highlighted. B) Despite having specific staining pattern of α-SMA, collagen type I staining needs further optimization. (Scale bar: 500 μm).

Confocal imaging for the optimization of human ECM protein staining

In this project, one of our aims is to develop a light-sheet fluorescence microscope which is compatible with clinical samples for 3D quantification. Therefore, we collaborated with the Physics department of Koç University to design a light-sheet microscope at KUTTAM. However, as it would take time to build up the custom light-sheet microscope, we proceeded to optimization experiments of targeted ECM proteins with a confocal microscope at the KUTTAM imaging centre.

Further, we proceeded to optimize the staining of cleared human liver samples by adjusting concentrations and secondary antibodies. First, we performed dual staining under the same conditions and imaged samples with a confocal laser scanning microscope. **Figure 3.10** shows the confocal images from stained cirrhotic liver tissue with α-SMA and collagen type I. However, this did not change any staining pattern in collagen type I, but α-SMA staining pattern was still promising.

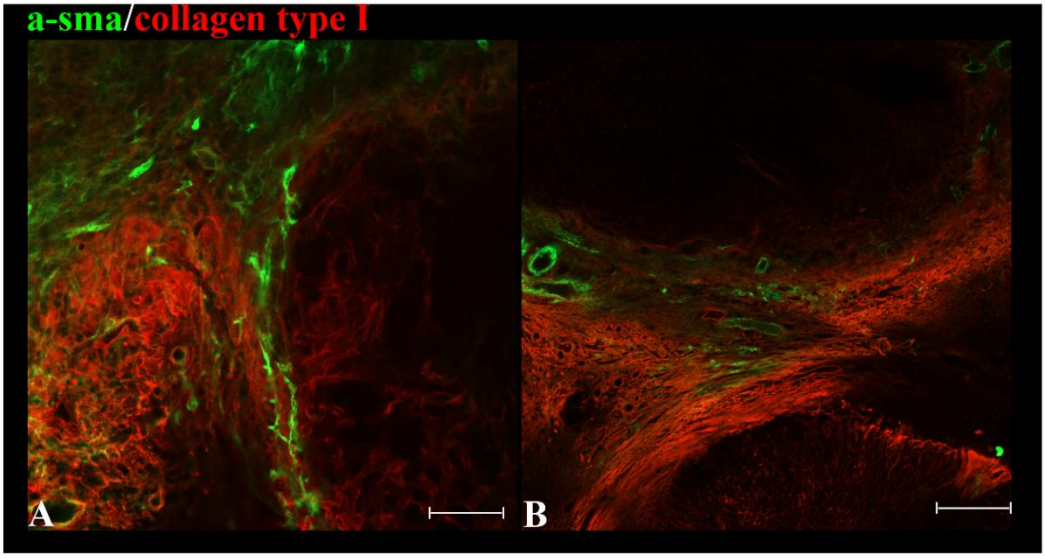

Figure 3.10 Confocal images of cleared human cirrhotic liver tissue. Dual staining images of cleared liver tissues with a confocal microscope were shown. A) High magnification image of α-SMA and collagen type I staining in cirrhotic liver shows a specific pattern of α-SMA protein in high resolution. (Image was captured with 20X magnification objectives, scale bar: 200 μm). B) Wider confocal image for dual staining of

a cleared cirrhotic liver. (Image was captured with 10X magnification objectives scale bar: 100 μm).

Then, we adjusted antibody concentrations and secondary antibodies that we used in the previous staining for collagen type I. Moreover, we added nuclei staining to see if the method preserved DNAs throughout the clearing process. **Figure 3.11 and figure 3.12** shows the stained cirrhotic livers with different concentrations of antibodies, which targets alpha-sma and collagen type I. Although the alpha-sma staining pattern was specific, still collagen type I staining pattern was not. Furthermore, nuclei staining of cleared liver tissue was successful and shows the method is able to preserve nucleic acids.

Additionally, we adjusted the secondary antibody concentration shown in **Figures 3.11C** and **D**. However, in both conditions, there was still non-specific binding of the antibody, which was a significant limitation for this staining.

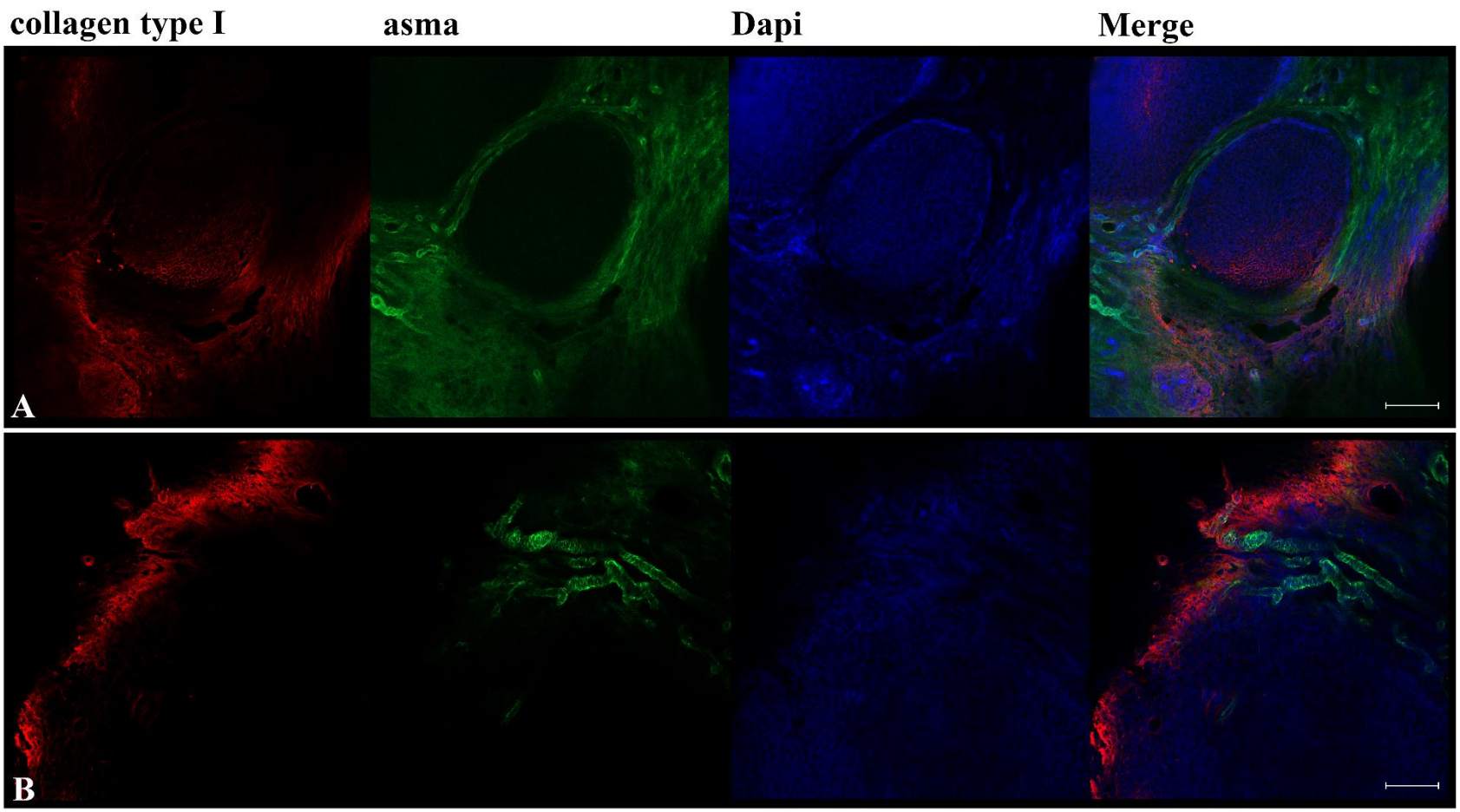
collagen type I
asma
Dapi
Merge
A
B

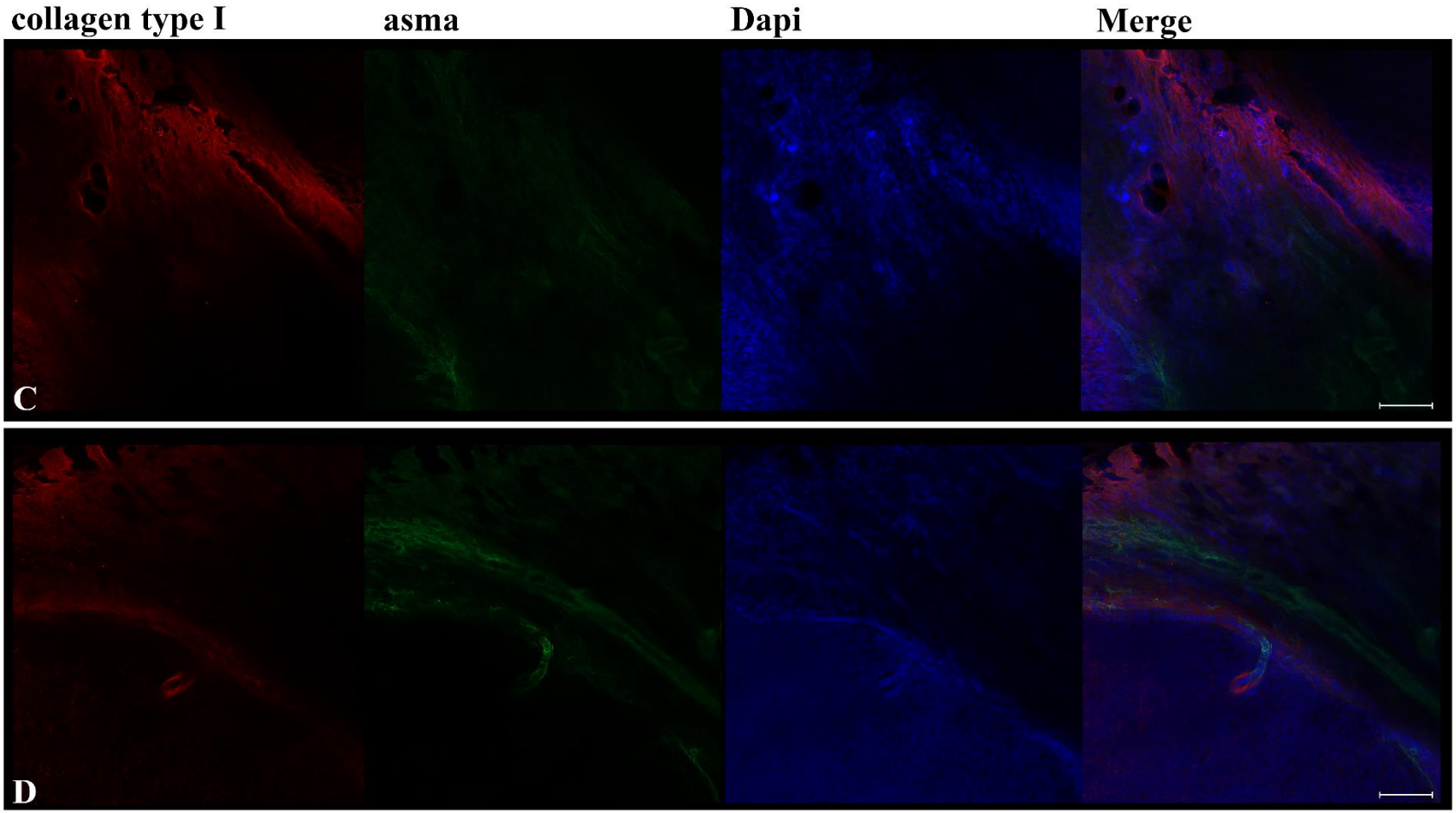

Figure 3.11 Examination of staining pattern for Collagen type I protein in human cleared liver tissues. Various Collagen type I antibody concentrations was utilized to find optimal staining patterns. Since α-SMA staining is optimized, we did not change staining conditions for this protein. **Figures 3.11A** and **B** show the staining of Collagen type I at 1:500, and 1:1000 dilution, respectively, while the secondary antibody is used at 1:100 concentration.

The immunofluorescence staining approach is a widely used technique in cellular and molecular imaging. The compatibility of secondary antibodies with the primary antibody is crucial for detecting desired molecules. Optimal conditions for specific staining patterns may need further implementations of the staining protocol. Therefore, we tested alternative secondary antibodies to highlight specific ECM proteins in cleared liver tissues. The CY3 (Cyanin-3) tagged secondary antibody was used to find a specific staining pattern for ECM protein detection. We aimed to see the deep penetration of primary antibodies and increase the imaging depth. Unfortunately, the staining pattern of Collagen type I-targeted antibody (Abcam, ab34710) was non-specific, and further optimization was needed. (**Figure 3.12**)

Another available secondary antibody for Collagen type I protein detection was a secondary antibody which belongs to the Alexa fluor dye family and has a fluorophore excitable at 568 nm laser. In contrast to staining with CY3 fluorophore, staining in the sinusoids was less. However, it still needs further optimization experiments. **Figure 3.13A** emphasizes the penetration in the hepatocellular region along with the ECM-rich area in the cirrhotic liver. However, there is still significant penetration in the non-ECM area. This may limit our accurate detection and quantification analysis and even lover sensitivity of the method. The non-specific binding that we observed in these examinations prevented the visualization of antigen-antibody binding of interest. Consequently, we carried out a blocking step to mitigate non-specific binding using serum samples of various animals. Generally, utilizing a serum that matches with the secondary antibody host organism is recommended. Therefore, we tested goat serum (CY3-conjugated secondary antibody is raised in Goat) and horse serum. Moreover, we examined Collagen type III primary antibody (Abcam, ab7778) staining with blocking and no blocking conditions (**Figure 3.14A-J**). Collagen type III is the second most abundant ECM protein accumulated in advanced fibrosis stages. Therefore, we tried to find an optimal working condition for Collagen type III antibody. We experimented with both ECM proteins to reduce non-specific binding with either Goat or Horse serum reagents (**Figure 3.14**). Blocking steps were implemented either prior to primary antibodies (**Figure 3.14B, G, D, and I)** or prior to primary and secondary antibodies (**Figure 3.14C, H, E, and J**).

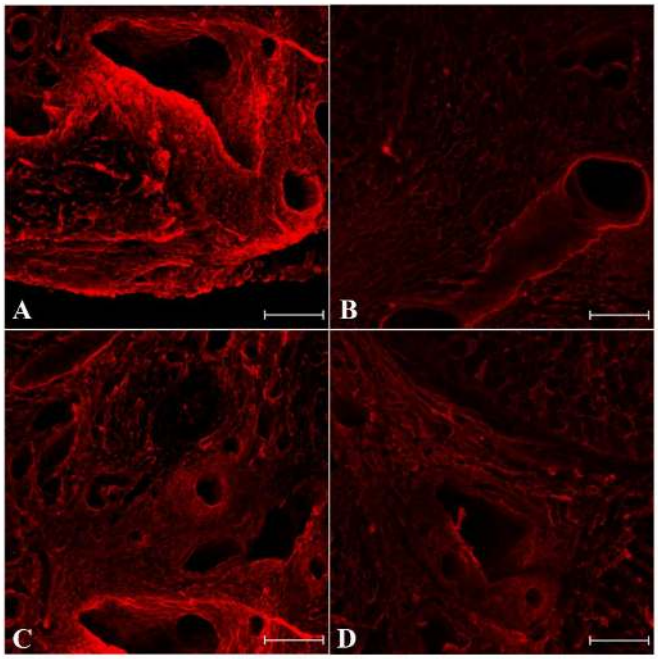

Figure 3.12 Staining of cleared liver tissues with the alternative secondary antibodies. The figure represents the examination of the staining pattern for Collagen type I protein tagged with CY3 conjugated secondary antibody. **Figure 3.12A** to **C** represents confocal imaging results of Collagen type I-stained cleared cirrhotic liver tissues. Figure 3.12D shows an image obtained using a multiphoton imaging system and a 1060 nm laser. Images were captured as multiple tiles and stitched using Lasx software. (Scale bar: 200 µm).

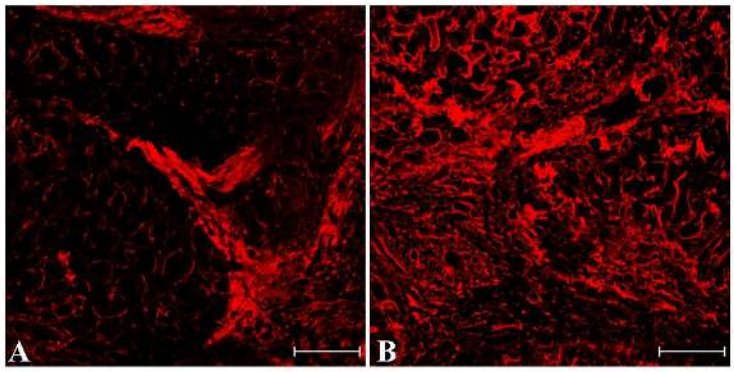

Figure 3.13 Staining of cleared liver tissues with the alternative secondary antibodies. Images display the staining efficiency of Alexa fluor 568 conjugated secondary antibodies for Collagen type I protein in cirrhotic liver. **Figure 3.13A** underlies comparable penetration of antibodies, while **figure 3.13B** underlies the need for additional adjustments in the staining protocol.

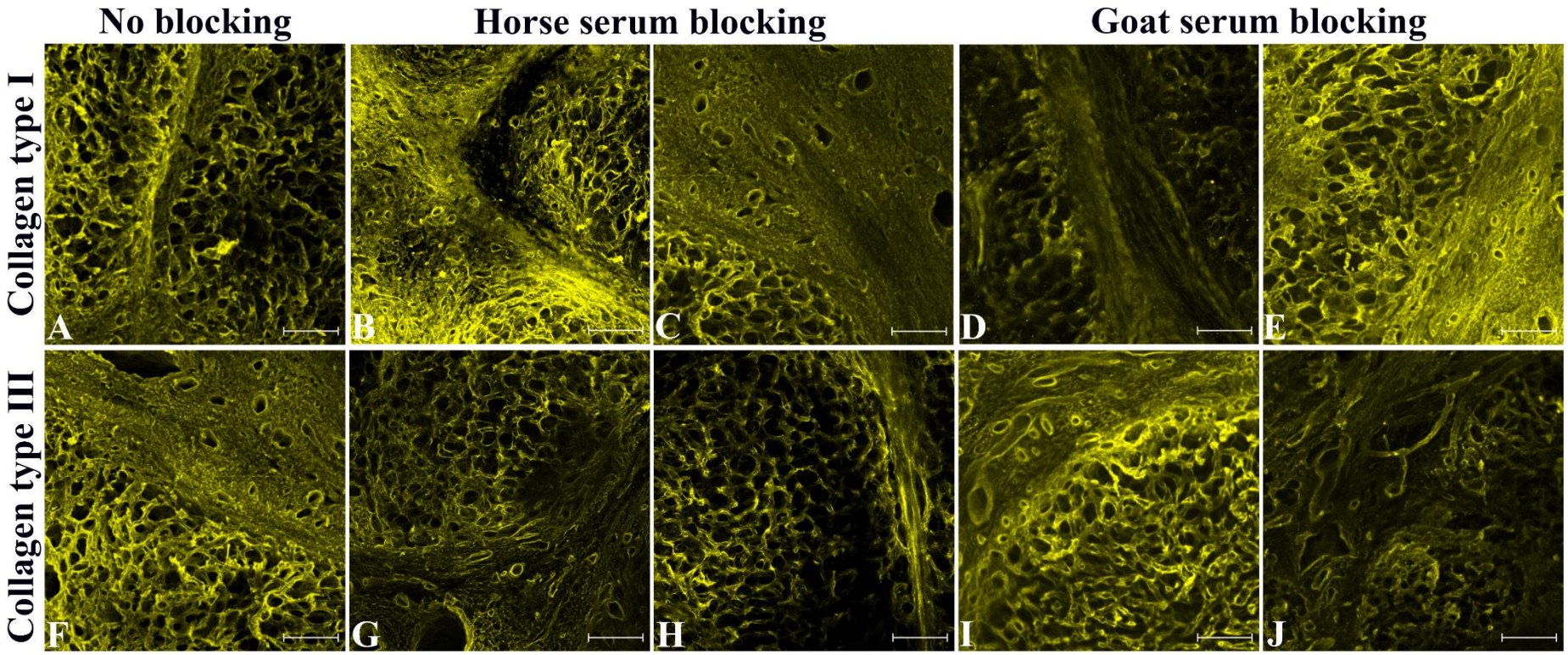

Figure 3.14 Blocking of non-specific binding of primary antibodies with various serum reagents for Collagen type I and III. Cirrhotic liver tissue was used to optimize Collagen type I and type III antibodies using various blocking and non-blocking conditions. The conditions were as follows, No-blocking (A&F), Horse serum blocking before primary antibody incubation (B&G), Horse serum blocking before primary and secondary antibody incubations (C&H), Goat serum blocking before primary antibody incubation (D&I), Goat serum blocking before primary and secondary antibody incubations (E&J). (Scale bar: 200 µm)

Consequently, there were no specific staining patterns for both ECM proteins. Then, we tried to prevent non-specific binding solely before the secondary antibody (Cy3), which is raised in goats, by using 5% goat serum in PBS-tween-20. The result was promising when a wider sample area was imaged with confocal imaging systems **(Figure 3.15).** Importantly, collagen deposition is abundant in fibrotic bundles besides in nodules of cirrhotic liver samples. The entire nodule was visualized to see the staining pattern in a wider manner and consequently concluded as optimized staining for collagen type I protein. The imaging was acquired as multiple tiles and 3D reconstructed with Lasx software (**Figure 3.16**).

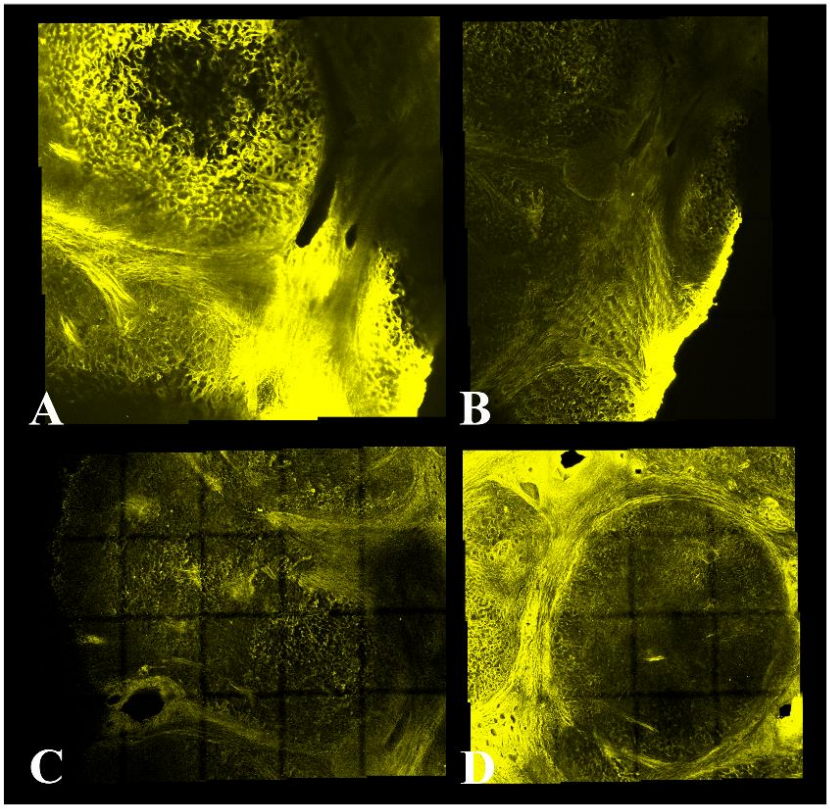

Figure 3.15 Examination of Collagen type I staining optimization in cirrhotic liver. A confocal microscope was used to observe the blocking of non-specific binding with Goat serum in cleared cirrhotic liver from various tissue regions and an entire regenerating nodule (A, B, C and D). Images were taken as multiple tiles and merged in Lasx software.

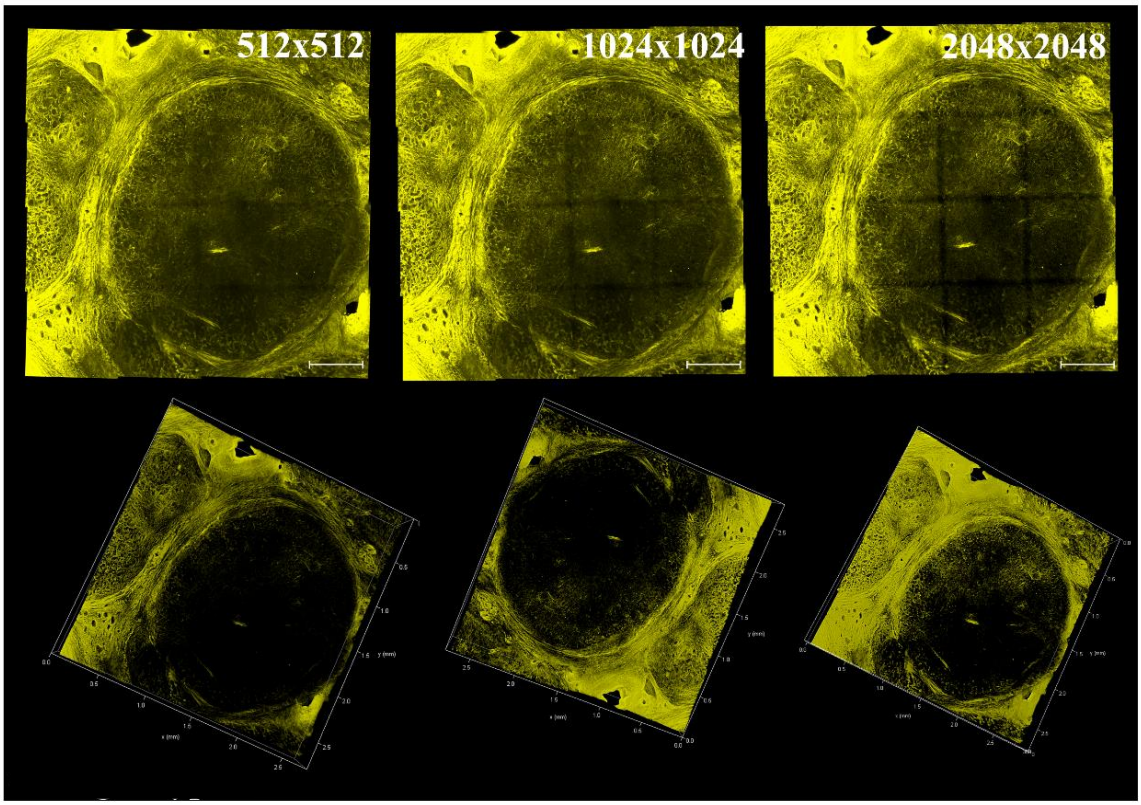

Figure 3.16 3D representation of entire nodule with optimized protocol for Collagen type I protein. Multiple tiles were acquired from a depicted nodule at various resolution settings in order to test if adjusted resolution may change the sensitivity of the analysis method. The image was 3D reconstructed in Lasx software.

The specific binding between antigen and antibody is important for successful immunostaining. Isotype control is used to differentiate non-specific background signals from specific antibody signals. Therefore, we applied isotype control for collagen type I and type III staining in order to see if the staining is specific **(Figure 3.17)**. Immunoglobulin G (IgG) controls were chosen the same as the primary antibody host species. Additionally, negative controls (No addition of primary antibody) were added to the experimental setup **(Figure 3.17)**.

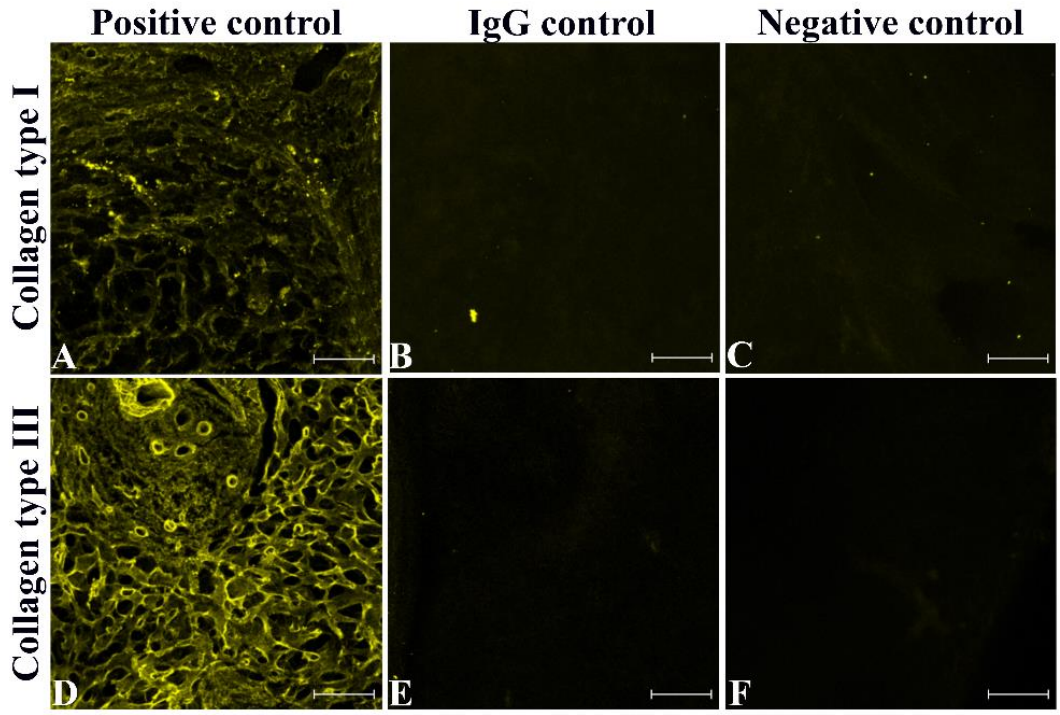

Figure 3.17 Isotype control staining for Collagen type I and Collagen type III. Isotype control staining examinations were displayed, Positive control staining (A&D), IgG control staining (B&E) and Negative control staining (C&F) for Collagen type I and Collagen type III. (Scale bar: 200 µm)

Thus far, optimization experiments have been performed using rabbit polyclonal Collagen type I antibody (Abcam, ab34710). Then, we tested a monoclonal antibody which is produced against Collagen type I (Abcam, ab90395) in cleared liver tissues. Liver tissues were stained for two days in the primary antibody at a concentration of 1:500, followed by washing with PBS-Tw for two days. Then, 5% of goat serum was applied, and a secondary antibody (Goat anti-mouse CY3) was added on the following day for two days. Then, nuclei staining was performed with Hoechst dye (Thermo Scientific, 33342) at 1:1000 concentration for 6 hours and washed with PBS-Tw. Non-fibrotic, F2 stage liver and cirrhotic liver tissues were used in this experiment. Images were captured with a confocal microscope in the KUTTAM imaging centre. The abovementioned staining protocol was specific in samples of non-fibrotic and F2 stage cleared liver tissues (**Figure 3.18A**). However, the staining pattern of Collagen type I in the cirrhotic liver was not specific, and further optimization was needed (**Figure 3.18A**). Only non-fibrotic and F2 stage liver tissues were 3D reconstructed using Lasx software (**Figure 3.18B**).

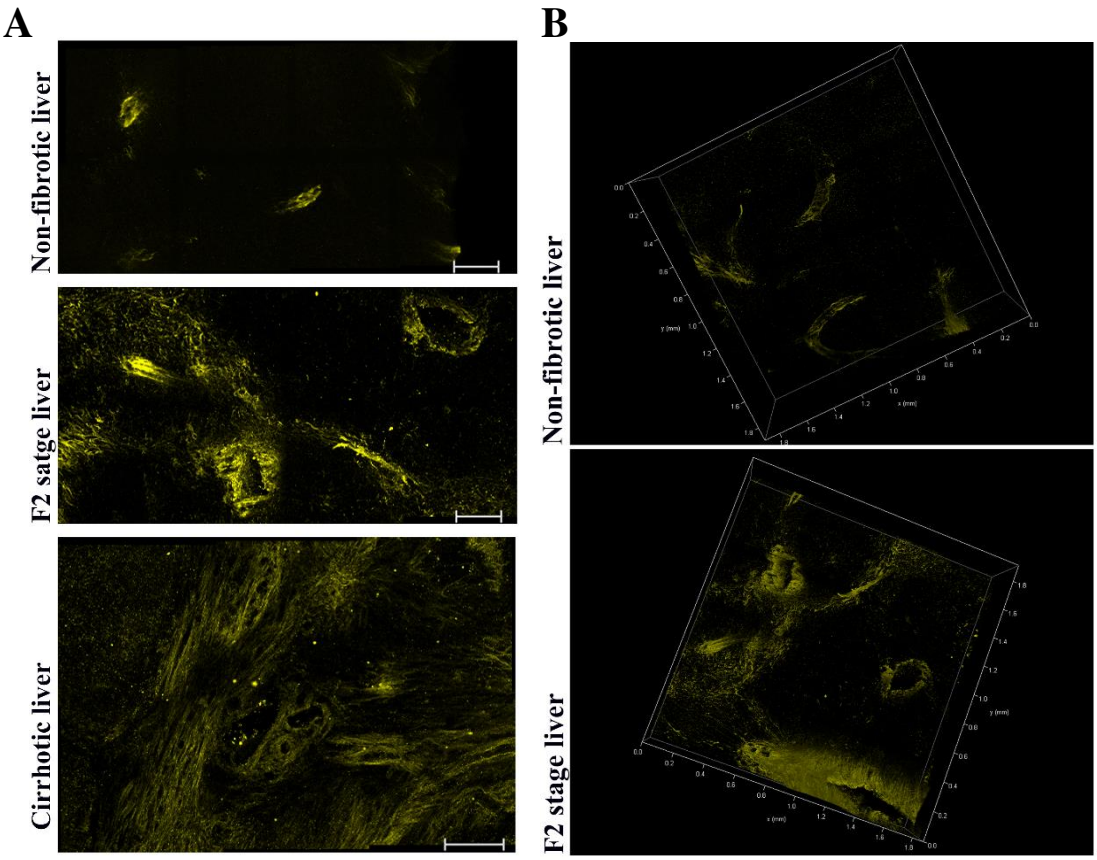

Figure 3.18 Examination of monoclonal Collagen type I antibody staining results. A) Monoclonal antibody was used to stain Collagen type I protein in various fibrotic cleared liver tissues. B) 3D representation of non-fibrotic and F2 stage cleared liver tissues were produced, acquiring images as tiles using a confocal microscope. (Scale bar: 200 µm).

We modified the blocking reagents and blocking steps in the protocol to optimize the staining pattern of collagen type I protein in cirrhotic liver. Therefore, in the experimental set-up, preparing primary antibody, blocking reagent and secondary antibody in a PBS-Tw containing sodium azide performed the best pattern for collagen type I detection in cleared liver tissues (**Figure 3.19**). Other adjustments with custom blocking reagents did not reveal any specific antibody binding, therefore not selected. We observed the best mitigation before secondary antibody blocking. This antibody was more promising than the previous collagen type I antibody (rabbit polyclonal) and performed a specific binding to the target protein and would allow us to specific quantification of the most abundant protein of ECM. Images were taken with a confocal microscope as multiple tiles and 3D reconstructed in Lasx software (**Figure 3.19**).

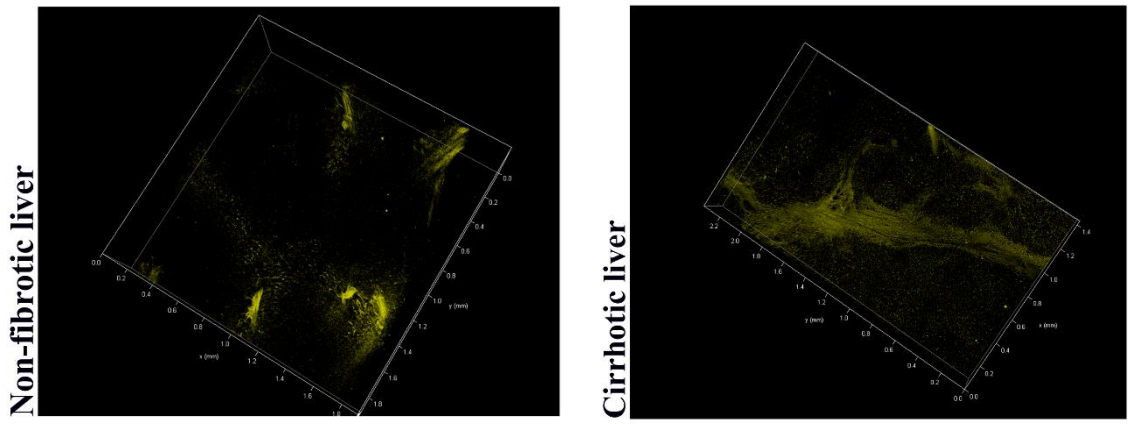

Figure 3.19 Examination of the staining pattern of monoclonal Collagen type I antibody in cleared liver tissues. Non-fibrotic and cirrhotic liver tissues were stained with monoclonal collagen type I protein and displayed a specific binding pattern after the implementation of blocking reagents. (Scale bar: 200 µm)

In the meantime, we also tested another commercial antibody that targets to detect both type I and III collagen proteins at the same time (Bio-Rad, 2150-2210). Since this antibody detects both proteins, it allows to stain multiple protein in one sample. Initially, we stained three types of cleared liver tissues in order to see the staining pattern. Initially, the staining pattern was promising in the confocal microscope imaging. Although there were promising staining pattern and but also a non-specific background in the non-ECM area. (**Figure 3.20**). Therefore, further optimization was needed. Images were captured as multiple tiles using confocal microscope.

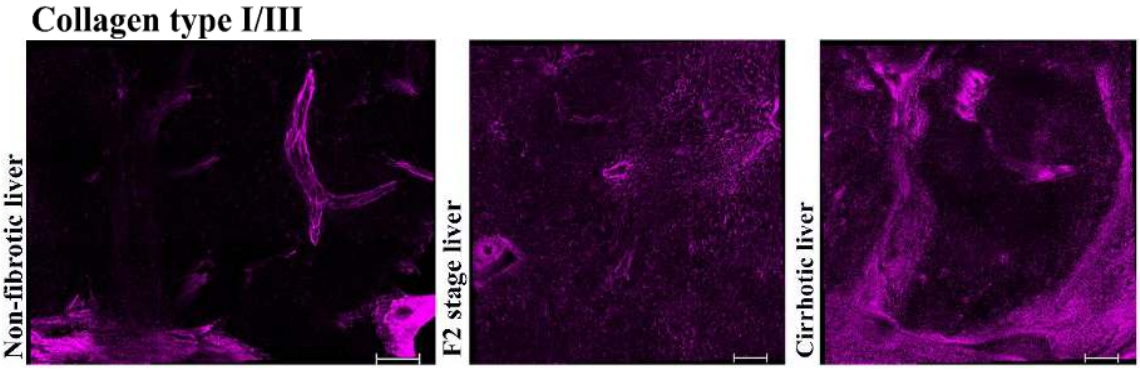

Figure 3.20 Examination of the staining Collagen type I and III protein with multi-targeted antibody in cleared liver tissues. Staining was applied to non-fibrotic, F2 stage and cirrhotic liver to see the antibody's staining efficiency. The staining pattern in non-fibrotic tissue was promising, however, other tissues have non-specific background (Scale bar: 200 µm)

To improve Collagen type I/III staining, we adjusted the staining temperature, blocking reagent, and a secondary antibody. In the previous staining, we saw a non-specific detection of the proteins, which we would not expect to observe. Therefore, we used an intense blocking reagent which we prepared in-house (B1) to provide a specific staining pattern. We also reduced the temperature at which the experiment was carried out during the staining procedure from 37°C to +4°C. Further, we adjusted the secondary antibody that we used. However, the implementations and using various blocking reagents did not change the pattern (**Figure 3.21**).

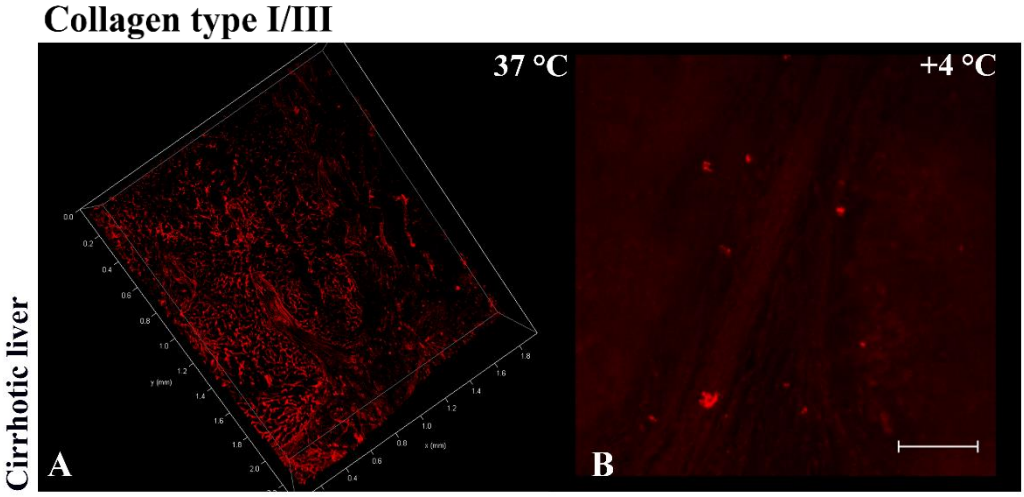

Figure 3.21 Optimization of Collagen type I/III antibody in cleared liver tissues. Cleared cirrhotic liver tissues stained with Collagen type I/III, blocked with custom blocking reagent, and tagged with Alexa fluor 594 secondary antibodies at 37°C (A) and +4°C (B). (Scale bar: 200 µm)

As liver fibrosis progresses, ECM proteins accumulate within the organ, such as elastin, fibronectin, and laminin. Elastin is one of the ECM proteins that accumulate in the whole spectrum of the disease, particularly in the advanced stages (F3-4). It gives elastic properties to the tissue and has resistance to its degradation enzymes. Elastin is considered the most stable component among the ECM associates (Chen et al., 2019). Fibronectin is a glycoprotein produced by the hepatic stellate cells upon injury (Liu et al., 2016). It is a multifunctional component of the ECM, and its expression is increased during fibrogenesis. Finally, laminin is the main component of the basal lamina in normal liver (Rosa & Parise, 2008). However, it is one of the important glycoproteins which has an effective function in hepatic fibrogenesis. Therefore, this project planned to quantify the abovementioned ECM proteins in cleared liver tissues.

We tested the staining pattern of Elastin monoclonal antibody (Merck Millipore, MAB2503) in cleared liver tissues. In the first experiment, we saw a specific binding of antigen-antibody and only adjusted antibody concentrations. Cleared cirrhotic liver was stained with Elastin antibody, and CY3 fluorophore was conjugated (**Figure 3.22A**). Fibronectin antibody staining efficiency was also tested in cirrhotic liver tissues; however, the staining was non-specific (**Figure 3.22B**). During confocal imaging, sample mounting elements (tack-it) prevented the tile imaging and resulted in a merged image in **Figure 3.22B**. However, it is apparent that Fibronectin staining was not specific in that condition.

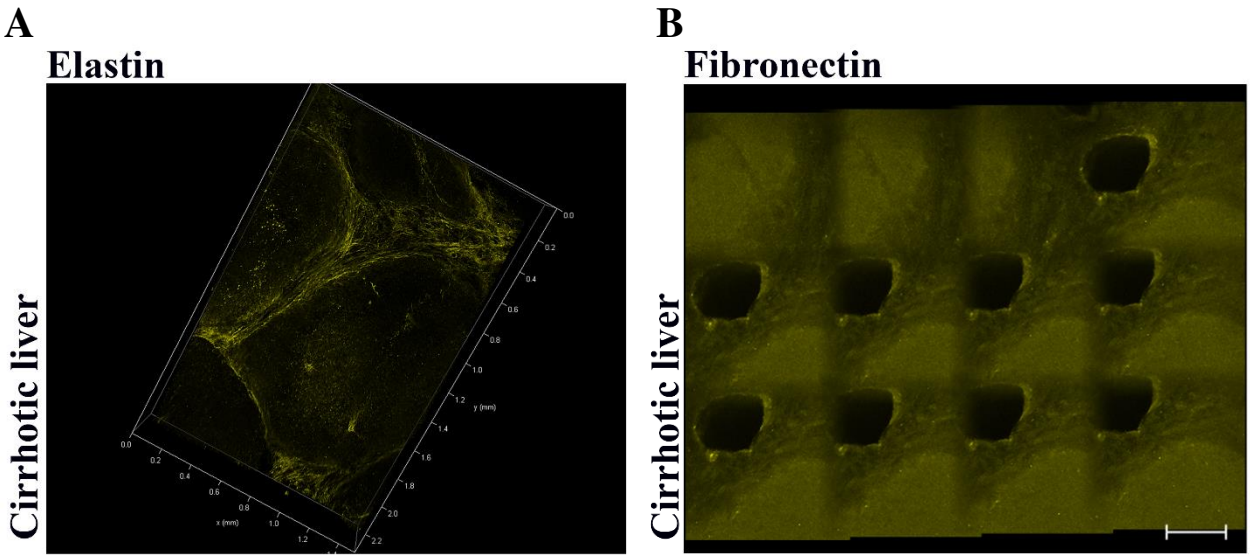

Figure 3.22 Examination of staining patterns of Elastin and Fibronectin proteins in cleared liver tissues. Staining of a cleared cirrhotic liver against Elastin (A) and Fibronectin (B) protein. Elastin-stained liver tissue was 3D reconstructed using Lasx software. (Scale bar: 200 µm)

To improve the staining efficiency of the Fibronectin antibody, we adjusted several steps and conditions of staining. Then, we implemented blocking steps with a custom blocking reagent (B1) and Goat serum (GS) blocking reagent and performed staining at 4°C. **Figure 3.23** shows the staining pattern of the Fibronectin antibody in various conditions and temperatures. It is seen from the belove images that low temperature and B1 blocking at 4°C perform the best staining pattern in cleared cirrhotic liver tissues.

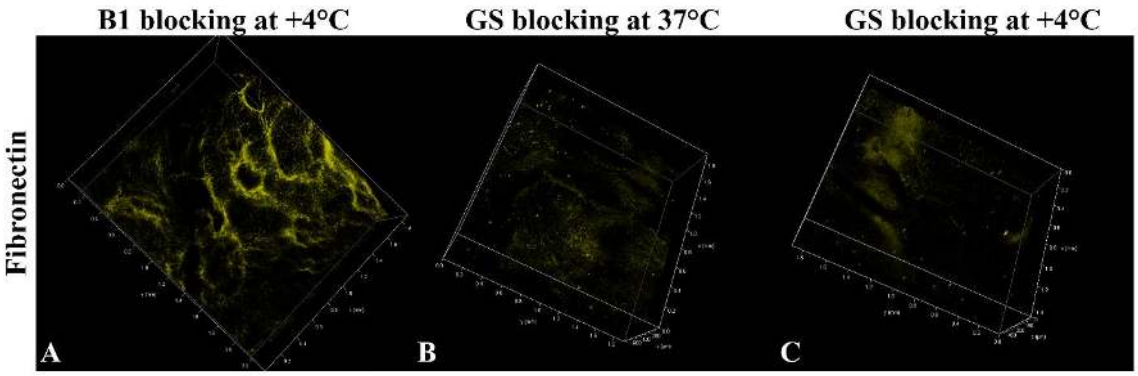

Figure 3.23 Optimization of Fibronectin staining in cleared human liver tissues. The pattern of Fibronectin staining was more specific in B1 blocking condition than staining in other conditions. Cleared cirrhotic liver blocked with B1 blocking at 4°C **(A)**, with GS blocking at 37°C **(B)** and at 4°C **(C)**. All steps were performed at 4°C or 37°C. Images were taken with confocal microscope. (B1: custom blocking reagent, GS: Goat serum)

Further, we checked the staining pattern of Laminin monoclonal antibody (lyophilized) in cleared liver tissues. It is known that non-collagen proteins such as fibronectin and laminin are known to be increased in the advanced stages of fibrosis. Therefore, cirrhotic and non-fibrotic cleared liver tissues were used to determine the Laminin staining for this project. Laminin staining was not specific in those liver tissues, and further optimization procedures were needed (**Figure 3.24**). Images were taken with a confocal microscope, and 3D reconstructed using Lasx software.

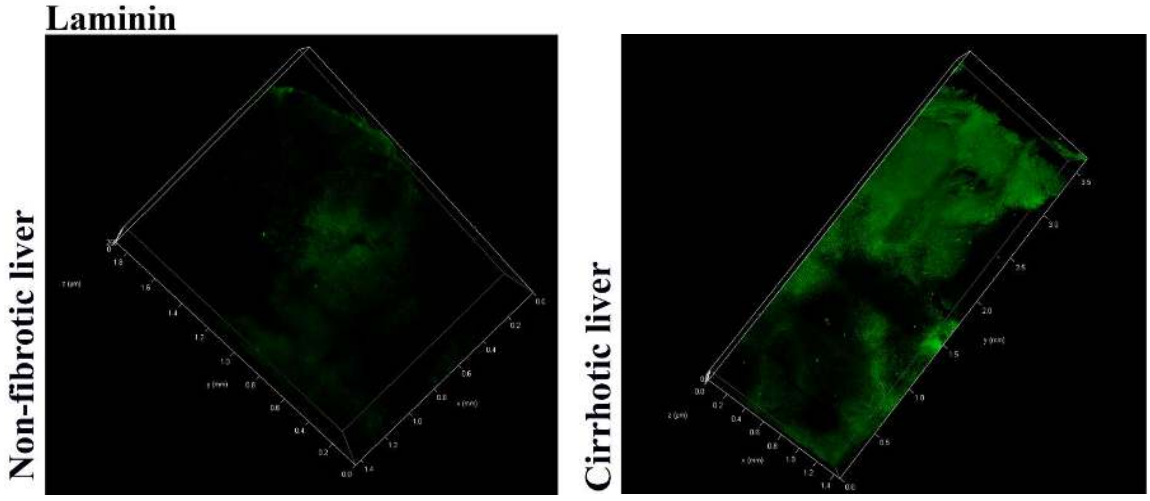

Figure 3.24 Evaluation of Laminin protein staining in cleared liver tissues. Staining efficiency of Laminin monoclonal antibody was checked using cleared non-fibrotic and

cirrhotic liver tissues. Images captured as multiple tiles and 3D reconstructed using Lasx software.

ECM remodelling occurs constantly in normal conditions to balance the tissue homeostasis. However, proteolytic enzymes which are released from the activated hepatic stellate cells lead to the altered remodelling due to the persistent injury. They express matrix metalloproteinases (MMPs) and tissue inhibitors of metalloproteinases (TIMPs) to balance the ECM turnover. However, the altered expression of TIMPs and MMPs can indirectly exacerbates the activation of hepatic stellate cells and thus they enhance the expression of ECM proteins. MMP-2 and MMP-9 are the key enzymes that secreted from the HSCs to degrade collagen Upon secretion of MMPs, they are regulated by its inhibitor enzymes (TIMP1) (Lachowski et al., 2019). In this project, we also aim to check the amount of secreted MMPs and TIMPs in cleared liver tissues. Therefore, staining was conducted by designing with blocking and no blocking conditions. First, we tried the staining with no blocking conditions and observed a staining pattern which could be promising in MMP-9 protein. However, the staining with MMP-2 antibody was non-specific (**Figure 3.25**).

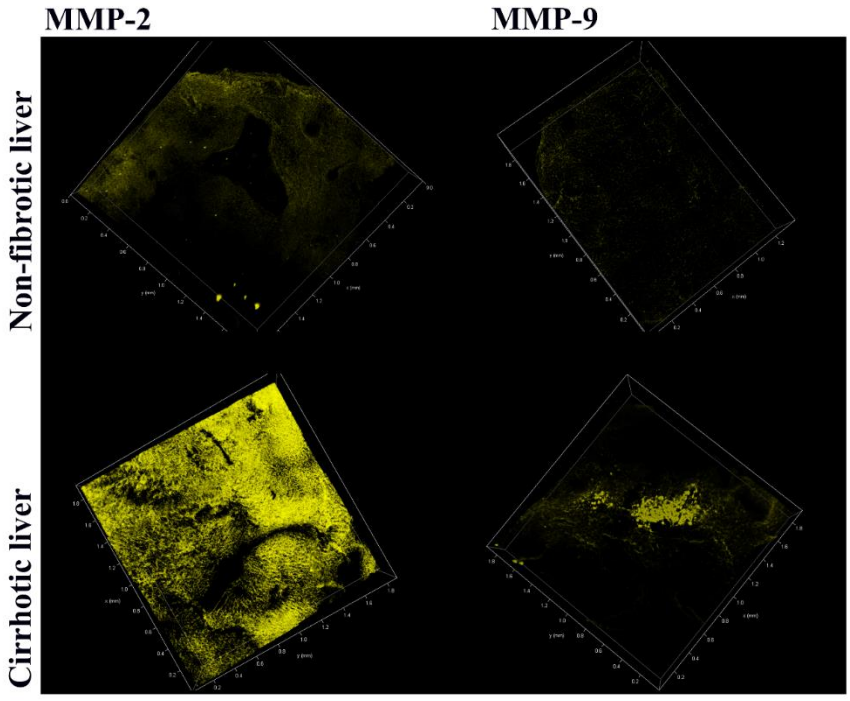

Figure 3.25 Evaluation of MMP-2 and MMP-9 staining pattern in cleared liver tissues. This image shows staining pattern of MMPs in cleared liver tissues with no blocking steps. Images were captured with confocal microscope and 3D reconstructed using Lasx software.

Blocking was implemented in the staining protocol from our experience with the staining of collagen type I protein. For both MMP antibodies, the staining pattern was not specific in both non-fibrotic and cirrhotic liver tissues. It is seen that goat serum blocking made no difference or did not change the staining pattern of both MMPs.

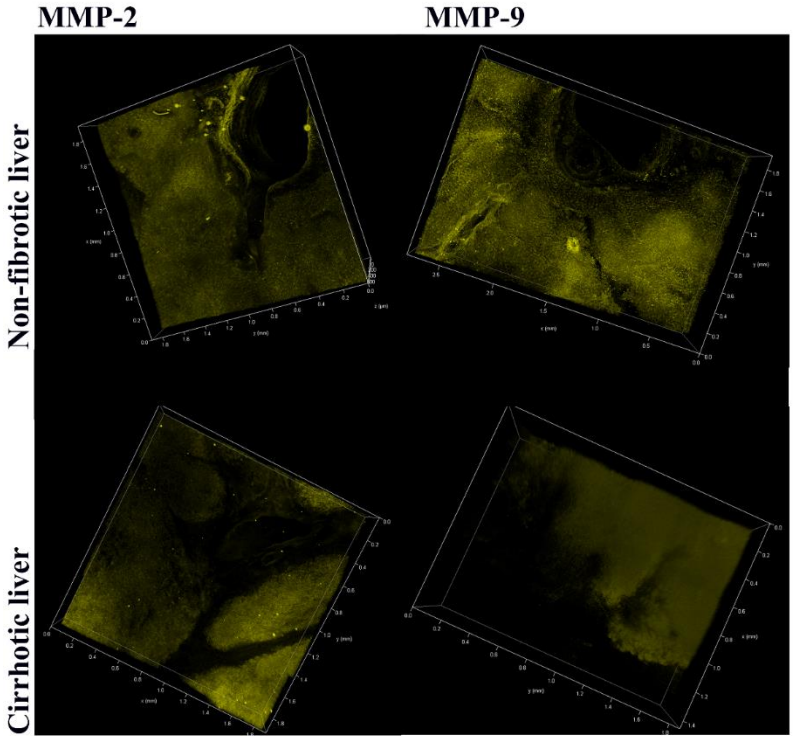

Figure 3.26 Evaluation of MMP-2 and MMP-9 staining pattern in cleared liver tissues. This image shows the staining pattern of MMPs in cleared liver tissues with Goat serum blocking. However, blocking did not increase the staining efficiency of the antibodies. Images were captured with a confocal microscope and 3D reconstructed using Lasx software.

Further, we stained cleared liver tissues with TIMP-1 antibody in order to quantify the expression. Therefore, we applied the antibody with blocking and no blocking conditions to various cleared liver tissues. However, in both conditions, we did not see any specific pattern to conclude (**Figure 3.27, Figure 3.28**). We could not observe any specific staining because of the type of proteins we investigated. Since they are proteolytic enzymes that are released into the extracellular environment, the quantification requires different methods.

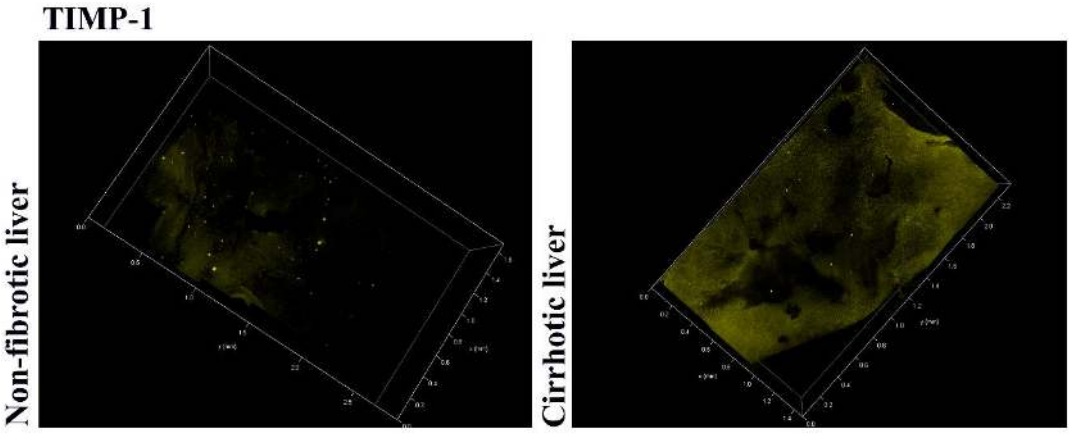

Figure 3.27 Examination of TIMP-1 staining in cleared liver tissues. This image shows the staining pattern of TIMP-1 in cleared liver tissues without blocking. It is seen that no specific pattern was observed. Images were captured with a confocal microscope and 3D reconstructed using Lasx software.

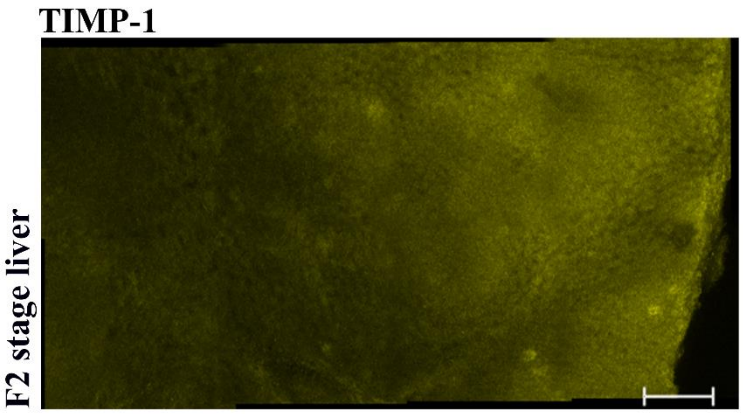

Figure 3.28 Examination of TIMP-1 staining in cleared liver tissues. This image shows the staining pattern of TIMP-1 in cleared liver tissues with Goat serum blocking. It is seen that no specific pattern was observed. Images were captured with a confocal microscope and 3D reconstructed using Lasx software. (Scale bar: 200 µm)

Light-sheet imaging of human ECM proteins

Thus far, imaging of optimization experiments was conducted using a confocal microscope at the KUTTAM imaging centre. Then, the facility added a Digital Light Sheet Microscope (Leica TCS SP8 DLS) to their inventory. The system allows light-sheet imaging by digitally scanning the sample using the mirrors which are placed on the detection objectives. Light sheet alignment and shape can be adjusted according to the experiment requirements. Since the system has an inverted microscope body, it is easily converted to the confocal microscope system. However, the illumination and detection axis should be perpendicular in a light sheet microscope. In order to do so, they produced a Twinflect mirror system which turns the confocal system into a versatile light sheet microscope by deflecting the laser beam at a 90° angle. Then, the digital light sheet (DLS) is generated by scanning the sample through the mirrors.

The digital light sheet microscope system requires special sample embedding and preparation methods. They provide a sample preparation guide for the users. The system has a narrow gap for sample imaging between the Twinflect mirrors. The largest area is 7.8 mm in the x direction in total with the sample and the embedding environment. We tested to image our cleared liver tissues with a Leica Digital Light Sheet microscope and followed their guide. The sample should be steady and placed in an environment that matches the refractive indices for the high resolution and good-quality images. However, one of the most significant limitations was the using water immersion objective in the system. Water has 1.33 refractive indices and is not compatible with CLARITY-processed liver tissues. Even though technical limitations have existed, we tested the sample preparation methods and imaging with a digital light sheet microscope. We use glycerol solution (87-89%) as an imaging environment since it has matched the refractive index with our samples. However, to keep samples as steady as possible, the DLS preparation guides offer using low melting agarose. We prepared agarose with water and embedded cleared samples in various methods to prevent the detachment from the glass bottom petri-dish. However, glycerol had a reaction with the agarose and resulted in detachment of the sample every time. Also, the reaction created a moving light beam through the sample and affected the alignment of the mirrors. Consequently, we concluded that currently available light sheet imaging systems do not have a compatible sample embedding method or sample holders for the clinical samples (Laroche et al., 2019). Additionally, our CLARITY-processed samples require dipping objectives which have matched RI to the samples.

In this study, we aimed to develop a custom-made light sheet microscope for samples processed with CLARITY. Then, we tested to image cleared liver tissues with the first prototype of a custom-designed light sheet microscope. We used the OpenSPIM platform to build the system in our university to configure the light sheet microscope (Pitrone et al., 2013). To complete all the necessary elements of the system (high-resolution CCD camera, glycerol dipping objective, a software, lenses, mirrors, lasers), we developed a prototype of a system and optimized the imaging, sample embedding and sample holder steps. Moreover, we utilized the most compatible optical systems for the optimization experiments. Initially, we utilized imaging of cleared samples using air and water objectives. For the illumination of samples, we used a Coherent Chameleon laser source. The cleared tissue was placed in the air and imaged with 1-1 match pair lenses, which transmitted the image without magnification. In water immersion method, the tissue was submerged in a water-filled sample cage (created using Plexiglass) and imaged with a 10X water dipping objective. In both conditions, the resolution of images was not optimal due to the RI mismatch (**Figure 3.29**). The RI of the samples processed with CLARITY is around 1.46, whereas the RI of the water is 1.33. This mismatch causes a significant level of light scattering, resulting in blurry images. On the other hand, lack of a medium between the sample and objective led to much higher light scattering and resulted in blurry images.

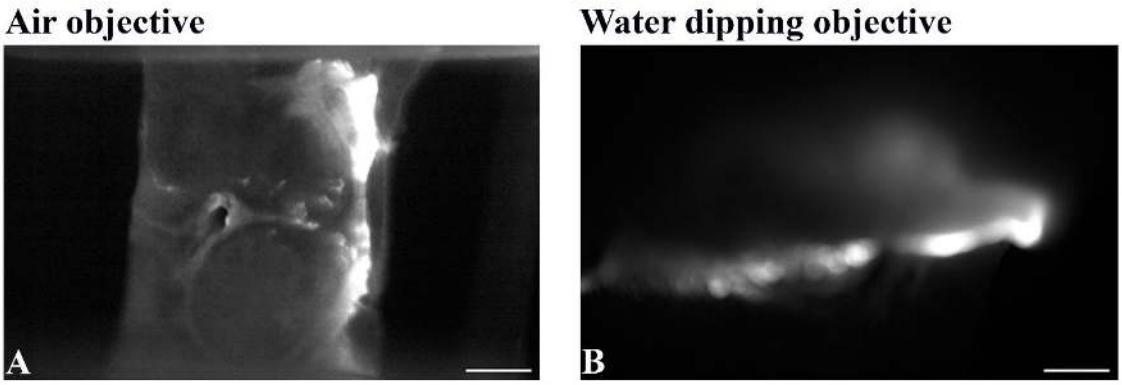

Figure 3.29 The first LSFM images that captured with a prototype light sheet microscope. Initial experiments for the development of a custom light sheet microscope using air (A) and water immersion (B) objectives. (Scale bar: 200 µm)

Since the air and water immersion methods resulted in a poor resolution, we tested different alternatives. Further, we utilized 20X NIKON objective and various digital cameras in order to optimize the set-up configuration. We tested 20X NIKON objective in a light sheet set-up by placing the tissue in a dry environment. Although the images had quite good resolution, the sample embedding method was not optimal for CLARITY-processed liver tissues (**Figure 3.30**).

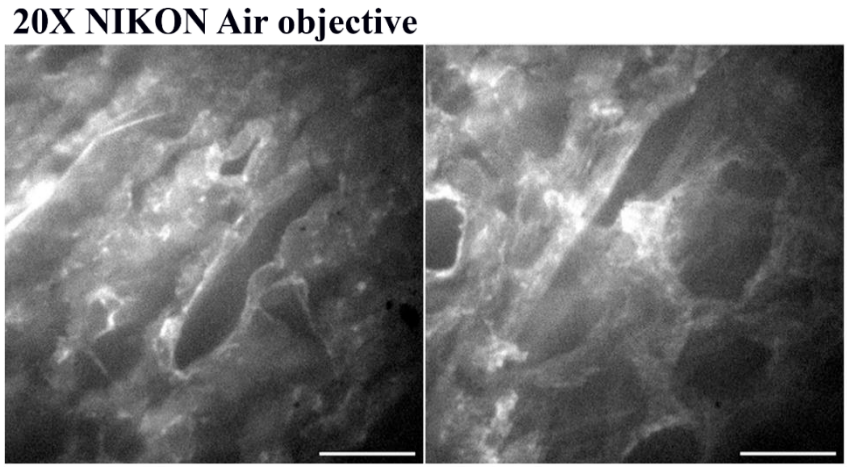

Figure 3.30 20X NIKON objective testing for optimal light sheet microscope configuration. 20X NIKON objective was implemented to the custom light sheet set-up, and cleared samples were imaged using Chameleon laser. The figure depicted two areas of a cleared liver tissue (scale bar: 100 µm).

Then, we tested two camera systems to get the best resolution from the samples. However, both cameras resulted in poor resolution (**Figure 3.31**). The images were taken using the 20X NIKON objective.

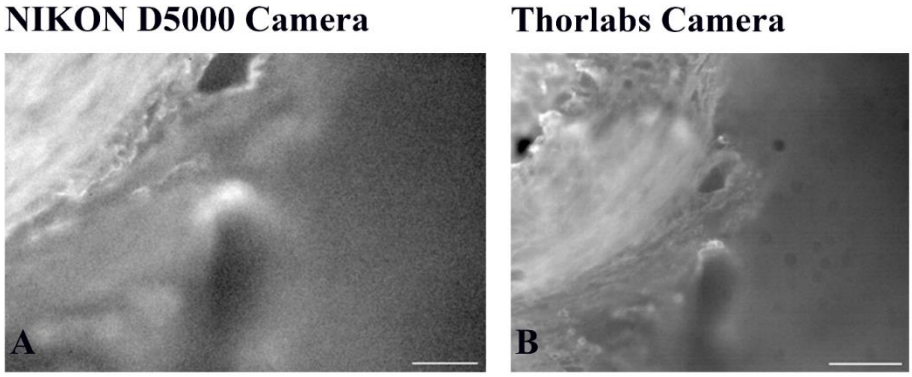

Figure 3.31 Examination of digital cameras for custom light sheet configuration. To improve the resolution of the light sheet microscope system, we

tested the NIKON D5000 camera (A) and Thorlabs camera (B). (A, scale bar: 500 µm, B, scale bar: 200 µm)

Further, we tested to image a stained liver tissue with an optimized protocol for Elastin protein. We visualized the same tissue with a custom light sheet microscope and expected to see the same pattern as in the confocal imaging system. In this configuration of light sheet set-up, we used 50X Mitutoyo objectives, and the sample was hung in the air with clips. As anticipated, the staining pattern was the same as we observed in the confocal system (**Figure 3.32**).

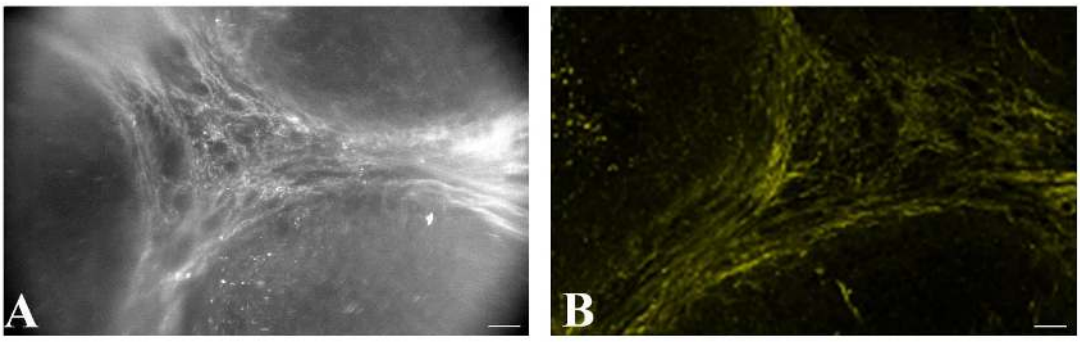

Figure 3.32 A light sheet vs Confocal imaging of the same tissue for the optimization experiments of a set-up. A cirrhotic cleared liver tissue which was stained against Elastin protein, used to image with a custom light sheet microscope (A) and confocal microscope (B) and showed the same pattern. (Scale bar: 100 µm)

Generally, light sheet microscopes require a high resolution and high scanning rate digital CMOS (Complementary metal–oxide–semiconductor) camera to visualize whole tissue in 3D. Therefore, we implemented ORCA Flash 4.0 Digital CMOS camera and 10X glycerol dipping objective (NIKON 10X/0.5 NA, 5.5 mm WD with a tuneable refractive index) to our system in order to have a high resolution and to get rid of the light scattering in the air, respectively. However, there was no optimized method for keeping tissues as steady as possible to image with our system. Therefore, we used a sample cage (Plexiglass) that is suitable for sample holder and has a slide at one side to transmit the light sheet to the sample without any scattering. Plexiglass was used as a sample cage material since it does not absorb the light. We have tested several methods to submerge the tissue in a glycerol-filled cage. First, we tested by using plexiglasses as a sample holder, and the tissue was placed on it using rubbers on the edges.

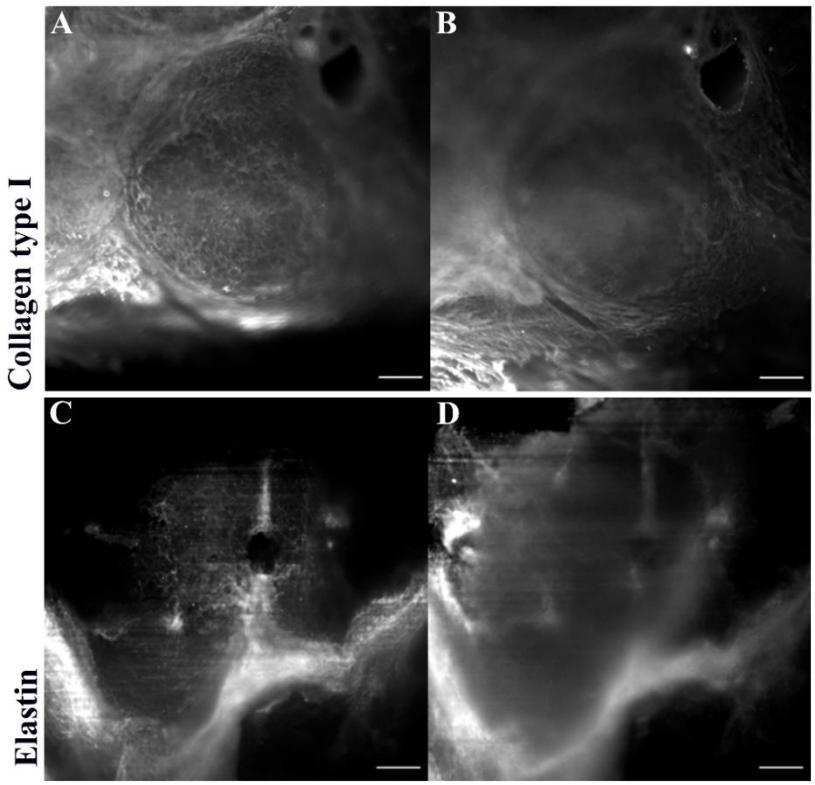

Figure 3.33 The light sheet images of cleared liver tissues with high resolution camera and dipping objective that were added to the LSFM set-up. The images were taken with a custom LSFM using a high-resolution camera and dipping objective, which has a tuneable refractive index. Cleared cirrhotic liver tissues, which were stained against Collagen type I (A,B) and Elastin (C,D), were used. (Scale bar: 200 µm)

According to the images, there was light dispersion, which resulted in blurry images possibly due to the plexiglass interference with the incoming laser. (**Figure 3.33**). Also, using rubber from the tissue edges disrupted a sample since it is tightened to keep it still. However, when the sample was submerged in a sample cage, every movement of the positional stage affected the sample position and focus of the camera. Therefore, we needed an embedding method which has no detrimental effect on sample position and light scattering. Then, we sought other methods to prevent sample movement in the sample cage. We found that Kapton tape has no light absorbance or bad effects on biological samples. Then, we used Kapton tape to prevent the movement of tissues on a plexiglass sample holder. We utilized the Kapton tape to the edges of the tissue on the sample holder and submerged it in a glycerol-filled sample cage. Additionally, one of the reasons for blurred images could be the lenses that were used to focus the light sheet for the illumination of a sample. Therefore, we adjusted the lenses we used in the LSFM configuration with best form lenses (f=40 mm). The adjustments

in the LSFM configuration resulted in promising images (**Figure 3.34**). Since we were dealing with the sample embedding methods, we did not image the whole sample. At that time, we manually saved the imaging files to the computer using camera software (HOKAWO).

To test the clinical applicability of the method, we design a system which has clinical sample-friendly holder types to avoid sample disruption. Therefore, we prepared liver tissue samples in a biopsy shape and stained them for the optimization experiments. **Figure 3.34** displays a biopsy-like CLARITY-processed and stained sample which was embedded with Kapton tape. The images were taken after the best form illumination lenses were installed in the LSFM setup.

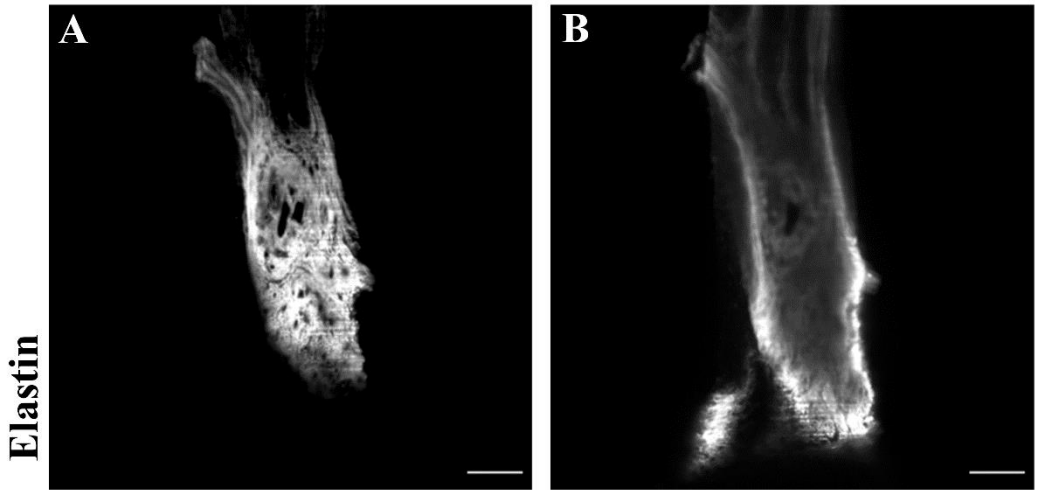

Figure 3.34 Examination of the adjustments in the LSFM set-up. The improvements in the LSFM set-up configuration resulted in preferable image resolution. Cirrhotic liver tissue, which was stained against Elastin protein, was imaged taken from different slices (A&B). However, the resolution deteriorated when taking images in the z-direction (B). (Scale bar: 500 µm)

The adjustments improved our knowledge of designing a custom light-sheet microscope and clinical sample-friendly holder types. Since our hypothesis was the imaging whole liver biopsy tissue without sectioning, we designed the LSFM set-up and image processing operations for this aim. The typical core liver biopsy sample is 2 cm in length and 1.6 mm in diameter. Therefore, we manually tested the tile imaging processes of biopsy-like samples and stitched them using Image J software. Meanwhile, we sought a way to automatize the image processing operations. We imaged the same staining in **Figure 3.33** by acquiring multiple sections and could cover a larger area than in previous experiments for the first time. We utilized the stitching function of the

Image J software for every z plane in the sample. Since stitching was performed manually, only a minor part of the sample was imaged with LSFM (**Figure 3.35**). Additionally, imaging a larger area gave us to interpret the staining pattern more effectively despite blurred areas. The staining resulted in numerous artefacts, possibly due to the insufficient wash steps. Also, using a concentrated dilution of a primary antibody might lead to unspecific binding of secondary antibody. The image was 3D reconstructed using Image J. Therefore, we concluded that optimization for Collagen type I protein still needs further adjustments.

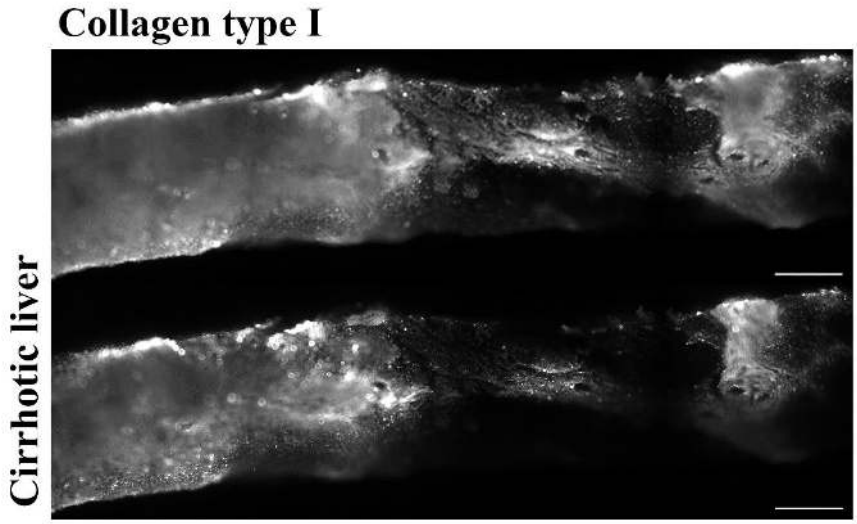

Figure 3.35 Tile experiment of a Collagen type I stained liver tissue using custom LSFM. Cleared biopsy-like cirrhotic liver tissue stained with monoclonal Collagen type I (Abcam, ab90395) at 1:250 dilution, displayed artefacts possibly due to the insufficient wash steps or concentrated primary antibody usage. The image was created using four consecutive tile imaging in *y* direction and stitched using Image J manually. (Scale bar: 500 µm)

Further, we tested to visualize Fibronectin stained liver tissue that we have seen a specific pattern in confocal imaging (**Figure 3.36**). We attempted to image the whole area in that tissue. Normally, the positional stage we used has a 25 mm range in all directions (xyz). However, the range was affected by the sample cage and holder dimensions. Therefore, creating suitable sample holders and sample cages have a significant role in having good quality images and practical usage of the platform. Additionally, the staining pattern was not specific as we observed in confocal images. We could not find the reason for it, but at least we experimented by taking multiple

images from the biopsy-like tissues. Moreover, we had some challenges while performing the imaging. The sample was placed on a Plexiglass holder and immobilized using Kapton tape from the edges. However, the tissue was still moving after forwarding the tissue to the y-direction to image the whole tissue parts. This condition led to blurred images due to the sample movements. Also, we moved sample in xyz direction using the stage controller and saved every image data to the computer manually. This process was also challenging since it was time-consuming. We also tested to reconstruct the images that we acquired. We used Image J as a 3D builder for light sheet images; however, we encountered a hardware problem. The problem was the insufficient system memory which was used by the Image J during the 3D processes. The computer we were using for imaging processes had 32 GB Ram, but we needed much more if we would render 3D of larger tissues. We overcame this issue by resizing the image and 3D reconstructing it in Image J.

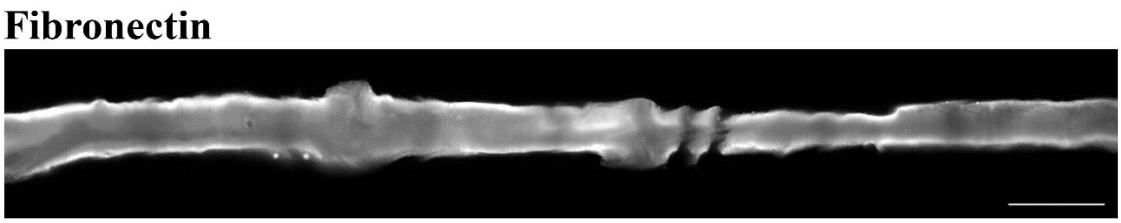

Figure 3.36 The imaging of a biopsy-like sample via custom LSFM. A cirrhotic cleared liver tissue which was stained against Fibronectin protein used for the whole tissue imaging with LSFM. Unfortunately, the system ranges could not cover whole tissue parts due to the restrictions in dimensions of the sample cage and holder. (Scale bar: 1000 µm)

In fact, if one looks from the bright side, we expanded our knowledge of LSFM and sample preparation in every imaging experiment. Moreover, we sought other methods to keep the tissue still on sample holder. The blurry images we obtained from the light sheet microscope could be due to the illuminated sample with a thick light sheet. To observe where the finest light sheet is generated, we checked tissue regions that are highly resolved in every imaging experiment.

The size of the tissue is 1.1 cm in length in **Figure 3.36**. Since biopsy samples will be more than a centimetre in length, we discovered a way to use maximum ranges given to the positional stage. Thus, we assessed the other sample embedding methods, such as narrow Plexiglass and cleared-unstained tissue cushion. For the first method, we used 3 mm width (narrower than previously used) Plexiglass in order to eliminate detrimental effects that would come from it (**Figure 3.37A**). The previously used Plexiglass holder was designed for wider tissue samples. Therefore, we adjusted the width of the Plexiglass for biopsy-like tissues. The latter method uses cleared but unstained liver tissue as a cushion for stained samples. Liver tissue has high autofluorescence, so we only blocked tissue with Goat serum and then used it as an intermediate layer between the plexiglass and stained tissue sample (**Figure 3.37B**).

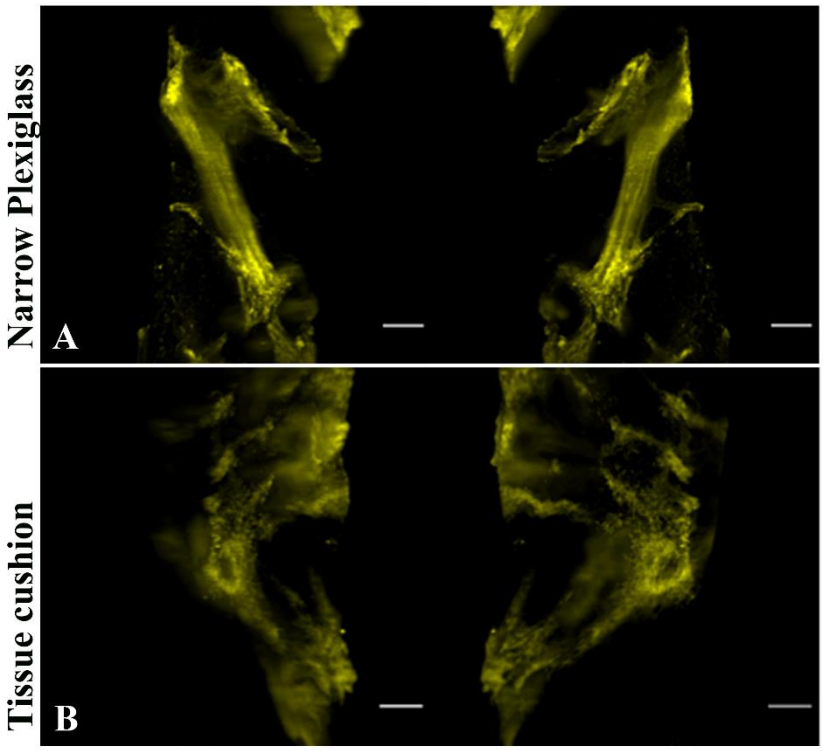

Figure 3.37 Examination of various sample embedding methods and LSFM images in 3D. A cleared cirrhotic liver tissue stained against Collagen type I protein was embedded on narrow Plexiglass (A) or tissue cushion (B). The same tissue sample was used in both experiments. Images reconstructed 3D using Image J. (Scale bar: 200 µm)

The depicted 3D images in **figure 3.37** revealed that sample embedding on a flat surface is not convenient for a good three-dimensional feature. Therefore, samples should be embedded in an environment that has matched refractive indices (RI) with the cleared tissue. This environment should also provide immobilization of the sample at the same time. Low melting agarose is used for sample preparation for light-sheet

microscope imaging. Therefore, we use low melting agarose for our imaging experiments. However, the refractive index matching solution was missing. Thus, we reviewed the literature and formulated a refractive index matching solution (RIMs) to reach the same RI with our cleared samples. Then, we prepared an environment with low melting agarose and RIMs to place our samples in order to image with a light sheet microscope. Regarding our experience with DLS from Leica, glycerol solution has a dissolving effect on Low melting agarose. Therefore, the agarose has to be separated from the glycerol in the sample cage. In this respect, we utilized two different glass tubes to show the best compatibility with the light scattering. The first one is Quartz tubes which are made from quartz crystals by fusing. They are used in array applications, including laboratories, semiconductors, and optics. We used 2% of low melting agarose and RIMs mixture to stabilize the tissue sample and conduct light sheet imaging. The latter type of tube is the borosilicate tube which is commonly used in laboratory glassware. The best compatible and practical product currently used in our lab is the glass Pasteur pipette used in cell culture experiments. We collaborated with the glassware services at Koç University Department of Physics and requested them to cut the Pasteur tubes at proper length for sample cage. Then, we used the same embedding mixture for CLARITY samples in both tubes and performed LSFM imaging. Imaging in low melting agarose was significantly compatible with our methodology and CLARITY samples. The embedding method does not have any detrimental effects, and conversely, the sample was still, and refractive indices were matched. In figure 3.38, we compared the 3D images of the tissues in two different type of tubes and their effect on light scattering and sample embedding. Since quartz tubes are quite costly and do not have a superior effect to Pasteur tubes, we proceeded with Pasteur tubes. The Pasteur tubes are cheap and easily accessible. 3D images in the Pasteur tube had high resolution and subordinated blurred areas (**Figure 3.38B**).

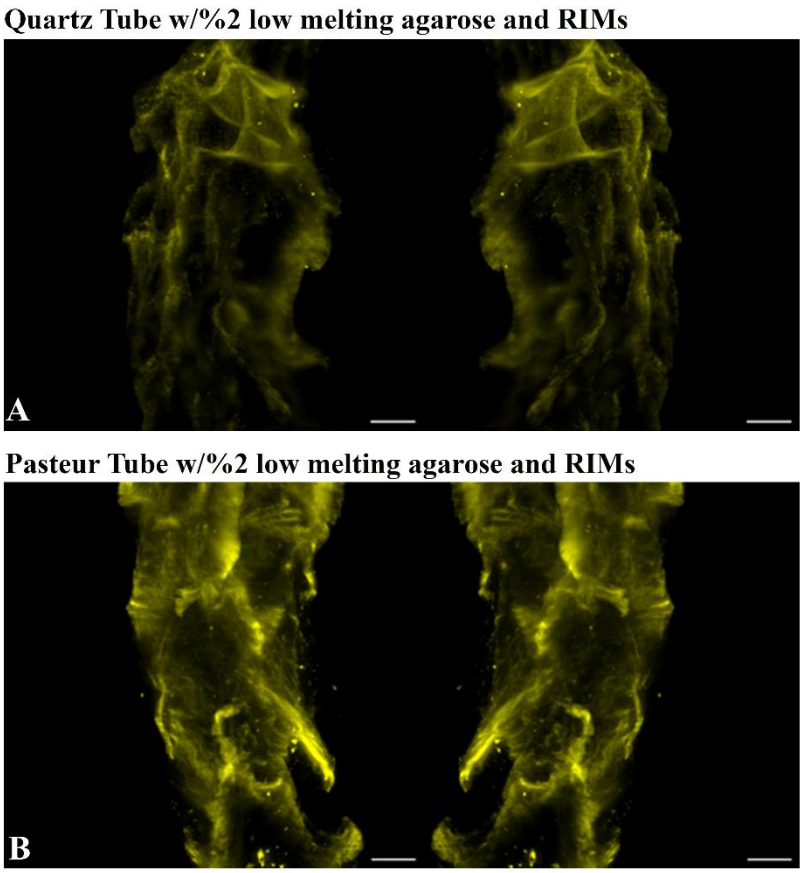

Figure 3.38 Comparison of imaging environments in various glass tubes. A cleared cirrhotic liver which was stained against Collagen type I protein at 1:500 dilution embedded with low melting agarose and RIMs mixture in Quartz tubes (A) and Pasteur tubes (B). The images were taken with a custom LSFM in a glycerol-filled sample cage and were 3D reconstructed using Image J. (scale bar: 200 µm)

Thus far, we have finally optimized the sample preparation processes of the LSFM imaging. The sample preparation processes included the sample cage, sample holder, and imaging environment. We used ABS-based 3D printed materials in order to produce the most suitable elements for the system. Then, we checked the system's point spread function (PSF) measurement to define the diffraction pattern of the emitted light from a small point in the specimen and transmitted to the image plane using fluorescent beads. While we were experiencing the PSF measurement in the glass tubes (Pasteur tube), we noticed that low melting agarose dissolving in RIMs by heating in microwave resulted in increased RI of the mixture due to the rapid evaporation of the liquid. The increase in the RI may cause blurred images and decreases the resolution. Therefore, we tackled this problem by dissolving it in a 75°C water bath.

Additionally, we developed a software for automatizing image acquisition from LSFM using indicated directions and laser options. The software was improved as we used it for imaging experiments. There were many challenges, such as data image file type, scanning parameters, and mechanical problems. We updated the software upon any problem and made it to the best fit system composition for the fast LSFM imaging. We also tested whether we could image the large samples (~1.5 cm) with our system. Some of the stained tissues had wider dimensions than biopsy samples, which required scanning in multiple x directions. However, the software could not scan the samples, and we encountered an error. We achieved to manage this error and update the software. Further, we tested to image with LSFM using previously stained liver tissues (**Figure 3.39**). We were confronted with previous problems.

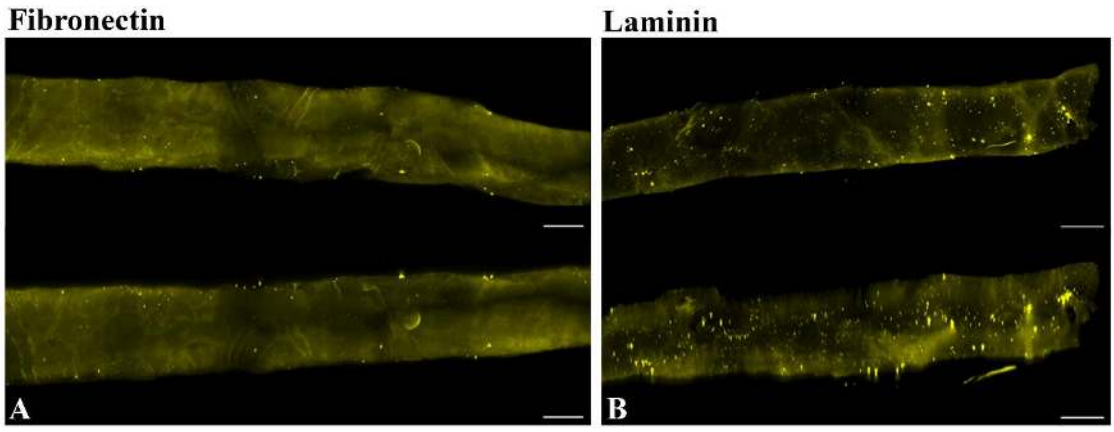

Figure 3.39 The LSFM images for the optimization of the system elements. Previously stained liver tissues were used for the LSFM setup optimization experiments. Fibronectin protein was targeted to stain in cleared liver tissue using primary antibody at 1:500) dilution in PBS-Tw containing the sodium azide to mitigate non-specific binding (A). And laminin stained liver tissue was imaged in the LSFM setup. The staining protocol was adjusted to improve the specificity of the antigen-antibody binding (B). However, the patterns were not specific in both staining. The images were 3D reconstructed using image J software. (Scale bar: 500 µm)

We proceeded to seek an optimal dilution to stain Collagen type I protein in cleared liver tissues. To this end, we stained cirrhotic and non-fibrotic cleared liver tissues with Collagen type I antibody in PBS-Tw containing sodium azide to improve the specificity of the pattern. We acknowledged from previous Collagen type I staining that we should use a more diluted antibody concentration for cirrhotic liver tissues. In order to do so, first, we used 1:1000 dilution and performed imaging with LSFM setup.

However, the staining was quite intense in cirrhotic liver tissue due to the insufficient dilution (**Figure 3.40A**). In contrast, non-fibrotic tissue was stained specifically against Collagen type I protein with this condition (**Figure 3.40B**).

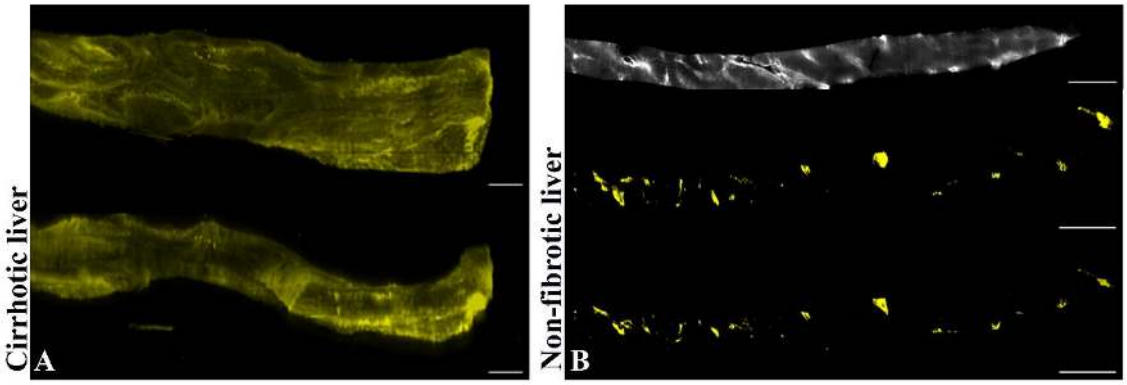

Figure 3.40 Examination of Collagen type I protein staining in cleared liver tissues using the diluted antibody. To improve the staining pattern in cirrhotic liver tissue, we used Collagen type I antibody at a 1:1000 concentration in cirrhotic liver (A) and non-fibrotic liver (B). Cirrhotic liver tissue was 3D reconstructed using Image J in order to see the staining pattern in the whole tissue (scale bar: 500 µm). Non-fibrotic tissue staining was still specific in that concentration, and 3D reconstructed using Image J (Scale bar: 1 mm)

Further, we attempted to image the sample stained against Elastin protein using custom LSFM. Additionally, we changed the dilution of the antibody since we observed high intensity of staining. In this condition, the staining of cirrhotic liver tissue had a specific pattern in the ECM area. The abundance of Elastin protein was higher than we expected. The images were taken as multiple tiles, stitched manually and 3D reconstructed using Image J (**Figure 3.41**).

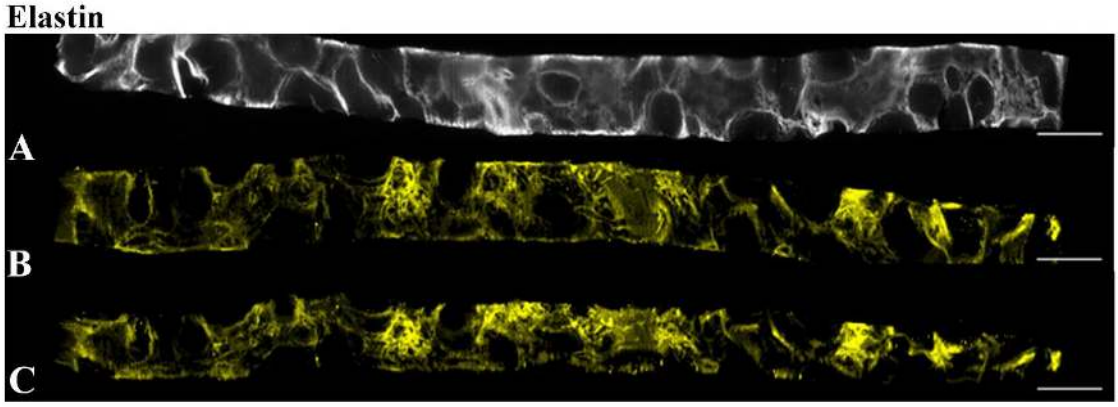

Figure 3.41 Assessment of Elastin staining and imaging with LSFM. A cirrhotic liver was stained at 1:2500 dilution and imaged with LSFM using higher dilution. A

greyscale image showed the specificity of the staining in the ECM area (A). Then, we reconstructed images and showed the Elastin protein distribution in the whole tissue by displaying in 3D from different angles (B&C). (Scale bar: 1 mm)

The Elastin staining was optimized in cleared liver tissues, and we could image biopsy-like samples using our platform. However, image processing remained time-consuming and labour-intensive. In the meantime, we were trying to automatize image processing steps, such as using automated code for image stitching and analysis.

At this time, the Collagen type I staining was not optimized in cirrhotic liver tissues. The concentration that we optimized for non-fibrotic liver tissues was insufficient for cirrhotic tissues, which contain much more ECM protein than non-fibrotic tissues. Then, we run an experiment which includes various dilutions such as 1:2500, 1:5000, 1:10000 and 1:25000 in two different blocking reagents. One of the blocking reagents was Goat serum in PBS-Tw (with Sodium azide). All the incubations were performed in PBS-Tw (w Sodium azide) except for the wash steps. The latter was B1 blocking reagent, which contains 10% Goat serum, 0.2% Triton-X and 0.05% Sodium azide. According to this staining experiment, first, we chose 1:5000 dilution with Goat serum blocking reagent since the staining pattern was the best (**Figure 3.42**).

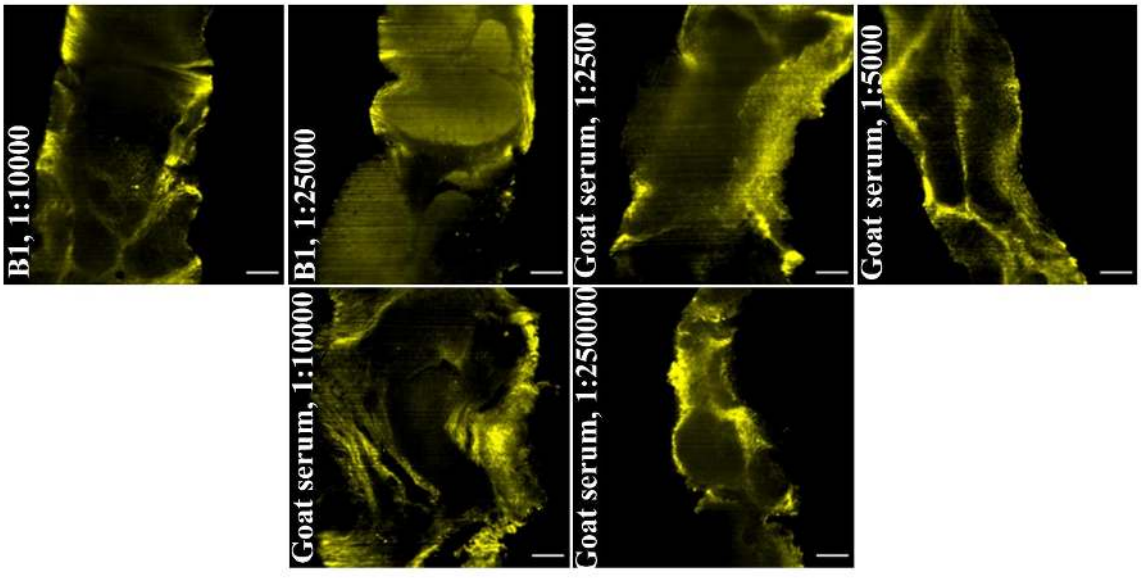

Figure 3.42 Examination of various dilutions of Collagen type I antibody in cirrhotic liver tissues with LSFM. We used various dilutions and blocking reagents to improve the staining specificity of the Collagen type I antibody (Abcam, ab90395). According to these images, we proceeded with 1:5000 dilution with Goat serum blocking. (Scale bar: 200 µm)

Further, we performed whole tissue imaging of the concentration we chose for the Collagen type I protein. We stitched all the images manually and reconstructed them in 3D using Image J to observe the distribution of the staining in the whole sample. Although the staining pattern was specific and was not dispersed in all regions, we observed that the staining faded in a very short period of time. Therefore, we proceeded to use 1:2500 dilution, which also has a specific Collagen type I protein pattern. The whole sample 3D images are shown in **figure 3.43**.

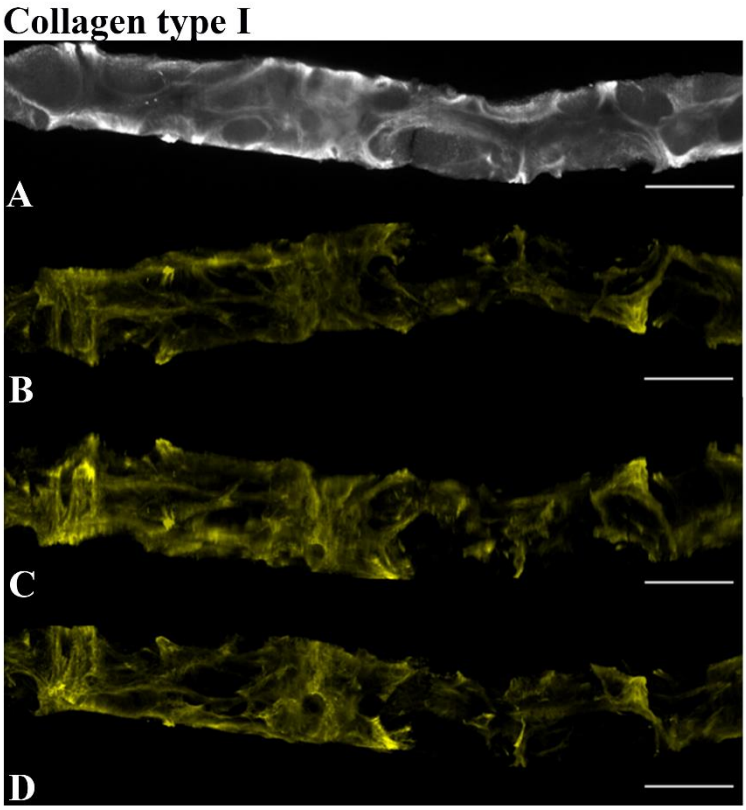

Figure 3.43 Imaging of biopsy-like liver tissue with LSFM to observe Collagen type I staining. The LSFM imaging and 3D representation of Collagen type I staining in biopsy-like liver tissue are displayed. 3D images were built using greyscale images (A) to show the staining distribution in different angles (B&C&D). (Scale bar: 1 mm)

In this project, we aimed to simultaneously detect and assess more than one protein in a sample. Thus far, we could not optimize staining that is applicable to use together in a sample because of the host mismatch. Furthermore, we attempted to perform dual staining with the antibody that we tried in the confocal microscope for **Collagen type I and III** (Bio-Rad 2150-2210) to observe staining specificity in this imaging system. We stained a cirrhotic liver tissue against Collagen type I/III (raised in

rabbit) and Elastin (raised in mouse) to detect three ECM proteins simultaneously in a sample. Additionally, we performed dual staining for Collagen type I (rabbit ab34710) and Elastin protein. We also performed dual imaging in a sample via our custom LSFM for the first time for this imaging experiment. We have updated our laser configurations by adding a 488 nm laser. However, we could not illuminate every section for both lasers simultaneously due to the setup configurations. We took sectional imaging for each channel separately. For instance, the imaging system return to zero position after determining the sample positions before performing latter channel imaging. Then, the imaging was started again. However, since we considered that light sheet imaging should lead to less photobleaching than confocal imaging, exposing samples second round of illumination was not optimal. However, using this configuration, we performed imaging, and a specific staining pattern was observed for Collagen type I/III protein. We almost accomplished our aim until we noticed that our emission filter was not ideally suitable for the 488 nm laser source. Imaging results are shown in the below figures. Elastin staining was specific at 530 nm laser; however, since we cannot prevent the intensities that come from the Elastin channel, we thought that staining was specific in Collagen type I/III or Collagen type I (**Figure 3.44 and Figure 3.45**). Then, we changed the emission filters with the proper filter sets. We observed that there was non-specific binding for Collagen type I/III or Collagen type I (**Figure 3.46**).

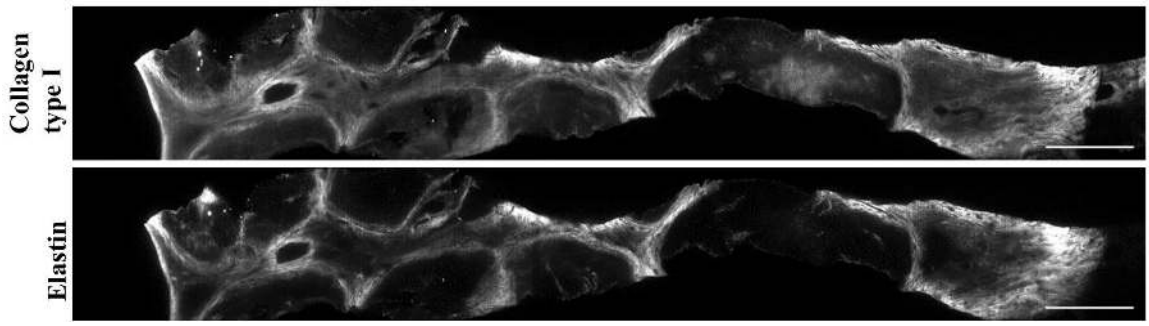

Figure 3.44 The light sheet images of dual staining in cleared cirrhotic liver tissues. Collagen type I/III and Elastin staining were performed and imaged using custom LFSM. Grayscale images show the overlap intensities that come from the 530 nm laser (A). Therefore, we only reconstructed the Elastin staining in 3D (B). (Scale bar: 1 mm)

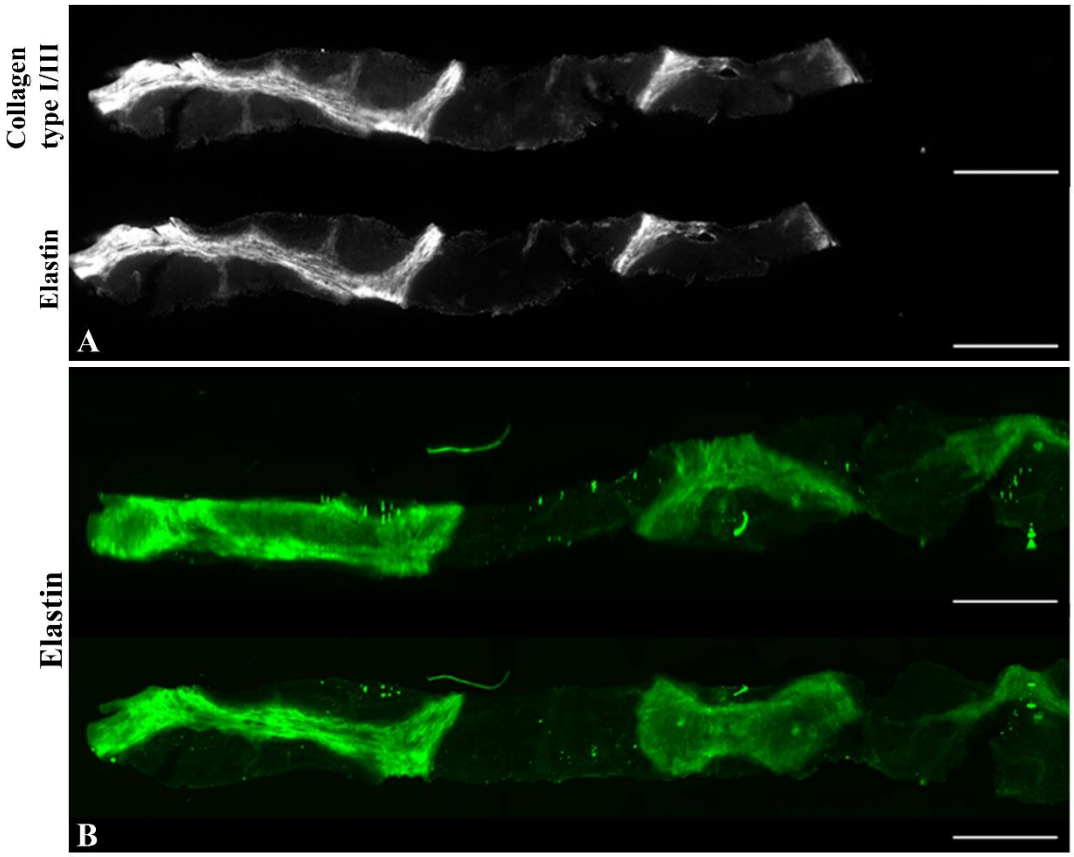

Figure 3.45 The light sheet images of dual staining in cleared cirrhotic liver tissues. Collagen type I and Elastin staining were performed and imaged using custom LSFM. Grayscale images show the overlap intensities that comes from the 530 nm laser. (Scale bar: 1 mm)

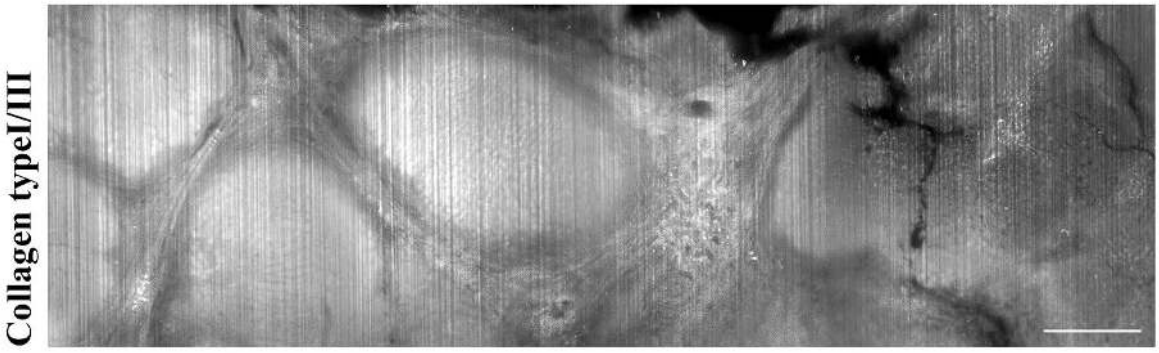

Figure 3.46 Collagen type I/III staining result in custom LSFM using matched emission filters. A cirrhotic liver shows the staining against Collagen type I/III using suitable emission filter sets in custom LSFM. (Scale bar: 500 µm)

Thus far, we optimized the antibodies against Collagen type I and Elastin proteins which are raised in mouse. Because of raising in the same type of host

organism, dual staining was not applicable. We opted to detect Collagen type I and Elastin proteins as Collagen type I/III antibody performance was not selective in cleared liver tissues. Moreover, we also tested optimized Elastin staining with non-fibrotic samples to see if the staining pattern changes when the fibrosis amount decreases. **Figure 3.47** shows specific staining of Elastin protein in non-fibrotic liver tissue.

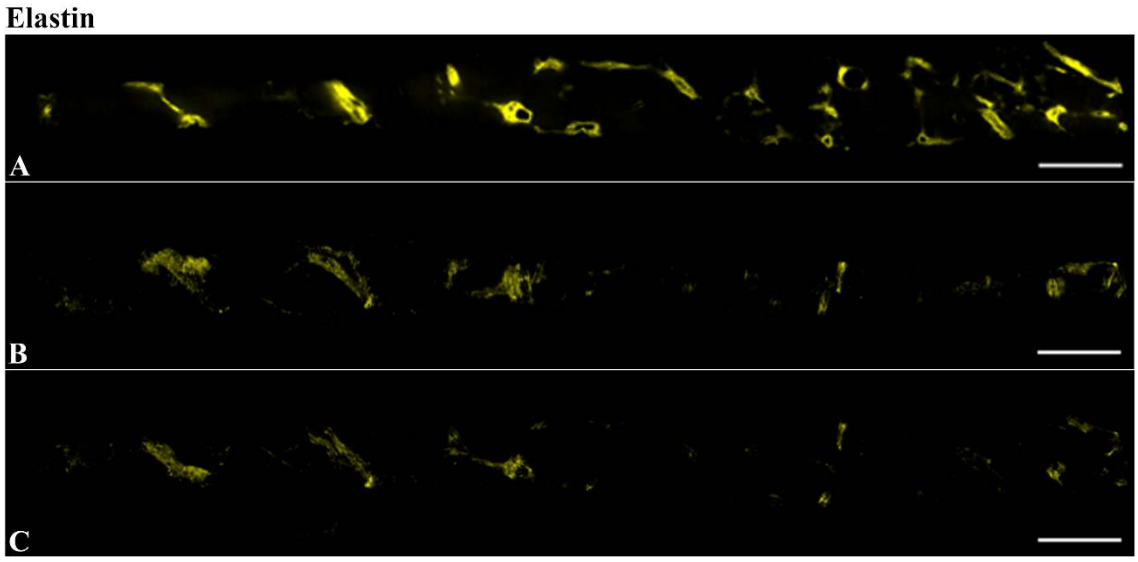

Figure 3.47 Assessment of Elastin staining and imaging with LSFM. A cleared non-fibrotic liver was stained with the optimized protocol for Elastin antibody. A pseudo colour (yellow) image showed the specificity of the staining in the ECM area (A). Then, we reconstructed images and showed the Elastin protein distribution in the whole tissue by displaying in 3D from different angles (B&C). (Scale bar: 1 mm)

Collagen type I and Elastin proteins are abundant in fibrotic liver ECM. When detecting those proteins in cleared liver tissues, positive pixels are quantified by the analysis code. Therefore, we should demonstrate the whole tissue structures to analyse the amount of the ECM proteins proportionate to the tissue area. As the CLARITY method preserves nucleic acids such as DNA and RNA, we used nuclei staining dyes in order to demonstrate the nuclei in hepatocytes and other liver cells to indicate the tissue borders. Therefore, we updated our LSFM configuration by adding a 405 UV laser. Then, we imaged Collagen type I and nuclei-stained cleared liver tissues and attempted to reconstruct them in 3D. We visualised each channel separately in dual imaging experiments since the LSFM configuration was not yet updated for simultaneous imaging. Additionally, 3D reconstructed images with Image J software were insufficient to generate merged and high-quality 3D data. Image J software uses computer system memory while creating 3D objects. Therefore, Image J requires high-power hardware

systems such as computer memory larger than at least 64 GB to create 3D images of whole liver biopsy samples with two channels. Then, we attempted to use Lasx software for 3D reconstruction. At that time, we did not know how to merge channels using Lasx; therefore, we used Image J for merging channels. However, Image J gave a size difference error due to the asynchronous imaging. Therefore, we could only create a 3D of Collagen type I channel using Lasx (**Figure 3.48**).

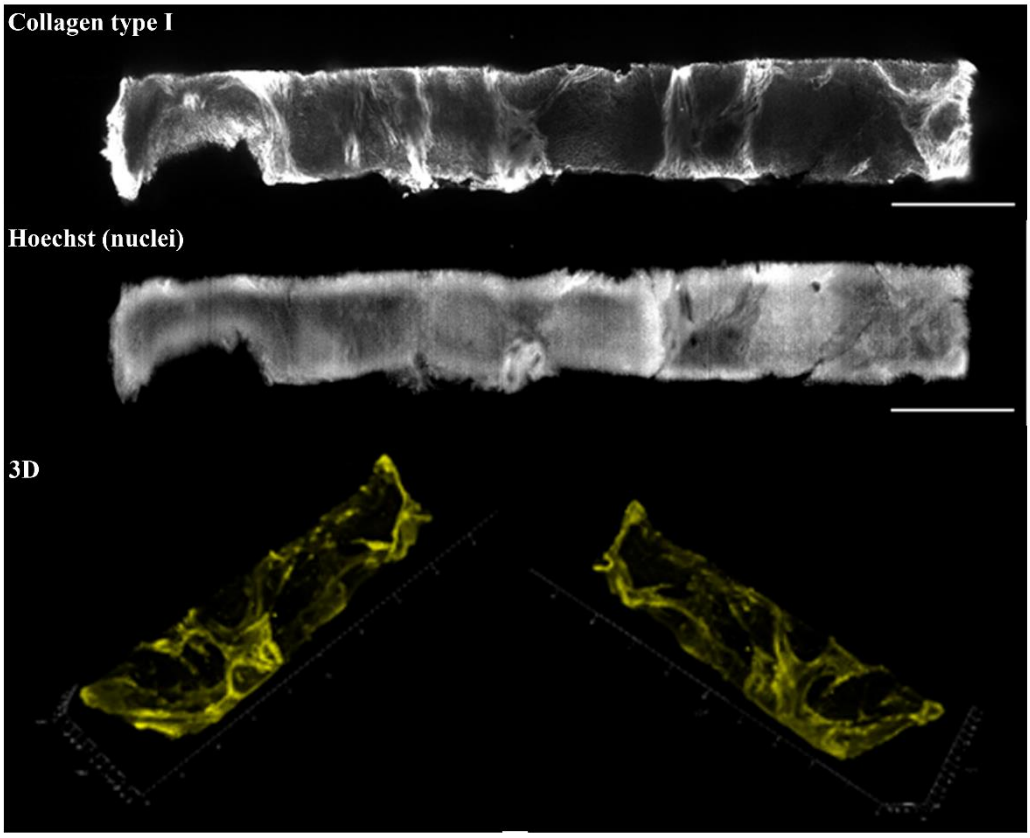

Figure 3.48 Evaluation of dual imaging using custom LSFM. A cleared cirrhotic liver stained against Collagen type I protein and nuclei detection. Grayscale images show the specificity of the staining pattern. The light sheet images were reconstructed in 3D using Lasx software without merging due to the size differences of the asynchronous imaging in LSFM. (Scale bar: 1 mm)

Additionally, we encountered several problems during LSFM imaging. When we were imaging Elastin and nuclei-stained liver tissue, we noticed that some of the images were missing (**Figure 3.49**). We interpreted this error due to the saving of imaging data directly to the external hard disc. We used an external disc to save LSFM images and leave free space in the imaging computer. The high-resolution camera of the

LSFM system generates a new image then saves it to the hard disc simultaneously. Due to the asynchronized imaging process, imaging files were missed. Then, we saved the imaging files directly to the imaging computer. However, this did not recover the condition, and we considered updating the imaging software.

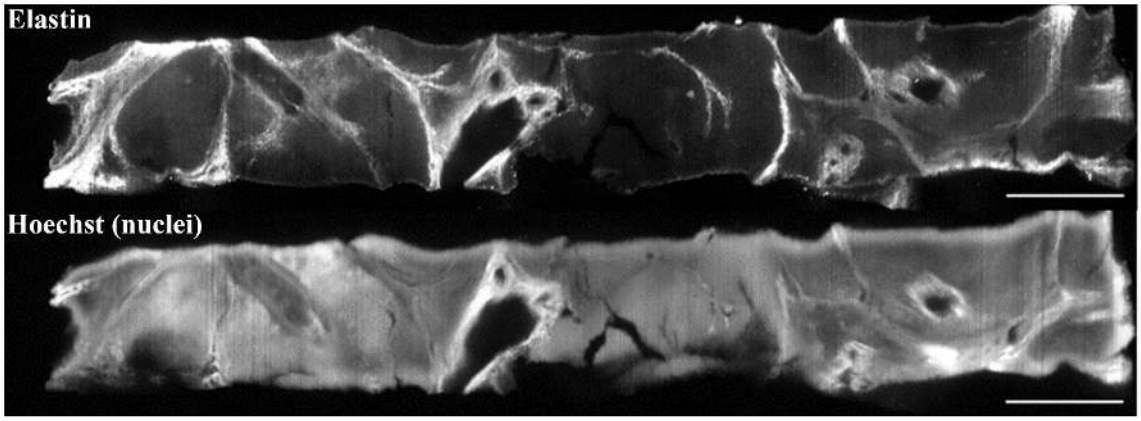

Figure 3.49 Evaluation of dual imaging using custom LSFM. A cleared cirrhotic liver stained against Elastin protein and nuclei. Grayscale images show the specificity of the staining pattern. However, images could not reconstruct in 3D due to the missing images. (Scale bar: 1 mm)

We updated our custom LSFM configuration by adding a mechanical shutter system which can be controlled by the imaging software for simultaneous imaging in LSFM. Additionally, we added a second illumination arm to the LSFM set-up to generate an equal sample illumination from both sides. We could finally create 3D images using both channels by updating the set-up with these improvements. LSFM images were merged in Image J software in the imaging computer of the DLS microscope. Because the DLS microscope's hardware system has a higher RAM capacity than our imaging computer, we could conduct the LSFM image processes there. So, we merged images from both channels using Image J, then changed the type of files to RGB, and finally uploaded them to Lasx as merged files. This process was the first solution to create merged images. Then we noticed that we could merge images using only Lasx software in itself. Since Lasx software is developed for images taken with Leica imaging systems. We used 16-bit tiff files instead of 8-bit RGB files to achieve 3D reconstruction. Then, we used the merging and cropping functions of Lasx software to create 3D images. We used 16-bit high-resolution stitched raw images to

create 3D images. **Figure 3.50** displays the first merged image of Collagen type I protein and nuclei staining in 3D.

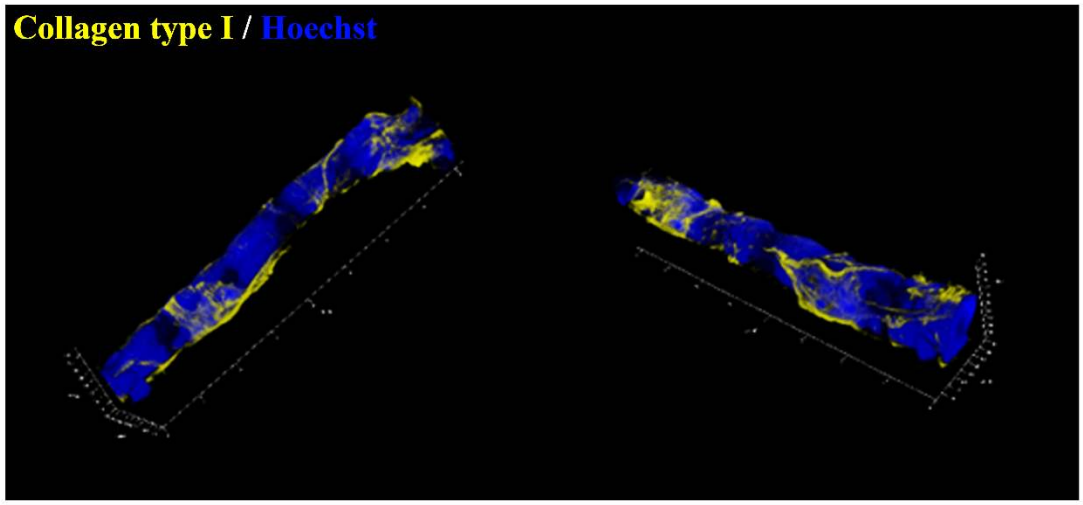

Figure 3.50 The first merged 3D LSFM image of a cirrhotic liver tissue. A cirrhotic liver stained against Collagen type I and nuclei were merged and reconstructed in 3D using Image J and Lasx software. (Yellow: Collagen type I, Blue: Nuclei)

We manually stitched tiles for a very long time due to the absence of written code to automatize it. Then, we minimized this process using macro recorder software, which is free to use. However, we finally created a macro code in Image J to stitch images automatically. All the improvements in the LSFM system were extensively beneficial for imaging experiments and this project.

Thus far, we have been trying to find antibodies with specific patterns to use with cleared liver tissues to detect more than one ECM protein. Consequently, we decided to stain liver biopsy samples with Collagen type I (raised in mice) and nuclei staining to quantify fibrosis. Then, we decided to stain explant liver tissues which we have more than one piece of tissue, with Collagen type I and Elastin antibodies separately. Therefore, we stained 25 NASH biopsy samples with Collagen type I and nuclei staining. Explant and non-fibrotic liver tissues were stained with Elastin in addition to Collagen type I staining. In this study, we used 57 NAFLD, 38 chronic hepatitis and 13 non-fibrotic patients were included.

Further, we visualized the sample stained against Collagen type III (Abcam, ab7778) with custom LSFM to observe the staining pattern. Unfortunately, the staining pattern was not specific and had an edge effect, even dispersed all around the tissue (**Figure 3.51**). We reconstructed the image in 3D to observe the staining pattern in the wider tissue regions. However, this did not affect our assessments of the antibody

staining. Then, we adjusted the protocol for specific staining of the Collagen type III antibody. Additionally, we ordered different commercial Collagen type III antibodies to specifically detect it in cleared liver tissues. However, none of the commercial antibodies had a specific pattern for detecting in cleared liver tissues. The optimization experiments and results are depicted in the below figures (**Figure 3.52, Figure 3.53**).

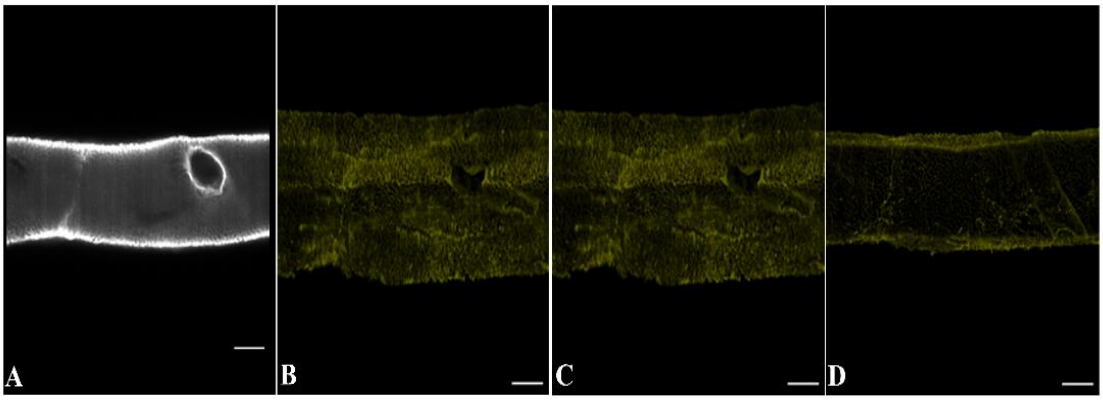

Figure 3.51 Evaluation of Collagen type III staining with custom LSFM. A non-fibrotic liver tissue was used to detect Collagen type III protein and visualized with custom LSFM. Grayscale images show the antibody's non-specific binding, especially in the edges of the tissue (A). We reconstructed it into 3D to see the staining pattern in a wider manner (B&C&D). (Scale
bar: 200 µm)

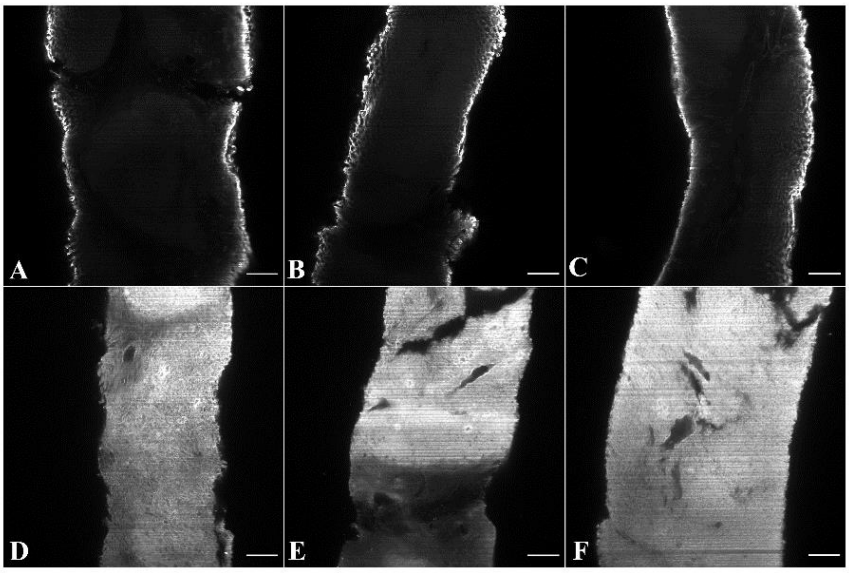

Figure 3.52 Staining optimisation for various commercial antibodies against Collagen III. A cirrhotic liver tissue was used to optimise the staining pattern. The

staining conditions were adjusted for Collagen type III (ab7778) by blocking 5% Goat serum before secondary antibody incubation (A), a no-blocking reagent was used (B), and 5% Goat serum blocking was utilised before primary antibody incubations (C). Then, we used the latter commercial antibody (Invitrogen, PA5-34787) against Collagen type III by blocking 5% Goat serum before secondary antibody incubation (D), the no-blocking reagent was used (E), and 5% Goat serum blocking was utilised before primary antibody incubations (F). (Scale bar: 200 μm)

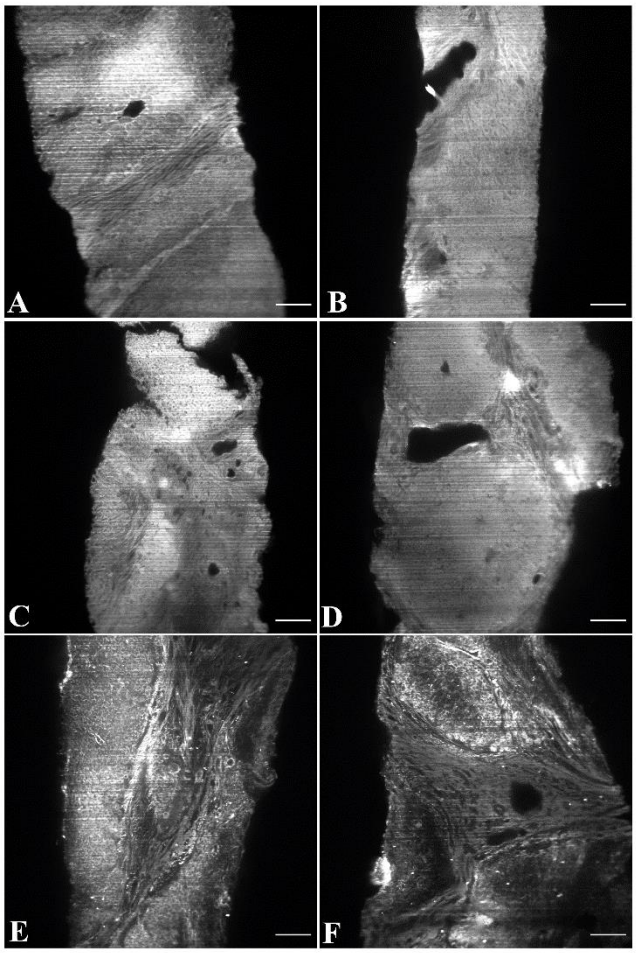

Figure 3.53 Staining optimisation for various commercial antibodies against Collagen III. A cirrhotic liver tissue was used to optimise the staining pattern. The staining conditions were adjusted for Collagen type III (Santa Cruz, 271249) at a 1:250 dilution with blocking 5% Goat serum before 488 conjugated secondary antibody incubation (A) and CY3 conjugated secondary antibody incubation (B), at a 1:1000 dilution with blocking 5% Goat serum before 488 conjugated secondary antibody incubation (C), and CY3 conjugated secondary antibody incubation (D). Then, we used

a 488-conjugated Collagen type III antibody (Abcam, ab277278) by blocking 5% Goat serum before primary antibody incubation (E&F). (Scale bar: 200 µm)

An optimal Collagen type III staining was not observed in the above figures. The staining in figure 3.53, which shows 488-conjugated antibody staining for Collagen type III, was promising. However, other staining patterns were not optimal or non-specific binding was observed extensively.

Further, we designed a staining experiment for other ECM proteins such as Fibronectin and Laminin. In the first staining experiments, Fibronectin and Laminin antibodies did not have a specific pattern with CLARITY-processed liver tissues. Therefore, we ordered additional antibodies and tested whether we could encounter a specific staining pattern.

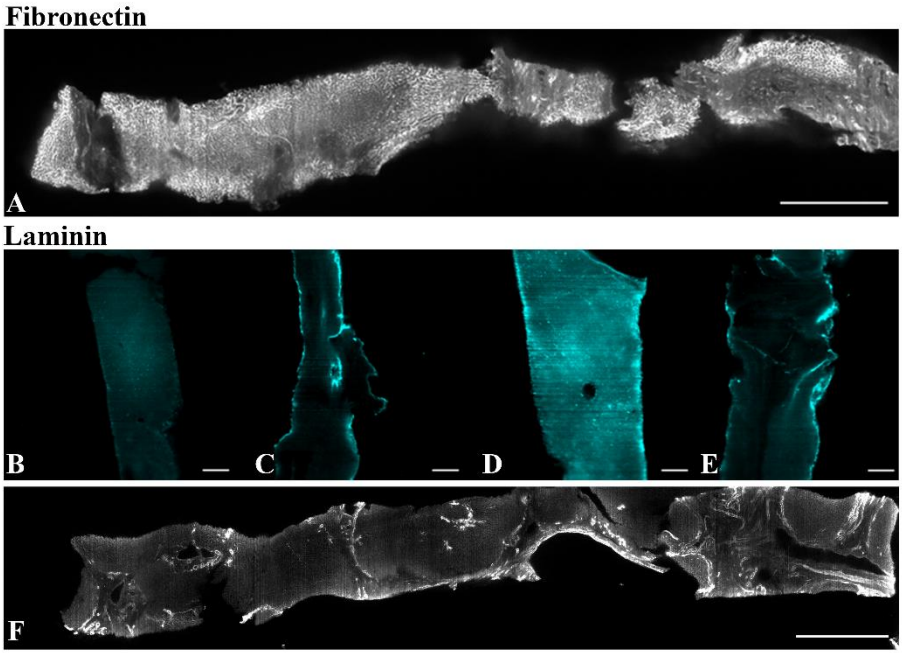

Figure 3.54 Optimization of other ECM proteins in cleared liver tissues. A cirrhotic and non-fibrotic cleared liver tissues were used to optimize the detection of Fibronectin (A) and Laminin ECM proteins in cleared liver tissues. Two blocking reagents and two different antibodies were used for Laminin staining. B1 blocking reagent (B&C) and 5% Goat serum blocking (D&E) were used for non-fibrotic and cirrhotic liver tissues. In both conditions, specific staining was not observed (Scale bar: 200 µm). We observed a specific staining pattern in one of the Laminin antibodies (Abcam, ab11575) (F); however, the pattern was only visible in the vasculature structure of the liver. (Scale bar: 1 mm)

Consequently, the staining experiments did not result in an optimal staining pattern of other ECM proteins for this project. Therefore, we stained and imaged our cohorts with monoclonal Collagen type I and Elastin antibodies. Two-dimensional optical slices taken via custom LSFM from each fibrosis stage were depicted in **figure 3.55**. Multiple optical sections were used to create 3D images for the manuscript. Three-dimensional images were reconstructed in 3D using Lasx software (**Figure 3.56**).

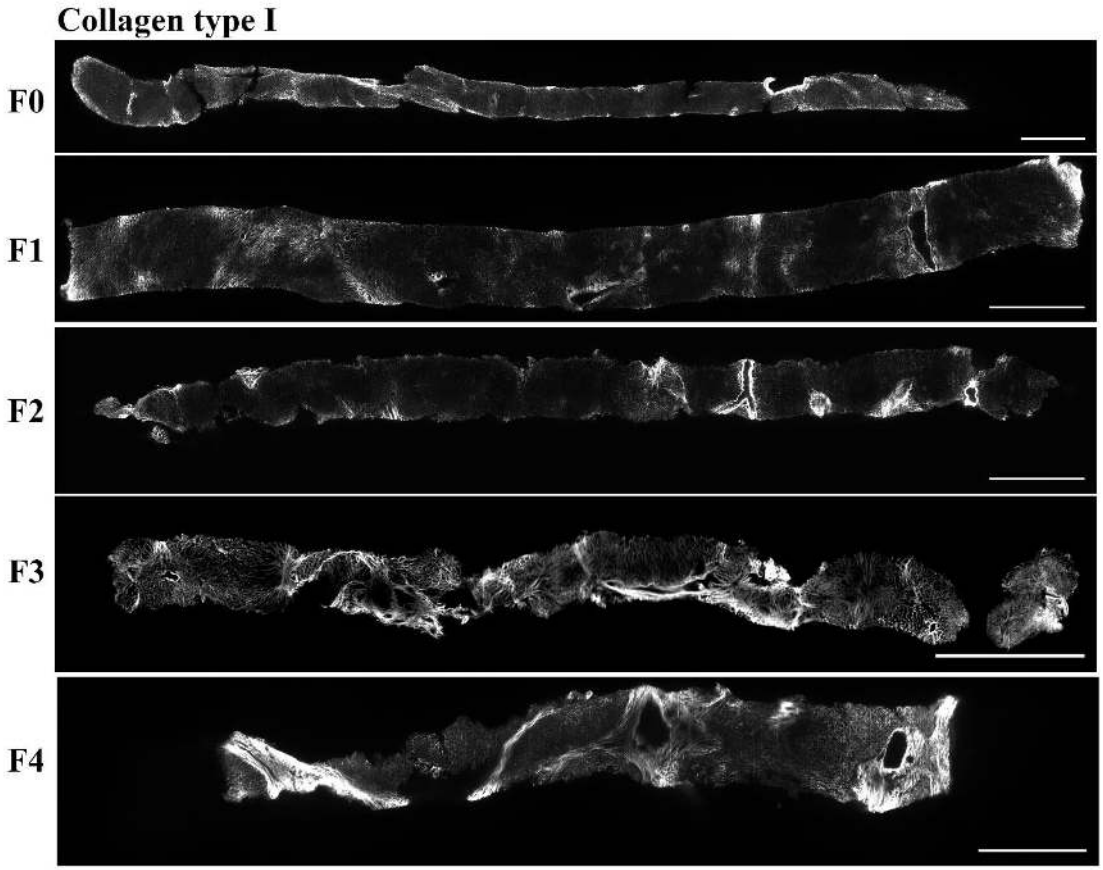

Figure 3.55. Collagen type I staining and LSFM imaging of various fibrosis stages of NAFLD patients. The grayscale images show the results of Collagen type I staining and imaging with custom LSFM. CLARITY-processed liver tissues from various fibrosis stages of NAFLD were stained against Collagen type I protein to quantify the amount of fibrosis within the sample. (Scale bar: 1 mm)

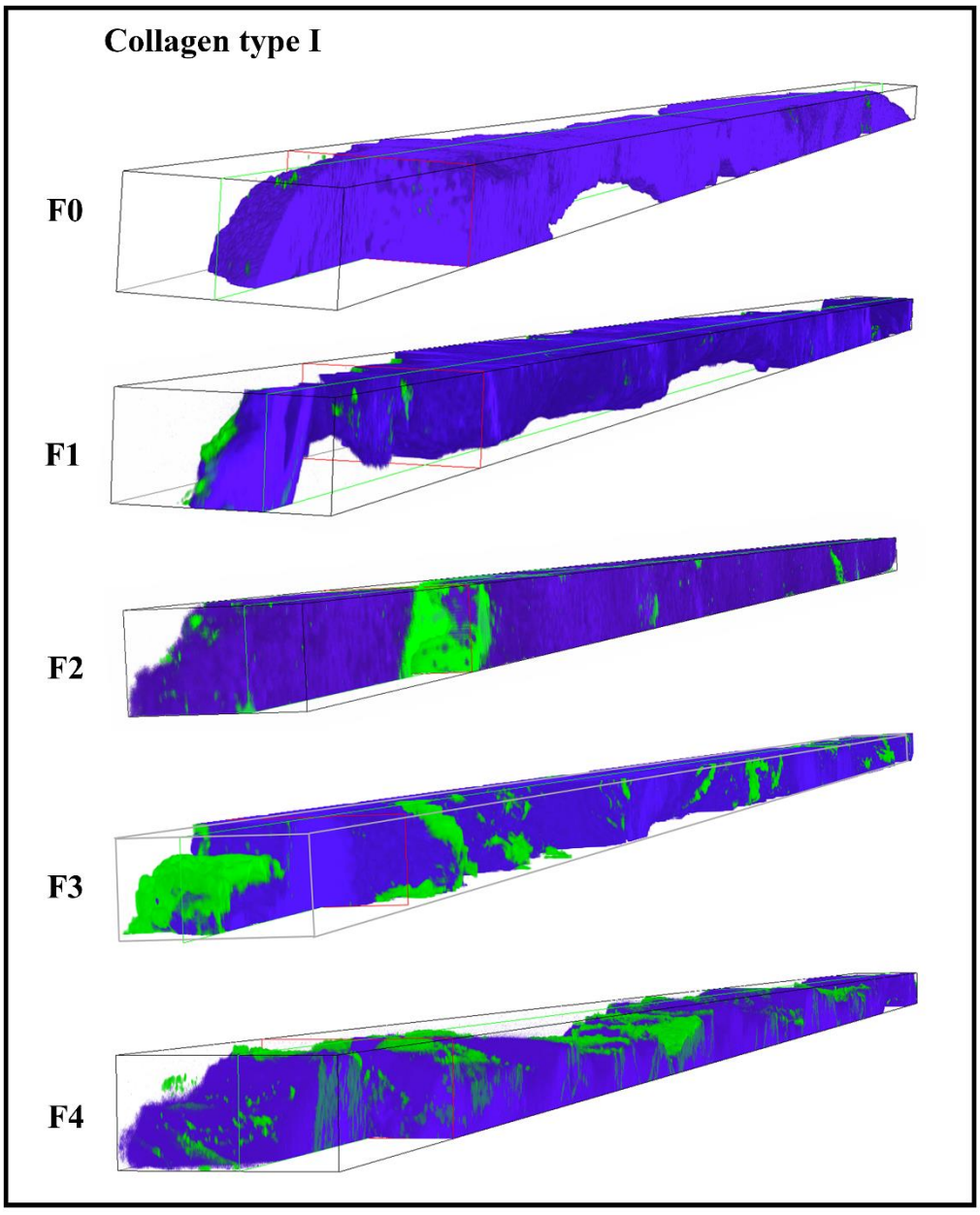

Figure 3.56 Collagen type I staining of CLARITY-processed whole liver biopsies and 3D images. Staining Collagen type I (Green) and nuclei (Magenta) in CLARITY-processed samples significantly show increasing fibrosis areas with the disease progression. 3D representation of whole liver biopsies from F0 (A), F1 (B), F2 (C), F3 (D) and F4 (E) stage liver tissues are displayed. *A: z=1 mm, y=1.7 cm, *B: z=800 µm, y= 1.8 cm, *C: z=830 µm, y=1.1 cm, *D: z=750 µm, y=1.3 cm, *E: z=1.4 mm, y= 1.5 cm.

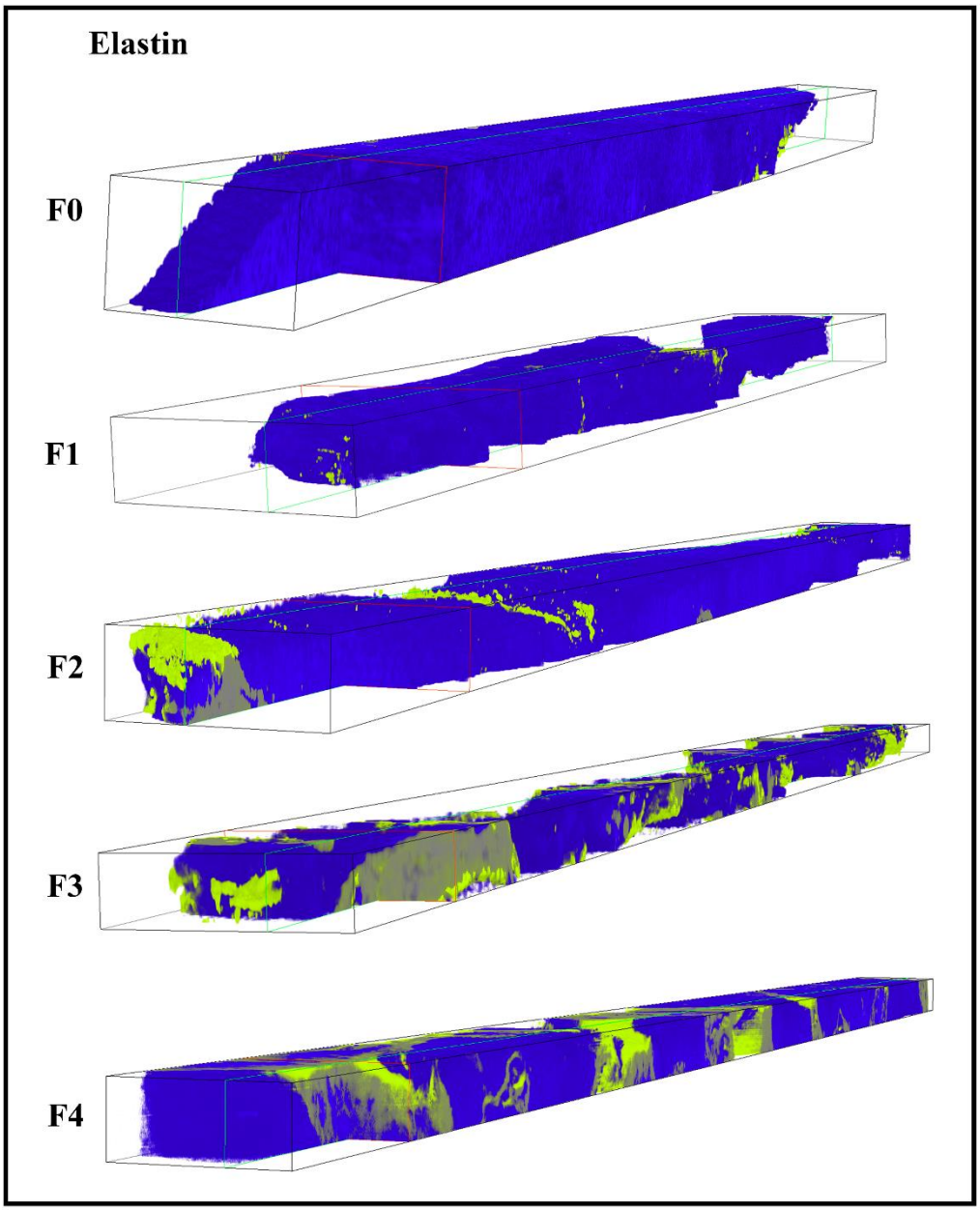

Figure 3.57 Elastin staining of CLARITY-processed whole liver biopsies and 3D images. Staining Elastin (Yellow) and nuclei (Magenta) in CLARITY-processed samples significantly shows increasing fibrosis areas with the disease progression. 3D representation of whole liver biopsies from F0 (A), F1 (B), F2 (C), F3 (D) and F4 (E) stage liver tissues are displayed. *A: z=1 mm, y=1.1 cm, *B: z=730 µm, y= 0.8 cm, *C: z=700 µm, y=1 cm, *D: z=970 µm, y=0.8 cm, *E: z=1.2 mm, y= 1.2 cm.

3.2.2 Staining of cleared mouse liver tissues

In this project, we also performed animal models to show the applicability of the modified-CLARITY model in mouse models of liver fibrosis. First, we optimized the staining of ECM proteins and imaged with a confocal microscope at KUTTAM imaging facility until our custom LSFM was ready to use.

Confocal imaging for the optimization of mouse ECM protein staining

We performed staining in cleared mouse liver tissues against the most abundant ECM proteins, Collagen type I and type III. First, we prepared an experiment using mouse liver tissues from various animal models of liver fibrosis. The staining of Collagen type I and type III in different animal models of liver fibrosis is shown in the below figure 3.58. Although we observed partially stained regions in the liver tissue, there was non-specific binding in the non-ECM areas for both Collagen type I and III protein staining. (**Figure 3.58**). We observed diffused staining because we did not apply a blocking reagent for non-specific binding. The images were taken with Confocal and Multiphoton imaging systems.

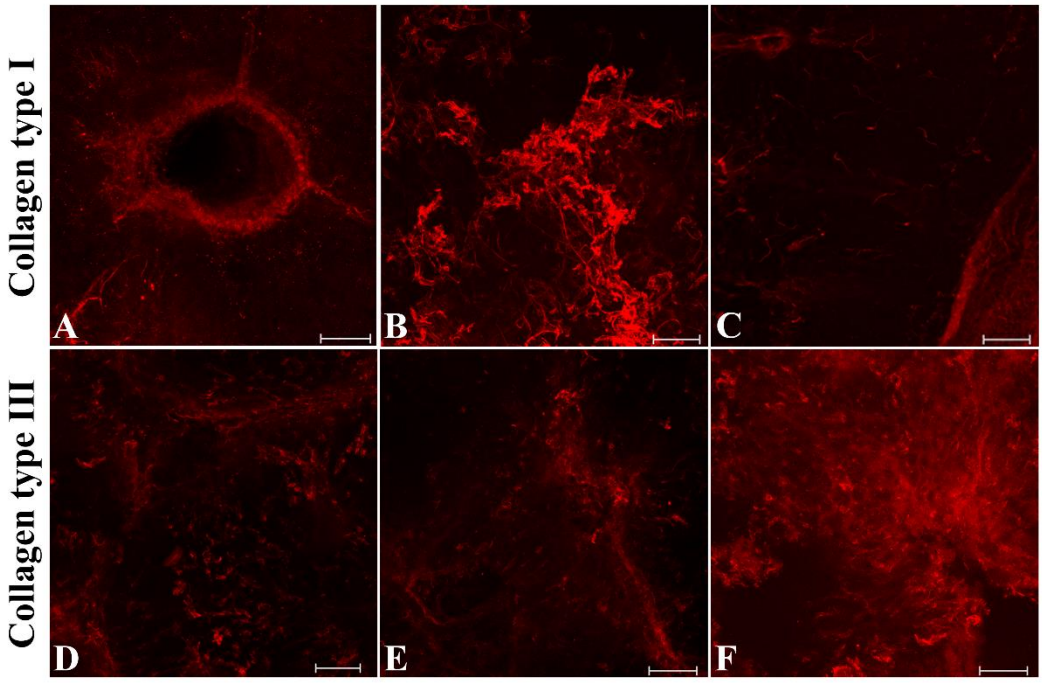

Figure 3.58 Observations of Collagen type I and type III staining in various mouse models of liver fibrosis. Cleared mouse liver tissues from carbon tetrachloride (CCl4) injection model (A), a high fat high sucrose diet induced (HFHS) model (B) and its control diet (Low fat diet) (C) stained against Collagen type I (ab34710) protein. Then, cleared mouse liver tissues from the CCl4 injection model were stained against

Collagen type III protein and images were taken with Confocal (D) and Multiphoton imaging systems (E&F). (Scale bar: 100 µm)

Further, we imaged cleared mouse liver tissues stained against α-SMA protein with a Confocal and Multiphoton microscope. We have seen specific binding of the antibody to its antigen in the diseased mouse liver tissues (**Figure 3.59**).

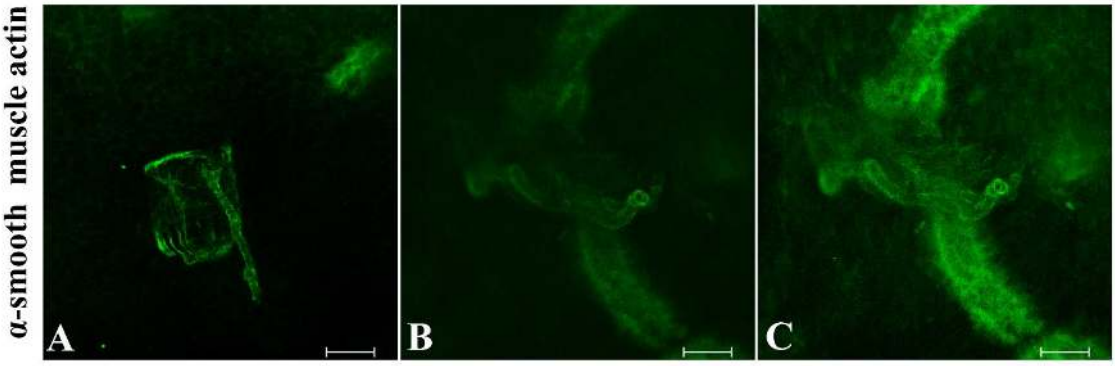

Figure 3.59 Evaluation of α-SMA staining in mouse liver tissues. Cleared mouse liver tissues from a high fat high sucrose diet induced (HFHS) model (A) and its control diet (Low fat diet) (B) stained against α-SMA protein. Multiphoton imaging was performed (C). (Scale bar: 100 µm)

Following that, we proceeded with the staining by reducing non-specific binding using Goat serum, just as we did with human samples. We stained liver tissues from the CCl4 animal model, which has early and advanced stage liver fibrosis. However, we did not see any specific pattern for this antibody (**Figure 3.60**).

Thus far, we were conducting mouse liver tissue staining at 37°C. Then, we adjusted the temperature of the process to +4°C and implemented various blocking reagents. For Collagen type I, Collagen type III and Collagen type I/III, we used 15% Goat serum blocking and 1% bovine serum albumin (BSA) blocking. However, none of them revealed a specific pattern for detection. We also repeated the first staining experiment for Collagen type I with minor adjustments. We prolonged the washing steps to get rid of free antibodies after antibody incubation (primary and secondary). Also, we did not use a blocking reagent to observe the prolonged wash steps effect on the staining. However, the staining was dispersed and not particular (**Figure 3.61**).

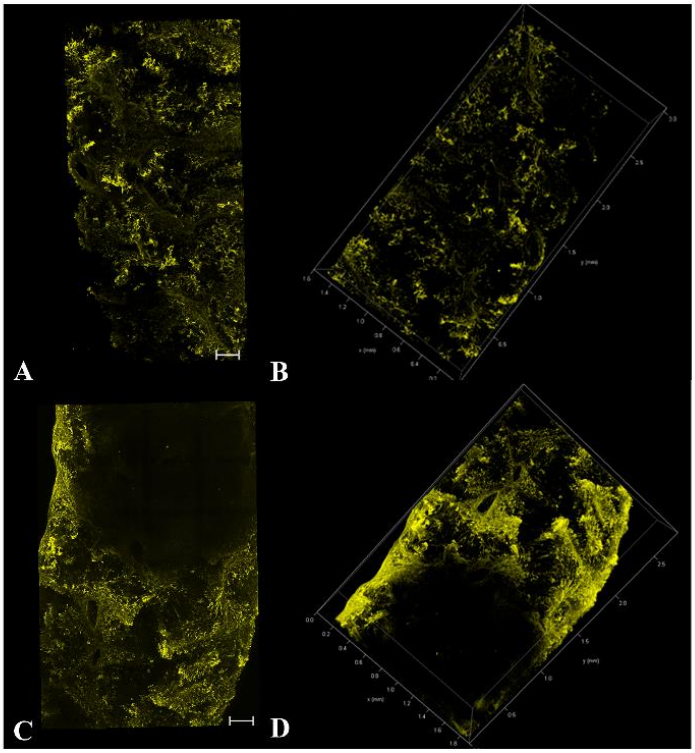

Figure 3.60 Collagen type I staining of cleared mouse liver tissues. Cleared mouse liver tissues from 4th l4 (A) and 8th weeks injection of CCl4 (C) were stained against Collagen type I. Images were reconstructed in 3D (B&D) via Lasx software. (Scale bar: 200 µm)

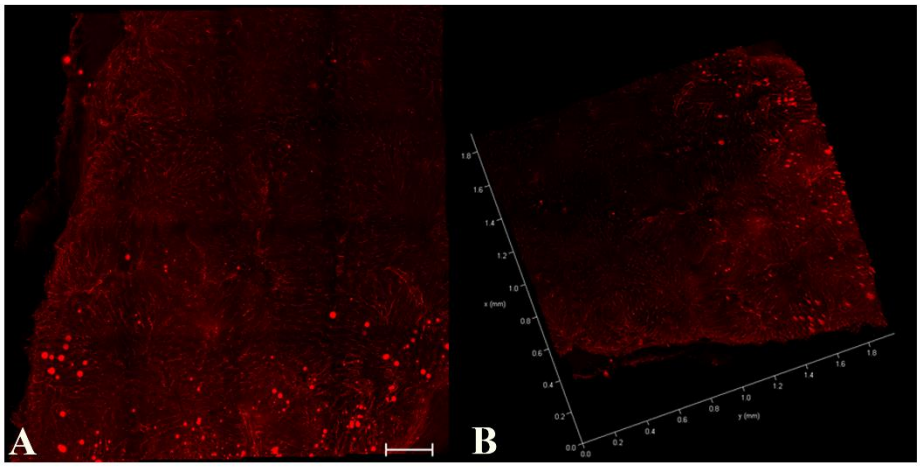

Figure 3.61 Collagen type I staining in cleared mouse liver tissues. Cleared mouse liver tissues from 6th weeks injection of CCl4 (A) stained against Collagen type I. Images were reconstructed in 3D (B via Lasx software. (Scale bar: 200 µm)

Further, we tested for staining other ECM proteins in mouse liver tissues. We used the Elastin antibody (same in human samples), which has reactivity to mouse samples, and histone-3 antibody to highlight nuclei. However, we did not observe any distinct pattern that would allow us to detect the quantification of proteins. Then, we

tested the Fibronectin antibody (Sigma Aldrich, SAB4200760) to stain mouse liver tissues. We used various blocking conditions, staining order, and antibody dilutions. Goat and horse serum blocking were tested before primary or secondary antibody incubation. Additionally, all antibodies were tested without blocking reagents. However, we did not observe any specific pattern (**Figure 3.62**).

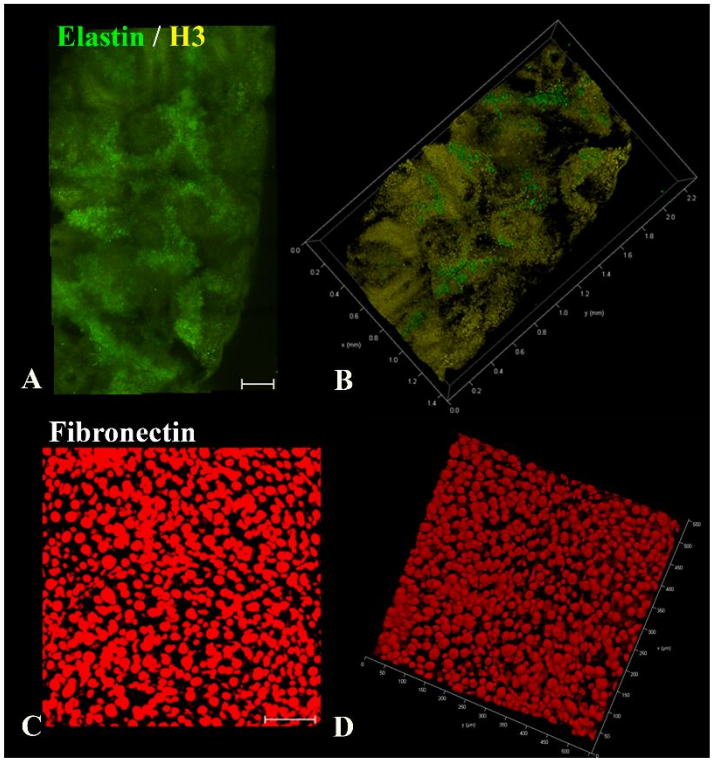

Figure 3.62 Optimization of other ECM proteins in cleared mouse liver tissues. Cleared mouse liver tissues were stained against Elastin (A) and Fibronectin (C) proteins. There was no specific pattern for both antibodies. The images were reconstructed in 3D via Lasx software. (Scale bar: 100 µm)

Further, we checked the staining of ECM remodelling proteins such as MMP-2, MMP-9, and its inhibitor TIMP-1. We employed a concentrated dilution of antibodies with Goat serum to prevent non-specific antibody binding (**Figure 3.63A, Figure 3.63E**). We observed a pattern in MMP-2 and MMP-9, but they were not distinct patterns. Hence, we proceeded to optimize the staining by using more diluted antibodies with various blocking reagents such as horse serum. As it is understood from the 2D and 3D images, the adjustment did not affect the staining pattern. For TIMP-1 staining, we did not observe any specific pattern using concentrated or diluted antibody concentration with or without blocking reagents (**Figure 3.63I, Figure 3.63K**). The absence of a distinct pattern for metalloproteinases could be attributed to their release in

the extracellular environment. Consequently, we did not observe any specific pattern for CLARITY-processed mouse liver tissues using a Confocal or Multiphoton imaging system.

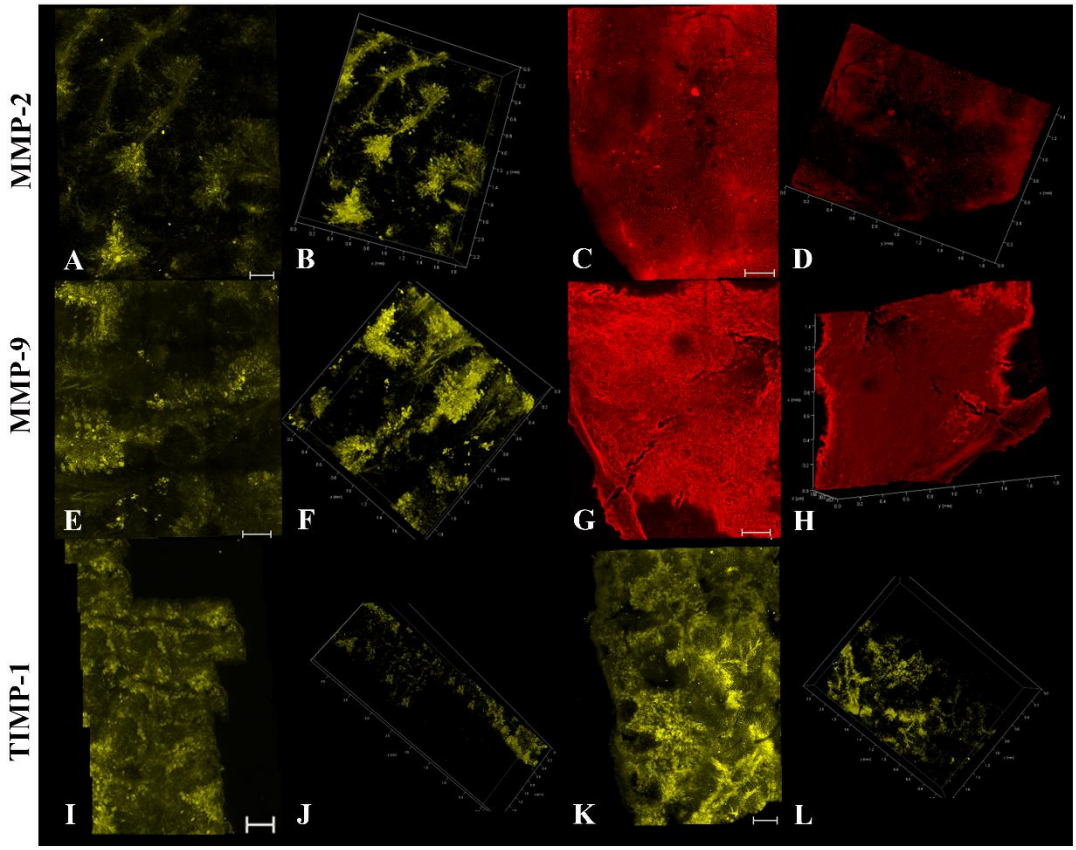

Figure 3.63 Evaluation of MMP-2, MMP-9 and TIMP-1 staining in cleared mouse liver tissues. Cleared mouse liver tissues from the CCl4 model were stained against MMP-2 (A-D), MMP-9 (E-H) and TIMP-1 (I-L) proteins. The images were reconstructed in 3D via Lasx software. (Scale bar: 200 µm)

Light-sheet imaging of mouse ECM proteins

Thus far, we have used a Confocal microscope at KUTTAM imaging facility for the optimization experiments. Upon developing a custom light sheet microscope, we proceeded to image all samples with LSFM. The staining of CLARITY-processed mouse liver tissue was more compelling than we expected. We should have seen at least one specific pattern of a commercial antibody, but we could not. Then, we purchased commercial antibodies targeting Collagen type I, III, and Elastin. Finally, we have seen specific staining patterns in our CLARITY-processed mouse liver tissues for ECM proteins.

First, we tested the antibody that we used in Confocal imaging experiments. Interestingly, we observed a promising staining pattern for Collagen type I. Even if the antigen-antibody binding in a sample was not optimum, and other implementations may be required, the staining was promising (**Figure 3.64**). However, there were some challenges in imaging the entire sample. The first one is the decreasing intensity when going deep in the tissue in the z-direction. It was presumably due to the insufficient antibody incubation time. The other challenge was limited usage of the positional stage. More clearly, sample positional stage is optimized for biopsy samples which have 2 cm in length. Therefore, we cannot automatically control the x direction due to mechanical errors. As it is understood from the below image, the tissue is wider than is seen in the figure. However, we could not conduct the imaging in the x direction due to dimensional limitation

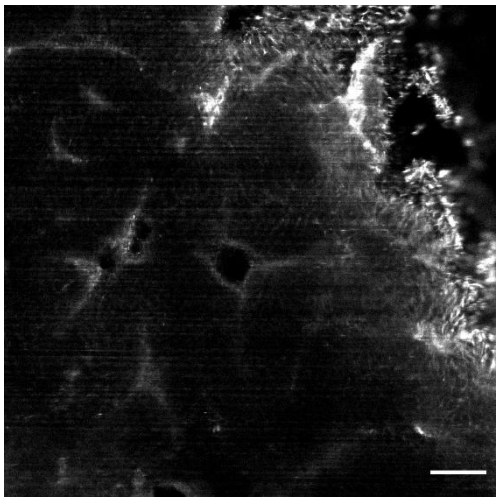

Figure 3.64 The LSFM imaging of mouse liver tissue for Collagen type I staining. A promising pattern was observed in CLARITY-processed mouse liver tissue stained against Collagen type I. (scale bar: 200 µm)

Then we tested other commercial antibodies that target Collagen type I protein to detect in mouse liver samples. Therefore, we used a monoclonal Collagen type I antibody with various concentrations to find optimal conditions. Although there were no significant differences between the concentration, there was a promising staining pattern for Collagen type I protein (**Figure 3.65**).

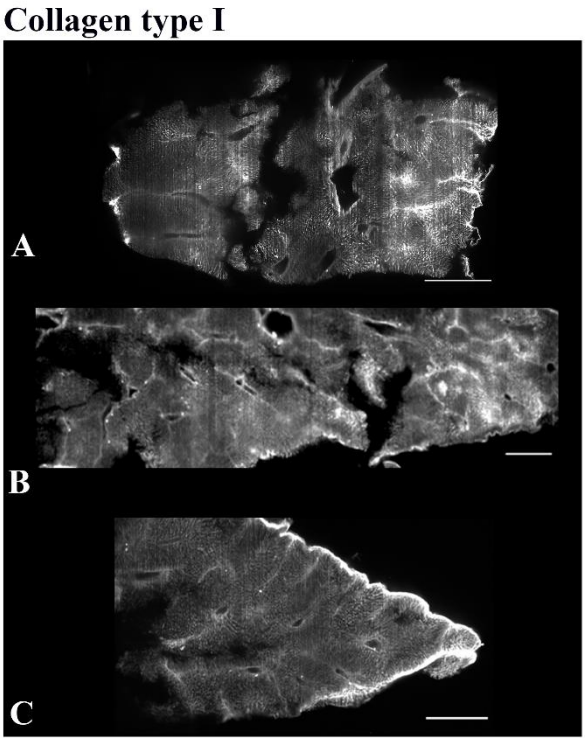

Figure 3.65 Evaluation of Collagen type I staining in cleared mouse liver tissues. Cleared mouse fibrotic liver tissues were stained against Collagen type I at 1:50 (A), 1:100 (B), and 1:500 (C) dilution. (Scale bar: 500 µm) (Santa Cruz, 293182)

Further, we used a polyclonal antibody that targets mouse Collagen type I protein in mouse liver samples. Therefore, we stained a cleared fibrotic mouse liver tissue at recommended dilution and imaged using custom LSFM. Since we observed decreasing intensity in the z-direction, we prolonged the incubation time for the primary antibody. Then, we observed a specific pattern in the fibrosis area and around the veins (**Figure 3.66**). Prolonged incubation time resulted in minimizing the decreased intensity level in the z-direction. The images were reconstructed in 3D to observe the staining pattern in whole tissue.

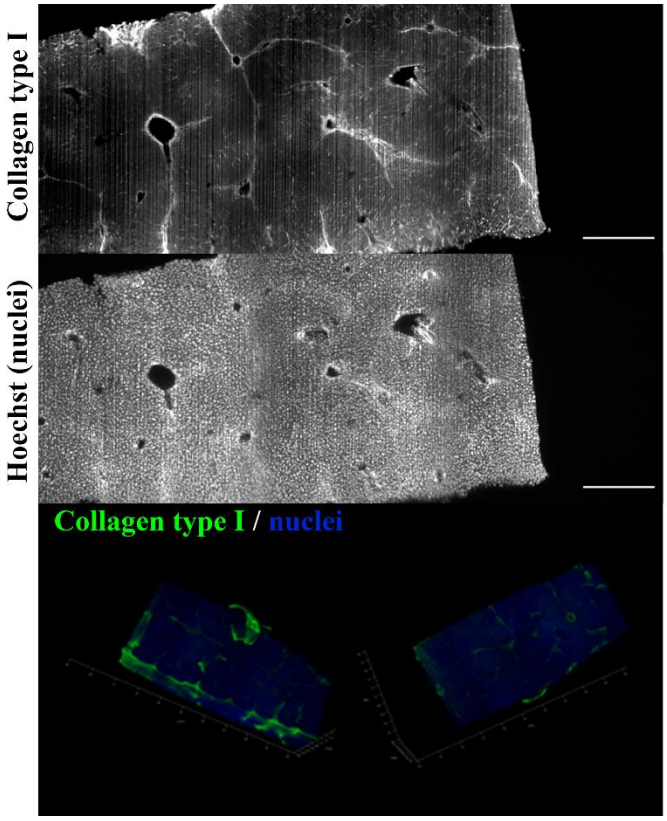

Figure 3.66 Examination of Collagen type I staining in cleared mouse liver tissue. A cleared fibrotic mouse liver tissue was stained against Collagen type I protein and nuclei. The tissue was incubated longer than in the previous staining experiment to increase the diffusion of the primary antibody to detect Collagen type I protein. The images were reconstructed in 3D using Lasx software. (Scale bar: 500 µm)

Further, we examined the staining, which was performed using a monoclonal Collagen type III antibody. We used various dilutions to detect the optimal pattern with suitable concentration. To this end, we stained a cleared fibrotic mouse liver against Collagen type III (**Figure 3.66**). There was a promising staining pattern at all concentrations, but the images were blurry. When performing imaging with LSFM, we often encountered a blurry image in mouse liver samples. This could be due to intensities in the non-ECM area. Therefore, the staining of mouse liver tissues required further optimizations.

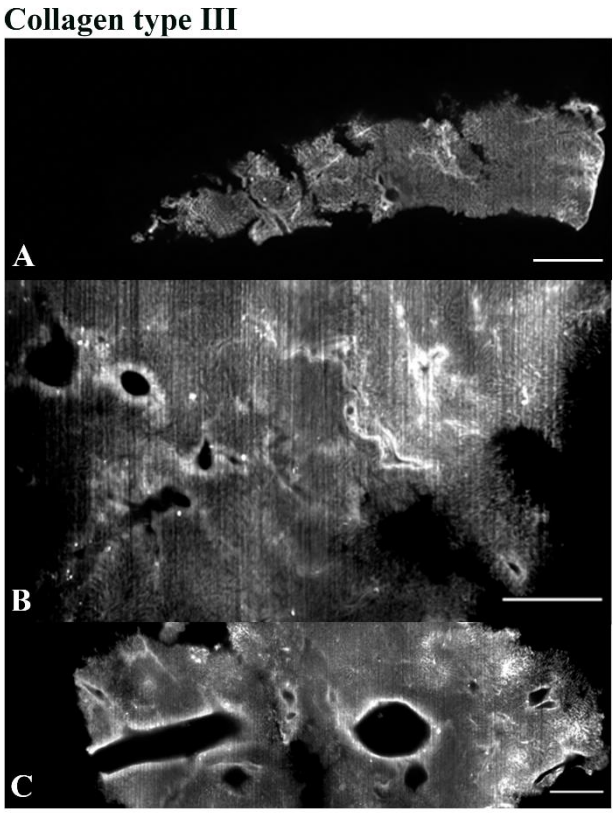

Figure 3.67 Evaluation of Collagen type III staining in cleared mouse liver tissues. Cleared mouse fibrotic liver tissues were stained against Collagen type III protein at 1:50 (A), 1:100 (B), and 1:500 (C) dilution. (Scale bar: 500 µm) (Santa Cruz, 271249)

Then, we tested a polyclonal Collagen type III antibody in CLARITY-processed mouse liver samples. We observed a promising staining pattern (**Figure 3.68**).

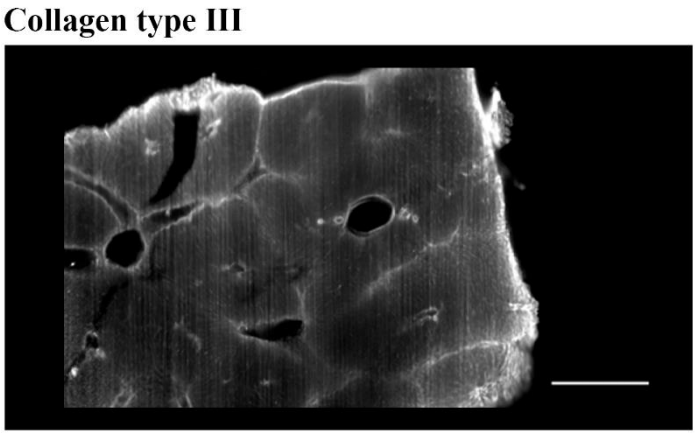

Figure 3.68 Examination of Collagen type III staining in cleared mouse liver tissue. A cleared fibrotic mouse liver tissue was stained against Collagen type III protein and a specific pattern was observed. (Scale bar: 500 µm)

Next we checked the staining of other ECM proteins in cleared mouse liver tissues. Elastin, Laminin, and Fibronectin protein staining were performed. We

observed promising staining patterns for Elastin and Laminin proteins but did not for Fibronectin protein. The staining was performed using cleared fibrotic mouse liver tissues and imaged via custom LSFM. Since we did not have the specific staining pattern, Fibronectin protein staining was not captured. Elastin protein detection was performed using various dilutions in mouse liver tissues (**Figure 3.69**). The staining pattern was promising and almost the same in every condition.

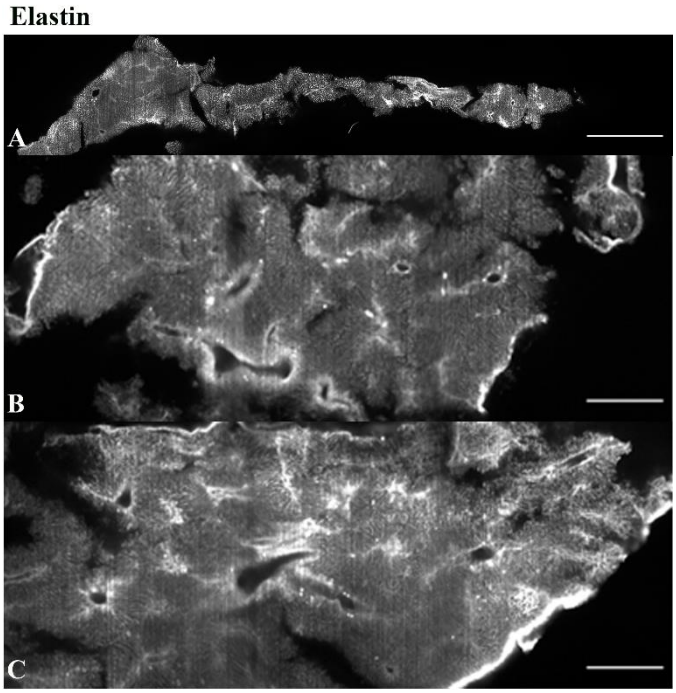

Figure 3.69 Examination of other ECM proteins in cleared mouse liver tissues. Cleared mouse fibrotic liver tissues were stained against Elastin protein at 1:50 (A), 1:100 (B), and 1:500 (C) dilution. (Scale bar: 500 µm) (Santa Cruz, 58756)

Laminin staining was performed in two different dilutions using cleared fibrotic and non-fibrotic mouse liver tissues to find the optimal conditions. In the below images, we observed a specific pattern in fibrotic and non-fibrotic mouse liver samples. However, the pattern was different in fibrotic and non-fibrotic samples. We concluded that this might be due to the protein location that the manufacturer targets.

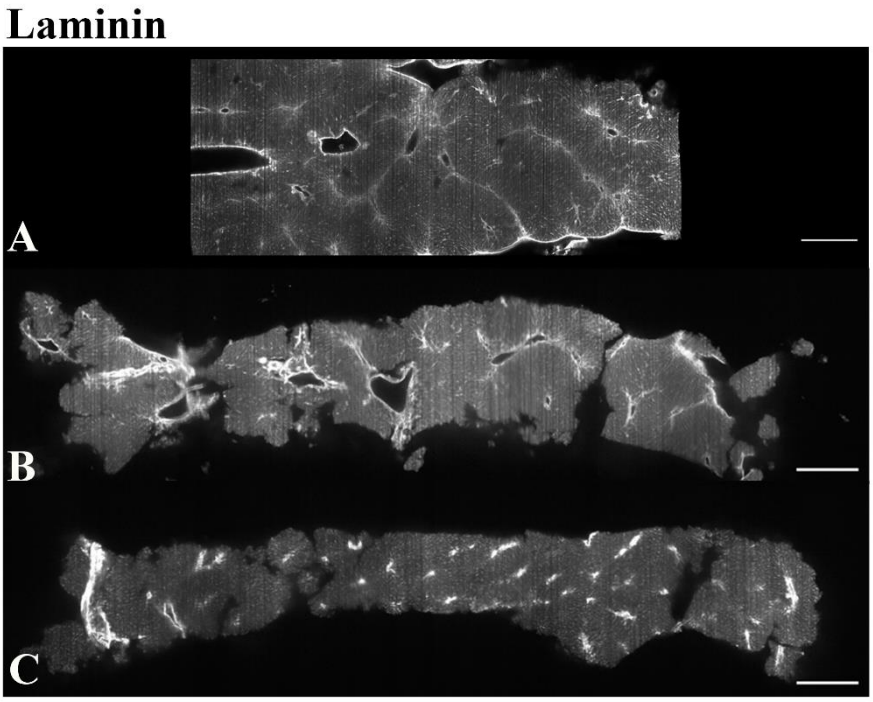

Figure 3.70 Examination of other ECM proteins in cleared mouse liver tissues. Cleared mouse fibrotic liver tissues were stained against Laminin protein at 1:100 (A), and 1:200 (B), non-fibrotic samples were stained against Laminin protein at 1:200 (C) dilution. (Scale bar: 500 µm) (Abcam, 11575)

Then, in order to increase image quality, we set up an experiment to block non-specific binding in mouse liver tissues to increase the contrast. We used Sudan Black blocking (SBB) for mouse liver tissues. Generally, Sudan Black is a lipid stain used to decrease the autofluorescence of the tissue. In CLARITY, SBB is utilized before hydrogel embedding of the tissue at 0.2% concentration. Since the SBB treatment turns tissue black, the clearing step helps to restore the tissue colour and lipid removal concurrently. However, we treated samples before primary antibody incubation and turning tissue black was our main obstacle. We incubated cleared samples with 70% ethanol for several hours to eliminate the dark tissue colour. Then we continued the staining experiment. Importantly, we used SBB dilutions on the logarithmic scale since our tissues are already cleared. Further, we stained SBB-treated samples with several ECM proteins and imaged them with LSFM. However, SBB treatment had no effect on image quality and instead reduced contrast (**Figure 3.71&Figure 3.72**).

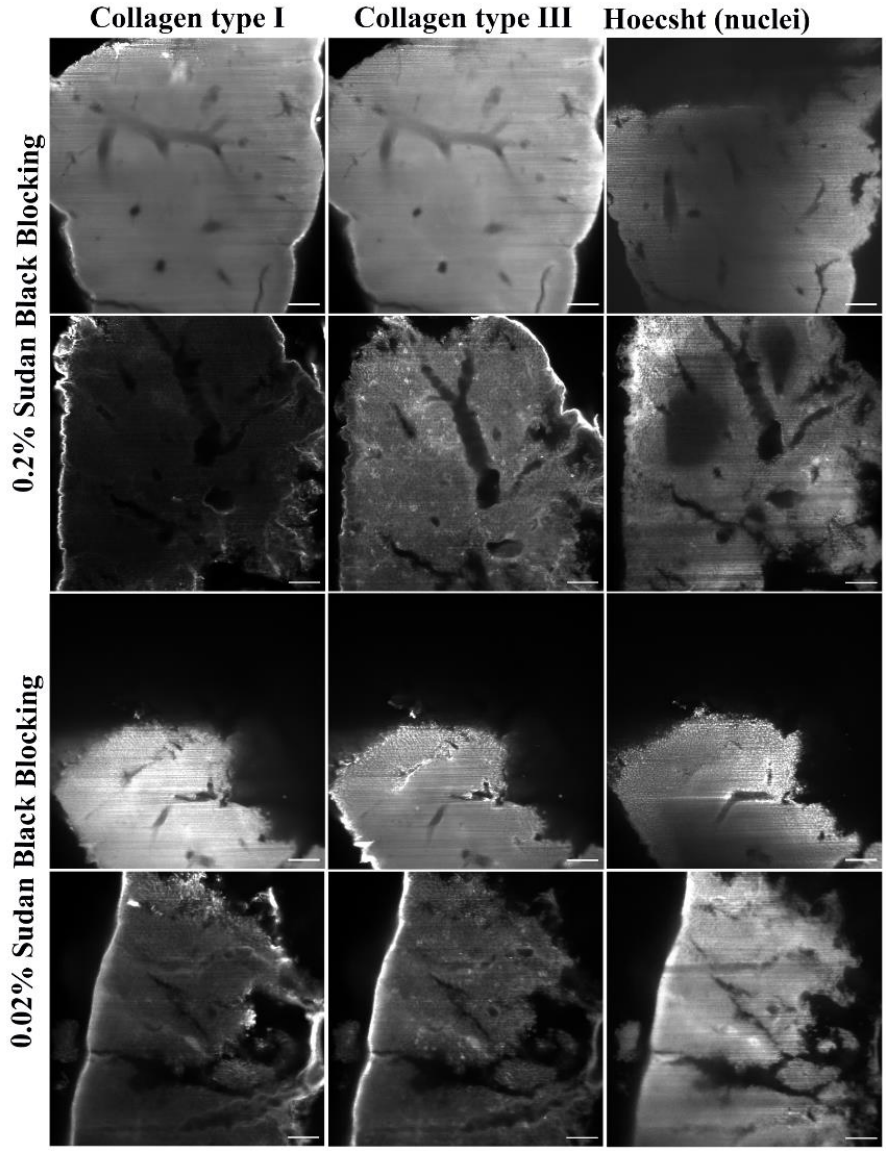

Figure 3.71 Examination of SBB treatment and staining in cleared mouse liver tissues. Cleared fibrotic mouse liver tissues were stained after SBB treatment against Collagen type I and type III. Nuclei were stained with Hoechst. (Scale bar: 200 µm)

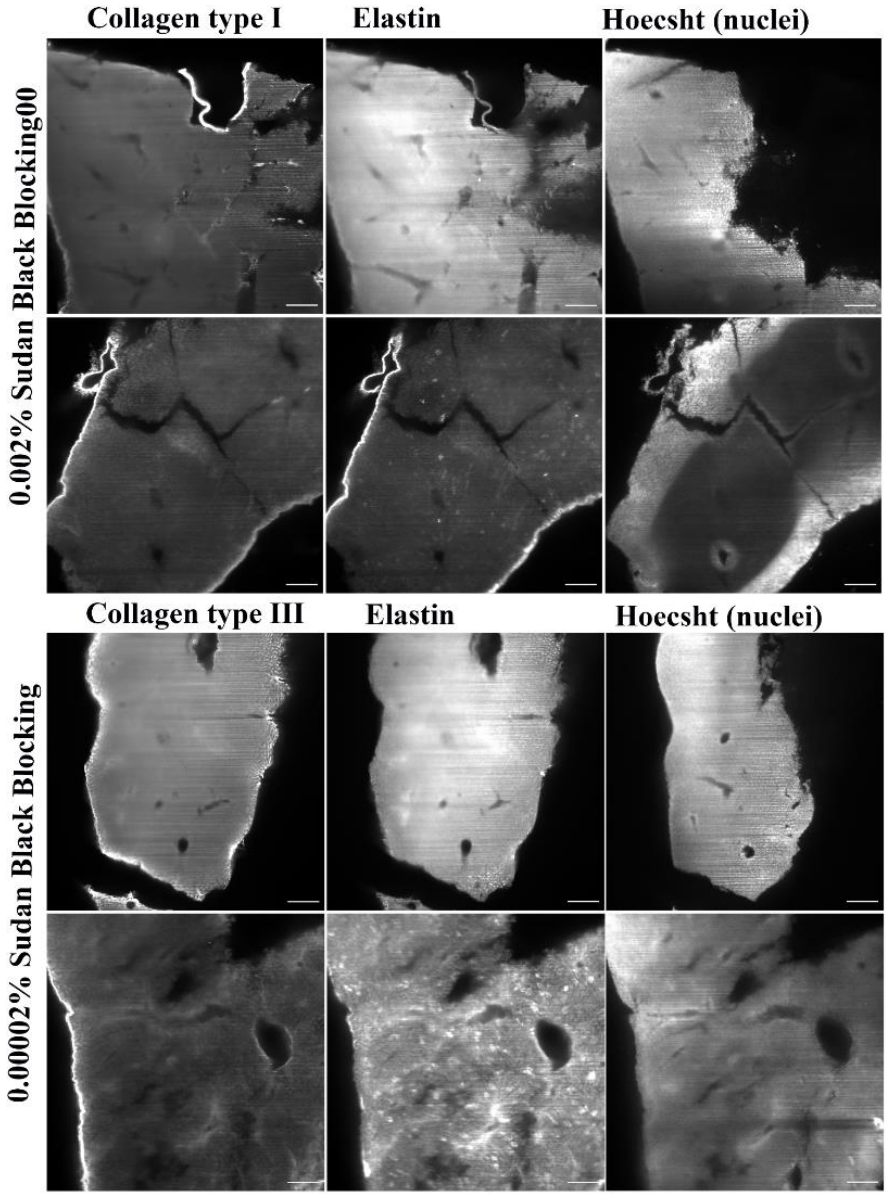

Figure 3.72 Examination of SBB treatment and staining in cleared mouse liver tissues. Cleared fibrotic mouse liver tissues were stained after SBB treatment against Collagen type I, Elastin and Collagen type III and Elastin. Nuclei were stained with Hoechst (Scale bar: 200 µm)

3.3 Molecular quantification of liver fibrosis

3.3.1 Gene expression analysis of COL1A1 and COL3A1

Liver fibrosis is characterized with the excessive deposition of extracellular matrix proteins within the tissue. Activated hepatic stellate cells are the major source of ECM proteins with an increased ECM gene expression profile. Collagen type I and type

III are the predominant ECM proteins known to be an increased expression in liver fibrosis. Therefore, we aimed to check the expressions of those genes in whole liver samples. We added all the CLARITY-processed samples into this experiment and grouped them according to their fibrosis level.

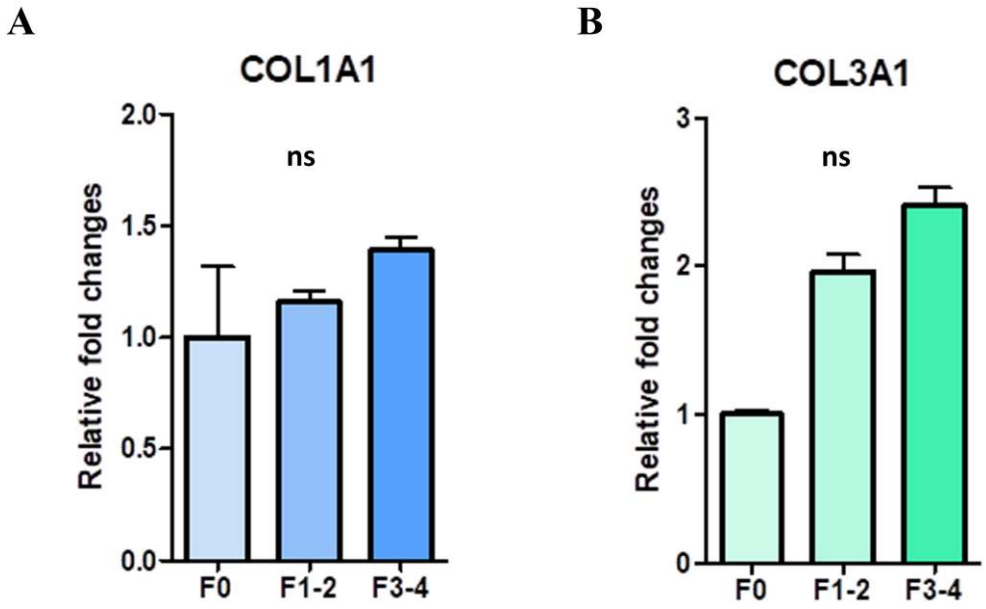

Figure 3.73 COL1A1 and COL3A1 expression of liver tissues in the study cohort. The liver tissues in the study cohort were included for gene expression analysis of COL1A1 (A). 10 patients from the non-fibrotic group, 26 from the F1-2 group and 78 from the F3-4 group of patients were included for COL1A1 gene expression analysis. The liver tissues in the study cohort were included for gene expression analysis of COL3A1 (B). 9 patients from the non-fibrotic group, 10 from the F1-2 group and 57 from the F3-4 group of patients were included for COL1A1 gene expression analysis.

There was a 1,16 fold change in the F1-2 group compared to F0 and a 1,40 fold change in the F3-4 group compared to the F0 group for COL1A1. Generally, the expected increase is more than two folds compared to the non-fibrotic group. However, we detected only 1,40 fold change, possibly due to the gene being completely active and not detectable further changes by real-time PCR. Additionally, there was a 1,97 fold change in the F1-2 group compared to F0 and 2,40 fold change in the F3-4 group compared to the F0 group for COL3A1. The increase in the gene expression of for COL1A1 and COL3A1is apparent as the disease progresses.

3.3.2 The quantification of Hydroxyproline content in liver tissues

Hydroxyproline is the protein amino acid in the Collagen protein. The detection of this protein can be used to quantify the Collagen. Therefore, we used whole liver tissue to quantify the hydroxyproline content in those CLARITY patient groups. Since we have a small amount of biopsy tissue, we did not include those patients in this experiment. Additionally, we checked the hydroxyproline content levels in animal models of liver fibrosis. We included MCD and CCl4 animal models in this experiment.

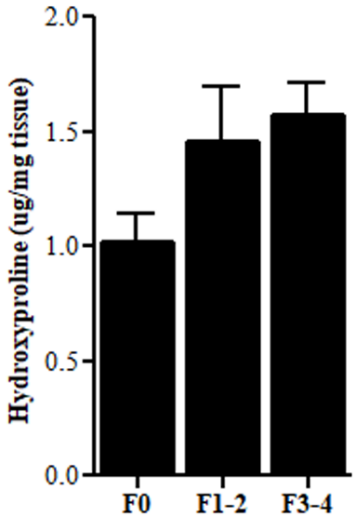

Figure 3.74 Hydroxyproline contents of human liver tissues. The content of hydroxyproline in various fibrotic tissues is depicted in the figure. There is an increase in the hydroxyproline contents as the disease progresses in liver tissues. 8 patients from the non-fibrotic group, 13 from the F1-2 group and 64 from the F3-4 group of patients were included for Hydroxyproline quantification analysis.

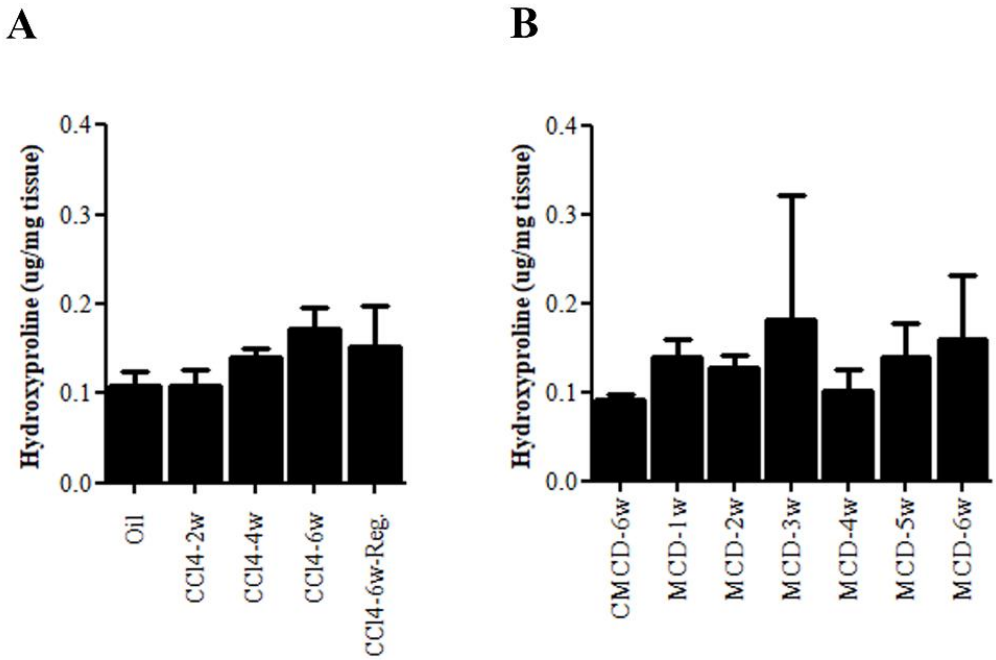

Figure 3.75 Hydroxyproline contents of mouse liver tissues. Hydroxyproline content was determined in CCl4 and MCD animal models. The hydroxyproline content was increased as the injury progressed over weeks. The five groups of the CCl4 animal model were included in this experiment and compared with the Oil group (A). We also saw a decline in the recovery group of CCl4 which we expected. The seven groups of MCD animal model were included in this experiment (B). The content was mildly increased, possibly due to the regenerative ability of the liver. CCl4: Carbon tetrachloride, CMCD: Control Methionine Choline Deficient, MCD: Methionine Choline Deficient. CCl4-Reg: Recovery group from CCl4.

3.4 Quantification of liver fibrosis using CLARITY-processed liver tissues

Liver fibrosis is semi-quantitatively assessed in routine histopathology. In this project, we aimed to quantify the fibrosis in all sections of a given tissue and result in an accurate quantification method for liver fibrosis. To this end, we utilized Collagen proportionate area (CPA) analysis to quantify the fibrosis in the tissue. Therefore, we calculated the CPA values of 2D histological slides stained with Sirius Red to compare with the 3D imaging results. We calculated CPA and EPA from each section for CLARITY-processed liver tissues and calculated CPV and EPV, respectively.

3.4.1 2D quantification of liver fibrosis

Collagen proportionate area analysis is used to quantify the fibrosis amount in liver sections. It is not a method used in the routine histopathological evaluation of liver biopsy samples. Research studies discovered the non-linear relationship between fibrosis amount and fibrosis stages of liver fibrosis using this method. Therefore, we used Sirius red-stained formalin-fixed paraffin-embedded 2D histological sections to assess the fibrosis content of the CLARITY cohort. We focused on calculating CPA values in the NAFLD and Chronic viral hepatitis cohort we generated for this project. CPA measurements are calculated using ten different areas with a 10X magnification objective. The fibrosis content and fibrosis stage correlation are given in figure 3.73. As we expected, there is a non-linear relationship between fibrosis stages and contents in both cohorts (**Figure 3.75**).

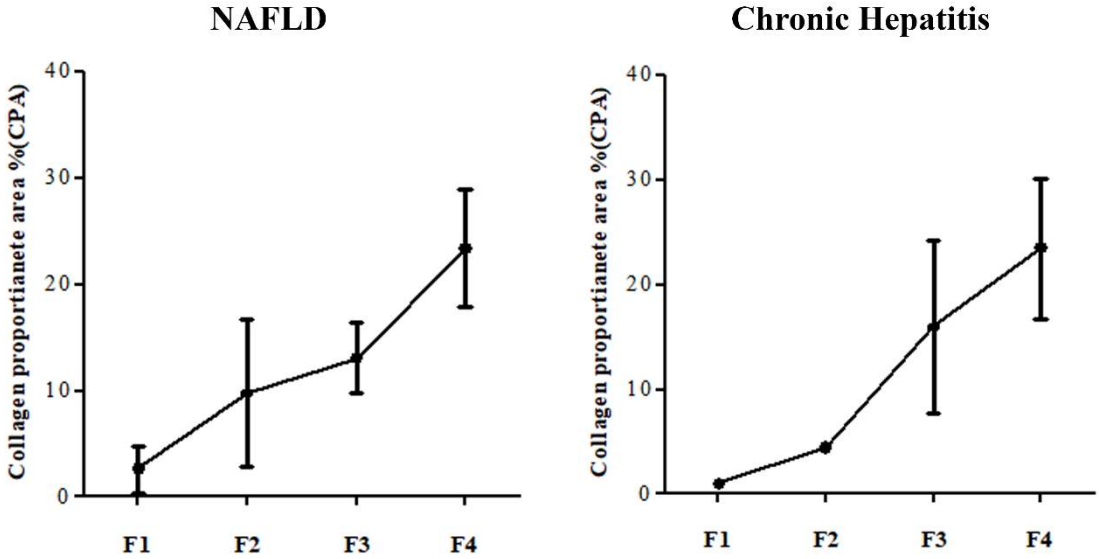

Figure 3.76 2D quantification of liver fibrosis in human samples using histological sections. CPA measurements were calculated in NAFLD and Chronic hepatitis cohorts. For the NAFLD cohort, the group means of CPA scores are as follows; F1: 2.67 ± 2.2, F2: 9.79 ± 6.9, F3: 13.11 ± 3.4, F4: 23.38 ± 5.4. For the Viral hepatitis cohort, the group means of CPA scores are as follows; F1: 1.10 ± 0, F2: 4.5 ± 0, F3: 16 ± 8.7, F4: 23.48 ± 6.6.

For animal models of liver fibrosis, we performed the same analysis for CPA calculations to quantify the fibrosis from 2D histological sections. We applied this method only for CCl4 and MCD model.

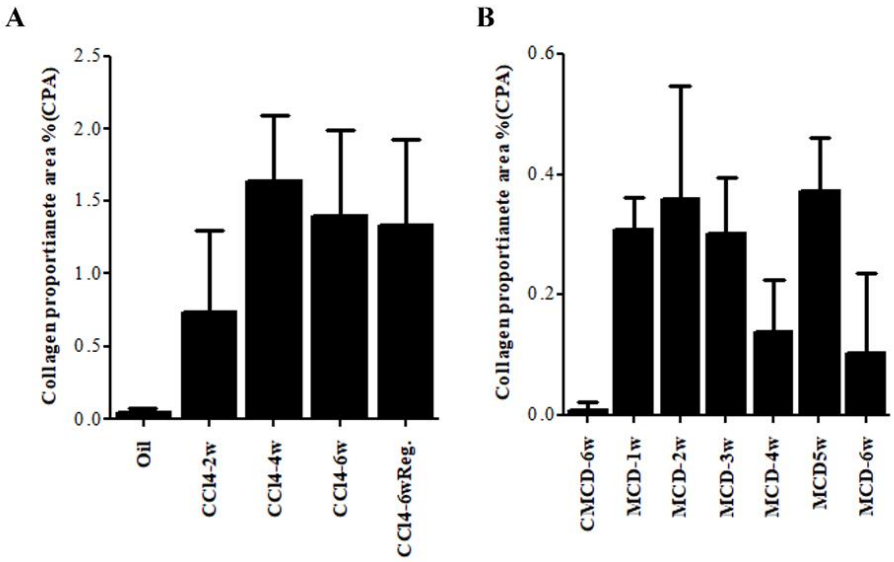

Figure 3.77 2D quantification of liver fibrosis in mouse samples using histological slides. CPA analyses were performed in CCl4 and MCD animal models. The fibrosis content was increased as the injury progressed over weeks. The five groups of CCl4

model were included in this experiment and compared to the Oil group (A). We also saw a decline in the recovery group of CCl4 which we expected. The seven groups of MCD animal model were included in this experiment (B). The content was mildly increased possibly due to the regenerative ability of the liver. CCl4: Carbon tetrachloride, CMCD: Control Methionine Choline Deficient, MCD: Methionine Choline Deficient, CCl4-Reg: Recovery group from CCl4.

3.4.2 3D quantification of liver fibrosis

Quantification of liver fibrosis in CLARITY-processed samples was performed utilizing the CPA analysis approach. We acquired multiple optical sections of whole biopsy samples or biopsy-like tissues using a slide-free technique. The CPA analysis was conducted manually using Image J software for the quantification from 2D histological sections. However, whole biopsy imaging with custom LSFM resulted in multiple sections; therefore, we automatized the CPA analysis by generating an analysis code. The calculated CPA from every section of a whole liver biopsy was used to conclude a Collagen proportionate volume (CPV) score, which referred to a 3D analysis of liver fibrosis. Additionally, we used the same analysis to quantify Elastin protein. The Elastin proportionate area (EPA) scores of each section were used to conclude an Elastin proportionate volume (EPV). We analysed 197 ±100 slices of each sample to calculate CPV or EPV. The fibrosis amount was calculated for each patient using volumetric imaging data. The standard deviations between the slices were also calculated for every patient's imaging data. There are two major differences between 2D and 3D quantification of liver fibrosis. The first one is the lacking subtraction of structural collagens from the fibrosis area due to the intense staining of collagen fibers in the 3D quantification method. The latter is the analysis of only one slice for measuring fibrosis from histology slides in the 2D semi-quantification method. In our methodology, we created a system which is specifically suitable for clinical samples for comprehensive analysis of fibrosis.

To accurately quantify fibrosis in CLARITY-processed samples, we determined the contrast enhancement ratio for every imaging data before running a CPA/EPA analysis. Moreover, some of the staining data were required background subtraction. We improved our analysis code to quantify fibrosis in samples which requires further processing.

In this study, we focused on the quantification of liver fibrosis using a slide-free approach in NAFLD. We recruited patients who underwent liver biopsy procedure due to NASH and their samples were cleared using the modified-CLARITY method. Since we had only a biopsy to stain for fibrosis quantification, we stained them against Collagen type I protein. However, non-fibrotic and explant samples were stained separately against Collagen type I and Elastin protein.

Table 3.1 Patients demographic table

Baseline Characteristics of NAFLD (NAFLD)		
Age (year)	mean ± 95%CI	53.21 (49.82-56.60)
Gender (male/female)	n (%)	39 (68.4%) / 18 (31.6%)
BMI (kg/m^2)	mean ± 95%CI	27.83 (26.06-29.61)
Diabetes (yes/no)	n (%)	23 (46%) / 27 (54%)
Albumin (g/dL)	mean ± 95%CI	3.97 (3.73-4.21)
ALT (IU/L)	mean ± 95%CI	40.34 (32.71-47.97)
AST (IU/L)	mean ± 95%CI	35.25 (29.37-41.13)
Platelets (x10^9)	mean ± 95%CI	165.6 (144.8-186.4)
Fibrosis Stage	n (%)	
0		1 (1.8%)
1		21 (36.8%)
2		5 (8.8%)
3		11 (19.3%)
4		19 (33.3%)

Baseline Characteristics of Viral cohort		
Age (year)	mean ± 95%CI	55.73 (53.34-58.12)
Gender (male/female)	n (%)	36 (87.8%) / 5 (12.2%)
BMI (kg/m^2)	mean ± 95%CI	27.54 (26.28-28.80)
Diabetes (yes/no)	n (%)	13 (31.7%) / 28 (68.3%)
Albumin (g/dL)	mean ± 95%CI	3.43 (3.20-3.66)
ALT (IU/L)	mean ± 95%CI	55.85 (38.40-73.31)
AST (IU/L)	mean ± 95%CI	72.41 (50.62-94.19)
Platelets (x10^9)	mean ± 95%CI	112.9 (90.18-135.7)
Fibrosis Stage	n (%)	
0		0 (0%)
1		1 (2.4%)
2		3 (7.3%)
3		3 (7.3%)
4		34 (82.9%)

Baseline Characteristics of Non-fibrotic cohort		
Age (year)	mean ± 95%CI	56.28 (47.45-64.72)
Gender (male/female)	n (%)	8 (66.6%) / 4 (33.3)
BMI (kg/m^2)	mean ± 95%CI	22.94 (21.33-24.55)
Albumin (g/dL)	mean ± 95%CI	4 (3.66-4.34)
ALT (IU/L)	mean ± 95%CI	25 (15.68-34.32)
AST (IU/L)	mean ± 95%CI	26.33 (20.15-32.51)
Platelets (x10^9)	mean ± 95%CI	213.1 (144-282.2)

NAFLD; Non-alcoholic fatty liver disease, BMI; Body mass index, ALT; Alanine aminotransferase, AST; Aspartate aminotransferase

Afterwards, we calculated CPV and EPV values for every sample to show the relationship between fibrosis stages and fibrosis contents (**Figure 3.75**).

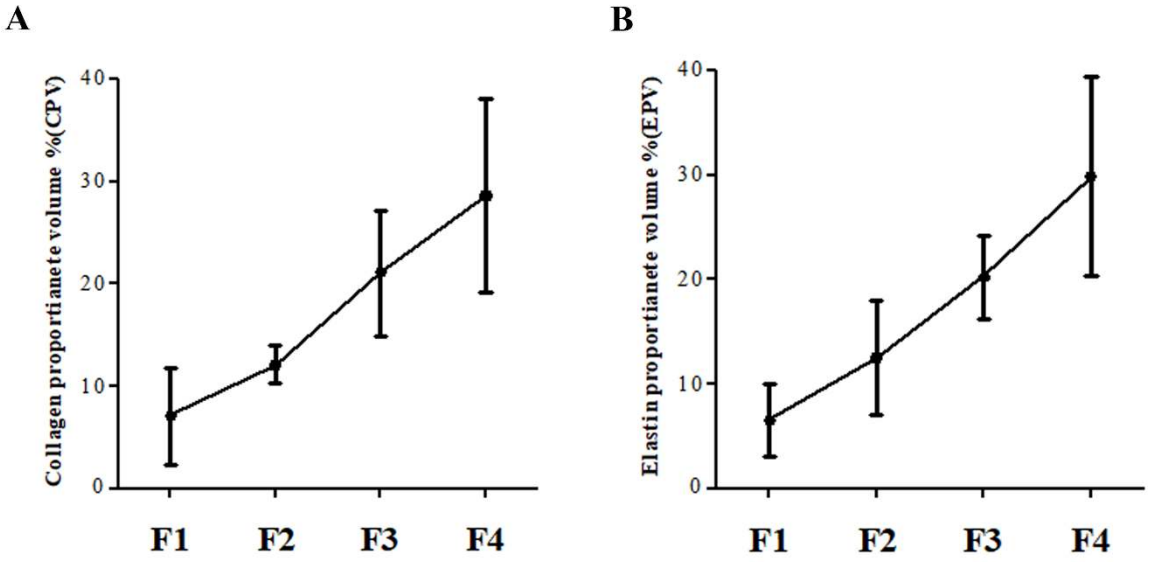

Figure 3.78 CPV and EPV correlation with fibrosis stages in NAFLD. The calculated CPV values from various fibrosis stages of NAFLD showed a non-linear relationship as the disease progresses (A). Similarly, the EPV values from various fibrosis stages of NAFLD showed a non-linear relationship as the disease progresses (B).

Afterwards, we compared the 3D ECM staining with the 2D Sirius Red histological fibrosis staining. We showed an increase in ECM protein expression as the disease progresses. We also compared the method's compatibility with the staining of perisinusoidal, periportal areas, bridging fibrosis and cirrhosis with 2D histological fibrosis staining. The 3D images from various fibrosis stages showed a significant increase in Collagen type I and Elastin expressions as the disease progressed (**Figure 3.79 and Figure 3.80**). We used corresponding Sirius Red stained histological sections for the comparison with 3D images acquired with custom LSFM.

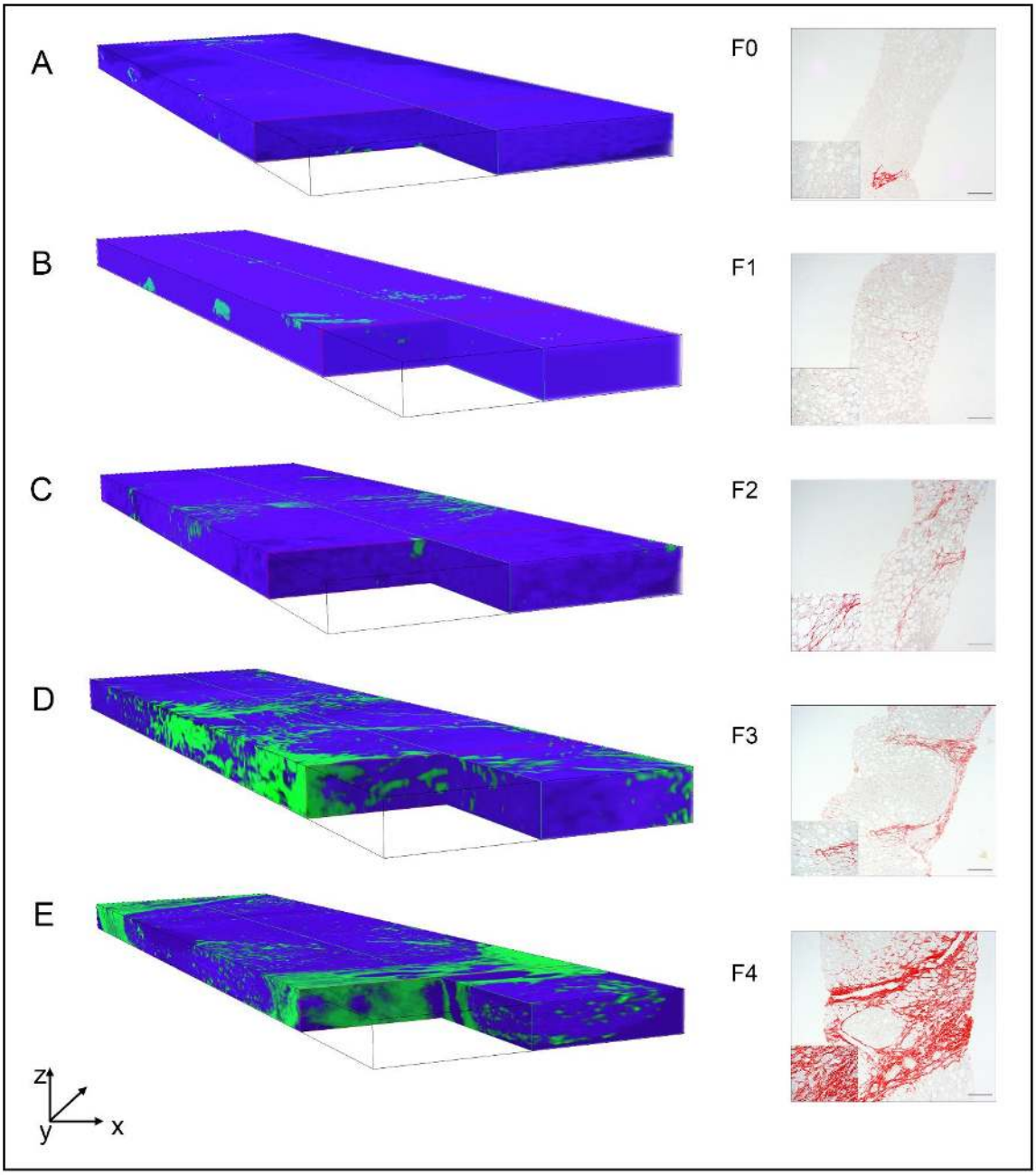

Figure 3.79 Comparison of Collagen type I stained 3D stacks from CLARITY-processed biopsy samples with corresponding 2D Sirius red stained liver sections. Staining Collagen type I (Green) and nuclei (Blue) in CLARITY-processed samples significantly show increasing fibrosis areas with the disease progression. 3D representation of stacks from F0 (A), F1 (B), F2 (C), F3 (D) and F4 (E) stage liver biopsy samples and their comparison with 2D Sirius Red staining were shown (scale bar: 200 µm, left-bottom images are captured with 40x magnification objective). *A: z=1 mm, y=1.4 mm, *B: z=800 µm, y=1.4 mm, *C: z=830 µm, y=1.4 mm, *D: z=750 µm, y=1.4 mm, *E: z=1400 µm, y=1.4 mm.

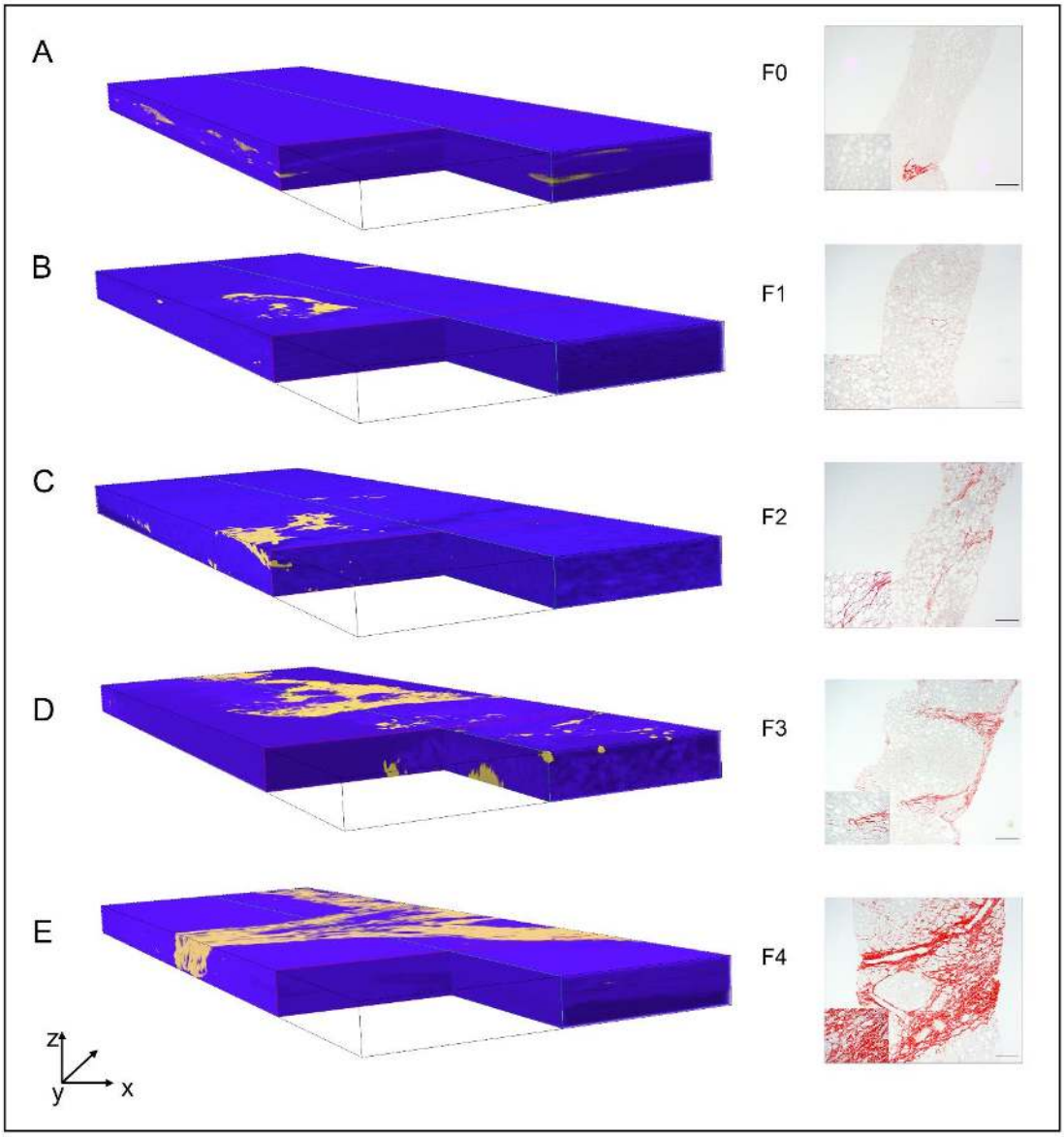

Figure 3.80 Comparison of Elastin stained 3D stacks of CLARITY-processed biopsy samples with corresponding 2D Sirius red stained liver sections. Staining Elastin (Yellow) and nuclei (Blue) in CLARITY-processed samples show significantly increasing fibrosis areas with the disease progression. 3D representation of stacks from F0 (A), F1 (B), F2 (C), F3 (D) and F4 (E) stage liver biopsy samples and their comparison with 2D Sirius Red staining (scale bar: 200 µm, left-bottom images are captured with 40x magnification objective). *A: z=1 mm, y=1.4 mm, *B: z=730 µm, y=1.4 mm, *C: z=700 µm, y=1.4 mm, *D: z=970 µm, y=1.4 mm, *E: z=1200 µm, y=1.4 mm.

3.5 Volumetric image analysis in NAFLD

We observed differential fibrosis contents in volumetric imaging data of CLARITY-processed liver tissues. Then, we consulted our expert pathologist to assess three different slices of F3 stage patients' samples who underwent liver transplantation surgery even if they had F3 stage fibrosis. The pathologist assessed the fibrosis stages of each slice differently. The results confirmed our observation of the sectional variability in NAFLD. The patient was scored as bridging fibrosis using 2D histological sections; however, three different optical slices were scored as F2, F3 and F4.

Further, we expanded the analysis of sectional variability by performing a histogram analysis of each fibrosis group. The histogram analyses revealed a high distribution of fibrosis content within a given tissue and emphasised the overlap in F3 and F4 stage fibrosis content (**Figure 3.81**). Then, we analysed multi-sectional imaging data results (CPV and EPV) by performing interquartile range (IQR) measurement. The IQR analysis showed that the nonlinear relationship between fibrosis stages and contents was still preserved (**Figure 3.82**). Notably, the IQR analysis showed variations between each fibrosis stage. Then, the variation was confirmed with the coefficient of variation (CV) analysis. The CV is the ratio of the standard deviation to the mean. We calculated the CV values of each sample using the standard deviation between the slices and the mean of the CPA- and EPA-performed slices. The high CV values refer to the high level of variation. The CV values were calculated using CPV/EPV values, and standard deviations between slices were expressed as a percentage to determine the extent of variations in fibrosis groups. The CV values of fibrosis groups (F1-2 and F3-4) were specified using the group mean of CV and group standard deviation of CV. Based on the published CV classification studies, three categories (low, intermediate, and high) were determined to classify CV values in fibrosis groups (Vaz et al., 2017). We found 84.6% and 95% intermediate or high levels of coefficient of variation in CPV and EPV samples of the F3-4 fibrosis stage of NAFLD, respectively. The coefficient of variation analysis confirmed the significance of sectional variation (**Figure 3.82**).

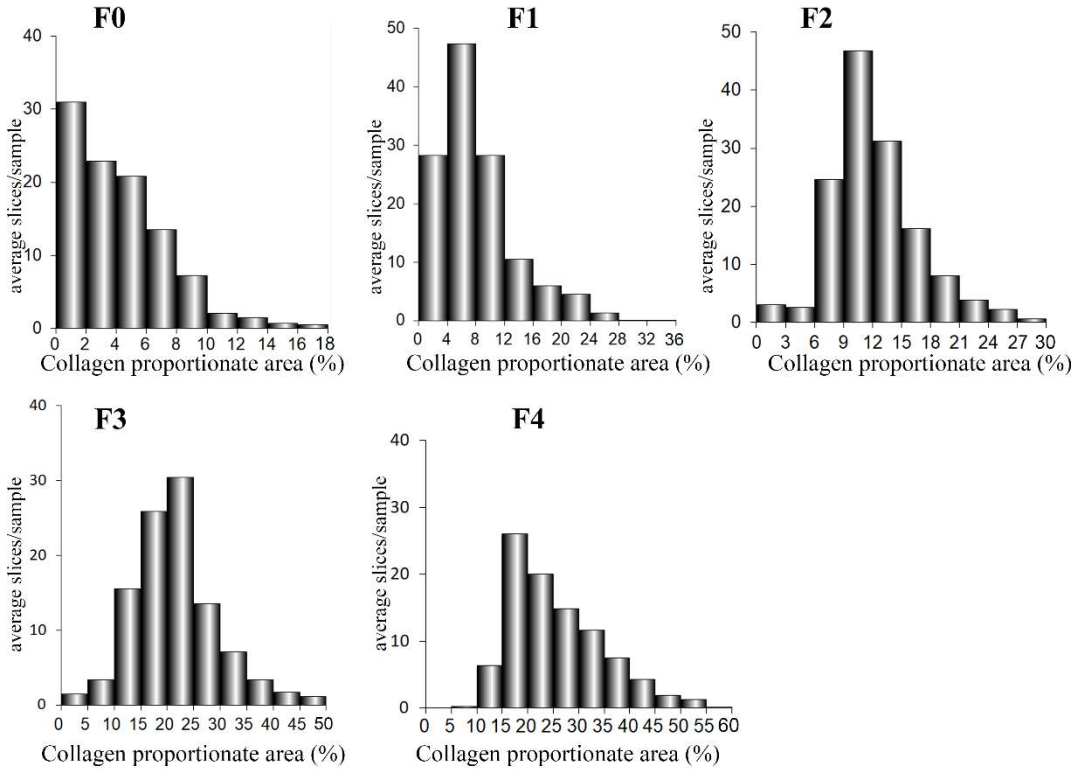

Figure 3.81 The histogram analysis of Collagen type I staining in CLARITY-processed liver tissues reveals extensive fibrosis heterogeneity between optical sections in NAFLD. Histogram analysis showed the distribution of average CPA-performed optical sections per whole biopsy samples in F0, F1, F2, F3 and F4 stage fibrosis groups of NAFLD.

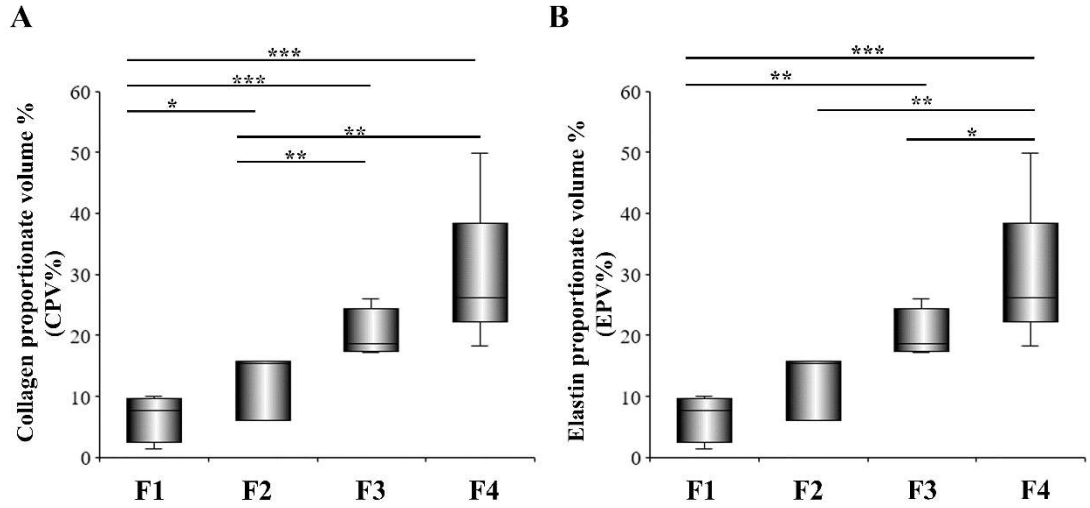

Figure 3.82 The IQR measurement of CPV and EPV values in various fibrosis stages of NAFLD. The measurement of spread with IQR analysis of CPV (A) and EPV (B) values was performed in the NAFLD cohort. The statistical analysis was performed using CPV and EPV group means. IQR: interquartile range; *p ≤ 0.05, **p ≤ 0.01, ***p ≤ 0.001.

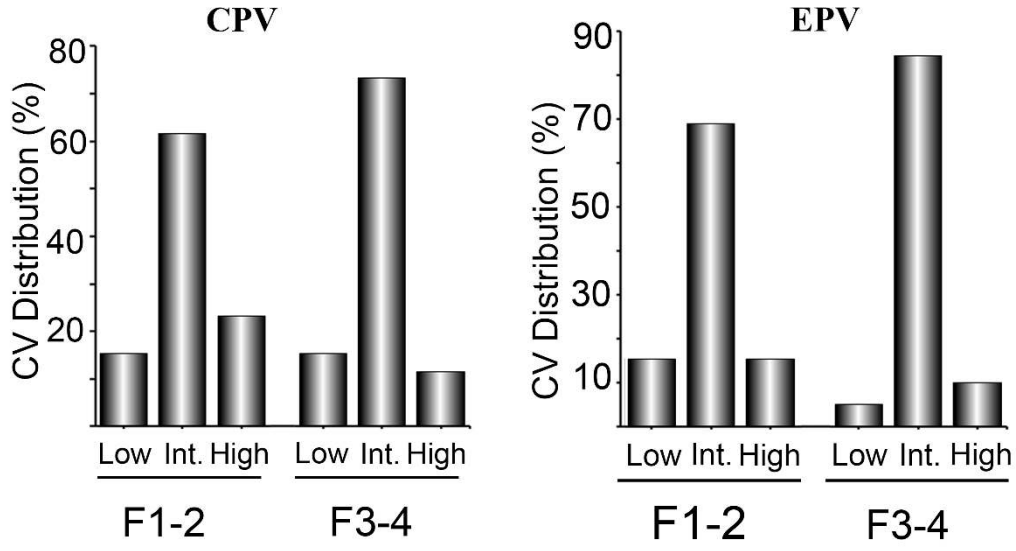

Figure 3.83 Coefficient of variation analysis in CPV and EPV samples of NAFLD. The CV analysis confirmed our observation of sectional variation in CPV and EPV samples of NAFLD. Int: Intermediate; Coefficient of variation: CV

The variation levels in the early stages were also high; however, since the means of the samples are close to 1, the coefficient of variation analysis is not reliable. Therefore, we focused on the F3-4 stage of fibrosis groups of NAFLD and compared

the variation levels with the viral cohort. When we checked the coefficient of variation and IQR measurement, we did not observe any significant difference between the aetiologies (**Figure 3.84**). The variation level increase was mildly higher in the NASH cohort compared to the viral cohort. Consequently, the sectional variation could be present in advanced stages of liver fibrosis with any chronic liver disease.

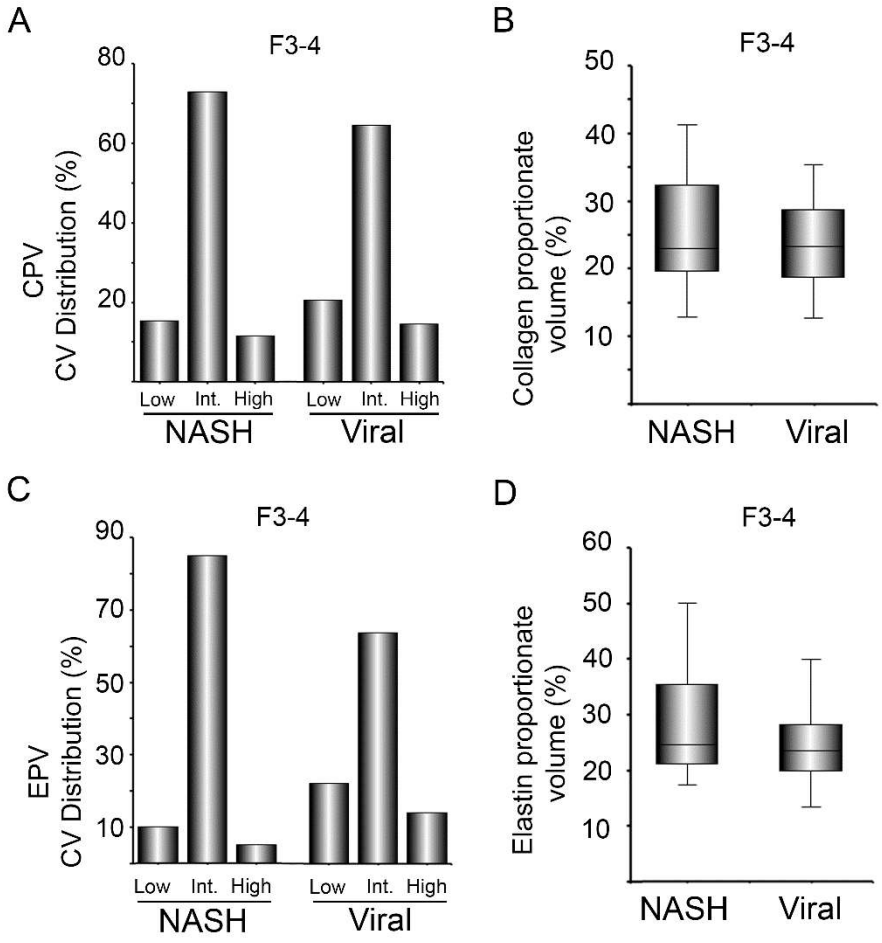

Figure 3.84 Comparison of sectional variation with other aetiologies. The sectional variation was compared with the viral hepatitis cohort for CPV samples using the coefficient of variation (A) and IQR measurement (B). The variation levels were mildly high in NASH cohort compared to viral cohort. Additionally, EPV samples of NASH and viral hepatitis cohorts were compared using the coefficient of variation (C) and IQR measurement (D).

3.6 Establishing cut-off values for three-dimensional fibrosis staging in NAFLD

We determined cut-off values to constitute a basis of three dimensional fibrosis staging. Therefore, we optimized cut-off values for CPA, CPV and EPV for 2D and 3D fibrosis staging, respectively. We determined a CPA cut-off for our cohort to quantification of fibrosis in 2D. The CPA, CPV and EPV cut-off values for the fibrosis stages were derived from the area below the receptor operator curve (AUROC). The best fit cut-off values were decided according to the Youden index (≥50%) (**Table 3.2**). The AUROC of CPA cut-offs used are F1:0.89 ($p<0.001$, 95% CI 0.78-1.00), F2:0.87 ($p<0.05$, 95% CI 0.67-1.07), F3:0.71 ($p=0.205$, 95% CI 0.36-1.05), F4: 0.93 ($p<0.001$, 95% CI 0.84-1.02). The AUROC of CPV cut-offs are F1:0.64 ($p=0.151$, 95% CI 0.46-0.83), F2:0.86 ($p<0.05$, 95% CI 0.71-1.01), F3:0.95 ($p<0.01$, 95% CI 0.85-1.06) and F4:0.73 ($p<0.05$, 95% CI 0.53-0.94). The AUROC of EPV cut-offs are F1:0.62 ($p=0.324$, 95% CI 0.37-0.87), F2:0.80 ($p= 0.128$, 95% CI -0.45-1.14), F3:1 ($p= 0.033$, 95% CI 1-1), F4:0.85 ($p<0.05$, 95% CI 0.63-1.08).

Table 3.2 Determined cut-off values for NAFLD

Fibrosis stage	CPA Cut-off	CPV Cut-off	EPV Cut-off
1	$2.3 \leq F1 \leq 7.7$	$4.3 \leq F1 \leq 8.7$	$5.4 \leq F1 \leq 9.8$
2	$7.7 < F2 \leq 13.2$	$8.7 < F2 \leq 17.7$	$9.8 < F2 \leq 16.6$
3	$13.2 < F3 \leq 23.7$	$17.7 < F3 \leq 24.7$	$16.6 < F3 \leq 26.9$
4	$23.7 < F4$	$24.7 < F4$	$26.9 < F4$

Then, we applied CPV and EPV cut-off values to the multiple sections from various fibrosis stages of NAFLD. According to the volumetric image analysis, the results indicated that 44% in F3 and 47% in F4 stage fibrosis would be the same (**Figure 3.85**). More clearly, the pathology report of liver biopsy staging might be correct under a 50% chance. This analysis evidently suggests that fibrosis assessment should be performed in 3D.

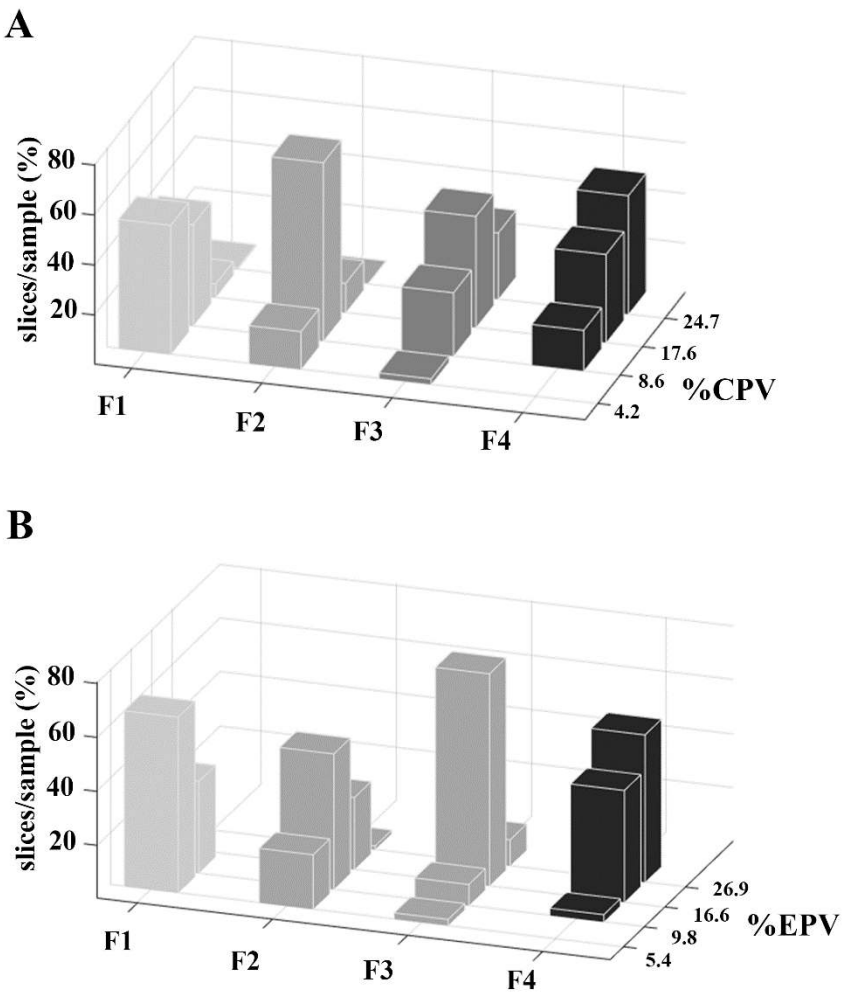

Figure 3.85 Assessment of fibrosis in NAFLD cohort using determined cut-off values for CPV and EPV. The established cut-off values for CPV (A) and EPV (B) were used to assess fibrosis in multiple optical sections of liver tissues from the NAFLD cohort. The results showed that 44% and 47% of F3 and F4 stage fibrosis would be staged at the same according to the volumetric analysis of liver fibrosis using a slide-free platform, respectively.

Chapter 4: Discussion

Accurate assessment of the liver fibrosis stage is an important instrument in management of chronic liver diseases. To date, the liver biopsy procedure is the gold standard for evaluating pathological features, diagnosis and grading the disease of any type of chronic liver injury. However, the procedure has several limitations, including sampling error, observer variability and semi-quantitative assessment. Evaluating the liver biopsy based on the assumption that small tissue fragments represent overall hepatic injury is challenging. Given biopsy samples represent 1/50000 of the total mass of the liver, which leads to a substantial possibility of sampling error. This proportion represents to 1% of total liver mass when 5 μm thickness of biopsy tissue is evaluated for fibrosis staging. The primary consideration of the presence of sampling error is the heterogeneous distribution of pathological features throughout the liver. A study demonstrated the difference in histological grading and staging between liver biopsy samples taken from the right and left lobes of the liver in Hepatitis C patients (Regev et al., 2002). The liver biopsy procedure is heavily used in diagnosing and staging NAFLD since there are no sufficient non-invasive tests for NASH yet available. Ratziu et al. demonstrated the effect of sampling error on NAFLD diagnosis and staging by collecting paired percutaneous liver biopsy samples from the patients (Ratziu et al., 2005). They reported that 41% discordance rate between the 2 biopsy samples and at least 1 stage difference. Notably, 12% of patients in one sample had no or mild fibrosis, while bridging fibrosis was found in the other, which had advanced stage fibrosis. Based on the publications, the discordance in the fibrosis staging may affect the significant outcome of NASH clinical trials. There is an unmet need for new modalities to assess the fibrosis stage accurately.

Combining cutting-edge imaging techniques, such as light sheet microscopy, with tissue clearing methods can improve conventional histology and provide comprehensive information. CLARITY is the pioneer method in the hydrogel embedding-based tissue clearing technique, which crosslinks macromolecules to the tissue-hydrogel hybrid to preserve the molecular information along the process (Tomer et al., 2014). Based on the CLARITY method, we optimized a method for liver tissues from various fibrosis stages of NAFLD and developed a custom-light-sheet fluorescence microscope, particularly for clinical samples. At the beginning of this

study, establishing a sample embedding method for light sheet imaging was challenging. Unfortunately, commercially available imaging systems do not have compatible embedding methods with clinical samples (Laroche et al., 2019). Therefore, establishing the best way to embed samples took a substantial time in the project. Consequently, a study inspired us to develop our sample embedding method using affordable glassware in the lab (Ding et al., 2018). The embedding environment should have matched the refractive index with cleared tissues. Finding a compatible embedding solution or chemical was also challenging. Even though there is a recipe for a suitable refractive index matching solution, we did not have the chemical in our stocks. Therefore, we adjusted the recipe and generated a new formulation for RIMs. RIMs is an important reagent for tissue clearing experiments since it is used as an equilibration of the refractive index within the tissue. Refractive index mismatch may create blurry images due to the scattering light and decrease the resolution (Diaspro et al., 2002).

Another critical element of this platform is sample holders. Since the sample holder will hold and move the sample along the light sheet with indicated directions, compatibility and design are extremely important. In the prototype of LSFM, the sample holder was in an L shape, limiting the objective movements in the y direction. I did not insist that this is the perfect shape for the sample holder, then suggested my design was suitable with the objective edges and did not limit the movement in the y direction. We used 3D printers for all custom-design sample holders and cages. Sample cage design is as important as sample holder design which determines the limits of the stage controller. Also, the light absorbance properties of the sample holder and cage material should not affect the imaging quality. Initially, we used a plexiglass sample cage and holder, then adjusted the material with ABS plastic (3D printer filament) which did not have detrimental effects on imaging. Plexiglass material interfered with the light and fluorescence signal of the tissue; therefore, we did not continue to use it. However, the enlargement of the sample holder after using it several times is a significant limitation of the design. Since the sample holder keeps the borosilicate tube aligned, it should not move while the stage controller changes its direction. Therefore, we use parafilm sheets to keep the tubes steady along the imaging process. However, we printed sample holders after they were overused for the imaging experiment.

Another limitation of the system we used in this study is the relatively high inertia of the fast-moving filter wheel. It caused self- oscillations as the rotating servo continuously overshot/undershot around the proper filter position. However, the servo

motor occasionally produces oscillations which affect the sample holder, objective, and camera. Due to this error in the system, images become flickering. As a first troubleshooting, we changed the old servo motor with a new one. Sometimes, we encountered this problem in the middle of the imaging experiment and were required to start imaging again. Recently, we tried another way to solve this error. We have introduced a slight friction to the movement of the wheel in order to dampen the oscillations. However, it may lead to another problem. Dust and microparticles are generated due to the contact. They might fall in the glycerol solution in the cage because particles inside the glycerol solution increase when we use the same solution for imaging experiments. Moreover, they interfere with the light sheet, resulting in image blurriness and the prevention of illumination of the samples. As a solution, we filtered glycerol solution and then used it again for other imaging experiments. Nevertheless, a permanent solution can be a closed sample cage or a more compatible emission filter wheel for the system.

One of the significant challenges is finding suitable commercial antibodies for ECM staining in cleared liver tissues. We aimed to detect more than one protein within a liver tissue simultaneously. However, since we could not find a suitable antibody, we were not able to achieve this due to the antibody limitation. We attempted various combinations of blocking reagents or antibody concentrations to increase the antibodies' specificity. Unfortunately, we optimized a limited number of antibodies for ECM proteins in cleared human liver tissues. Even though we quantify two major ECM proteins in human liver tissue separately, we discovered substantial information to quantify liver fibrosis accurately. Simultaneous detection of ECM proteins, such as Collagen type I and III, may result in other significant outcomes. As an alternative technique, primary commercial antibodies can be conjugated with fluorescent tags after simple incubation steps using iFluor antibody conjugation kits. This approach may increase the staining efficiency and shorten the staining time of the targeted protein (AAT Bioquest).

Additionally, a recently published study suggested using a fluorescent analogue of haematoxylin and eosin (H&E), routinely used chemical dyes in pathology (Serafin et al., 2020). This important study implies the clinical adoption of fluorescence-based 3D pathology techniques. It creates grayscale fluorescence images that mimic the appearance of standard H&E. We can apply this approach to CLARITY-processed liver tissues and provide other disease-specific structures and ECM quantification.

Histopathological alterations are assessed from 2D slide-based H&E images in the liver. Evaluation of disease characteristic patterns, such as steatosis, hepatocyte ballooning and inflammation, are examined through H&E images. Therefore, using this approach may improve the study outcome for NAFLD patients. A recent study used a machine learning approach to assess liver histology and characterize disease severity and heterogenicity to sensitively quantify treatment response in NASH (Taylor-Weiner et al., 2021). In this study, their machine learning model revealed heterogeneity of fibrosis in advanced stages (F3-4) even within patients. Their model observed differential fibrosis areas within the section corresponding to lower or higher fibrosis stages. Consequently, this study supports our observation of sectional variation in NASH liver fibrosis tissues.

When liver tissues are processed with the modified-CLARITY method, quantifying hepatic fibrosis is accomplishable throughout the specimen. We quantified the most abundant ECM proteins, collagen type I and elastin, in liver tissues of various fibrotic stages of NAFLD. Comparison of 3D volumetric images with 2D Sirius red stained histological sections showed the specificity of the method as the fibrosis progresses. However, when multiple optical sections are measured regarding fibrosis areas, a substantial heterogenicity of fibrosis was observed. This is an important outcome that reveals the extent of fibrosis distribution within the biopsy samples. Liver biopsy procedure is an imperfect gold standard due to the estimation of disease severity from a small tissue fragment. Fibrosis stage assessment relies on the semi-quantitative evaluation of 2D histological slides, and the pathologist estimates the severity of the fibrosis using one section. Indeed, these limitations may decrease the accuracy of the determined fibrosis stage. However, quantifying multiple sections and concluding a fibrosis stage according to 3D volumetric analysis may improve staging accuracy.

Histogram analysis of each fibrosis stage group revealed the extent of fibrosis within the given tissues. We calculated average slices per sample, which shows the distribution of CPA-performed optical sections throughout the specimen. This analysis showed the variation in liver tissue simply by a histogram analysis using volumetric imaging. Notably, this analysis emphasized the overlap in F3 and F4 stage fibrosis groups. The histogram graph followed similar patterns with close CPA values in both stages. Even though there are variations within liver biopsy itself, there is also patient-to-patient variation. Notably, the progression rate of fibrosis varies between individuals. Sanyal et al. reported a rapid progression of bridging fibrosis to cirrhosis in 29 months

of a clinical trial (Sanyal et al., 2019). Further, we performed IQR analysis to see the spread of CPV/EPV values within the group of fibrosis stages. The range of CPV values was high in the advanced stage of fibrosis. Then, we calculated the extent of variation using CV analysis for each sample and determined the level of variation based on the cut-off values of the F1-2 and F3-4 fibrosis groups. When we assessed the CV distributions of fibrosis groups, there was more than 80% high and intermediate level of variations in advanced stage fibrosis. CV analysis determines the level of variation sample by sample using each sample's standard deviation and mean. Therefore, the analysis emphasized that section-to-section variation is substantially high in advanced fibrosis stages.

Quantitative assessment of liver fibrosis is an important issue when concluding a fibrosis stage. Current classification systems semi-quantitatively assess liver fibrosis which is one of the significant limitations of the liver biopsy procedure. Standish et al. proposed a method that measures fibrosis areas in biopsy sections and showed a nonlinear increase in fibrosis content as the disease progresses (Standish et al., 2006). This method gives the proportional area of fibrosis content to the whole section by excluding structural collagens, veins, and lumens. Several studies reported CPA cut-off values for 2D liver fibrosis quantification in different aetiologies (Buzzetti et al., 2019; Israelsen et al., 2020; Tsochatzis et al., 2014). In this study, we established cut-off values for CPA, CPV and EPV in the NAFLD cohort and performed an analysis using whole optical sections of each sample. The CPA cut-off was determined for 2D fibrosis quantification, CPV and EPV were determined for 3D fibrosis quantification from volumetric imaging data. Notably, cut-off analysis of volumetric imaging data revealed considerable outcomes that show fibrosis is not uniform throughout the specimen, which means that there can be differential fibrosis amounting to different stages of fibrosis. The variation analysis confirmed our observation of sectional variability in NAFLD. Then, we determined our cut-off values for CPV and EPV to stage fibrosis in volumetric imaging data of NAFLD. The volumetric analysis revealed that less than 50% of the optical slices would be classified in the same stage for F3 and F4 patients. Therefore, clinicians may encounter under or over-staging fibrosis due to the substantial overlap in F3 and F4 stage fibrosis when evaluating only one section.

The major limitation of this study is to unable to image more than one protein simultaneously in a biopsy sample. 60-70% of the commercially available antibodies were compatible with the CLARITY method. Therefore, finding suitable antibodies

with specific patterns for our targeted proteins was challenging. We tested the applicability of the modified-CLARITY to animal models of liver fibrosis and managed to optimize the most abundant ECM protein in mouse liver tissues. However, we could not image the groups of animal models due to focusing on the manuscript data. Consequently, we developed a platform to quantify liver fibrosis in clinical samples accurately. However, the lack of morphological evaluations using optical slices was possibly one of the significant limitations of our study. Another limitation of this study is that having a small sample size in the early stages of NAFLD, specifically the F2 stage. The final possible limitation is the lacking data on portal hypertension for F3 and F4 patients to confirm the misdiagnosis of cirrhotic patients. Notably, since we deal with the clearing of tissues with passive CLARITY, clearing time of the procedure is a significant limitation of the study. Although our assessment method is not currently feasible for use in clinical practice due to limitations, it will be the first study to use in 3D imaging to assess liver fibrosis.

Combining new technologies to aid conventional histology in routine practice has a growing interest in recent years. We focused on adapting the CLARITY method and developed custom LSFM to accurately quantify fibrosis in clinical specimens. This study delivered substantial results by utilizing a 3D digital platform for assessing liver fibrosis stages in whole liver biopsy samples. Moreover, it allowed us to quantify fibrosis in multiple optical sections of liver tissues via automatized analysis code. However, implementation of the analysis of other pathological features such as inflammation, steatosis, and hepatocyte ballooning which are the hallmarks of NASH, would be valuable for diagnosis as well. For such analysis, implementing the fluorescent analogue of haematoxylin, i.e., TO-PRO3, analysis of inflammation in cleared liver tissues would result in a significant outcome for this study (Serafin et al., 2020). High magnification objectives can be added to the LSFM system to provide cellular resolution to image other pathological features and cellular proteins.

In conclusion, utilizing such new technologies to improve current histopathological evaluation systems is a significant advancement. This platform provided comprehensive information by mapping the hepatic fibrosis in the entire biopsy sample and revealed a substantial heterogenicity in advanced fibrosis stages in NAFLD. The histological assessment of liver biopsy samples guides the development of anti-fibrotic therapies and non-invasive tests for NASH. Due to the low reliability of the histological classification systems, NASH clinical trials often fails (Davison et al.,

2020). Hence, there is no sufficient non-invasive test or accurate staging system for stratification of NASH patients yet. However, our study may pave the way for improvements in staging inaccuracy to quantify liver fibrosis more precisely.

Chapter 5: Conclusion and Future Perspectives

- Modified-CLARITY method is able to clear human dense fibrotic tissues from various aetiologies.

- We optimized modified-CLARITY method for animal models of liver fibrosis and NASH. We tested the applicability of the procedure to the mice and efficiently cleared whole mouse liver tissues.

- Liver fibrosis can be quantified using modified-CLARITY method in 3D using slide-free approach by custom-made light sheet fluorescence microscopy and may provide hepatic ECM amount within the whole liver tissue.

- The cut-off values were determined for volumetric fibrosis quantification for Collagen type I and Elastin protein using 3D digital pathology platform.

- Custom-made light sheet fluorescence microscopy slide-free imaging of whole liver biopsy specimen and allows accurate quantification of fibrosis.

- Designing sample holders and cages are important elements of a custom-made 3D imaging platform and affect image quality and method reproducibility.

- This method discovered a sectional variation within the biopsy specimens of NAFLD patients and concluded that volumetric imaging is a promising tool for precise quantification of fibrosis.

- A slide-free 3D digital platform can be used for investigating complicated liver pathologies.

References

Abenavoli, L., & Beaugrand, M. (2012). Transient elastography in non-alcoholic fatty liver disease. *Ann Hepatol*, *11*(2), 172-178.

Adams, L. A., Bulsara, M., Rossi, E., DeBoer, B., Speers, D., George, J., . . . Jeffrey, G. P. (2005). Hepascore: An Accurate Validated Predictor of Liver Fibrosis in Chronic Hepatitis C Infection. *Clinical Chemistry*, *51*(10), 1867-1873. https://doi.org/10.1373/clinchem.2005.048389 %J Clinical Chemistry

Agbim, U., & Asrani, S. K. (2019). Non-invasive assessment of liver fibrosis and prognosis: an update on serum and elastography markers. *Expert Rev Gastroenterol Hepatol*, *13*(4), 361-374. https://doi.org/10.1080/17474124.2019.1579641

Aoyagi, Y., Kawakami, R., Osanai, H., Hibi, T., & Nemoto, T. (2015). A Rapid Optical Clearing Protocol Using 2,2′-Thiodiethanol for Microscopic Observation of Fixed Mouse Brain. *PLoS One*, *10*(1), e0116280. https://doi.org/10.1371/journal.pone.0116280

Arteel, G. E., & Naba, A. (2020). The liver matrisome - looking beyond collagens. *JHEP Rep*, *2*(4), 100115. https://doi.org/10.1016/j.jhepr.2020.100115

Barner, L. A., Glaser, A. K., Huang, H., True, L. D., & Liu, J. T. C. (2020). Multi-resolution open-top light-sheet microscopy to enable efficient 3D pathology workflows. *Biomed Opt Express*, *11*(11), 6605-6619. https://doi.org/10.1364/boe.408684

Bataller, R., & Brenner, D. A. (2005). Liver fibrosis. *J Clin Invest*, *115*(2), 209-218. https://doi.org/10.1172/JCI24282

Batts, K. P., & Ludwig, J. (1995). Chronic hepatitis. An update on terminology and reporting. *Am J Surg Pathol*, *19*(12), 1409-1417. https://doi.org/10.1097/00000478-199512000-00007

Bedossa, P. (2016). Histological Assessment of NAFLD. *Dig Dis Sci*, *61*(5), 1348-1355. https://doi.org/10.1007/s10620-016-4062-0

Bedossa, P., & Consortium, F. P. (2014). Utility and appropriateness of the fatty liver inhibition of progression (FLIP) algorithm and steatosis, activity, and fibrosis (SAF) score in the evaluation of biopsies of nonalcoholic fatty liver disease. *Hepatology*, *60*(2), 565-575. https://doi.org/10.1002/hep.27173

Bondini, S., Kleiner, D. E., Goodman, Z. D., Gramlich, T., & Younossi, Z. M. (2007). Pathologic assessment of non-alcoholic fatty liver disease. *Clin Liver Dis*, *11*(1), 17-23, vii. https://doi.org/10.1016/j.cld.2007.02.002

Boursier, J., Vergniol, J., Guillet, A., Hiriart, J. B., Lannes, A., Le Bail, B., . . . de Ledinghen, V. (2016). Diagnostic accuracy and prognostic significance of blood fibrosis tests and liver stiffness measurement by FibroScan in non-alcoholic fatty liver disease. *J Hepatol*, *65*(3), 570-578. https://doi.org/10.1016/j.jhep.2016.04.023

Brunt, E. M., Janney, C. G., Di Bisceglie, A. M., Neuschwander-Tetri, B. A., & Bacon, B. R. (1999). Nonalcoholic steatohepatitis: a proposal for grading and staging the histological lesions. *Am J Gastroenterol*, *94*(9), 2467-2474. https://doi.org/10.1111/j.1572-0241.1999.01377.x

Buzzetti, E., Hall, A., Ekstedt, M., Manuguerra, R., Guerrero Misas, M., Covelli, C., . . . Tsochatzis, E. A. (2019). Collagen proportionate area is an independent predictor of long-term outcome in patients with non-alcoholic fatty liver disease. *Aliment Pharmacol Ther*, *49*(9), 1214-1222. https://doi.org/10.1111/apt.15219

Cai, R., Pan, C., Ghasemigharagoz, A., Todorov, M. I., Förstera, B., Zhao, S., . . . Ertürk, A. (2019). Panoptic imaging of transparent mice reveals whole-body neuronal projections and skull–meninges connections. *Nature Neuroscience*, *22*(2), 317-327. https://doi.org/10.1038/s41593-018-0301-3

Chen, W., Yan, X., Xu, A., Sun, Y., Wang, B., Huang, T., . . . You, H. (2019). Dynamics of elastin in liver fibrosis: Accumulates late during progression and degrades slowly in regression. *J Cell Physiol*, *234*(12), 22613-22622. https://doi.org/10.1002/jcp.28827

Chung, K., Wallace, J., Kim, S. Y., Kalyanasundaram, S., Andalman, A. S., Davidson, T. J., . . . Deisseroth, K. (2013). Structural and molecular interrogation of intact biological systems. *Nature*, *497*(7449), 332-337. https://doi.org/10.1038/nature12107

Costantini, I., Ghobril, J. P., Di Giovanna, A. P., Allegra Mascaro, A. L., Silvestri, L., Müllenbroich, M. C., . . . Pavone, F. S. (2015). A versatile clearing agent for multi-modal brain imaging. *Sci Rep*, *5*, 9808. https://doi.org/10.1038/srep09808

Cui, J., Heba, E., Hernandez, C., Haufe, W., Hooker, J., Andre, M. P., . . . Loomba, R. (2016). Magnetic resonance elastography is superior to acoustic radiation force impulse for the Diagnosis of fibrosis in patients with biopsy-proven nonalcoholic fatty liver disease: A prospective study. *Hepatology*, *63*(2), 453-461. https://doi.org/10.1002/hep.28337

Daniels, S. J., Leeming, D. J., Eslam, M., Hashem, A. M., Nielsen, M. J., Krag, A., . . . George, J. (2019). ADAPT: An Algorithm Incorporating PRO-C3 Accurately Identifies Patients With NAFLD and Advanced Fibrosis. *Hepatology*, *69*(3), 1075-1086. https://doi.org/10.1002/hep.30163

Davison, B. A., Harrison, S. A., Cotter, G., Alkhouri, N., Sanyal, A., Edwards, C., . . . Dittrich, H. C. (2020). Suboptimal reliability of liver biopsy evaluation has implications for randomized clinical trials. *J Hepatol*, *73*(6), 1322-1332. https://doi.org/10.1016/j.jhep.2020.06.025

de Lédinghen, V., & Vergniol, J. (2008). Transient elastography (FibroScan). *Gastroenterol Clin Biol*, *32*(6 Suppl 1), 58-67. https://doi.org/10.1016/s0399-8320(08)73994-0

Diaspro, A., Federici, F., & Robello, M. (2002). Influence of refractive-index mismatch in high-resolution three-dimensional confocal microscopy. *Applied Optics*, *41*(4), 685-690. https://doi.org/10.1364/AO.41.000685

Ding, Y., Bailey, Z., Messerschmidt, V., Nie, J., Bryant, R., Rugonyi, S., . . . Hsiai, T. K. (2018). Light-sheet Fluorescence Microscopy for the Study of the Murine Heart. *J Vis Exp*(139). https://doi.org/10.3791/57769

Dodt, H. U., Leischner, U., Schierloh, A., Jahrling, N., Mauch, C. P., Deininger, K., . . . Becker, K. (2007). Ultramicroscopy: three-dimensional visualization of neuronal networks in the whole mouse brain. *Nat Methods*, *4*(4), 331-336. https://doi.org/10.1038/nmeth1036

Ellis, E. L., & Mann, D. A. (2012). Clinical evidence for the regression of liver fibrosis. *J Hepatol*, *56*(5), 1171-1180. https://doi.org/10.1016/j.jhep.2011.09.024

Erturk, A., Becker, K., Jahrling, N., Mauch, C. P., Hojer, C. D., Egen, J. G., . . . Dodt, H. U. (2012). Three-dimensional imaging of solvent-cleared organs using 3DISCO. *Nat Protoc*, *7*(11), 1983-1995. https://doi.org/10.1038/nprot.2012.119

Fischer, R. S., Wu, Y., Kanchanawong, P., Shroff, H., & Waterman, C. M. (2011). Microscopy in 3D: a biologist's toolbox. *Trends Cell Biol*, *21*(12), 682-691. https://doi.org/10.1016/j.tcb.2011.09.008

Forlano, R., Mullish, B. H., Giannakeas, N., Maurice, J. B., Angkathunyakul, N., Lloyd, J., . . . Manousou, P. (2020). High-Throughput, Machine Learning-Based Quantification of Steatosis, Inflammation, Ballooning, and Fibrosis in Biopsies From Patients With Nonalcoholic Fatty Liver Disease. *Clin Gastroenterol Hepatol*, *18*(9), 2081-2090 e2089. https://doi.org/10.1016/j.cgh.2019.12.025

Friedman, S. L. (2008). Mechanisms of hepatic fibrogenesis. *Gastroenterology*, *134*(6), 1655-1669. https://doi.org/10.1053/j.gastro.2008.03.003

Friedman, S. L. (2010). Extracellular Matrix. In J.-F. Dufour & P.-A. Clavien (Eds.), *Signaling Pathways in Liver Diseases* (pp. 93-104). Springer Berlin Heidelberg. https://doi.org/10.1007/978-3-642-00150-5_6

Fujii, T., Fuchs, B. C., Yamada, S., Lauwers, G. Y., Kulu, Y., Goodwin, J. M., . . . Tanabe, K. K. (2010). Mouse model of carbon tetrachloride induced liver fibrosis: Histopathological changes and expression of CD133 and epidermal growth factor. *BMC Gastroenterology*, *10*(1), 79. https://doi.org/10.1186/1471-230X-10-79

Gailhouste, L., Grand, Y. L., Odin, C., Guyader, D., Turlin, B., Ezan, F., . . . Baffet, G. (2010). Fibrillar collagen scoring by second harmonic microscopy: A new tool in the assessment of liver fibrosis. *Journal of Hepatology*, *52*(3), 398-406. https://doi.org/https://doi.org/10.1016/j.jhep.2009.12.009

Garcia-Tsao, G., Friedman, S., Iredale, J., & Pinzani, M. (2010). Now there are many (stages) where before there was one: In search of a pathophysiological classification of cirrhosis. *Hepatology*, *51*(4), 1445-1449. https://doi.org/10.1002/hep.23478

Glaser, A. K., Reder, N. P., Chen, Y., Yin, C., Wei, L., Kang, S., . . . Liu, J. T. C. (2019). Multi-immersion open-top light-sheet microscope for high-throughput imaging of cleared tissues. *Nature Communications*, *10*(1), 2781. https://doi.org/10.1038/s41467-019-10534-0

Gressner, O. A., Weiskirchen, R., & Gressner, A. M. (2007). Biomarkers of liver fibrosis: Clinical translation of molecular pathogenesis or based on liver-dependent malfunction tests. *Clinica Chimica Acta*, *381*(2), 107-113. https://doi.org/https://doi.org/10.1016/j.cca.2007.02.038

Group, T. F. M. C. S. (1994). Intraobserver and interobserver variations in liver biopsy interpretation in patients with chronic hepatitis C. . *Hepatology*, *20*(1), 15-20.

Guo, Y., Parthasarathy, S., Goyal, P., McCarthy, R. J., Larson, A. C., & Miller, F. H. (2015). Magnetic resonance elastography and acoustic radiation force impulse for staging hepatic fibrosis: a meta-analysis. *Abdominal Imaging*, *40*(4), 818-834. https://doi.org/10.1007/s00261-014-0137-6

Hahn, C., Becker, K., Saghafi, S., Pende, M., Avdibasic, A., Foroughipour, M., . . . Dodt, H. U. (2019). High-resolution imaging of fluorescent whole mouse brains using stabilised organic media (sDISCO). *J Biophotonics*, *12*(8), e201800368. https://doi.org/10.1002/jbio.201800368

Hama, H., Hioki, H., Namiki, K., Hoshida, T., Kurokawa, H., Ishidate, F., . . . Miyawaki, A. (2015). ScaleS: an optical clearing palette for biological imaging. *Nature Neuroscience*, *18*(10), 1518-1529. https://doi.org/10.1038/nn.4107

Hama, H., Kurokawa, H., Kawano, H., Ando, R., Shimogori, T., Noda, H., . . . Miyawaki, A. (2011). Scale: a chemical approach for fluorescence imaging and reconstruction of transparent mouse brain. *Nature Neuroscience*, *14*(11), 1481-1488. https://doi.org/10.1038/nn.2928

Henning, Y., Osadnik, C., & Malkemper, E. P. (2019). EyeCi: Optical clearing and imaging of immunolabeled mouse eyes using light-sheet fluorescence

microscopy. *Exp Eye Res*, *180*, 137-145. https://doi.org/10.1016/j.exer.2018.12.001

Hou, B., Zhang, D., Zhao, S., Wei, M., Yang, Z., Wang, S., . . . Jiang, T. (2015). Scalable and DiI-compatible optical clearance of the mammalian brain [Methods]. *9*. https://doi.org/10.3389/fnana.2015.00019

Iredale, J. P., Thompson, A., & Henderson, N. C. (2013). Extracellular matrix degradation in liver fibrosis: Biochemistry and regulation. *Biochim Biophys Acta*, *1832*(7), 876-883. https://doi.org/10.1016/j.bbadis.2012.11.002

Ishak, K., Baptista, A., Bianchi, L., Callea, F., De Groote, J., Gudat, F., . . . et al. (1995). Histological grading and staging of chronic hepatitis. *J Hepatol*, *22*(6), 696-699. https://doi.org/10.1016/0168-8278(95)80226-6

Israelsen, M., Guerrero Misas, M., Koutsoumourakis, A., Huang, Y., Thiele, M., Hall, A., . . . Tsochatzis, E. A. (2020). Collagen proportionate area predicts clinical outcomes in patients with alcohol-related liver disease. *Aliment Pharmacol Ther*, *52*(11-12), 1728-1739. https://doi.org/10.1111/apt.16111

Jing, D., Zhang, S., Luo, W., Gao, X., Men, Y., Ma, C., . . . Zhao, H. (2018). Tissue clearing of both hard and soft tissue organs with the PEGASOS method. *Cell Research*, *28*(8), 803-818. https://doi.org/10.1038/s41422-018-0049-z

Ke, M.-T., Fujimoto, S., & Imai, T. (2013). SeeDB: a simple and morphology-preserving optical clearing agent for neuronal circuit reconstruction. *Nature Neuroscience*, *16*(8), 1154-1161. https://doi.org/10.1038/nn.3447

Khalifa, A., & Rockey, D. C. (2020). The utility of liver biopsy in 2020. *Curr Opin Gastroenterol*, *36*(3), 184-191. https://doi.org/10.1097/MOG.0000000000000621

Kim, M. Y., Cho, M. Y., Baik, S. K., Park, H. J., Jeon, H. K., Im, C. K., . . . Lee, S. S. (2011). Histological subclassification of cirrhosis using the Laennec fibrosis scoring system correlates with clinical stage and grade of portal hypertension. *J Hepatol*, *55*(5), 1004-1009. https://doi.org/10.1016/j.jhep.2011.02.012

Kim, S.-Y., Cho, J. H., Murray, E., Bakh, N., Choi, H., Ohn, K., . . . Chung, K. (2015). Stochastic electrotransport selectively enhances the transport of highly electromobile molecules. *112*(46), E6274-E6283. https://doi.org/doi:10.1073/pnas.1510133112

Kleiner, D. E., Brunt, E. M., Van Natta, M., Behling, C., Contos, M. J., Cummings, O. W., . . . Nonalcoholic Steatohepatitis Clinical Research, N. (2005). Design and validation of a histological scoring system for nonalcoholic fatty liver disease. *Hepatology*, *41*(6), 1313-1321. https://doi.org/10.1002/hep.20701

Klingberg, A., Hasenberg, A., Ludwig-Portugall, I., Medyukhina, A., Mann, L., Brenzel, A., . . . Gunzer, M. (2017). Fully Automated Evaluation of Total Glomerular Number and Capillary Tuft Size in Nephritic Kidneys Using Lightsheet Microscopy. *J Am Soc Nephrol*, *28*(2), 452-459. https://doi.org/10.1681/ASN.2016020232

Knodell, R. G., Ishak, K. G., Black, W. C., Chen, T. S., Craig, R., Kaplowitz, N., . . . Wollman, J. (1981). Formulation and application of a numerical scoring system for assessing histological activity in asymptomatic chronic active hepatitis. *Hepatology*, *1*(5), 431-435. https://doi.org/10.1002/hep.1840010511

Kutami, R., Girgrah, N., Wanless, I. R., Sniderman, K. W., Wong, F., Sherman, M., . . . Lilly, L. B. (2000). The Laennec grading system for assessment of hepatic fibrosis Validation by correlation with wedged hepatic vein pressure and clinical features.

Kuwajima, T., Sitko, A. A., Bhansali, P., Jurgens, C., Guido, W., & Mason, C. (2013). ClearT: a detergent- and solvent-free clearing method for neuronal and non-neuronal tissue. *Development*, *140*(6), 1364-1368. https://doi.org/10.1242/dev.091844

Lachowski, D., Cortes, E., Rice, A., Pinato, D., Rombouts, K., & Del Rio Hernandez, A. (2019). Matrix stiffness modulates the activity of MMP-9 and TIMP-1 in hepatic stellate cells to perpetuate fibrosis. *Sci Rep*, *9*(1), 7299. https://doi.org/10.1038/s41598-019-43759-6

Laroche, T., Burri, O., Dubey, L. K., & Seitz, A. (2019). Development of Sample-Adaptable Holders for Lightsheet Microscopy [Protocols]. *13*. https://doi.org/10.3389/fnana.2019.00026

Lee, E., Choi, J., Jo, Y., Kim, J. Y., Jang, Y. J., Lee, H. M., . . . Sun, W. (2016). ACT-PRESTO: Rapid and consistent tissue clearing and labeling method for 3-dimensional (3D) imaging. *Scientific Reports*, *6*(1), 18631. https://doi.org/10.1038/srep18631

Lee, J., Vali, Y., Boursier, J., Spijker, R., Anstee, Q. M., Bossuyt, P. M., & Zafarmand, M. H. (2021). Prognostic accuracy of FIB-4, NAFLD fibrosis score and APRI for NAFLD-related events: A systematic review. *Liver Int*, *41*(2), 261-270. https://doi.org/10.1111/liv.14669

Leroy, V., Sturm, N., Faure, P., Trocme, C., Marlu, A., Hilleret, M. N., . . . Zarski, J. P. (2014). Prospective evaluation of FibroTest(R), FibroMeter(R), and HepaScore(R) for staging liver fibrosis in chronic hepatitis B: comparison with hepatitis C. *J Hepatol*, *61*(1), 28-34. https://doi.org/10.1016/j.jhep.2014.02.029

Li, A., Gong, H., Zhang, B., Wang, Q., Yan, C., Wu, J., . . . Luo, Q. (2010). Micro-optical sectioning tomography to obtain a high-resolution atlas of the mouse brain. *Science*, *330*(6009), 1404-1408. https://doi.org/10.1126/science.1191776

Li, Y., Xu, J., Wan, P., Yu, T., & Zhu, D. (2018). Optimization of GFP Fluorescence Preservation by a Modified uDISCO Clearing Protocol. *Front Neuroanat*, *12*, 67. https://doi.org/10.3389/fnana.2018.00067

Lichtinghagen, R., Pietsch, D., Bantel, H., Manns, M. P., Brand, K., & Bahr, M. J. (2013). The Enhanced Liver Fibrosis (ELF) score: normal values, influence factors and proposed cut-off values. *J Hepatol*, *59*(2), 236-242. https://doi.org/10.1016/j.jhep.2013.03.016

Liu, J. T. C., Glaser, A. K., Bera, K., True, L. D., Reder, N. P., Eliceiri, K. W., & Madabhushi, A. (2021). Harnessing non-destructive 3D pathology. *Nat Biomed Eng*, *5*(3), 203-218. https://doi.org/10.1038/s41551-020-00681-x

Liu, T., Yang, L., Han, X., Ding, X., Li, J., & Yang, J. (2020). Local sympathetic innervations modulate the lung innate immune responses. *6*(20), eaay1497. https://doi.org/doi:10.1126/sciadv.aay1497

Liu, X. Y., Liu, R. X., Hou, F., Cui, L. J., Li, C. Y., Chi, C., . . . Yin, C. H. (2016). Fibronectin expression is critical for liver fibrogenesis in vivo and in vitro. *Mol Med Rep*, *14*(4), 3669-3675. https://doi.org/10.3892/mmr.2016.5673

Masselink, W., Reumann, D., Murawala, P., Pasierbek, P., Taniguchi, Y., Bonnay, F., . . . Tanaka, E. M. (2019). Broad applicability of a streamlined ethyl cinnamate-based clearing procedure. *Development*, *146*(3). https://doi.org/10.1242/dev.166884

Masuzaki, R., Kanda, T., Sasaki, R., Matsumoto, N., Ogawa, M., Matsuoka, S., . . . Moriyama, M. (2020). Noninvasive Assessment of Liver Fibrosis: Current and Future Clinical and Molecular Perspectives. *Int J Mol Sci*, *21*(14). https://doi.org/10.3390/ijms21144906

McCormick, B. H., Koh, W., Choe, Y., Abbott, L. C., Keyser, J., Mayerich, D., . . . Doddapaneni, P. (2004). Construction of anatomically correct models of mouse brain networks. *Neurocomputing*, *58-60*, 379-386. https://doi.org/https://doi.org/10.1016/j.neucom.2004.01.070

Meglinski, I. V., Churmakov, D. Y., Bashkatov, A. N., Genina, E. A., & Tuchin, V. V. J. L. P. (2003). The Enhancement of Confocal Images of Tissues at Bulk Optical Immersion. *13*, 65-69.

Merz, S. F., Korste, S., Bornemann, L., Michel, L., Stock, P., Squire, A., . . . Totzeck, M. (2019). Contemporaneous 3D characterization of acute and chronic myocardial I/R injury and response. *Nature Communications*, *10*(1), 2312. https://doi.org/10.1038/s41467-019-10338-2

Murray, E., Cho, J. H., Goodwin, D., Ku, T., Swaney, J., Kim, S. Y., . . . Chung, K. (2015). Simple, Scalable Proteomic Imaging for High-Dimensional Profiling of Intact Systems. *Cell*, *163*(6), 1500-1514. https://doi.org/10.1016/j.cell.2015.11.025

Nagula, S., Jain, D., Groszmann, R. J., & Garcia-Tsao, G. (2006). Histological-hemodynamic correlation in cirrhosis-a histological classification of the severity of cirrhosis. *J Hepatol*, *44*(1), 111-117. https://doi.org/10.1016/j.jhep.2005.07.036

Neuberger, J., Patel, J., Caldwell, H., Davies, S., Hebditch, V., Hollywood, C., . . . Heydtmann, M. (2020). Guidelines on the use of liver biopsy in clinical practice from the British Society of Gastroenterology, the Royal College of Radiologists and the Royal College of Pathology. *Gut*, *69*(8), 1382-1403. https://doi.org/10.1136/gutjnl-2020-321299

Nevzorova, Y. A., Boyer-Diaz, Z., Cubero, F. J., & Gracia-Sancho, J. (2020). Animal models for liver disease - A practical approach for translational research. *J Hepatol*, *73*(2), 423-440. https://doi.org/10.1016/j.jhep.2020.04.011

Nojima, S., Susaki, E. A., Yoshida, K., Takemoto, H., Tsujimura, N., Iijima, S., . . . Ueda, H. R. (2017). CUBIC pathology: three-dimensional imaging for pathological diagnosis. *Scientific Reports*, *7*(1), 9269. https://doi.org/10.1038/s41598-017-09117-0

Nudell, V., Wang, Y., Pang, Z., Lal, N. K., Huang, M., Shaabani, N., . . . Ye, L. (2022). HYBRiD: hydrogel-reinforced DISCO for clearing mammalian bodies. *Nature Methods*, *19*(4), 479-485. https://doi.org/10.1038/s41592-022-01427-0

Ohtsuki, G., Nishiyama, M., Yoshida, T., Murakami, T., Histed, M., Lois, C., & Ohki, K. (2012). Similarity of Visual Selectivity among Clonally Related Neurons in Visual Cortex. *Neuron*, *75*(1), 65-72. https://doi.org/https://doi.org/10.1016/j.neuron.2012.05.023

Olson, E., Levene, M. J., & Torres, R. (2016). Multiphoton microscopy with clearing for three dimensional histology of kidney biopsies. *Biomedical Optics Express*, *7*(8), 3089-3096. https://doi.org/10.1364/BOE.7.003089

Pan, C., Cai, R., Quacquarelli, F. P., Ghasemigharagoz, A., Lourbopoulos, A., Matryba, P., . . . Ertürk, A. (2016). Shrinkage-mediated imaging of entire organs and organisms using uDISCO. *Nature Methods*, *13*(10), 859-867. https://doi.org/10.1038/nmeth.3964

Park, Y.-G., Sohn, C. H., Chen, R., McCue, M., Yun, D. H., Drummond, G. T., . . . Chung, K. (2019). Protection of tissue physicochemical properties using polyfunctional crosslinkers. *Nature Biotechnology*, *37*(1), 73-83. https://doi.org/10.1038/nbt.4281

Parlati, L., Régnier, M., Guillou, H., & Postic, C. (2021). New targets for NAFLD. *JHEP Rep*, *3*(6), 100346. https://doi.org/10.1016/j.jhepr.2021.100346

Patel, K., & Sebastiani, G. (2020). Limitations of non-invasive tests for assessment of liver fibrosis. *JHEP Rep*, *2*(2), 100067. https://doi.org/10.1016/j.jhepr.2020.100067

Pimpin, L., Cortez-Pinto, H., Negro, F., Corbould, E., Lazarus, J. V., Webber, L., . . . Committee, E. H. S. (2018). Burden of liver disease in Europe: Epidemiology and analysis of risk factors to identify prevention policies. *J Hepatol*, *69*(3), 718-735. https://doi.org/10.1016/j.jhep.2018.05.011

Pitrone, P. G., Schindelin, J., Stuyvenberg, L., Preibisch, S., Weber, M., Eliceiri, K. W., . . . Tomancak, P. (2013). OpenSPIM: an open-access light-sheet microscopy platform. *Nature Methods*, *10*(7), 598-599. https://doi.org/10.1038/nmeth.2507

Pournik, O., Alavian, S. M., Ghalichi, L., Seifizarei, B., Mehrnoush, L., Aslani, A., . . . Eslami, S. (2014). Inter-observer and Intra-observer Agreement in Pathological Evaluation of Non-alcoholic Fatty Liver Disease Suspected Liver Biopsies. *Hepat Mon*, *14*(1), e15167. https://doi.org/10.5812/hepatmon.15167

Qi, Y., Yu, T., Xu, J., Wan, P., Ma, Y., Zhu, J., . . . Zhu, D. (2019). FDISCO: Advanced solvent-based clearing method for imaging whole organs. *5*(1), eaau8355. https://doi.org/doi:10.1126/sciadv.aau8355

Ratziu, V., Charlotte, F., Heurtier, A., Gombert, S., Giral, P., Bruckert, E., . . . Group, L. S. (2005). Sampling variability of liver biopsy in nonalcoholic fatty liver disease. *Gastroenterology*, *128*(7), 1898-1906. https://doi.org/10.1053/j.gastro.2005.03.084

Ratziu, V., & Friedman, S. L. (2020). Why do so many NASH trials fail? *Gastroenterology*. https://doi.org/10.1053/j.gastro.2020.05.046

Regev, A., Berho, M., Jeffers, L. J., Milikowski, C., Molina, E. G., Pyrsopoulos, N. T., . . . Schiff, E. R. (2002). Sampling error and intraobserver variation in liver biopsy in patients with chronic HCV infection. *Am J Gastroenterol*, *97*(10), 2614-2618. https://doi.org/10.1111/j.1572-0241.2002.06038.x

Renier, N., Adams, E. L., Kirst, C., Wu, Z., Azevedo, R., Kohl, J., . . . Tessier-Lavigne, M. (2016). Mapping of Brain Activity by Automated Volume Analysis of Immediate Early Genes. *Cell*, *165*(7), 1789-1802. https://doi.org/10.1016/j.cell.2016.05.007

Renier, N., Wu, Z., Simon, D. J., Yang, J., Ariel, P., & Tessier-Lavigne, M. (2014). iDISCO: a simple, rapid method to immunolabel large tissue samples for volume imaging. *Cell*, *159*(4), 896-910. https://doi.org/10.1016/j.cell.2014.10.010

Richardson, D. S., & Lichtman, J. W. (2015). Clarifying Tissue Clearing. *Cell*, *162*(2), 246-257. https://doi.org/10.1016/j.cell.2015.06.067

Rosa, H., & Parise, E. R. (2008). Is there a place for serum laminin determination in patients with liver disease and cancer? *World J Gastroenterol*, *14*(23), 3628-3632. https://doi.org/10.3748/wjg.14.3628

Sabdyusheva Litschauer, I., Becker, K., Saghafi, S., Ballke, S., Bollwein, C., Foroughipour, M., . . . Dodt, H. U. (2020). 3D histopathology of human tumours by fast clearing and ultramicroscopy. *Sci Rep*, *10*(1), 17619. https://doi.org/10.1038/s41598-020-71737-w

Sanyal, A. J., Harrison, S. A., Ratziu, V., Abdelmalek, M. F., Diehl, A. M., Caldwell, S., . . . Goodman, Z. (2019). The Natural History of Advanced Fibrosis Due to Nonalcoholic Steatohepatitis: Data From the Simtuzumab Trials. *Hepatology*, *70*(6), 1913-1927. https://doi.org/10.1002/hep.30664

Scheuer, P. J. (1991). Classification of chronic viral hepatitis: a need for reassessment. *J Hepatol*, *13*(3), 372-374. https://doi.org/10.1016/0168-8278(91)90084-o

Schwarz, M. K., Scherbarth, A., Sprengel, R., Engelhardt, J., Theer, P., & Giese, G. (2015). Fluorescent-protein stabilization and high-resolution imaging of cleared, intact mouse brains. *PLoS One*, *10*(5), e0124650. https://doi.org/10.1371/journal.pone.0124650

Segovia-Miranda, F., Morales-Navarrete, H., Kucken, M., Moser, V., Seifert, S., Repnik, U., . . . Zerial, M. (2019). Three-dimensional spatially resolved geometrical and functional models of human liver tissue reveal new aspects of NAFLD progression. *Nat Med*, *25*(12), 1885-1893. https://doi.org/10.1038/s41591-019-0660-7

Serafin, R., Xie, W., Glaser, A. K., & Liu, J. T. C. (2020). FalseColor-Python: A rapid intensity-leveling and digital-staining package for fluorescence-based slide-free digital pathology. *PLoS One*, *15*(10), e0233198. https://doi.org/10.1371/journal.pone.0233198

Singh, S., Venkatesh, S. K., Wang, Z., Miller, F. H., Motosugi, U., Low, R. N., . . . Ehman, R. L. (2015). Diagnostic performance of magnetic resonance elastography in staging liver fibrosis: a systematic review and meta-analysis of individual participant data. *Clin Gastroenterol Hepatol*, *13*(3), 440-451.e446. https://doi.org/10.1016/j.cgh.2014.09.046

Spalteholz, W. (1914). *Uber das Durchsichtigmachen von menschlichen und tierischen Pr??paraten und seine theoretischen Bedingungen, nebst Anhang: Uber Knochenf??rbung*. S. Hirzel.

Sporea, I., Sirli, R., Deleanu, A., Tudora, A., Popescu, A., Curescu, M., & Bota, S. (2010). Liver stiffness measurements in patients with HBV vs HCV chronic hepatitis: a comparative study. *World J Gastroenterol*, *16*(38), 4832-4837. https://doi.org/10.3748/wjg.v16.i38.4832

Standish, R. A., Cholongitas, E., Dhillon, A., Burroughs, A. K., & Dhillon, A. P. (2006). An appraisal of the histopathological assessment of liver fibrosis. *Gut*, *55*(4), 569-578. https://doi.org/10.1136/gut.2005.084475

Staudt, T., Lang, M. C., Medda, R., Engelhardt, J., & Hell, S. W. (2007). 2,2'-thiodiethanol: a new water soluble mounting medium for high resolution optical microscopy. *Microsc Res Tech*, *70*(1), 1-9. https://doi.org/10.1002/jemt.20396

Steinke, H., & Wolff, W. (2001). A modified Spalteholz technique with preservation of the histology. *Ann Anat*, *183*(1), 91-95. https://doi.org/10.1016/s0940-9602(01)80020-0

Stelzer, E. H. K., Strobl, F., Chang, B.-J., Preusser, F., Preibisch, S., McDole, K., & Fiolka, R. (2021). Light sheet fluorescence microscopy. *Nature Reviews Methods Primers*, *1*(1), 73. https://doi.org/10.1038/s43586-021-00069-4

Suk, K. T. (2014). Hepatic venous pressure gradient: clinical use in chronic liver disease. *Clin Mol Hepatol*, *20*(1), 6-14. https://doi.org/10.3350/cmh.2014.20.1.6

Susaki, E. A., Tainaka, K., Perrin, D., Kishino, F., Tawara, T., Watanabe, T. M., . . . Ueda, H. R. (2014). Whole-brain imaging with single-cell resolution using chemical cocktails and computational analysis. *Cell*, *157*(3), 726-739. https://doi.org/10.1016/j.cell.2014.03.042

Susaki, E. A., Tainaka, K., Perrin, D., Yukinaga, H., Kuno, A., & Ueda, H. R. (2015). Advanced CUBIC protocols for whole-brain and whole-body clearing and imaging. *Nature Protocols*, *10*(11), 1709-1727. https://doi.org/10.1038/nprot.2015.085

Suzuki, A., Angulo, P., Lymp, J., Li, D., Satomura, S., & Lindor, K. (2005). Hyaluronic acid, an accurate serum marker for severe hepatic fibrosis in patients with non-alcoholic fatty liver disease. *Liver Int*, *25*(4), 779-786. https://doi.org/10.1111/j.1478-3231.2005.01064.x

Tainaka, K., Murakami, T. C., Susaki, E. A., Shimizu, C., Saito, R., Takahashi, K., . . . Ueda, H. R. (2018). Chemical Landscape for Tissue Clearing Based on Hydrophilic Reagents. *Cell Rep*, *24*(8), 2196-2210.e2199. https://doi.org/10.1016/j.celrep.2018.07.056

Taylor-Weiner, A., Pokkalla, H., Han, L., Jia, C., Huss, R., Chung, C., . . . Younossi, Z. M. (2021). A Machine Learning Approach Enables Quantitative Measurement of Liver Histology and Disease Monitoring in NASH. *Hepatology*, *74*(1), 133-147. https://doi.org/10.1002/hep.31750

Tomer, R., Ye, L., Hsueh, B., & Deisseroth, K. (2014). Advanced CLARITY for rapid and high-resolution imaging of intact tissues. *Nature Protocols*, *9*(7), 1682-1697. https://doi.org/10.1038/nprot.2014.123

Tovo, C. V., Villela-Nogueira, C. A., Leite, N. C., Panke, C. L., Port, G. Z., Fernandes, S., . . . de Mattos, A. A. (2019). Transient hepatic elastography has the best performance to evaluate liver fibrosis in non-alcoholic fatty liver disease (NAFLD). *Ann Hepatol*, *18*(3), 445-449. https://doi.org/10.1016/j.aohep.2018.09.003

Tsai, P. S., Kaufhold, J. P., Blinder, P., Friedman, B., Drew, P. J., Karten, H. J., . . . Kleinfeld, D. (2009). Correlations of neuronal and microvascular densities in murine cortex revealed by direct counting and colocalization of nuclei and vessels. *J Neurosci*, *29*(46), 14553-14570. https://doi.org/10.1523/JNEUROSCI.3287-09.2009

Tsochatzis, E., Bruno, S., Isgro, G., Hall, A., Theocharidou, E., Manousou, P., . . . Luong, T. V. (2014). Collagen proportionate area is superior to other histological methods for sub-classifying cirrhosis and determining prognosis. *J Hepatol*, *60*(5), 948-954. https://doi.org/10.1016/j.jhep.2013.12.023

Tsuchida, T., Lee, Y. A., Fujiwara, N., Ybanez, M., Allen, B., Martins, S., . . . Friedman, S. L. (2018). A simple diet- and chemical-induced murine NASH model with rapid progression of steatohepatitis, fibrosis and liver cancer. *J Hepatol*, *69*(2), 385-395. https://doi.org/10.1016/j.jhep.2018.03.011

Vaz, M. A. B., Pacheco, P. S., Seidel, E. J., & Ansuj, A. P. (2017). Classification of the coefficient of variation to variables in beef cattle experiments. *Ciência Rural*, *47*(11). https://doi.org/10.1590/0103-8478cr20160946

Wang, Y., Wong, G. L.-H., He, F.-P., Sun, J., Chan, A. W.-H., Yang, J., . . . Wong, V. W.-S. (2020). Quantifying and monitoring fibrosis in non-alcoholic fatty liver disease using dual-photon microscopy. *Gut*, *69*(6), 1116. https://doi.org/10.1136/gutjnl-2019-318841

Wang, Y., Zhang, D. H., Zhang, J. Y., Chen, N., & Zhi, G. Y. (2016). High-yield synthesis of bioactive ethyl cinnamate by enzymatic esterification of cinnamic acid. *Food Chem*, *190*, 629-633. https://doi.org/10.1016/j.foodchem.2015.06.017

Wells, R. G. (2008). Cellular sources of extracellular matrix in hepatic fibrosis. *Clin Liver Dis*, *12*(4), 759-768, viii. https://doi.org/10.1016/j.cld.2008.07.008

Woo, J., Lee, M., Seo, J. M., Park, H.-S., Cho, Y. E. J. E., & Medicine, M. (2016). Optimization of the optical transparency of rodent tissues by modified PACT-based passive clearing. *48*.

Xu, J., & Kisseleva, T. (2015). Bone marrow-derived fibrocytes contribute to liver fibrosis. *Exp Biol Med (Maywood)*, *240*(6), 691-700. https://doi.org/10.1177/1535370215584933

Xu, Q., Sheng, L., Bao, H., Chen, X., Guo, C., Li, H., . . . Hua, J. (2017). Evaluation of transient elastography in assessing liver fibrosis in patients with autoimmune hepatitis. *J Gastroenterol Hepatol*, *32*(3), 639-644. https://doi.org/10.1111/jgh.13508

Yang, B., Treweek, J. B., Kulkarni, R. P., Deverman, B. E., Chen, C. K., Lubeck, E., . . . Gradinaru, V. (2014). Single-cell phenotyping within transparent intact tissue through whole-body clearing. *Cell*, *158*(4), 945-958. https://doi.org/10.1016/j.cell.2014.07.017

Younossi, Z., Anstee, Q. M., Marietti, M., Hardy, T., Henry, L., Eslam, M., . . . Bugianesi, E. (2018). Global burden of NAFLD and NASH: trends, predictions, risk factors and prevention. *Nat Rev Gastroenterol Hepatol*, *15*(1), 11-20. https://doi.org/10.1038/nrgastro.2017.109

Yu, T., Qi, Y., Zhu, J., Xu, J., Gong, H., Luo, Q., & Zhu, D. (2017). Elevated-temperature-induced acceleration of PACT clearing process of mouse brain tissue. *Scientific Reports*, *7*(1), 38848. https://doi.org/10.1038/srep38848

Yushchenko, D. A., & Schultz, C. (2013). Tissue clearing for optical anatomy. *Angew Chem Int Ed Engl*, *52*(42), 10949-10951. https://doi.org/10.1002/anie.201306039

Zhao, S., Todorov, M. I., Cai, R., Maskari, R. A., Steinke, H., Kemter, E., . . . Erturk, A. (2020). Cellular and Molecular Probing of Intact Human Organs. *Cell*, *180*(4), 796-812 e719. https://doi.org/10.1016/j.cell.2020.01.030

Zheng, H., & Rinaman, L. (2016). Simplified CLARITY for visualizing immunofluorescence labeling in the developing rat brain. *Brain Struct Funct*, *221*(4), 2375-2383. https://doi.org/10.1007/s00429-015-1020-0

Zhu, J., Ma, Y., Xu, J., Li, Y., Wan, P., Qi, Y., . . . Zhu, D. (2021). Dec-DISCO: decolorization DISCO clearing for seeing through the biological architectures of heme-rich organs. *Biomed Opt Express*, *12*(9), 5499-5513. https://doi.org/10.1364/BOE.431397

Zhu, J., Yu, T., Li, Y., Xu, J., Qi, Y., Yao, Y., . . . Zhu, D. (2020). MACS: Rapid Aqueous Clearing System for 3D Mapping of Intact Organs. *Adv Sci (Weinh)*, *7*(8), 1903185. https://doi.org/10.1002/advs.201903185